Fall 5-22-2015

Electrolyte Effects on the Kinetics of Comproportionation Electron-Transfer Reactions and on Intervalence Charge-Transfer Band Energies of Binuclear Ruthenium Ammine Complexes

Zhiji Han
galaxyhan@gmail.com

Electrolyte Effects on the Kinetics of Comproportionation Electron-Transfer Reactions and on Intervalence Charge-Transfer Band Energies of Binuclear Ruthenium Ammine Complexes

A Thesis Presented to the Faculty
of the Department of Chemistry
at the University of San Francisco
in partial fulfillment of the requirements for the Degree of
Master of Science in Chemistry

Written by

Zhiji Han

06/01/12

Electrolyte Effects on the Kinetics of Comproportionation Electron-Transfer Reactions and on Intervalence Charge-Transfer Band Energies of Binuclear Ruthenium Ammine Complexes

Thesis Written by Zhiji Han

This thesis is written under the guidance of the Faculty Advisory Committee, and approved by all its members, has been accepted in partial fulfillment of the requirements for the degree of

Master of Science
in Chemistry
at
the University of San Francisco

Thesis Committee

Prof. Jeff C. Curtis, Ph.D.
Research Advisor

Prof. Lawrence Margerum, Ph.D.
Professor

Prof. Jie Jack Li, Ph.D.
Associate Professor

Prof. Marcelo Camperi, Ph.D.
Dean, College of Arts and Sciences

Acknowledgement

I would like to thank my advisor Professor Jeff Curtis for his invaluable guidance and support during my study. I would also like to thank Dr. Margerum for his support and guidance in teaching. I also like to thank Drs. Melaugh, Cobley, Li for their invaluable support and advice.

I also wish to thank the chemistry staff for their great help: Messrs. Jeff Oda, Andy Huang, Charles George, Javier Lacayo, Nick Spina, Ms. Deidre Shymanski, and Dorothy Stuebner.

I want to thank all the members from the Curtis's group, and especially Po-Kai Chen, Prakash Sista, Yishun Qin for helpful discussions.

Last but not least, I would like to thank my family and Feifei Wang for always being supportive.

Table of Contents

List of Tables

List of Figures

Abstract

Chapter 1 describes an overview of electron-transfer reactions. The kinetic equations for ET reactions have also been described in detail.

Chapter 2 describes a series of novel kinetic accelerations which deviate strongly from the predictions of the classical Debye-Huckle theory with a range of different added “inert” electrolytes. The greater catalytic effects seen with the heavier halides and other catalytic electrolytes (especially certain dicarboxylates) indicate an important role for hole-transfer superexchange in the ET transition state. The hypothesis of a catalytic ternary association complex, [RuII--X--RuIII] has also been explored by kinetic modeling of the reaction. An increasing ratio of anion-catalyzed k_{etx} to uncatalyzed k_{et} is obtained when proceeding down the halide series. Activation parameters show a strong enthalpy-entropy compensation effect according to the identity of the added halide. Interestingly, the enthalpy activation decreases successively upon going to the heavier halides and in fact $\Delta H^{\ddagger}$ becomes negative in the most extreme case of added I^-.

Chapter 3 describes a detailed study of electrolyte effects on the position and band shape of the intervalence charge transfer (IVCT) band of dimeric systems in aqueous solution such as $(NH_3)_5Ru^{II}$-(bis-bipyridylethylene)-$Ru^{III}(NH_3)_5$(5+). Unexpectedly, the energetics of optical electron transfer blue shift upon adding F^- but red shift upon adding other halides. This interesting observation correlates with the known water structure “making” or “breaking” effects of the added halide anions

Chapter One

Introduction to Electron Transfer Reactions

Electron exchange between an acceptor and a donor can be described as one of the most basic of all chemical reactions. We know that animals and plants live by the action of their biochemical respiration and photosynthesis systems. These complex reaction networks depend, inpart, on the facile exchange of protons and/or electrons at various elementary steps embedded within these networks.[1]

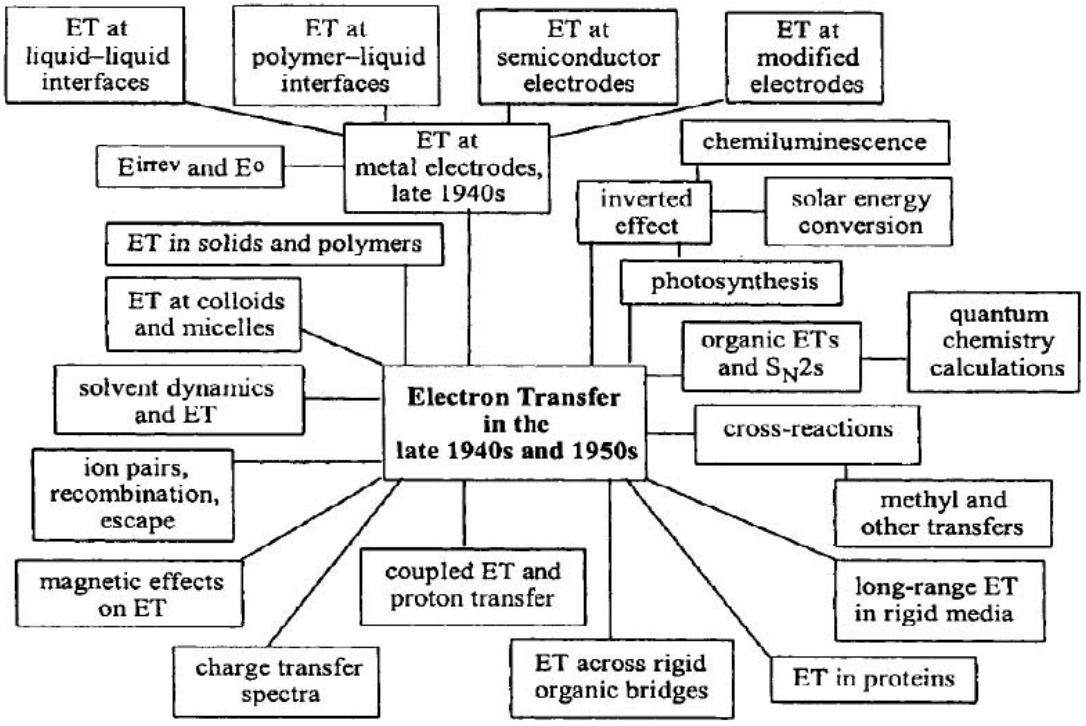

Figure 1-1. Examples of various topics relevant to the electron transfer field (see

ref. 1)

From the 1950s onward, the field of electron-transfer (ET) studies became one of the most active research areas in chemistry. After its tremendous expansion into different applied disciplines (see Figure 1-1) and theoretical areas over the past half century, now it plays a fundamental role in efforts towards solving some of the urgent problems facing humanity such as the energy crisis and environment pollution. Each advance towards a deeper understanding of electron transfer also brings potential progress towards solving related problems in inorganic, organic, bio-, and physical chemistry.

Based on the differences in mechanism grasped early on by 1983 Nobel laureate Henry Taube,[1a] ET reactions were found to be divisible into two broad categories; “inner-sphere” and “outer-sphere” ET. The inner-sphere mechanism was first described by Taube in his elegant experiments using first-row transition metal complexes. In the experiment, substitution a labile $[Cr(H_2O)_6]^{2+}$ reductant and an inert $[CoCl(NH_3)_6]^{2+}$ oxidant were shown to form a well-organized μ-Cl-bridged precursor complex as crucial step in the mechanism. After an electron was transferred to form the new inert $[CrCl(H_2O)_5]^{2+}$ and labile $[Co(NH_3)_5(H_2O)]^{2+}$ complexes, the Cl^- as a ligand originally attached to cobalt (III) was transferred to form a bond with the now kinetically-inert aqueous chromic (III). Radioactive $^{36}Cl^-$ tracer ion was used to prove that the transfer of Cl^- was from the oxidizing reagent.[1a] The overall reaction is as shown below,

$$[CoCl(NH_3)_6]^{2+} + [Cr(H_2O)_6]^{2+} \rightarrow [CrCl(H_2O)_5]^{2+} + [Co(NH_3)_5(H_2O)]^{2+} \qquad (1\text{-}0)$$

In outer-sphere ET reactions, there is no chemical bond breaking or forming and there is no direct bridging ligand between oxidant and reductant during the electron-transfer process. Libby[1e] was the first to apply the Frank-Condon principle in attempts to explain the rates of self-exchange ET reactions. Marcus[3] proposed a more complete explanation by reconciling both Frank-Condon and formalized energy conservation conditions in his approach and he received the Nobel Prize in 1992 for his theoretical contributions. He explained that in order for thermally-induced electron-transfer to happen stochastic fluctuations along some definable nuclear coordinate had to occur. He introduced the important concept of the reorganization energy "λ" (which will be further described in the coming section) in his interpretation of the factors governing the rate of ET.

Electron transfer in solution can occur between redox reactants through two clearly separable pathways, either optically or thermally (see Figure 1-2). In the optical pathway, as the electron donor (2+) and the acceptor (3+) continually collide in the solvent and come close enough to each other at times, the overlap of their electronic wave functions may be sufficient to allow for radiation-induced electron transfer. In other words, there is a probability that a photon of the correct energy can be absorbed so as to excite the electron in its HOMO (largely centered on the donor) to the LUMO of the acceptor (3+). This spectroscopic absorption process occurs rapidly on the timescale of nuclear motions and thus obeys the Franck-Condon principle. A pair of high energy intermediates ("λ" above the ground state, see Figure 1-3) is generated at this step before they have enough

time for any nuclear reorganization (hence the asterisk on the non-equilibrated product ion pair in the upper branch of figure 1-2). Finally, the intermediate relaxes to products by reorganizing to the appropriate nuclear wave function corresponding to the products' electronic distribution (followed in this case by diffusion apart to form separated product ions).

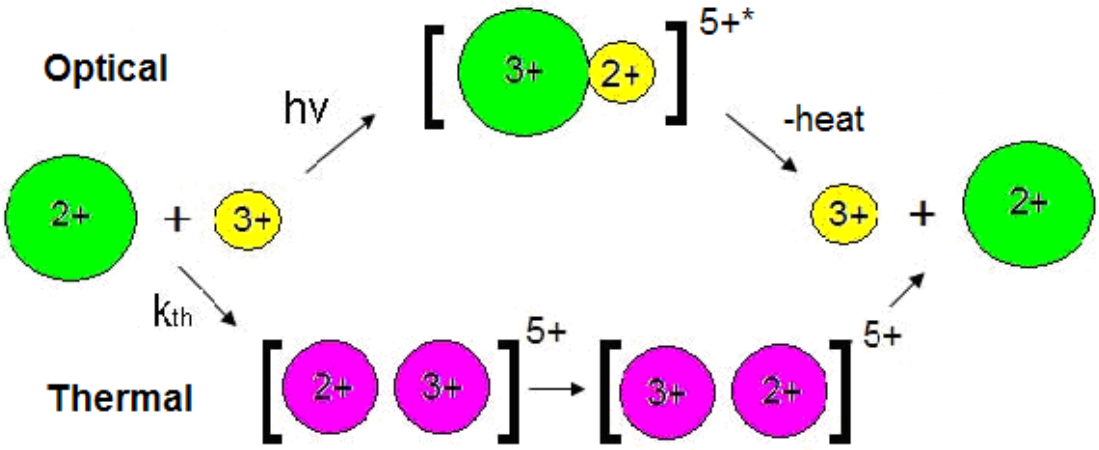

Figure 1-2 Schematic illustration of the optical and thermal electron-transfer pathways. (The 2+ ion is the "donor" and 3+ is the acceptor)

In the thermal pathway, in the absence of any incident radiation, the electron donor and acceptor with different nuclear configurations in the encounter complex need to adjust their first and second coordination shells to the same configuration and the same total energy as a necessary step towards electron-transfer. The overlap of the donor and acceptor electronic wave functions in this encounter complex is called the "resonance energy" H_{AB} (see Figure 1-3) and this is what

makes it possible for the electron to tunnel from donor to acceptor. This electron-transfer step is also an “electronic transition” and thus it is governed by the Franck-Condon principle which requires it to happen at essentially constant nuclear configuration and momentum. The product ion-pair formed after the electron-transfer then relaxes and dissociates to the final separated products. Both photo-induced (or “optical”) electron-transfer and thermal electron-transfer were studied in the work to be described in this thesis and will be discussed in greater detail in the following chapters.

In the case of optical electron transfer, the reactants are taken “vertically” to the product’s electronic configuration by absorbing a photon which satisfied the resonance condition defined by λ (see Figure 1-3). This is called a “vertical” process because the nuclei remain fixed on the timescale of the photon absorption event (which is on the order of optical frequencies, ~ 10^{-15} sec). In the thermally-activated case, ET happens (at least sometimes, *vide infra*) when stochastic fluctuations bring the reactants to the intersection region on Figure 1-3 where the zero-order surfaces cross.

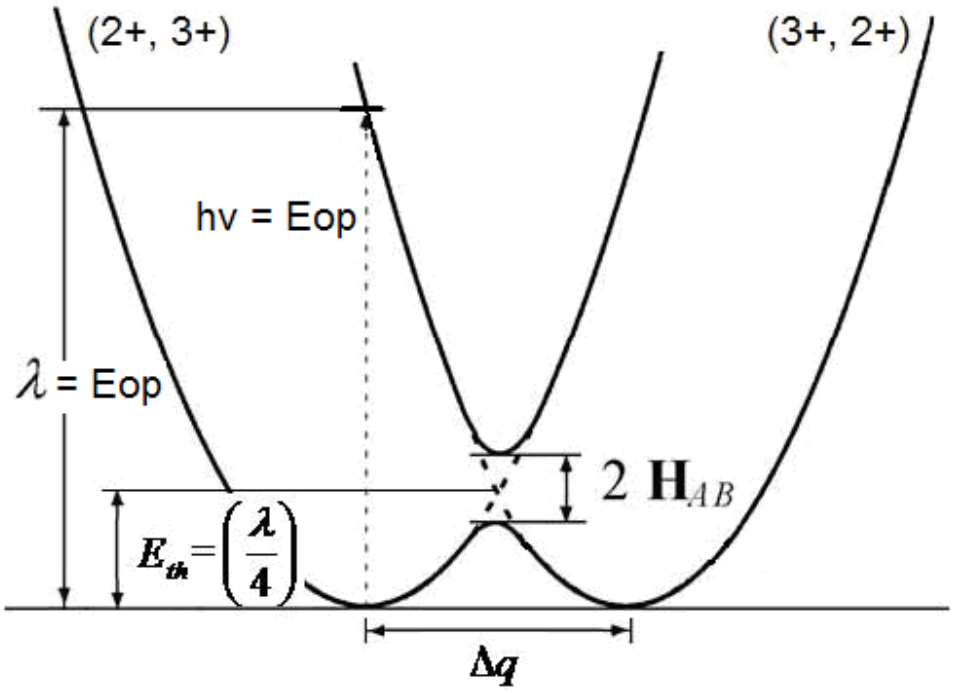

Figure 1-3 Schematic diagram showing a simple two-dimensional representation of potential energy surfaces governing a true "self-exchange" electron-transfer reaction. Here the driving force $\Delta G^0 = 0$ and $\triangle q$ is the change in the nuclear coordinates between reactants and products. H_{ab} is the electronic "coupling element" (or "resonce energy") between donor and acceptor at the intersection region and λ is the nuclear reorganization (or Franck-Condon) energy.

The bimolecular outer-sphere electron-transfer reaction between hexacoordinate metal complexes is shown below

$$ML_6^{3+} + ML_6^{2+} \overset{k_{ex}}{\rightleftharpoons} ML_6^{2+} + ML_6^{3+} \qquad (1\text{-}1)$$

It is the simplest case in deriving the electron transfer rate equation because no bonds are formed or broken along the reaction coordinated. Equation 1-1 is

generally treated as a sequence of identifiable steps,[2]

$$ML_6^{3+} + ML_6^{2+} \underset{k_d}{\overset{k_a}{\rightleftharpoons}} ML_6^{3+} \,|\, ML_6^{2+} \qquad (1\text{-}2)$$

$$ML_6^{3+} \,|\, ML_6^{2+} \underset{k_{-et}}{\overset{k_{et}}{\rightleftharpoons}} ML_6^{2+} \,|\, ML_6^{3+} \qquad (1\text{-}3)$$

$$ML_6^{2+} \,|\, ML_6^{3+} \underset{k_{a2}}{\overset{k_{d2}}{\rightleftharpoons}} ML_6^{2+} + ML_6^{3+} \qquad (1\text{-}4)$$

In the first step of this thermal electron-transfer reaction, the reactants associate to form a “precursor complex” (eq. 1-2). Second step involves an electron-transfer step within this precursor complex to form a successor complex (see eq. 1-3). The final step is the dissociation for the successor complex to form the products (eq. 1-4).

According to classical electron-transfer theories, electron transfer is required to occur at the intersection region of the 3N-6-dimensional potential energy surface describing reactants/products/surrounding solvent system where N is the number of the nuclear coordinates which respond to the electronic distribution (see Figure 1-3).[9] Any effective orbital resonance interaction between the reactants will create a larger distortion of the potential surfaces at the intersection thus causing a decrease in the thermal activation energy. If the resonance energy H_{AB} is large enough, then electron transfer to occur with unit probability whenever the system oscillates into the intersection region (the “adiabatic” case). The first-order rate

constant for the electron transfer within the precursor (encounter) complex in the high temperature limit is then described as below,

$$k_{et} = \nu_n e^{-E_{th}/RT} \qquad \text{(1-5)}^{3,4a}$$

where ν_n is the effective vibration frequency of the reactants (see equation 1-6) and is usually taken to about $k_b T/h$ or 10^{13} H_z,[6,7] and E_{th} is the activation energy for thermal electron-transfer,

$$\nu_n{}^2 = \frac{\nu_{in}{}^2 E_{in} + \nu_{out}{}^2 E_{out}}{E_{in} + E_{out}} \approx \frac{k_b T}{h} \qquad \text{(1-6)}^{7}$$

Here E_{in} and E_{out} are the (assumed) temperature-independent inner-sphere and outer-sphere reorganization energies; ν_{in} and ν_{out} are the inner-sphere and outer-sphere effective nuclear vibration frequencies (k_b is the Boltzmann's constant and the h is the Planck constant).

In the classical model, the entropy contribution to the activational energy is usually assumed to be negligible, so that E_{th} (an internal potential energy due to nuclear displacement) is then approximately equal to ΔG^*_{th}. Marcus[3] theory describes this activation energy as,

$$E_{th} = \Delta G^*_{th} = \frac{\lambda}{4}\left(1 + \frac{\Delta G^o}{\lambda}\right)^2 \qquad \text{(1-7)}^{3,8}$$

where ΔG^*_{th} is the free energy required to achieve the activated-complex configuration, and ΔG^0 is the thermodynamic driving force of the reaction.

The reorganization energy λ is considered as the total reorganization energy which is composed of two major parts (equation 1-8, 1-9 and 1-10). The inner-sphere λ_{in} is due to intramolecular bond length and bond angle vibration. The outer-sphere component λ_{out} is due to solvent-solute interactions and solvent dipole-dipole interactions and can be treated approximately using dielectric continuum theory (*vide infra*).

$$\lambda = \lambda_{in} + \lambda_{out} \qquad \text{(1-8)}^{2b,8,9}$$

$$\lambda_{in} = E_{in} - RT \ln \frac{Q^*}{\prod_i Q_i}$$

$$= \sum_i \left[\frac{(2 f_M f_L)}{f_M + f_L} \right]_i (\Delta d_{M-L})_i^2 - RT \ln \frac{Q^*}{\prod_i Q_i} \qquad \text{(1-9)}^{4a}$$

Here the sum and products are taken into account of all ligands bonded to the metal center, f_M and f_L are the symmetric breathing force constants of the metal center and the bonded ligand groups, Δd_{M-L} is the metal to ligand distance change in Angstrom units upon going from reactants to products, and the Q are resulting vibrational partition functions.

Applying dielectric continuum theory to the reorganization energy of the surrounding medium, both Marcus[3] and Hush[4b] were able to show that λ_{out} could be approximately as,

$$\lambda_{out} = E_{out} = (\Delta e_0)^2 \left(\frac{1}{2a_2} + \frac{1}{2a_3} - \frac{1}{r} \right) \left(\frac{1}{n^2} - \frac{1}{D_s} \right) \quad \text{(1-10)}^{2b,8,9}$$

where Δe_0 is the charge transferred, λ and λ are the radii of the donor and acceptor sites, r is the separation of the metal centers in the activated complex (generally taken as the close-contact distance a_2 + a_3), n is the refractive index which is equal to $\sqrt{\varepsilon_r \mu_r}$ (λ is the material's relative permittivity , and μ_r is its relative permeability), and D_s is the static dielectric constant of the medium which depends on the temperature and density (78.54 for water at 25°C).[10]

By considering the "diabatic" case in which H_{AB} is small and electron transfer does not occur with unit probability at the intersection region, the electronic transmission coefficient κ_{el} ($0 \leq \kappa_{el} \leq 1$) is introduced to link the classical and quantum mechanical rate expressions. Eq 1-5 can then be expressed as,

$$k_{et} = \nu_n \kappa_{el} e^{-\Delta G_{th} / RI} \quad \text{(1-11)}^{11}$$

and κ_{el} is given by

$$\kappa_{el} = \frac{2P_{12}{}^{o}}{1 + P_{12}{}^{o}} \quad \text{(1-12)}^{11}$$

In 1-12 $P_{12}{}^{o}$ is the probability for the electron transfer to occur per single passage into the intersection and it is quantitatively determined by the resonance energy H_{AB} and the slopes of the potential surface (s_A, s_B) on either side of the intersection

region. A weaker resonance interaction between the reactants and steeper slopes of the potential curves will mean that the electron transfer probability is less. $P_{12}{}^{o}$ is given by,

$$P_{12}{}^{o} = 1 - e^{\frac{-4\pi^2 H_{AB}{}^2}{h v |s_A - s_B|}} \qquad (1\text{-}13)^{12}$$

where v is the average velocity of the system as it moves through the intersection and is taken as the Boltzmann averaged velocity $(2RT/\mu\pi)^{1/2}$ where μ is the effective mass.[12]

According to Ulstrup,[11] $v|s_A - s_B|$ is equal to $4v_n(\pi RT(E_{out} + E_{in}))^{1/2}$. Eq 1-11 can be written in the "semi-classical"[4a] form as,

$$k_{et} = \frac{2H_{AB}{}^2}{h}\left(\frac{\pi^3}{(E_{out} + E_{in})RT}\right)^{1/2} e^{-(\lambda_{in}+\lambda_{out})/4RT} \qquad (1\text{-}14)$$

The temperature-dependence of the rate constants of electron-transfer reactions is complicated, but relevant information can be obtained from equations 1-9, 1-10 and 1-14 (the temperature dependence of H_{AB} is not considered here).

For a self-exchange ET reaction ($\Delta G^o = 0$, and assumed $\Delta G^*{}_\lambda = \lambda/4$ where $\Delta G^*{}_\lambda$ is the free energy required to reorganize the reactants prior to ET (= $\Delta G_o{}^{\neq}$)) and according to Brunschwig and Sutin,[4a] $\Delta H^*{}_\lambda$ (the enthalpic contribution to $\Delta G^*{}_\lambda$) is given by,

$$\Delta H^*{}_\lambda = \Delta H^*{}_{in} + \Delta H^*{}_{out} \qquad (1\text{-}15)$$

$$\Delta H^{*}_{in} = \left\langle E^{a}{}_{in} \right\rangle_{R} + \frac{RT}{2}\left(\frac{E_{in}}{E_{in}+E_{out}}\right) \qquad (1\text{-}16)^{4a}$$

$$\Delta H^{*}_{out} = \left\langle E^{a}{}_{out} \right\rangle_{R} + \frac{RT}{2}\left(\frac{E_{out}}{E_{in}+E_{out}}\right) \qquad (1\text{-}17)^{4a}$$

where $\left\langle E^{a}{}_{in} \right\rangle_{R}$ and $\left\langle E^{a}{}_{out} \right\rangle_{R}$ are the averaged inner- and outer- sphere reorganization energies of all the molecules.

Nuclear tunneling under/through the activational barrier is considered to be negligible at high temperatures (generally including room temperature as well for the solvent modes)[4a] The tunneling correction is only important at low temperatures for ET reactions with large inner-sphere barriers. The nuclear tunneling factor "Γ_n" is defined as the ratio of the rate constant at temperature T to the rate constant at the high temperature limit,

$$\Gamma_n = \frac{k_{et}(T)}{k_{et}(T=\infty)} = e^{\frac{-(4\lambda_{in}-E_{in})}{4RT}} \qquad (1\text{-}18)^{4a}$$

where λ in and E_{in} are the same definitions as in equations 1-5 through 1-10.

From eq 1-14, the rate constant within the precursor complex is dependent on three major terms, the driving force of the reaction, the temperature dependent/ independent reorganization energies, and the resonance energy H_{AB}.

The ET driving force is determined by the redox potential difference between the two redox couples in the reaction. The reorganization energy (also called Frank–Condon barrier), as described earlier, is the total energy for the nuclear

relaxation to equilibrium with the new molecular electronic wave function. Importantly, this quantity includes the outer-sphere solvent shell reorganization (consisting primarily of charge-mainly dipole interactions) which happens after optical electron-transfer (see equation 1-10) or during the course of thermally-activated ET. Central to the work to be described in this thesis is the fact that added "innocent" or inert electrolyte species can directly affect the rates of bimolecular ET reactions by modulating the association equilibrium shown in equation 1-2. Additionally, electrolytes can change the structure of water and thus affect the solvent reorganization energy λ. This will have effects on both thermal and optical ET (details of these effects on optical ET topic will be discussed in Chapter 3).

H_{AB} (see Figure 1-3 and equation 1-13 and 1-14) is the electronic wave function coupling matrix element between the reactant and product states. Larger coupling will favor the electron tunneling which takes the system from the reactant's to the product's electronic surface whenever thermal fluctuations bring the system to the crossing point in Figure 1-3. A larger H_{AB} will thus make the electron-transfer reaction faster. The magnitude of this electronic interaction is dependent on the detailed nature of the donor and acceptor wavefunctions and also the distance between them and the nature of the intervening medium (which might be solvent or some covalent bridge or even some electrolyte species). Longer separations (as are common in the biological systems such as ET through proteins), will slow down ET rate constants exponentially,[13] but the presence of the

proteinaceous bridging material linking the donor and acceptor is known to dramatically increase the ET rate compared to what it would be if only vaccum filled this space. Extensive work on inorganic systems[9] has shown that providing a bridging conjugated system between donor and acceptor can greatly enhance the electronic coupling even at fairly large separations.[14]

Figure 1-4 shows us a sequential picture of how the relationship between the electronic coupling element H_{AB} and the reorganizational energy λ affect the reaction potential energy surfaces. When H_{AB} is close to 0 (Fig 1-4a), the coupling is so small that the system and the probability of ET with each excursion into the intersection region is small (see equation 1-12 and 1-13). As H_{AB} increases (panel b) there is a moderate interaction between the reactants and the degeneracy of the two potential surfaces at the intersection region will be removed and the reaction will become "adiabatic" with κ_{el} in equation 1-12 tending towards unity. Fig. 1-4c is the extreme case when the electronic coupling is so great that it exceeds $\lambda/2$ and the activation energy goes to zero in the "delocalized limit".[9]

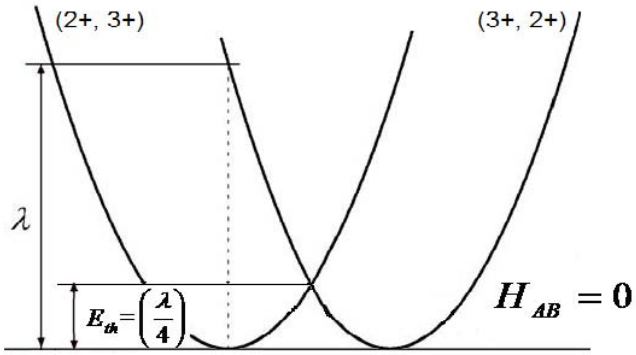

(a)

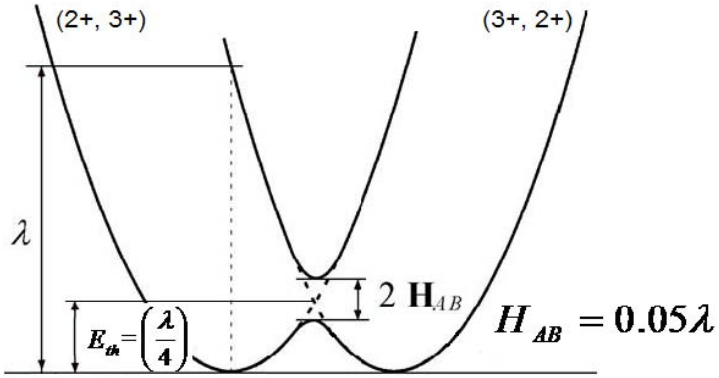

(b)

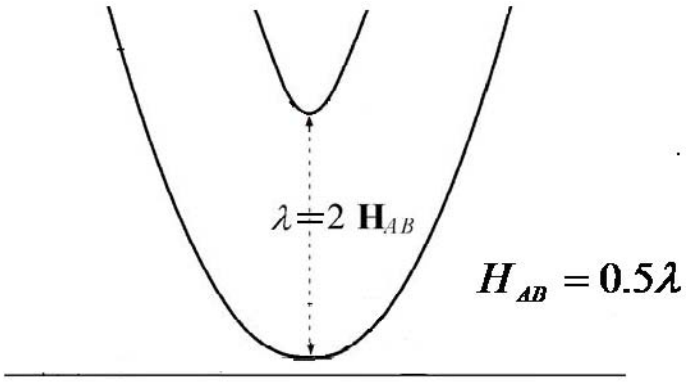

(c)

Figure 1-4. Potential energy *vs.* nuclear configuration for a symmetric mixed-valence complex as a function of H_{AB} and λ

For a non-adiabatic electron-transfer reaction where the probability for the electron transfer at the intersection region is small, Fermi's golden rule as modified by Levich[15], Van Duyne and Fisher[16c] and others provides us with a quantum mechanical treatment for the probability that electron tunneling will take the system from one vibronic energy through one energy eigenstate of the reactant's surface to an energy-matched eigenstate of the product's. The probability per unit time that a quantum system in an initial vibronic state "Av" will pass to a continuum set of continuum of vibronic levels is given by,

$$W_{Av} = \frac{4\pi^2 H_{AB}{}^2}{h} \rho_w \qquad (1\text{-}19)^{15,16}$$

where ρ_w is the density of final states (number of states per unit of energy). This is the origin of the factor of H_{AB}^2 in the pre-exponential term in equation 1-14.

"Quantum superexchange"[17] and "electron hopping"[18] are two quantum mechanisms which are used broadly in explaining the details of long range electron-transfer biological in systems.[19] For example, an electron "hole" can be generated by photoexcitation such that a low-oxidation potential site (such as guanine) holds a mobile positive charge carrier (hole) on a strand of DNA. This hole can move down the nucleotide chain to another low-potential site for the completion of the electron-transfer reaction. In this process, intervening base sites such as adenine, thymine, and cytosine can act as bridges between the guanines. In the quantum superexchange picture, the electron tunneling between donor and acceptor takes place due to the presence of "virtual" states in which either

electrons or holes (electron vaconcies) are localized on intervening bridge sites. The virtual states are not “populated” and have no definable lifetime. They play a role analogous to the central barrier in the case of electron tunneling through a “rectangular” energy barrier in a well-known modification of the “particle in a box” problem.[17] This rectangular barrier problem (also known as the double square-well problem) is illustrated in Figure 1-5.

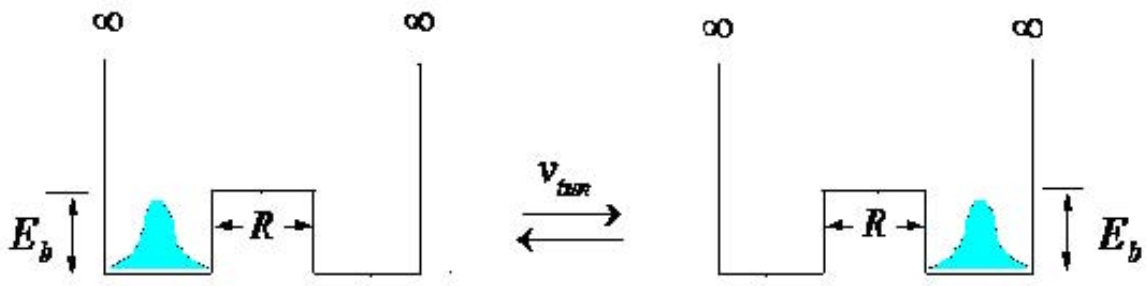

Figure 1-5. Electron tunneling through a double square-well potential field at frequency v_{tun} between localized states, E_b is the activation energy barrier height and R is the tunneling distance.

In the “hopping” mechanism, electrons or holes actually become localized as chemically-reduced or oxidized sites along with the bridging chain or medium. These then act as mobile charge carriers and “hop” from point to point along the medium between donor and acceptor according to Boltzman statistics.[18]

The energies of the “virtual states” in quantum superexchange are analogous to the barrier height E_b in Figure 1-5. Superexchange-mediated electron tunneling

is mainly affected by two factors, the distance between the donor and acceptor and the energy barrier height. It has been shown that the tunneling rate will decrease exponentially as the distance or energy barrier height increases. This relationship can be described as below,

$$k_{et} \propto v_{tun} \propto \left(\frac{1}{\sqrt{E_b}}\right) e^{-R\sqrt{E_b}} \qquad \text{(1-20)}^{19c,20}$$

The electron-transfer superexchange mechanism can occur *via* two distinct pathways; these are “electron transfer” superexchange and “hole transfer” superexchange pathways (as mentioned above). Which pathway dominates depends on details of the molecular orbital configuration of the bridging medium. A high energy HOMO at some point along the bridge can act as an oxidizable site for electron “hopping” or as a virtual hole state in quantum superexchanges. A low energy LUMO on the bridge will favor the “electron” transfer superexchange in which the virtual state is defined by electron transfer from electronic donor to the bridge. Similarly, if the electron actually resides for a finite period on some reduced bridge site, then electron “hopping” can be the dominant mechanism. When bridges are short, the superexchange mechanism dominates and the donor-to-bridge spectroscopic energy gap (which is dependent in part on bridge LUMO levels) will determine the magnitude of the “electron” transfer superexchange contribution to the observe ET rate. The bridge-to-acceptor spectroscopic energy gap will determine the “hole” transfer superexhcange contribution.

Previous work in this lab has shown that the rates of like-charge bimolecular electron-transfer reactions can be very sensitive to the nature of the anion of added electrolytes.[21] Some of these added anions appear to provide their catalytic effect by establishing a superexchange interaction between donor and acceptor, which would otherwise not be there in the intervening solvent medium. Some added salts, however, are relatively poor catalysts and appear to enhance ET rates simply by the idealized or "innocent" salt effects predicted by Debye-Huckel theory. In Chapter 2, we will detail electrolyte effects on the rates of bimolecular ruthenium ammine complex electron-transfer reactions. One example of strong catalysis is the rate increase observed upon addition of a salt with conjugated dicarboxylate dianions such as sodium muconate.[21a] Similarly, we will describe how the rates increase progressively by adding softer (lower first ionization energy) halide electrolytes such as bromide and iodide (which catalyze ET much more strongly than fluoride).

Reference

1. (a) H. Taube, *Chem. Rev.* **1952**, 50, 69

   (b) R.A. Marcus and P. Siddarth, *in Photoprocesses in Transition Metal Complexes, Biosystems and Other Molecules: Experiment and Theory*

   (c) Vincenzo Balzani (Ed.) *Electron Transfer in Chemistry* WILEY-VCH, Germany, **2001**

   (d) Chance, B., DeVault, D. C., Frauenfelder, H., Marcus, R. A., Schrieffer, J. B., Sutin, N., Eds. "*Tunneling in Biological Systems*"; Academic Press: New York, **1979**.

   (e) Libby, W. F. *J. Phys. Chem.* 1952, 56, 863.

2. (a) Sutin, N. "*Bioinorganic Chemistry*", Vol. 2, G. L. Eichhorn, Ed., American Elsevier, New York, N.Y., 1973, Chapter 19, P611

   (b) Brown, G. M.; Sutin, N. *J. Am. Chem. Soc*. **1979**, 101, 883

   (c) Sutin, N. *Acc. Chem. Res.* **1968**, 1, 225

3. (a) Marcus, R. A. *J. Chem. Phys*. **1956,** 24, 966

   (b) Marcus, R. A. *Discuss. Faraday Soc.* **1960,** 29, 21

   (c) Marcus, R. A. *J. Chem. Phys*. **1965,** 43, 679

   (d) Marcus, R. A. *Annu. Rev. Phys. Chem.* **1964,** 15, 155

   (e) Marcus, R. A.; Sutin, N. *Biochem. Biophys. Acta* **1985**, 811, 265

   (f) Marcus, R. A. *J. Chem. Phys*. **1963,** 67,853

4. (a) Brunswig B. S.; Logan J.; Newton, M.D.; Sutin, N. *J. Am. Chem. Soc*. **1980**, 102, 5798

(b) N. S. Hush *Prog*. *Inorg*. *Chem*. **1967**, 8, *391*

5. Brown, G. M.; Sutin, N. *J. Am. Chem. Soc*. **1979**, 101, 883

6. Saxton, R. *Proc. R. Soc. London, Ser. A* **1952**, 213, 473

7. (a) Dogonadze, R. R. In "Reactions of Molecules at Electrodes", Hush, N. S., Ed.; Wiley-Interscience: New York, **1971**; Chapter 3, p 135

(b) Vorotyntsev, M. A,; Dogonadze, R. R.; Kuznetsov, A. M. *Dokl. Akad. Nauk SSSR* **1970**, 195, 1135.

(c) German, E. D.; Dvali, V. G.; Dogonadze, R. R.; Kuznetsov, A. M. *Elektrokimiya* **1976**, 12, 639.

(d) Dogonadze, R. R.; Kuznetsov, A. M. *Prog. Surf. Sci.* **1975**, 6, 1 .

(e) Dogonadze, R. R.; Kuznetsov, A. M.; Levich, V. G. *Electrochim. Acta* **1968**, 13, 1025.

8. Sutin, N. *Prog. Inorg. Chem.* **1983**, 30, 441

9. Creutz, C. *Prog. Inorg. Chem.* **1983**, 30, 1

10. Marshall, W. L. Nature Precedings : *Dielectric Constant of Water Discovered to be Simple Function of Density over Extreme Ranges from – 35 to + 600^{o}C and to 1200 MPa (12000 Atm.), Believed Universal*

11. Ulstrup, J. In "*charge-Transfer Processed in Condensed Media*", Springer-Verlag; West Berlin, **1979**, p. 171 ff.

12. (a) Landau, L. *Phys. Z. Sowejtunian* **1932**, 2, 46

(b) Zener, C. *Proc. R. Soc. London Ser. A* **1932**, 137, 696; **1933**, 140, 660

13. (a) Balzani, V. And Balzani, V., Eds., *Electron Transfer in Chemistry*,

Wiley-VCH, Weinheim, **2001**; Vol. III, pp. 710

(b) Wasielewski, M. R., Fox, M. A., and Chanon, M., Eds. *Distance Dependencies of Electron-Transfer Reactions,* Elsevier, Amsterdam, The Netherlans, **1998**.

(c) Marcus, R. A. and Sutin, N. *Biochim. Biophys. Acta* **1985**, 811, 265-322

(d) Gray, H. B. and Winkler, J. R., *Q. Rev. Biophys.* **2003**, 36, 321-372

14. Curtis, J. C.; Inagaki, M.; Chun, S. J.; Eskandari, V.; Luo, V. X.; Pan, N. Z.; Sankararaman, U.; Pengra, G. E.; Zhou, J.; Hailey, P.; Laurent, J.; Utalan, D. *Chem. Phys.* **2006**, 326, 43
15. Levich, V. G. *Adv. Electrochem. Electrochem. Eng.* **1966**, 4, 249
16. (a) Ulstrup, J.; Jortner, J. *J. Chem. Phys*. **1975,** 63, 4358

    (b) Efrima, S.; Bixon, M. *Chem. Phys*. **1976,** 13, 447

    (c) Van Duyne, R. P.; Fisher, S. F. *Chem. Phys.* **1974,** 5, 183
17. (a) Lewis, F. D.; Wu, T.; Zhang, Y.; Letsinger, R. L.; Greenfield, S.R.; Wasielewski, M. R. *Science* **1997**, 277, 673-676.

    (b) Fukui, K.; Tanaka, K. *Angew. Chem. Int. Ed.* **1998**, 37, 158-161.

    (c) Meggers, E.; Kusch, D.; Spichty, M.; Wille, U.; Giese, B. *Angew. Chem. Int. Ed.* **1998**, 37, 460-462.
18. (a) Giese, B.; Wessely, S.; Spormann, M.; Lindemann, U.; Meggers, E.; Michel-Beyerle, M. E. *Angew. Chem., Int. Ed.* **1999**, 38, 996

    (b) Breslin, D. T.; Schuster, G. B. *J. Am. Chem. Soc.* **1996**, 118, 2311-

2319.

(c) Gasper, S. M.; Schuster, G. B. *J. Am. Chem. Soc*. **1997**, 119, 12762-12771.

19. (a) Ratner, M. *Nature* **1999**, vol. 397, p. 480.

(b) Jortner, J., Bixon, M., Landenbacher, T., and Michel-Beyerle, M.E. *Proc. Natl. Acad. Sci.* USA **1998**, vol. 95, p. 12759.

(c) Bixon, M. and Jortner, J. *J. Phys. Chem. B* **2000**, vol. 104, p. 3906.

(d) Lakhno, V. D. and Sultanov, V. B. *Biophysics* **2003**; Vol. 48, No. 5, p. 741–745

20. (a) Jobnson, C.S.; Anderson, L.G. *Problems and Solutions for Quantum Chemistry and Physics*; Dover Publications, Inc.: New York, **1986**; p. 104-107, 130 (b) Deutchman, P.A. *Am. Journal of Physics*, **1971**, 39, 3324

21. (a) Curtis, J. C.; Inagaki, M.; Chun, S. J.; Eskandari, V.; Luo, V. X.; Pan, N. Z.;Sankararaman, U.; Pengra, G. E.; Zhou, J.; Hailey, P.; Laurent, J.; Utalan, D. *Chem. Phys*. **2006**, *326*, 43

(b) Endicott, J.F.; Ramasami, T. *J. Am. Chem. Soc.* **1982**, 104, 5252

(c) Ramasami, T.; Endicott, J.F. *Inorg. Chem.* **1984**, 23, 3324

Chapter Two

Kinetic Studies of Aqueous Electrolyte Effects on Comproportionation Electron-Transfer Reactions between Ruthenium Ammine Dimeric Complexes

2.1 Introduction

It is well-known that added electrolytes influence the rates of reactions between like-charged reactants by weakening interractant Columbic forces (see Figure 2-1).[1,2]

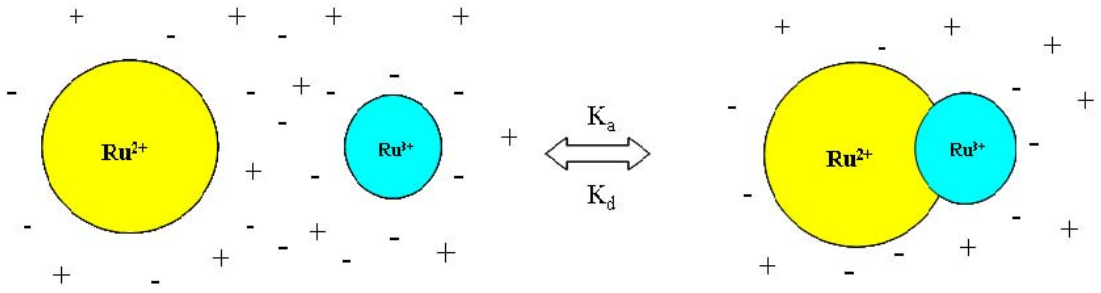

Figure 2-1 Schematic illustration of ionic atmospheres surrounding a pair of charged reactants and their encounter complex.

In the case shown above, we see that the positively-charged ruthenium reactants are surrounded by an “ion-atmosphere” of oppositely-charged ions (and their counter ions) as described by the Debye-Hückel (DH) theory of electrolyte effects

on activity coefficients.[5,6] This ion atmosphere can effectively shield the electric fields of the reactants from each other and this decreases the columbic work of associating the reactant ions to a close enough distance for the electron-transfer reaction to occur.

In the prototypical ET pseudo-self exchange reaction (1) and bimolecular comproportionation reaction (2) shown in figure 2-2 below,

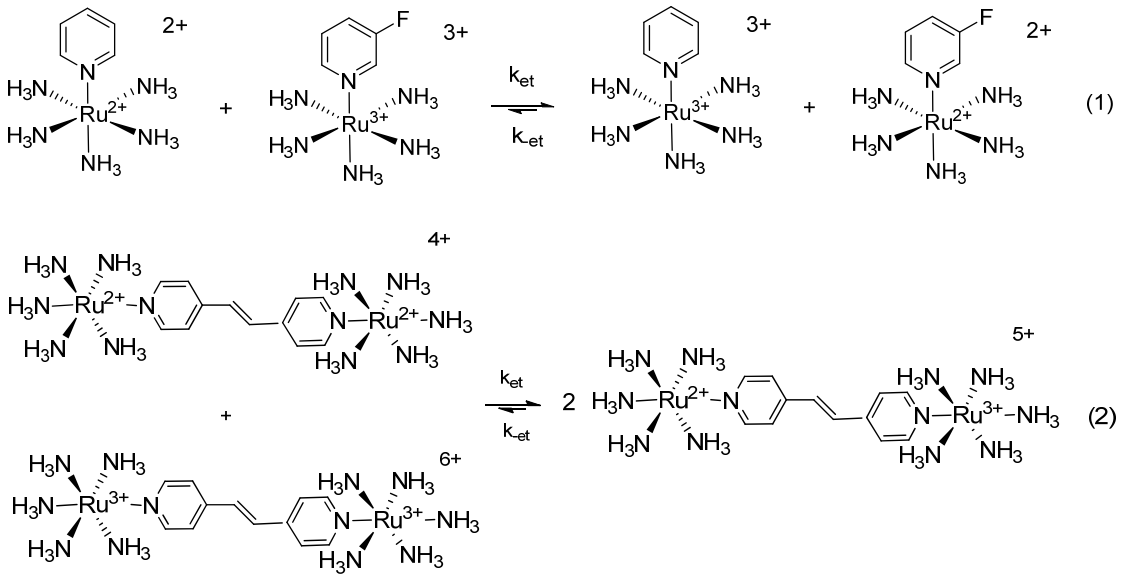

Figure 2-2. Pseudo-self exchange reaction (1) and bimolecular comproportionation reaction (2) used in the kinetic work to be described in this chapter.

based on the ion-pair pre-equilibrium assumption[3] (see eq. 1-2, 1-3 and 1-4 in chapter 1), the predicted rate constant for these reaction (1 and 2) can be derived

by applying a steady state kinetic analysis,[4] expression below, and this results in the kinetic rate expression,

$$k_{ex} = \frac{k_{et} k_a}{k_d + k_{et}} \tag{2-1}$$

where k_{ex} is the predicted second-order rate constant for the overall reaction, k_{et} is the first-order rate constant for ET inside the associated pair, k_a and k_d are the association and dissociation rate constants for formation of the precursor complex , and $K_A = k_a / k_d$ is the precursor formation equilibrium constant.

In the diffusional pre-equilibrium limit, which is defined when $k_d >> k_{et}$, eq. 2-1 becomes,

$$k_{ex} = \frac{k_a}{k_d} k_{et} = K_A k_{et} \tag{2-2}$$

The DH theory[5,6] of salt effects on activity coefficients and ion atmospheres makes use of Poisson's equation and Boltzman's principle[5c] to quantitatively model this electrostatic interaction energy between a charged reactant ion and its ionic atmosphere. The theory assumes that every reactant ion is surrounded by a polarized ionic atmosphere (as shown in Figure 2-1) which has an average potential P_0 with an opposite sign to that of the reactant ion's charge (this physics applies to non-reactant ions in the solution as well). The spatial distribution of this potential is determined by the ionic strength which will be reduced to a limit at infinite dilution as given by the expression,[5c]

$$P_0 = -\frac{zeB}{D_s} \tag{2-3}$$

$$B^2 = \frac{8\pi e^2 \mu}{D_s k_b T} \tag{2-4}$$

where "z" represents the valence of the reactant ion, "e" is the electronic charge, D_s is the dielectric constant of the solution, k_b is the Boltzmann's constant, T is the absolute temperature, and μ is the ionic strength in the form of $1/2\sum_i c_i z_i^2$ (where c_i is the concentration of the ion of the i th sort).

The DH limiting law which follows from eq. 2-3 and 2-4 above is valid for describing the resulting ionic strength dependence of the activity coefficient of an ionic reactant at low ionic strength (μ <~ 0.0005 M) is as shown below,[5c]

$$\log \gamma_i = -z_i^2 A \mu^{1/2} \tag{2-5}$$

where r_i is the activity coefficient of i th reactant ion, and "A" as a temperature-dependent constant of the theory (equal to 0.5085 for an aqueous solution at 298K) as given by Manov *et al*.[7]

The limiting law will start to fail at higher ionic strength, so the "extended" Debye-Huckel law was introduced later and is given by,

$$\log \gamma_i = -\frac{z_i^2 A \mu^{1/2}}{1 + \beta d \mu^{1/2}} \tag{2-6}$$[8]

where d is the effective radius of the reactant ion (or precursor complex such that for the encounter complex $A|B$, $d=r_A+r_B$) and β is a temperature dependent

constant of the theory (equal to 0.3281 for an aqueous solution at 298K) as given by Robinson and Stokes.[8]

As discussed in the chapter 1, for a simple outer-sphere bimolecular electron-transfer reaction (eq. 2-7), the mechanism can be broken down into steps,

$$A^{n+} + B^{(n+1)+} \underset{k_{d1}}{\overset{k_{a1}}{\rightleftharpoons}} A^{n+}\,|\,B^{(n+1)+} \underset{k_{-et}}{\overset{k_{et}}{\rightleftharpoons}} A^{(n+1)+}\,|\,B^{n+} \underset{k_{a2}}{\overset{k_{d2}}{\rightleftharpoons}} A^{(n+1)+} + B^{n+} \qquad (2\text{-}7)$$

and in this like-charged reactants case, the rate of electron-transfer reaction will thus be accelerated by added electrolytes due to the charge-screening action of their ionic atmospheres as discussed above . In 1922, Bronsted[9] proposed an equation later proven by Bjerrum[10] to link the bimolecular reaction rate constant with the activity coefficient in the Debye-Huckle expression,

$$k_{ex} = k_{ex}^{\mu=0} \frac{\gamma_{A^{n+}}\gamma_{B^{(n+1)+}}}{\gamma_{A^{n+}|B^{(n+1)+}}} \qquad (2\text{-}8)^{9,11}$$

where $k_{ex}^{\mu=0}$ is the overall rate constant at infinite dilution, and $\gamma_{A^{n+}|B^{(n+1)+}}$ is the activity coefficient of precursor complex.

Thus, the well-known Debye-Hückle-Bronsted equation can be obtained by combining eq. 2-7 and 2-9 as shown below,

$$\log k_{ex} = \log k_{ex}^{\mu=0} + \frac{1.02 z_{A^{n+}} z_{B^{(n+1)+}} \mu^{1/2}}{1 + \beta d \mu^{1/2}} \qquad (2\text{-}9)$$

Guggenheim[12a,b] later provided a similar expression to eq. 2-9 but “with certain advantage over it” by approximating the “βd” term to ~1 since d in the eq. 2-9

is often on the order of 3 angstroms. Thus eq. 2-9 becomes

$$\log k_{ex} = \log k_{ex}{}^{\mu=0} + 1.02 z_{A^{n+}} z_{B^{(n+1)+}} GP \qquad (2\text{-}10)$$

where

$$GP = \frac{\mu^{1/2}}{1+\mu^{1/2}} \qquad (2\text{-}11)$$

So, if the Guggenheim approximation applies, we can expect kinetic behavior yielding a straight line with slope of $1.02(z_{A^{n+}} z_{B^{(n+1)+}})$ for a plot of $\log k_{ex}$ *vs.* GP in the case of a reaction between species A^{n+} and $B^{(n+1)+}$. For the two ET reactions studied in this work (Fig. 2-2), we thus predict a slope of 6.12 for reaction (1) and a slope of 24.5 for reaction (2).

DH theory was formally derived on the assumptions of point-charge reactants at very high dilution. There can be strong deviations from the theory when introducing certain counter ions (ions of charge opposite to the reactants) if specific "ion-pairing" take place.[12c] The effects of such specific interactions are different from the diffuse ion atmospheres considered by Debye and Hückel. In this case, the added ions are able to form either very tight ion pairs with the reactants (usually called "contact" ion pairs), or in some cases looser ion pairs which still have intact solvation shells for both ions (so-called "solvent-separated" ion pairs). The kinetic effects of added salts capable of forming such ion pairs have a quantitatively different kind of impact on reaction rates than the simple ion atmosphere screening effect captured by eq. 2-9 and 2-10. In our studies, we will consider kinetic effects arising from both simple ionic strength and contact-ion pairing interactions.

Ion pair association and dissociation constants and the encounter ion pair equilibrium constant can be calculated separately using the well known Debye-Smoluchoswski[13,14], Debye-Eigen[14,15] and Fuoss[16] equations (eq. 2-12 to 2-14).

$$k_a = \frac{2000 k_b T N}{3\eta d \int_d^\infty r^{-2} \exp[w(r,\mu)/k_b T] dr} \left(2 + \frac{r_a}{r_b} + \frac{r_b}{r_a}\right) \quad \text{(2-12)}^{13,14,17}$$

$$k_d = \frac{10^{30} k_b T \{\exp[w(r,\mu)/k_b T] dr\}}{3\pi\eta d^3 \int_d^\infty r^{-2} \exp[w(r,\mu)/k_b T] dr} \left(\frac{1}{r_b} + \frac{1}{r_a}\right) \quad \text{(2-13)}^{14,15,17}$$

$$K_A = \frac{k_a}{k_d} = \frac{4\pi N d^3}{3000} \exp[w(r,\mu)/RT \quad \text{(2-14)}^{16,17}$$

where k_B is Boltzmann's constant, N is Avogadro's number, η is the solvent viscosity (8.9 x 10^{-4} kg/m*s for water at 298K), r_a and r_b are the radii of the reactant ions in Angstroms, d = r_a + r_b, D_s is the static dielectric constant of medium, R is the molar gas constant (8.3145 J K^{-1} mol^{-1}), and $w(r,\mu)$ is the "work term" which describes the free-energy change required in order to bring the changed reactants together from infinity. $w(r,\mu)$ can be expressed from Debye-Huckel theory[6] and can be simplified as,

$$w(r,\mu) = \frac{10^{10} e^2 Z_a Z_b}{4\pi\varepsilon_0 D_s d} \left(\frac{1}{1 + \beta d\sqrt{\mu}}\right) \quad \text{(2-15)}^{18}$$

where e^2 is the square of the elementary charge (taken as 1.388 x 10^6 J/mol), β is the Debye inverse length and is 0.329 $A^{-1}M^{-1/2}$ for water at 298K, and Z_a, Z_b are

the (integral) ionic charges of the reactants.

In 1949, Olson and Simonson[19] observed that the salt dependence of rates of reaction between ions is not in always due solely to the added ionic strength, but in some cases depends more directly on the simple molar concentration of one of the ions of some added salt. For reactions between like-charge reactants, the Olson-Simonson rate effect is found to depend on the concentration of the opposite charged ion of the added salt. For reactants of opposite-charge, the rate will usually be dominated by one type added ion though both charge types may affect the rate. Olson-Simonson type behavior is now taken as an indication that some kind of specific ion-pairing interaction is affecting the rate as salt is added. An empirical equation was proposed by Olson and Simoson to fit a variety of experimental data. The idea was to consider the overall rate constant of the reaction as the sum of two fractions of rate constants occurring through different pathways, one from the ion-paired species and another from the non-ion-paired species. Their expression was,[19-20]

$$k_{ex} = \frac{k_{nip}}{1 + K_{ip}[X]} + \frac{k_{ip} K_{ip}[X]}{1 + K_{ip}[X]} \qquad \text{(2-16)}$$

where K_{ip} is the ion-pair formation constant for the 1:1 pairing between one (or both) reactant ions and its various counter ions, and k_{nip} and k_{ip} are the ideal rate constants for the non-ion-paired and 100% ion-paired reactive pathways. Based on eq. 16, a prediction can be made that plotting $K_{ip}[X]$ *vs.* $k_{ex}(1 + K_{ip}[X])$ will give a slope of k_{ip} and an intercept of k_{nip}.

The Olson-Simonson effect has now been observed for a number of electron-transfer reactions between ions with the same sign. Rampi *et al.* [21] showed the kinetics of the excited-state quenching reaction between $*Ru(bpy)_3^{3+}$ and $Co(sep)^{3+}$ (called cobalt sepulchrate[22]) with different added electrolytes was correlated directly with the nature and molar concentration of the added anions and not with ionic strength (or GP). For expample NaCl, $BaCl_2$, and $LaCl_3$ gave apparently different electrolyte effects on the rate when plotted as $\log k_q$ *vs.* GP, but showed no difference if plotted as logk *vs.* $[Cl]^-$.[21] When salts of different univalent anions such as F^-, Cl^-, Br^- and ClO_4^- were added they showed that the rates of the electron-transfer quenching reaction depended remarkably on the nature of the anions. The accelerating effect on the rate was found to follow the order $F^- < Cl^- < Br^-$ (see also ref. 23). Chiorboli[24] also showed that the quenching rate constant for a similar reaction was in better correlation with $[Cl^-]$ than with ionic strength.

In chemical reactions, rates generally depend on temperature exponentially. At high temperature, the reacting molecules have greater energy to cross the activation barrier. The relation between rate constant and the absolute temperature can be described by the empirical Arrhenius equation[25] arrived at by Jacobus van't Hoff and Svante Arrhenius in 1889 as given by,

$$k_{ex} = Ae^{-Ea/RT} \tag{2-17}$$

where E_a is the activation energy and A is the pre-exponential factor. It is important to note that this equation was developed on the basis of empirical

observations and trial-and-error mathematical modeling and does not incorporate detailed mechanistic considerations such as the existence of reactive intermediates which might be involved in the overall reaction.[26]

Transition State Theory (TST)[25] developed by Henry Eyring and Michael Polanyi in 1935 provides a first-principles description of how chemical reactions proceed through some high energy critical geometric configuration known as the "activated state" or "activated complex" or "transition state". Eyring included an important feature into the TST by showing that the rate is proportional to the effective frequency (approximately $k_b T / h$) with which reactants are converted to products once the transition geometry was been reached.[27] This formulation is as shown below,

$$k = \kappa \frac{k_b T}{h} K^{\neq} \qquad \text{(2-18)}^{27}$$

where κ is the "transmission coefficient" and $K^{\neq}$ is the equilibrium constant for formation of the high (local maximum) energy activated complex.

From the standard thermodynamic definitions, we can write,

$$K^{\neq} = e^{-\Delta G^{\neq} / RT} \qquad \text{(2-19)}$$

and

$$\Delta G^{\neq} = \Delta H^{\neq} - T\Delta S^{\neq} \qquad \text{(2-20)}$$

where $\Delta H^{\neq}$ and $\Delta S^{\neq}$ are the activation enthalpy and entropy (by convention we use the superscript "$\neq$" to indicate that rate eq. 2-18 is being used). In the context of ET reactions, eq. 2-18 can be written as,

$$k_{ex} = \kappa_{el} \frac{k_b T}{h} e^{\Delta S^{\neq}/R} e^{-\Delta H^{\neq}/RT} \qquad (2\text{-}21)$$

To understand the relationship between rate constant and temperature, we can divide both sides of eq. 2-21 by T and then take the natural log of both sides to obtain:

$$\ln \frac{k_{ex}}{T} = \ln(\kappa_{el} \frac{k_b}{h}) + \frac{\Delta S^{\neq}}{R} - \frac{\Delta H^{\neq}}{RT} \qquad (2\text{-}22)$$

Thus, an "Eyring plot" of $\ln k_{ex}/T$ *vs.* 1/T can be used to obtain the activation enthalpy and entropy information from its slope ($-\Delta H^{\neq}/R$) and intercept ($\ln(\kappa_{el} k_b / h) + \Delta S^{\neq}/R$), respectively. In multi-step reaction mechanisms, such as the pre-equilibrium limit of the bimolecular ET reactions to be described here, modifications can be necessary and it may become important to replace the "$\neq$" of TST with the more general acitvational superscript "$*$". This will be explained later in this chapter when we address the role of specific ion-pairing catalysis of reaction 2 by added halide and other anions. The origin of the anion-catalysis of reaction 2 will be discussed in the context of solvation energy effects and presumed quantum superexchange interactions taking place in the precursor complex of the ET reaction (similar to those already reported on and analyzed by Inagaki *et al.*[12c] and Chen[37] and Sista[41] of this laboratory). As will be shown, reaction 2 behaves similarly to reaction (1) in many respects, but the quantitative application of eq. 2-9 fails (probably due to the rod-like geometry of the dimer), and in the case of iodide as added salt we find the very unusual occurrence of a distinctly *negative* enthalpy of activation.

2.2.1 Synthesis of Ruthenium Complexes

Chloropentaammineruthenium(III)dichloride (FW = 292.62) was synthesized according to the method of Vogt *et al.*[28] Rutheniumtrichloride hydrate (5.0g, Aldrich) was mixed with distilled water (62.5 mL) in a 1000 mL round-bottom flask with a ground glass joint. In a fume hood, 62.5 ml of hydrazine monohydrate (N_2H_4 64-65%) was added slowly over a period of 10 min into the stirring mixture which was pre-cooled in an ice bath. A dark purple solution was formed after continuous stirring of the mixture for 4 h at room temperature. The flask was cooled to around zero degrees in an ice bath, and then 125 mL of 12 N HCl was added slowly (dropwise in the beginning) to the mixture over a period of 20 min. After the vigorous exothermic reaction had subsided, the solution was then heated at reflux for 2 h and then chilled to 0 ^{o}C gradually for maximum crystallization. The yellow-colored product was collected by filtration and washed with 0.1 M HCl (10-15 mL) and acetone (20 mL), and finally dried in a vacuum desiccator. Yields were 60-70%.

Aquopentaammineruthenium(II)hexafluorophosphate (FW = 494) was synthesized based on a modification of the method of Baumann.[29-30] $[(NH_3)_5Ru^{III}Cl]Cl_2$ (0.15 g) starting material was reduced by ~1.5 g of Zn/Hg amalgam in ~6 mL argon-degassed, distilled water which was being agitated with bubbling argon. A pale yellow solution of ruthenium(II) aquopentaammine

formed in 10-20 min indicating that all of the ruthenium(III) chloropentaammine had been reduced. The $[(NH_3)_5Ru^{II}(H_2O)^{2+}$ solution was filtered under an argon blanket into a 10 mL Erlenmeyer flask containing five molar equivalents of solid NH_4PF_6 for the maximum precipitation of the product. Larger amounts of NH_4PF_6 precipitated undesirable white-colored zinc complexes. The flask was capped and swirled for a few seconds, then chilled to 0 ^oC in the freezer for 30 min to maximize crystal formation. The pale yellow compound was collected by rapid filtration under a blanket of argon and dried in a vacuum desiccator after all the mother liquor had drained. Yields were 95-98%.

μ-L-bis(pentaammineruthenium(II))hexafluorophosphate (L= 4,4′-dipyridyl (BPY), 4,4′-dipyridylethylene (BPE)) was prepared and purified by modifiying the literature methods.[31,32] A 30-40 mg sample of ligand was dissolved in ~8 mL of thoroughly argon-degassed acetone to which ~250 mg of $[(NH_3)_5Ru^{II}(H_2O)(PF_6)_2$ in 2.5:1 stoichiometry with respect to the bridging ligand was added. This mixture was allowed to react under argon at room temperature for about 2-3 h. The acetone solution containing the crude product was mixed with 2 equivalents NH_4PF_6 and about 10 ml of distilled water in a 50 mL round-bottom flask for rotory evaporation at room temperature. The oxo-bridged ruthenium and monomer impurities from the reaction mixture remained dissolved in the water giving it a grape-wine color, and the purple-black product precipitated out upon evaporation of the acetone from the mixture. The product should be reisolated 2-3 times using this acetone/NH_4PF_6/water method. An

acetone/ether re-precipitation method was used as a final treatment to purify the dimer products prior to analysis for purity and subsequent kinetic or spectroscopic work. The binuclear ruthenium(II) complex was dissolved in a small amount of acetone (~15 ml) in an Erlenmeyer flask and then near-quantitatively precipitated out by slow addition of ~4 volumes of ether. This final product was filtered by suction filtration and dried in a vacuum desiccator. The final dimer product was judged to be pure only when the λ_{max} values of the MLCT bands were at 542 nm for 4,4′-dipyridyl (BPY) complex, and at 568 nm for 4,4′-dipyridylethylene (BPE) complex (both measured in acetone). Final yields were 70-80%. Calculated CHN microanalytical data for the BPE dimer: C, 12.70; H, 3.55; N, 14.82. Found: C, 13.06; H, 3.20; N, 14.42. Calculated CHN microanalytical data for BPY dimer: C, 10.83; H, 3.46; N, 15.17. Found: C, 10.47; H, 3.11; N, 15.07. Note: It has been shown previously that the MLCT λ_{max} values of these binuclear complexes shift to shorter wavelengths if synthesis is followed by reduction of a Ru^{III} complex as starting material using a strong reducing agent such as Zn/Hg amalgam.[33]

μ-L-bis(pentaammineruthenium(II))tetrachloride (L=4,4′-dipyridylethylene, 4,4′-dipyridyl) was synthesized by dissolving ~100 mg of the purified PF_6^- salt of the (II,II) dimer in ~100 mL reagent grade acetone. Slow addition of *dry* 1/32 saturated TEACl (tetraethylammonium chloride) which was dissolved in a mixture of water-free acetone and methanol (7:3) gradually precipitated the purple

chloride salt of the II,II dimer product. TEACl addition was continued until most of the original dimer had come out and the color of the remaining solution was a light purple. The purple-black precipitate was collected by suction filtration, washed with 5 ml of reagent grade acetone (repeated 3 times washing) and then dried in vacuum desiccator. The electrochemical and UV-vis-near-IR spectral properties of the chloride salts of these (II,II) dimer products in water agreed with literature reports.[31] Note: these pure chloride products cannot be dissolved in acetone. For the 4,4′-dipyridylethylene complex, impurities (possibly the $[(NH_3)_5Ru^{II}]_2BPE(PF_6)_xCl_y$) mixed salts were also precipitated out, if there was not enough TEACl added during the precipitation or if insufficient acetone was used to dissolve the PF_6^- salt. This impurity shows a red purple color in water. Such mixed salts can be salvaged by repeating the acetone/NH_4PF_6/water purification method described previously. Typical yields were 98%.

μ-L-bis(pentaammineruthenium(III))hexachloride (L= 4,4′-dipyridylethylene, 4,4′-dipyridyl) was synthesized by dissolving ~30 mg of $[(NH_3)_5Ru^{II}]_2LCl_4$ in ~6mL HCl solution (0.1 M HCl for 4,4′-dipyridylethylene complex, and 1.0 M HCl for 4,4′-dipyridyl complex). The purple ruthenium (II,II) solution was then oxidized to the dark orange (III,III) dimer (L=BPE) or the yellow (III,III) (L=BPY) solutions by adding 3-4 drops of 30% H_2O_2 (note: more concentrated HCl or a larger amount of H_2O_2 can introduce some impurities due to too-strongly oxidizing conditions for the BPE complex). The product was precipitated by slowly

adding ~50 mL of reagent grade ethanol with stirring. The flocculent precipitate was collected by suction filtration and dried in a vacuum desiccator. The yields were 90-95%. The purity of the compounds was checked by the UV-Visible spectroscopy by first reducing the (III,III) complex over ~1 g Zn/Hg amalgam for ~10 min (which gives superior reproducibility compared to added hydrazine as reductant) and then using the known λ_{max} and ε_{max} values of the (II,II) dimers to infer the purity of the chloride salt products.

2.2.2 Synthesis of the Sodium Salts of the Dicarboxylic Acids

Sodium *trans,trans*-muconate, and adipate were prepared by mixing ~1 g of the dicarboxylic acid with ~100ml deionized water. The pH of the solution was adjusted to 6.5 by slowly adding 0.1 M NaOH solution. The solution was filtered and the sodium salt was then precipitated by slowly adding the filtrate into a stirring ~5-fold volume excess of reagent grade acetone. The products were collected by suction filtration and dried in a vacuum desiccator. Yields were 95-98%.

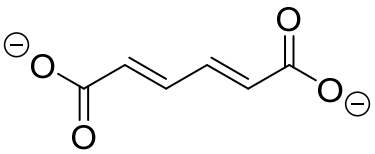

Muconate (Muc)

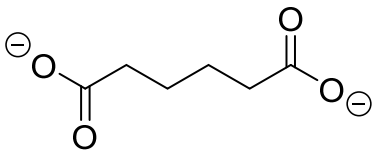

Adipate (Adip)

2.3 Stopped-Flow Kinetic Spectroscopy

Stopped-flow kinetic spectroscopy is the most popular rapid-mixing tool used for fast chemical kinetics studies in solution.[34] Small volumes (typically 0.5-1.2 ml) of "run" solutions are driven from syringes using external (pneumatic) forces and are rapidly mixed as they flow into a stopping syringe/trigger assembly. As the freshly-mixed solution replaces the old solution (from some prior shot) in the optical cell, the expelled solution pushes the plunger of the stopping syringe out so as to activate a microswitch which initiates data collection. Within a few milliseconds the real-time kinetic signal is generated as monochromatic light of some carefully-selected wavelength passes through the reaction cell and is received by the detector. The time-varying photo-voltage as reaction proceeds is picked up using an A/D board interfaced to a computer and the data are finally plotted into a voltage *vs.* time graph. Detailed illustrations of the Cantech TDI MarkIV stopped-flow apparatus used have been given by Chun,[35] Eskandari[36] and Chen.[37] In this work we used a Keithley KPCI-1301 A/D board and the ExeLINX software utility for data collection in Windows98 (*vide infra*).

The great advantage of the stopped-flow instrument as compared to simple mixing in a cuvette is its short mixing and "dead" time. Depending on construction and solution viscosity, this is often in the range from 0.3 milliseconds to a few tens of milliseconds.[39] This dead time, which is specifically the time between the end of the mixing and the beginning of the kinetic data collection, is affected by a few factors, such as the electronic trigger delay time, the solution

flow rate, the distance from the mixer to the reaction cell, and the detector response time. The electronic trigger delay time was proven to be negligible with our apparatus compared to the half life of the fastest reactions in our previous study by Chun.[32] More importantly, careful mixing experiments with our instrument (see figure 2-3) shows a maximum time interval of 30-40 ms from the beginning of mixing the reagent solutions to the beginning of the useful data generation (note the 12 points taken during the “push” recorded at ~1 sec in the figure). Thus we see that it is very important to optimize the distance between the mixer and the reaction cell in order to eliminate the time wasted during the travel of the solutions.

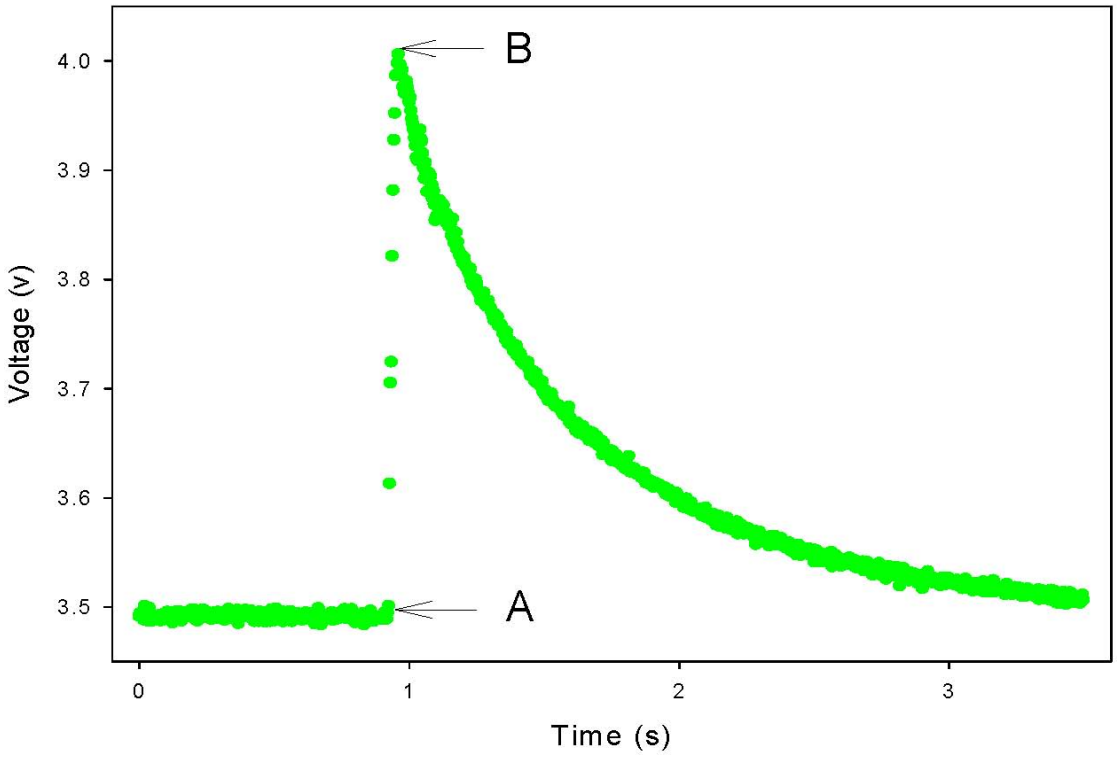

Figure 2-3. A stopped-flow kinetic data trace generated in "free-running" mode by starting on "command" instead of "digital trigger" using ExceLINX program (figure 2-4). The time interval of each data point here is 3.3 ms (f = 300 Hz). Point A shows where the reaction solutions start moving the old solution out of the cell and point B shows where the freshly-mixed solution is stopped in the cell and begins to react according to reaction (2). The total mixing interval of 30-40 ms would require that kinetic half-lives be on the order of as least 150 ms for good quantitation of rates.

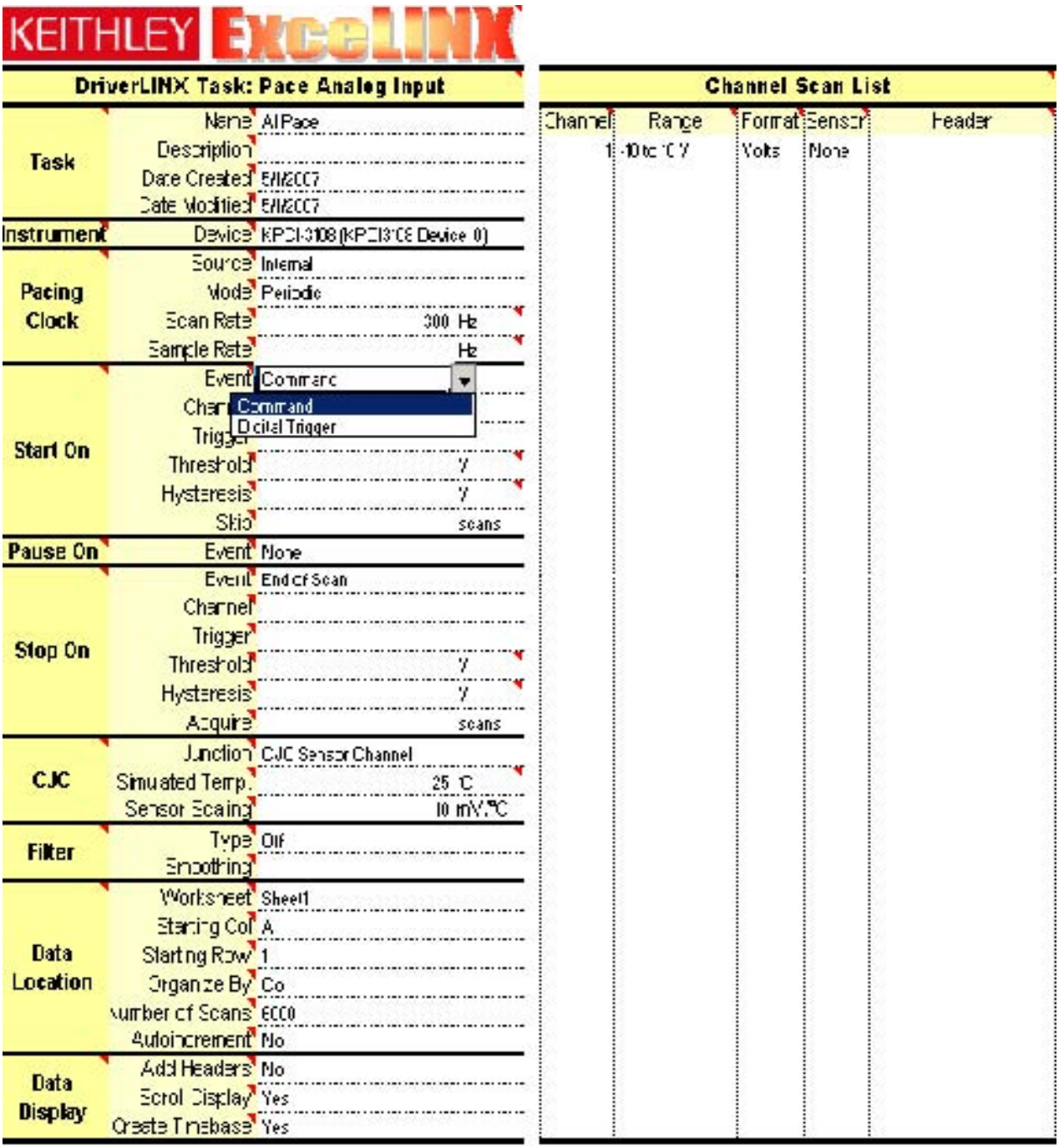

Figure 2-4. KPCI-1301 A/D board control panel parameters setup within the ExceLINX extension of Excel provided by Keithley

Photodetection

The photo-detector used in our experiments was built by Dr. Jeff Curtis. It is consisted of a silicon photodiode (Edmund Scientific 100 mm^2 blue-sensitive) running in unbiased mode amplified by the circuit shown in Figure 2-5.

.

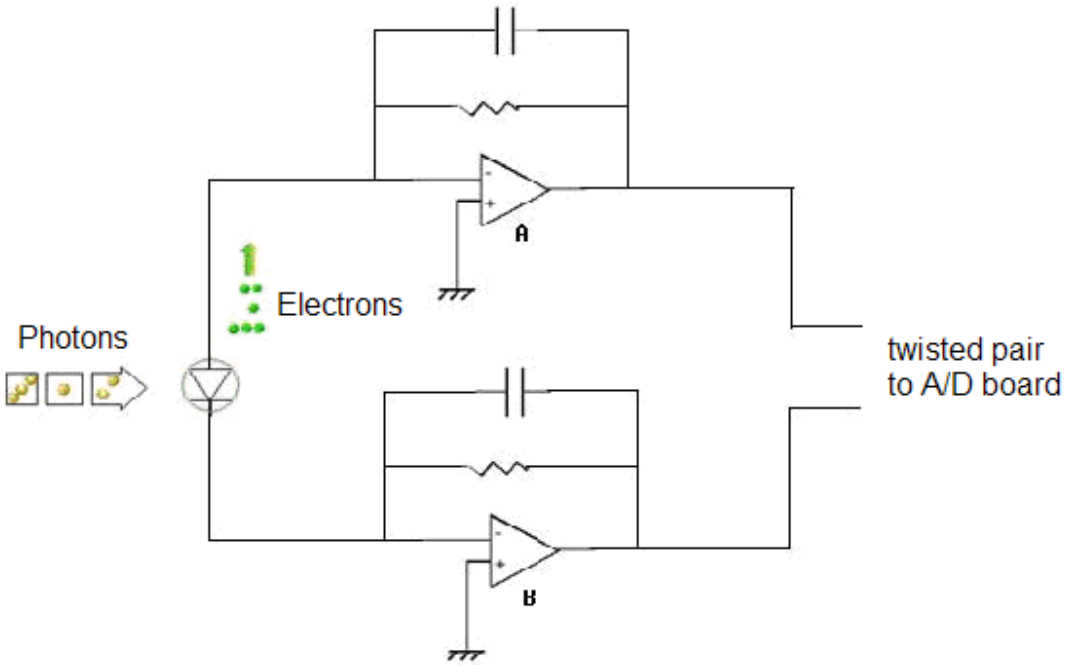

Figure 2-5. Circuit diagram for the photo-detection amplifier used in our stopped-flow apparatus (with R = 15 MΩ and C = 22pf).

The electronic response time of the photodetector contributes to our effective stopped-flow dead time and thus limits the time resolution. To study the roll-off frequency of the circuit, we challenged the response limit of the circuit by directing a variable frequency pulsed light source onto the photodetector. As

the frequency is varied from low to high, the detector eventually fails to record the full voltage signal and shows an attenuation at high frequency. The roll off frequency (f_{3db}) was measured by the experiment (Figure 2-6) and also calculated from the following (approximately applicable) RC circuit equation,

$$f_{3db} \equiv \frac{1}{2\pi RC} \qquad (2\text{-}21)^{39}$$

where R is the resistance and C is the capacitance in the feedback loop of the amplifier. Gain (or attenuation) in decibels for any such circuit can be expressed as,

$$G_{dB} = 20\log_{10}(\frac{V_1}{V_0}) \qquad (2\text{-}22)^{14}$$

where V_1 is the voltage output being measured and V_0 is a specified reference voltage (in this case the photovoltage due to pulsed light source delivered at low frequency)

The calculated roll off frequency is in reasonably good agreement with the value experimentally measured. From our pulsed-light source experiments, a maximum detection frequency of 300 to 350 Hz was indicated for obtaining accurate time fluctuations in photo-voltage signals arriving at the detector. This translates to an electronic a dead time of ~ 3 ms which would then contribute to the scan rate limit of the instrument. This limitation was clearly less severe than the 30-40 ms mixing time measured in our free-running mixing experiments described in Figure 2-3.

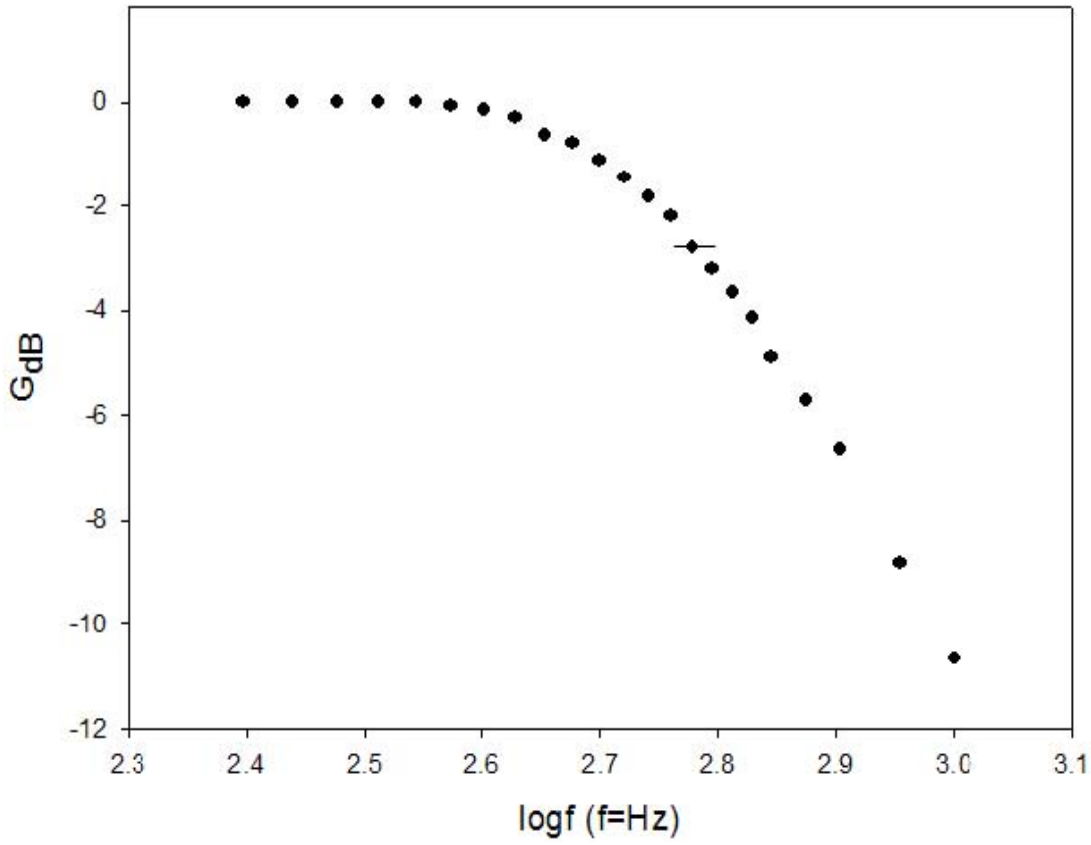

Figure 2-6. Experimentally observed Bode plot for the photo-detector/amplifier shown in Figure 2-5. From this graph, f_{3dB} = 562 Hz at -3 dB which corresponds to ~70% of the inputted V_0 (f_{3dB} was calculated to be 482 Hz using equation 2-21)

Light Source

Stopped-flow experiments require that the reactants and products have different extinction coefficients at least some wavelengths so that a time-varying absorbance signal (or "color change") can be monitored as a reaction proceeds from the beginning (when the solutions are first mixed in the instrument) to the final equilibrium at $t \cong \infty$. The kinetic information is contained in the changing

voltage signal which is subsequently converted into the time-varying absorbance change and finally the reactant/product concentration changes taking place during the reaction. Different light sources are applied to specific reactions depending on the wavelength of maximum absorbance change. This is true either for pseudo-self-exchange reaction (1)[35,36] or for comproportionation reaction (2).[37]

To determine the most appropriate monitoring wavelength region for a given reaction, the UV-Vis absorption spectra, dominated by the metal-to-ligand-charge-transfer (MLCT) bands in our case for both the reactants and the products, were measured using a Cary 5G UV-Vis spectrophotometer. The maximum absorbance change for pseudo-self-exchange reaction (1) was found to be at 422 nm,[41] and for the comproportionation reaction (2) it was found to be at 645 nm (see Figure 2-7).

The light source for reaction (2) was built by connecting a 6 V red LED with a narrow-bandwidth optical interference filter from Edmund Scientific (Lot Code# 1-37-05). Only a narrow range of wavelengths of light from 640 nm to 660 nm were allowed to pass through the reaction cell to gain the most useful kinetic information of reactions. The intensity profile of the light source was measured using a CHEM2000-UV-VIS Miniature Fiber Optic Spectrophotometer (Ocean Optics, Inc., see Figure 2-8). An Agilent 8453 diode array UV-Visble Spectrophotometer (Agilent Technologies, Inc.) was used to characterize the interference filter (Figure 2-9).

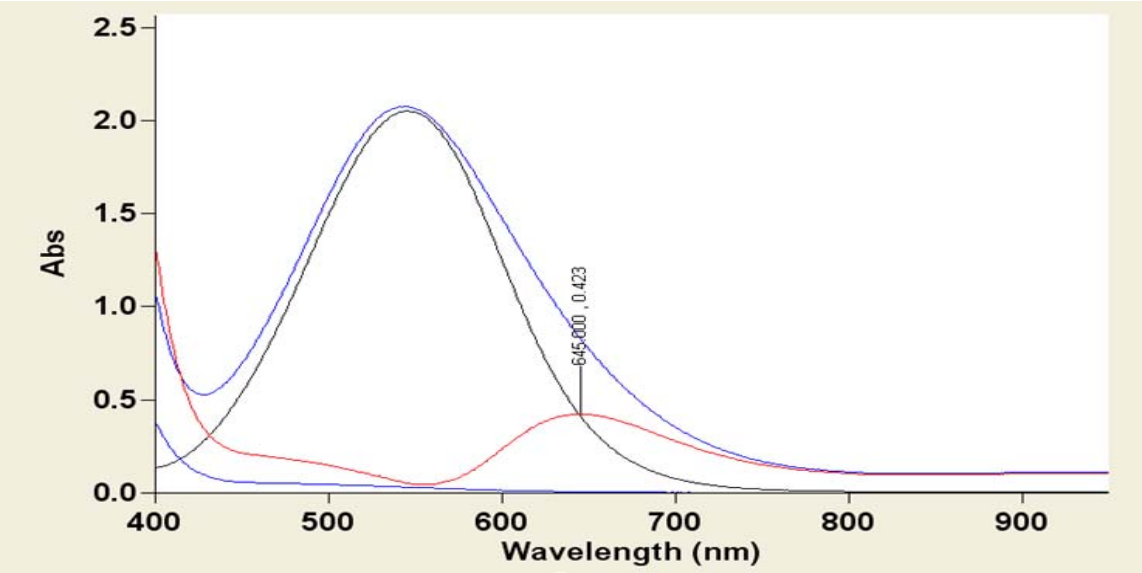

Figure 2-7. Red line: difference spectrum (products-reactants) arising from reaction (2) in water; bottom blue line: BPE dimer (III,III) at 10^{-4} M; top blue line: BPE dimer (II,II) at 10^{-4} M; black line: mixture of BPE dimer (II,II) solution (10^{-4} M) with the same number of equivalents solid BPE dimer (III,III).

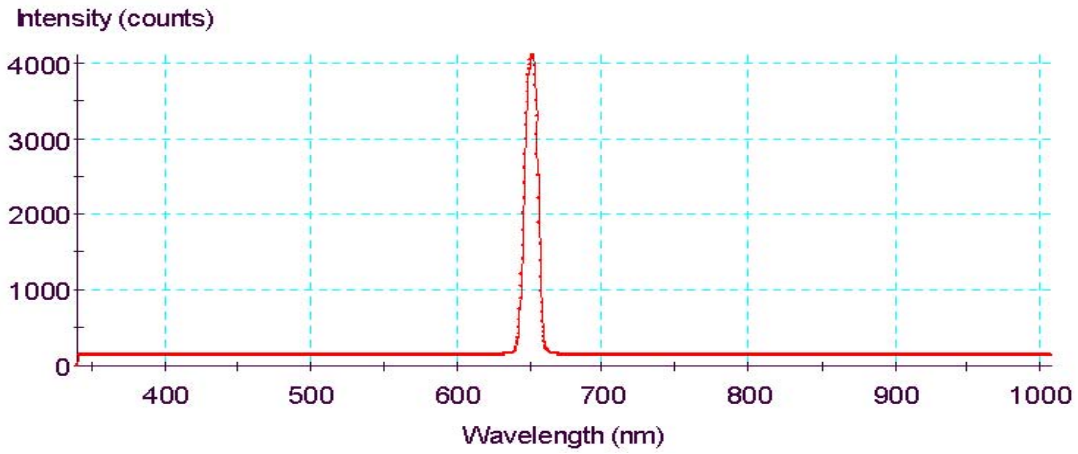

Figure 2-8. The intensity profile of the filtered light source as measured by an Ocean Optics fiber optic spectrophotometer using OOIBase32 software.

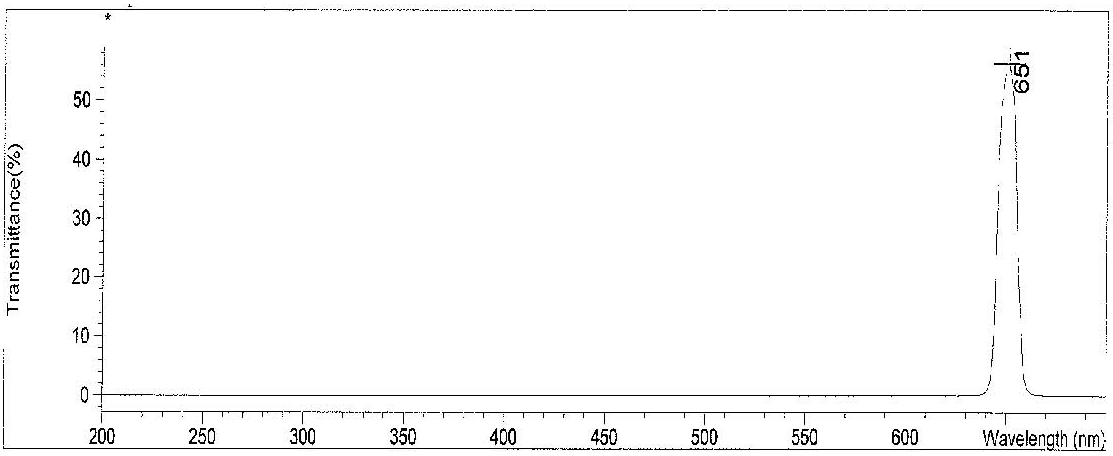

Figure 2-9. Transmittance of the filter used in construction of the light source as measured by a diode array spectrophotometer.

Stopped-Flow Kinetic Data Collection and Processing

Preparation for the experiments

Stopped-flow kinetic experiments especially at low ionic strength proved to be very sensitive and difficult to control. Thus, careful and consistent run solution preparation work was indispensable in order to get reproducible data from the instrument.

First, the instrument (including the sample reservoirs, driving syringes, mixing chamber, and the observation cell) was washed with 4 M nitric acid for about 15 min. The acid was rinsed out with distilled water until the pH of the drained water is close to 6.5.

Second, all volumetric flasks and/or graduated cylinders used for preparing the reagent solutions were made of plastic. This was because previous work by

Sista[41] had shown that there were large positive apparent deviations of the reaction rate constant when measured at concentrations lower than ~10^{-4} M if the stock or run solutions had been exposed to glass surfaces for more than a few seconds. Evidently, exposure to glass gives rise to some strong catalyst which speeds up the reaction rate by up to 10 times. Further discussion on this topic will be presented later in this section.

The temperature of the instrument was adjusted to the designated value for a specific experiment using a VWR 1165 Refrigerated Constant Temperature Circulator. The coolant used in our experiment was a 50:50 mixture of distilled water and antifreeze. The coolant was kept circulating during the stopped-flow experiments, so that the experimental temperature was correlated as closely as possible to the temperature of the coolant. Exact temperature readings at the cell were obtained by a platinum digital thermometer (VWR Scientific Model# 100A) which was in direct metal-metal contact with the thermal block holding the reaction cell.

All circuit connections (light source, photodetector, A/D board) were checked carefully to make sure they were correct before connecting to any power. The LED light source was connected with a 6 V battery and detector was connected with two common-ground 12 V batteries so as to supply $\pm$12 V to the photodetector circuit. The batteries must be fully charged and at the same voltage level. The circuit was connected for at least 10 min so as to yield a stable voltage with just water in the cell before the measurement. The AIO Panel of

the Keithley software was used to check the electrical noise and signal levels. The signal voltage (obtained by toggling the light source on/off) should be less than 10 V and the noise voltage should be less than ±10 mV.

All solutions were prepared with distilled, deionized reagent water (purchased from EMD, cat NO. 34172-073) to minimize catalytic effects of any ions in the water. All run solutions were prepared twice as concentrated as the objective reactant solutions because the two run solutions dilute each other by a factor of two upon mixing.

Running the experiments

When the solutions were ready for experiments, the run solutions were carefully transferred into the two plastic reservoir syringes. Next, the two solutions were drawn into the drive syringes by slowly pulling back the plungers of the syringes with the 3-way valves in "fill" position. The 3-way valves were then switched to "run" position so that the solutions could be mixed by pushing the drive syringes. Even if this step was done very slowly, it was still possible to introduce some air bubbles inside the instrument. Bubbles can be cleared by pushing the drive syringes back and forth slowly with the valves on "fill" until there are no more air bubbles coming out.

Once the solutions were mixed, the collection of the voltage signal from the photodetector was triggered and the voltage *vs.* time data were passed through a Keithley STP-36 terminal box on to a Keithley KPCI 1301 A/D board. The signal

was finally recorded into digital data by an ExceLINX program. Detailed procedure of using the software has been described by Chun,[35] Inagaki, [36] Chen, [38] and Sista. [41]

Data Processing and Rate Constant Determination

The raw stopped-flow data recorded on the Excel sheets were in voltage *vs.* time. In order to be fitted by the second-order kinetic rate equations so as to extract the rate constant, the data were converted into absorbance *vs.* time using the equation shown below,

$$A = -\log_{10} T = -\log_{10}(I_t / I_0) = -\log_{10}(V_t / V_0) \qquad (2\text{-}23)$$

where A is absorbance, T is the transmittance, I_t and V_t represent the current and voltage at time t, I_0 and V_0 represent the current and voltage for the pure solvent (which must be measured and recorded prior to each set of runs). SigmaPlot 10.0 software was used for these data conversions and the kinetic fitting, and detailed procedures have been described by Chen[37] and Sista.[41]

Pearson[42] and Pladziewicz[43] proposed two similar methods of deriving the rate equations for second-order reversible reactions such as the ones studied here. The different forms of equations described by them were obtained by using different initial concentration conditions during the integration steps. King[44] has shown that using different integrated equations for different initial concentration conditions is unnecessary. Both methods were used in our calculation of the second order rate constant and proved to give the exact same

results. Details of the derivation of the fitting equations are described bellow.

For the second-order comproportionation reaction (dimer case) used in our work, we can write,

$$A + B \underset{kd}{\overset{ka}{\rightleftharpoons}} 2\,C \qquad (2\text{-}24)$$

where A = [Ru^{II}, Ru^{II}] and C = [Ru^{II}, Ru^{III}] are "colored" species and B = [Ru^{III}, Ru^{III}] is colorless. Since we at all times kept [A] = [B], we can let the initial reactant's concentrations be denoted by Ru_0. X_e can be thought of as the extent of reaction at equilibrium and will denote the change in concentration of each of the reactants at equilibrium. The equilibrium constant K_{eq} can then be expressed as:

$$K_{eq} = \frac{(2X_e)^2}{(Ru_0 - X_e)^2} \qquad (2\text{-}25)$$

We can solve for X_e by taking the square root of both sides and taking the positive solution of the equation, or by reorganizing the equation in order to solve it using the quadratic formula as follows,

$$(K_{eq} - 4)X_e^{\,2} - 2K_{eq}Ru_0X_e + K_{eq}Ru_0 = 0 \qquad (2\text{-}26)$$

$$X_e = \frac{2Ru_0K_{eq} \pm \sqrt{4Ru_0^{\,2}K_{eq}^{\,2} - 4(K_{eq} - 4)Ru_0K_{eq}}}{2(K_{eq} - 4)} \qquad (2\text{-}27)$$

Because $Ru_0 > X_e$, equation (2-27) can be simplified to

$$X_e = Ru_0 \frac{1 - \sqrt{\frac{4}{K_{eq}}}}{1 - \frac{4}{K_{eq}}} \qquad (2\text{-}28)$$

If we then define w and Q as,

$$w = 1 - \frac{4}{K_{eq}} \tag{2-29}$$

$$Q = \frac{1 - \sqrt{1 - w}}{w} \tag{2-30}$$

Then equation (2-28) for calculation of X_e becomes,

$$X_e = Ru_0 * Q \tag{2-31}$$

Concentrations of species A, B, C in equation (2-24) at any time t can be represented by $[A]_t$, $[B]_t$, $[C]_t$, and their equilibrium values by $[A]_e$, $[B]_e$, $[C]_e$. By denoting $[A]_t = [A]_e + \triangle_t$ ($\triangle_t$ is the *concentration "distance"* from equilibrium at time t), and integrating the rate equation of the reaction

$$\frac{-d[A]}{dt} = k_a[A][B] - k_d[C]^2$$

we obtain,

$$\ln \frac{\Delta_t}{\Delta_t(1-(4/K_{eq})) + [A]_e + [B]_e + (4/K_{eq})[C]_e} = -k_a\{[A]_e + [B]_e + (4/K)[C]_e\}t + C$$

(2-32)[43]

Substituting (2-29), (2-30) and $[A]_e = [B]_e = Ru_0 - X_e$ into (2-32), it can be rearranged to,

$$\ln \frac{\Delta_t}{\Delta_t * w + 2Ru_0(1-Q) + 8Ru_0 * Q/K_{eq}} = -k_a\{2Ru_0(1-Q) + 8Ru_0 * Q/K_{eq}\}t + C$$

(2-33)

We know $[A]_t = [A]_e + \triangle_t$ and $[C]_t = [C]_e - 2*\triangle_t$

In order to get the constant (denoted "C" in 2-32), we set t = 0, so we have $[A]_0 = [A]_e + \triangle_0$ and $[C]_e = 2*\triangle_0$ (thus $\triangle_0 = \triangle_{max} = X_e = Ru_0 *Q$). Rearranging (2-33), we obtain,

$$C = \ln \frac{Q}{Q*w + 2(1-Q) + 8Q/K_{eq}} \tag{2-34}$$

By denoting $B = 2Ru_0(1-Q) + 8Ru_0 * Q/K_{eq}$, Equation 2-33 becomes

$$\frac{\Delta_t}{\Delta_t * w + B} = \exp(-k_a * B * t + C) \tag{2-35}$$

By denoting

$$E = \exp(-k_a * B * t + C) \tag{2-36}$$

Equation (2-35) can be rearranged as,

$$\Delta_t = \frac{E * B}{1 - w * E} \tag{2-37}$$

We know that the concentration of a given reactive species is often in direct proportion with other system properties (such as absorbance, conductivity, vapor pressure etc.). In stopped-flow spectroscopy, we use absorbance and Beer's law and so we write,

$$\Delta_t = \frac{A_f - A_t}{A_f - A_i} * X_e \tag{2-38}$$

where A_f, A_i, A_t are the absorbances at the final, initial and intermediate (time = t) states. By denoting V = $\triangle_t$ and employing equation 2-13, (2-38) can be rearranged to,

$$A_t = \frac{V*(A_i - A_f)}{Ru_0 * Q} + A_f \qquad (2\text{-}39)$$

Now we fit the experimental A_t values by finding the optimum k_f in SigmaPlot using the user-defined regression utility setup as shown in Table 2-1.

Equation		Variables
Keq= Ru0= Af= Ai= W=1-4/Keq Q=(1-(1-W)^0.5)/W C=ln(Q/(Q*W+2*(1-Q)+8*Q/Keq)) B=2*Ru0*(1-Q)+8*Ru0*Q/Keq E=exp(-kf*B*t+C) V=E*B/(1-W*E) h=V*(Ai-Af)/(Ru0*Q)+Af fit h to abst		t = col(1) abst = col (4)
Initial parameters	Constraints	Options
kf= Ai=	kf > 100	Iterations: 18000 Step size: 25 Tolerance: 0.0000010

Table 2-1. Regression transform used for fitting the comproportionation reaction stopped-flow kinetic data.

For the pseudo-self-exchange reaction (monomer case) used in our study, the reaction can be written as,

$$A + B \underset{kd}{\overset{ka}{\rightleftharpoons}} C + D \qquad (2\text{-}40)$$

The X_e can be obtained the same way as described above for the dimer case (see equation 2-27). Following the method described by Pearson,[33] we will integrate the rate equation,

$$-dX/dt = k_a[A][B] - k_d[C][D] \qquad (2\text{-}41)$$

where X is now the extent of reaction at any time t,

$$\ln\frac{X\{[A]_0[B]_0 - ([A]_0 + [B]_0)X_e\} + [A]_0[B]_0X_e}{[A]_0[B]_0(X_e + X)} = k_a\frac{2[A]_0[B]_0 - ([A]_0 + [B]_0)X_e}{X_e}t \qquad (2\text{-}42)$$

Substituting $[A]_0 = [B]_0 = Ru_0$ (equal initial concentrations) in (2-42), and rearranging we obtain,

$$\ln\frac{X(Ru_0 - 2X_e) + Ru_0X_e}{Ru_0(X_e + X)} = k_a\frac{2Ru_0(Ru_0 - X_e)}{X_e}t \qquad (2\text{-}43)$$

At this point we define quantities C and E as,

$$C = \frac{2Ru_0(Ru_0 - X_e)}{X_e} \qquad (2\text{-}44)$$

$$E = \exp(k_a * C * t) \qquad (2\text{-}45)$$

and substituting them in Equation (2-43), we obtain,

$$X = \frac{Ru_0 * X_e * (E-1)}{Ru_0 - 2X_e + E * Ru_0} \qquad (2\text{-}46)$$

Assuming applicability of Beer's law over our range of absorbances, we know that,

$$X = \frac{A_t - A_i}{A_f - A_i} * X_e \qquad (2\text{-}47)$$

and after rearranging we get,

$$A_t = \frac{X(A_f - A_i)}{X_e} + A_i \qquad (2\text{-}48)$$

The Sigmaplot template used for user-defined regressions (fitting the experimental A_t values with optimum k_f *via* equation 2-48) is as shown in the following table.

Equation	Variables
Keq = Ru0 = Af = Ai =	t = col(1)
W=1-1/Keq Q=(1-(1-W)^0.5)/W	abst = col (4)
Xe=Q*Ru0 C=2*Ru0*(Ru0-Xe)/Xe	
E=exp(kf*C*t)	
X=(Ru0*Xe*(E-1))/(Ru0-2*Xe+E*Ru0)	
h=X*(Af-Ai)/Xe+Ai fit h to abst	

Table 2-2. (above) User-defined regression setup and functions for pseudo-self exchange monomer reaction (most parameters are defined similarly as in Table 2-1)

Since the BPE dimer Ru^{II}-Ru^{III} is not long-term stable in solution because it can be oxidized slowly when exposed to the air,[31] the absorbance *vs.* time graph of Reaction (II) showed a very small dropping tail after the reaction reached equilibrium. Even though the oxidation process was negligibly slow compared with the ET reaction rate, the slightly bent tail caused difficulty in fitting of the data at long t. An average of three spectra (from multiple shots in stopped-flow experiments) was used for fitting to obtain the rate constant. If the slight decrease in A_f was still observed after averaging the data after maximum A_f was reached (where the curve flattened) were deleted so that fitting became possible. Deleting long-t sections of decreasing absorbance data in the graph (typically a problem only at times longer than 60 sec) and adjusting the final absorbance value (A_f) in the fitting transform led to nearly perfect fits of the data in most cases (*vide infra*). (Figure 2-10).

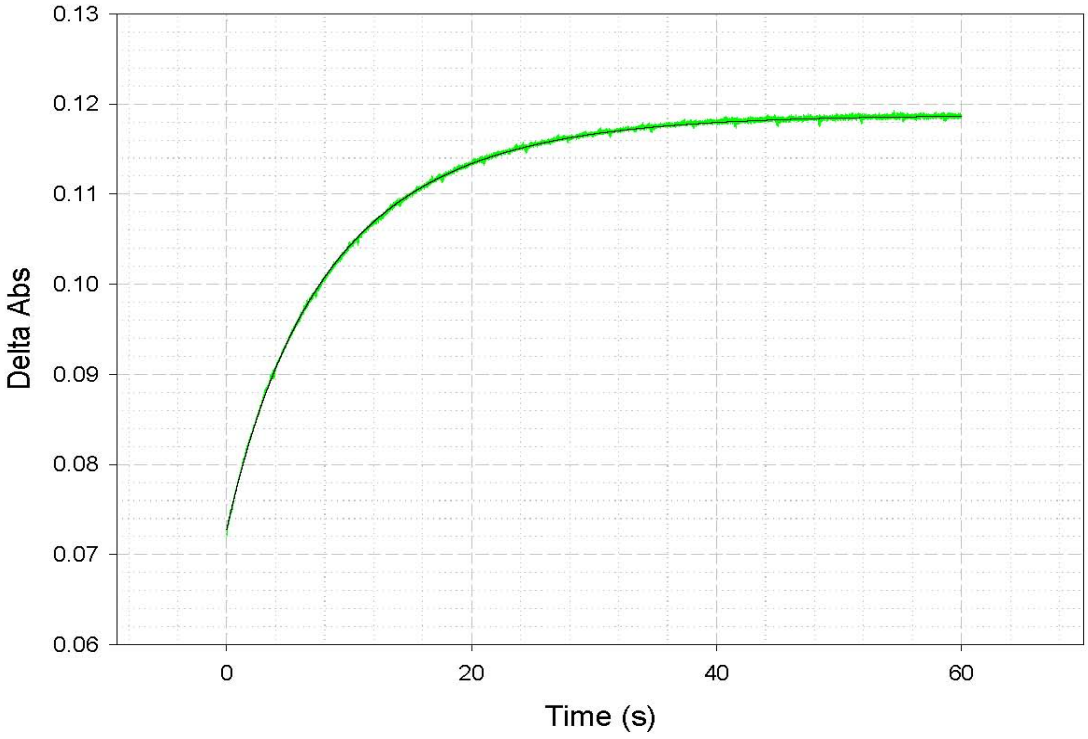

Figure 2-10. A kinetic fit (black line) of a typical stopped-flow dimer reaction data (green line) in SigmaPlot 10.0 software.

Stopped-Flow Experiments on Added-electrolyte Effects

In these experiments, either monomeric ruthenium(III) or dimeric [Ru^{III}, Ru^{III}] stock solutions and electrolyte "stock solutions" at the designated concentrations (the reactant stock solutions were usually ten times concentrated as compared to the run solutions) were prepared and then combined and diluted so as to arrive at the "run" solution concentration. The ruthenium(II) solution was prepared as a single 30-40ml run solution for a given series of stopped-flow experiments and used without further dilution. All ruthenium solutions should be kept in the dark

to avoid photo-decomposition.

The first data point in all studies was for the no “inert” or “spectator” added electrolyte case, just the pure II,II and III,III ruthenium dimer solutions. The ruthenium run solutions were prepared from the stock solution by simple dilution methods. Digital transfer pipets with standard plastic tips (200mml and 1000mml) were used to transfer an accurate amount stock solution into an empty *plastic* volumetric cylinder (3 mL is the minimum volume of the run solution required for running a stopped-flow experiment). Deionized reagent-grade water stored in plastic was used throughout. After preparation, a volume of 3-5ml of each of the two ruthenium run solutions was transferred into one of the reservoir syringes of the stopped-flow instrument. These were then rapidly mixed and spectrophotometrically monitored in the machine at the controlled temperature of 22^{o}C as described in references 35, 36 and 37.

The ruthenium II,II BPE and BPY dimer solutions were found to be slightly light sensitive. They should be covered with aluminum foil and stored in a cabinet before using. Also, the Ru^{II}-Ru^{II} dimer solution can be oxidized slowly to Ru^{III}-Ru^{II} and Ru^{III}-Ru^{III} by exposure to the air. For this reason, the Ru^{II}-Ru^{II} solution should be protected by a blanket of argon and sealed with parafilm. The various added-electrolytes to be studied in a given experiment were added to the ruthenium(III) reactant solution so as to minimize the exposure of the ruthenium(II) solution to the air. A disadvantage of this was that it exposed the Ru(III) oxidant to the possibility of reduction by the added salt’s anion. Iodide (I^-)

was the strongest reducing electrolyte used in our experiments, and it showed only a very small reducing effect on the ruthenium(III) solution even at [KI] = 1mM in simple mixing experiments (see Figure 2-11). This effect was negligibly small (<1%) compared with the absorbance change due to the ET reaction between ruthenium complexes. In the temperature-dependant (Eyring) kinetic experiment involving fixed I^- concentration, the I^- was added to the Ru(II) and Ru(II,II) reactant solution so as to avoid this problem completely.

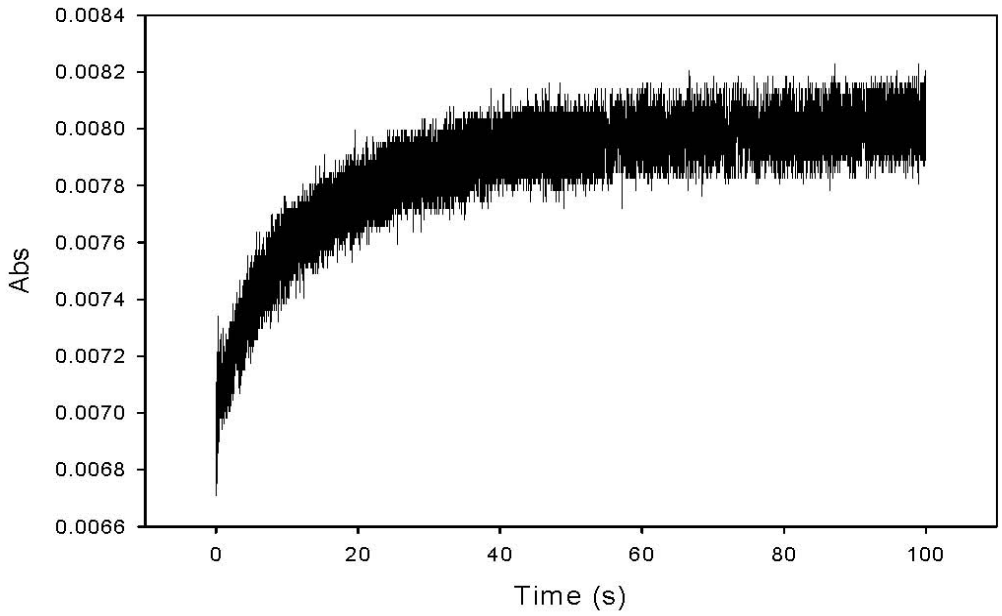

Figure 2-11. Mixing Ru^{III}-Ru^{III} BPE dimer solution (at 10^{-4} M concentration) with KI solution (at 10^{-3} M concentration, high end of experimental range for most of our added I^- studies) in stopped-flow instrument. The eventual change in absorbance was ~0.0012, while the Ru^{III}-Ru^{III} BPE dimer reaction solution at 10^{-4} M had an absorbance change of about 0.13.

It is very important that all ruthenium stock solutions should be freshly prepared and used in less than 45 min so that the reactant's aging effect on the rate constant is kept within an acceptable range compared to the statistical experimental error bars. Figures 2-12 and Figure 2-13 show that the aging of the ruthenium solutions can cause an increase in the rate constant of 0.072 $\pm$ 0.004 Logarithm unit per hour of aging and a simultaneous drop in the absorbance change due to reaction (2). Thus, running the experiments quickly is important for the dimer reaction experiments. Because of this, the ruthenium stock solutions prepared each time could be used only for evaluating a single added electrolyte over a maximum range of 8-9 data points.

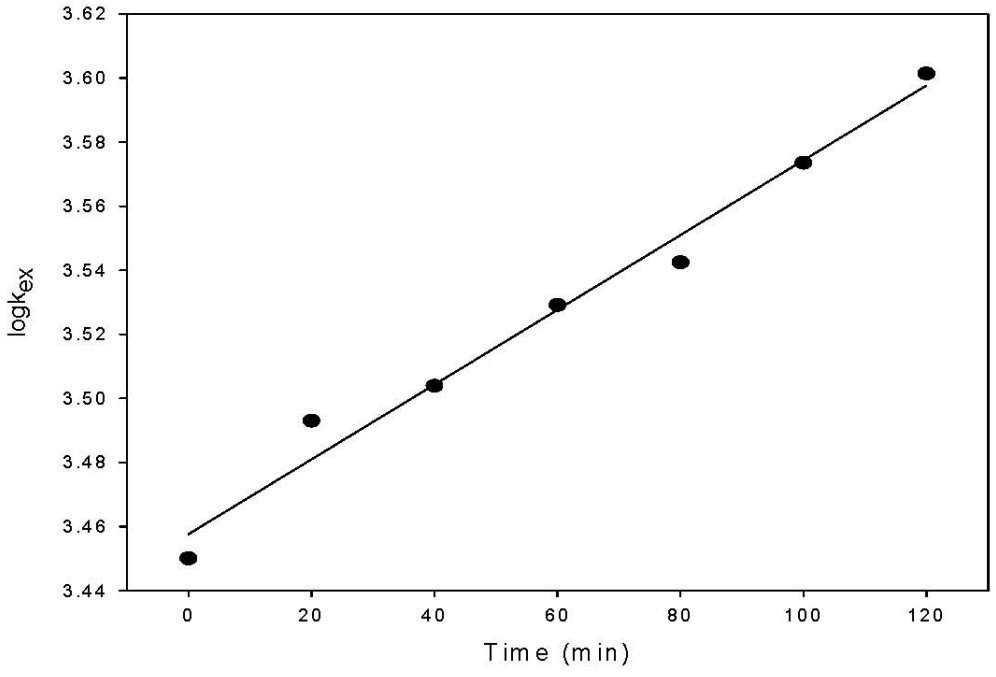

Figure 2-12. Aging effect on reaction (2) at ruthenium concentration 2.0 x 10^{-4} M (regression line computed using SigmaPlot 10.0).

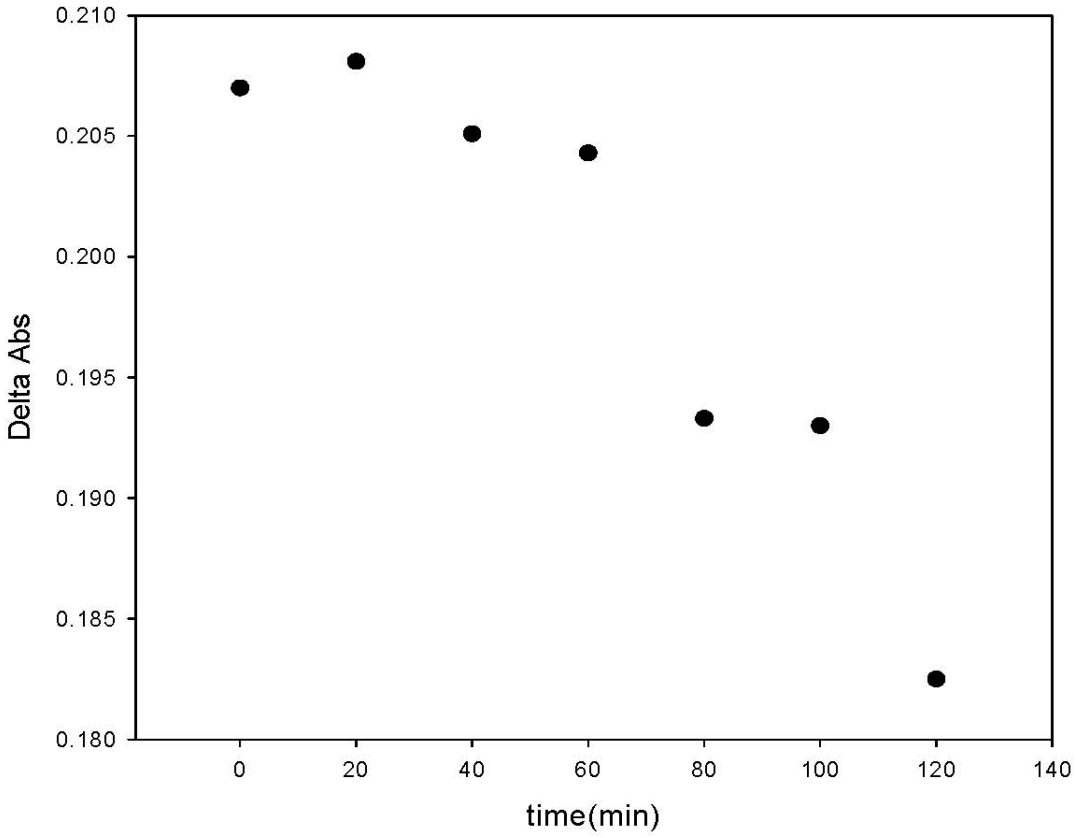

Figure 2-13. Aging effect of reactants on △A of reaction (2) at ruthenium concentration 2.0 x 10^{-4} M.

Extrapolation of the Early-Time Data in the Case of Highly-Catalytic Anions

Some electrolytes (such as sodium *trans,trans*-muconate) behave as very strong catalysts and are able to speed up the reaction rate significantly even at low added ionic strength. When the first half-life of the reaction was close to the stopped-flow dead time (3-15 ms), the detector started failing to capture all kinetic data. The absorbance *vs.* time graph (see Figure 2-14 (b) for a typical example) showed a loss of about 40% of the delta absorbance as compared with

the slow reaction without added electrolyte (Figure 2-14 (a)).

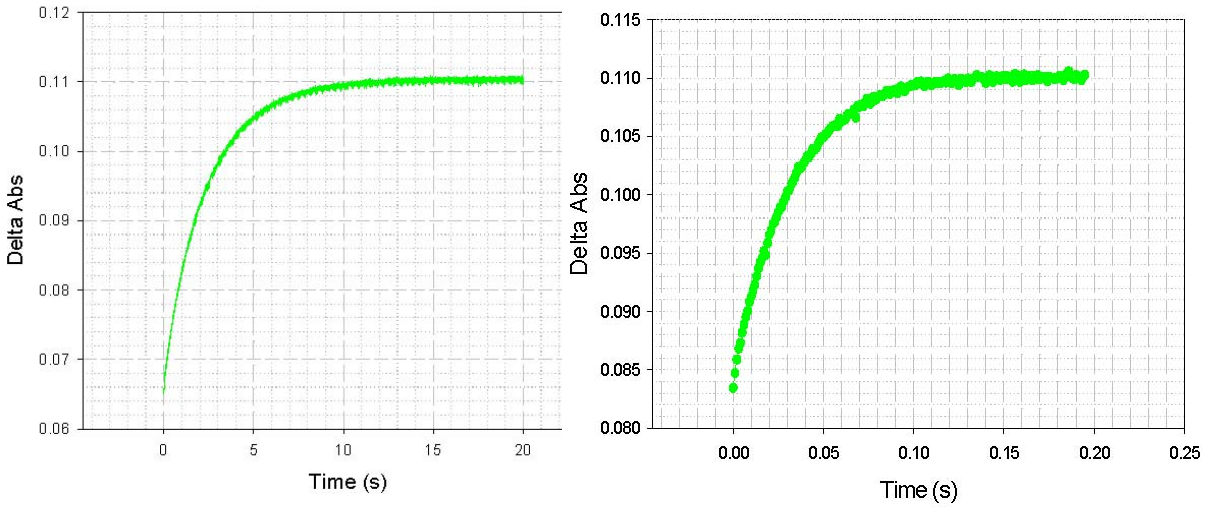

(

(a) (b)

Figure 2-14. (a) Kinetic trace of reaction (2) with ruthenium concentration at 5.0 x 10^{-5} M without added electrolyte. (b) Kinetic trace of reaction (2) with ruthenium concentration at 5.0 x 10^{-5} M and added Sodium *trans,trans*-muconate at 2.0 x 10^{-3} M concentration.

In order to obtain a proper fit and calculate a valid rate constant in such cases, it was necessary to do some extrapolation of the early time portion of the graph. The first step is to figure out the dead time of that particular shot in the stopped-flow experiment. Usually, there were a few bad data points at the very start of the data due to vibration and mixing artifacts which were deleted (as they

clearly did not lie on the subsequent decay curve). In applying the fitting procedure to the rest of the curve, the instrumental dead time can be estimated by introducing a variable time increment (as an X-axis shift) into our fitting equations described previously. This was done by replacing the "t" term in the regression equation with a "t + dt" term and adding "dt = xx" as an initial parameter. The A_t data were fit only to the absorbance values from the slowly-varying later kinetic data which did not have any absorbance lost at short t. By running the regression equations, a best-fit estimate of the dead time was then shown in the "Fit Results" window. We then went back to the numeric data table and added this dead time value to the experimental time values for all data points and re-fitted the curve. Another measure was to add a reasonable data point at time zero (0, Ai) to the graph where the Ai estimate was taken from an uncatalyzed experiment which had no loss of absorbance at early times in the decay. We can see an example for such a corrected fast reaction trace in Figure 2-15. Finally, this extrapolated/corrected graph was fitted using the normal fitting procedure and valid rates obtained (as judged from the fact that these rates joined up smoothly with other, slower rates in a given salt or catalyst study where such corrections were unnecessary, *vide infra*).

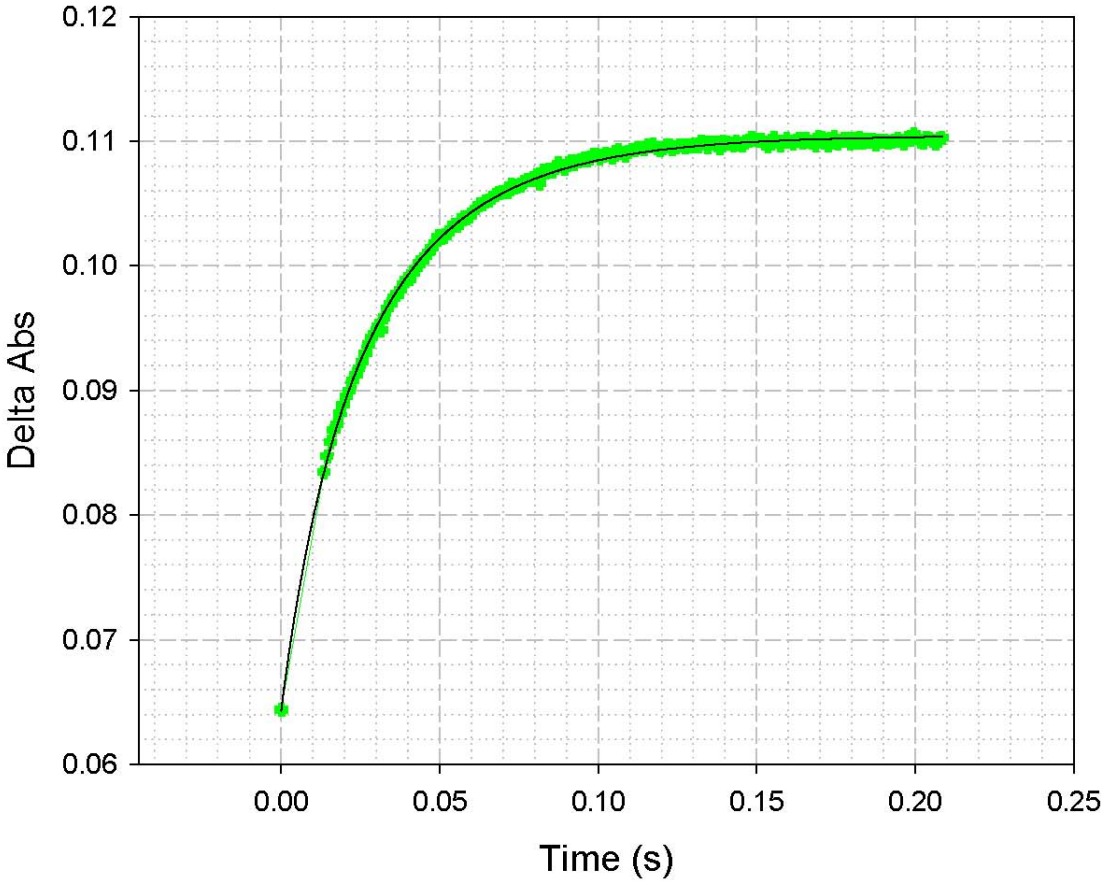

Figure 2-15. Extrapolated/corrected data from Figure 2-14 (b) with dt = 11.5 ms and Ai from Figure 2-14 (a). The black line is the subsequent fit obtained using the normal fitting method.

Figure 2.16 shows a linear relation between the delta absorbance and the concentration of reactants. These data, taken over many days and batches of reactants, indicate the purity consistency of the compounds used in the experiments, and demonstrate that the stopped-flow detector (essentially a single-beam spectrophotometer) is able to respond linearly to concentration (as

expected from Beer's Law) over the entire investigated range from 1 X 10^{-6} M to 5 X 10^{-4} M.

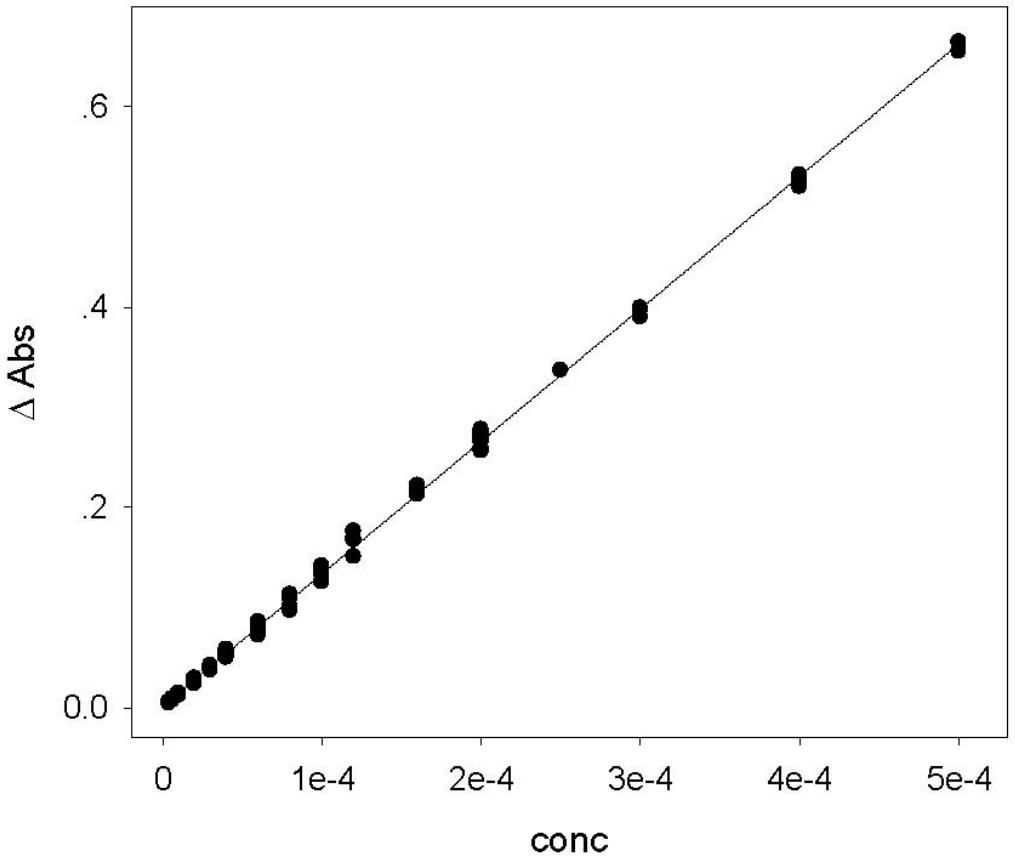

Figure 2.16 Measured absorbance change (products absorbance minus the reactants absorbance) *vs.* the reactants concentration for comproportionation reaction 2

Temperature-Dependent Stopped-Flow Experiments

The temperature of the stopped-flow instrument was controlled with a refrigerated constant temperature circulator over the range of 8-32 ^{o}C for studies

of the temperature dependence of reaction (2). The experimental T range was limited due to the driving syringes of the instrument which become too tight at low T and too loose at high T (which can cause syringe breaking or leaking problems). The reaction temperature was measured using a VWR Scientific (Model 100A) Pt thermometer with its metallic probe in direct contact with the aluminum thermal block bolding the optical cell of the stopped-flow bench (rather than relying on the bath readout). After the desired bench temperature was reached and had become stable for at least 10 min at the cell, the run solutions were pre-adjusted to the same temperature in a separate cooling/ heating water bath prior to transferring them to the reservoir syringes (which were kept thermally insulated but are not actively temperature-controlled on our instrument). The solutions were then drawn down into the thermally-controlled drive syringes and kept there for 1-2 min before mixing so as to beome equilibrated to the same temperature as the whole system. The solutions should not be left in the instrument for more than 5 min since the drive syringes are made of glass which has been shown to give rise to unknown reaction products with our reactants which serve as ET catalysts for reactions (1) and (2) at low reactant concentrations (below about 10^{-4} M, *vide infra*).[41]

We observed that even if the voltage driving the light source was kept rigorously constant, the voltage of a given water *vs.* water (w/w) shot recorded by the instrument depended slightly on the temperature at which the shot was carried out. Figure (2-17) shows the linear relation so-obtained between temperature and the w/w voltage (presumably due to refractive index effects of

the water in the cell). Thus, the w/w reference voltage has to be measured at each temperature before the kinetic measurement in order for valid absorbance values to be calculable. Separate water-mixing experiments in the stopped-flow (Figure 2-18) showed that without the careful temperature pre-adjustment steps described above, it could take as long as 10-15 seconds for water freshly driven into the cell to reach the instrument temperature (as indicated by finally approaching a stable voltage reading). The kinetic decay times of most of the reactions in this study were completed in less then 10 seconds, so pre-adjusting the temperatures of the run solutions to the bench temperature was crucial to the validity of the experiments.

Since the temperature dependence of the reaction rate constant at a given salt concentration was not a large effect as compared to salt-induced rate variations, any aging effects leading to catalytic contaminants could have a significant impact on the derived activational parameters. This impact would be most significant when doing experiments without electrolytes added to the ruthenium solutions (since these would be the slowest reactions and hence the ones most effected by a trace amount of catalyst). By carefully studying the temperature effect with added electrolytes, this aging effect was found to be negligible (control experiments show no difference in the measured rate for the same pair of reactant solutions within two hours). In our experiments, all ruthenium solutions were prepared and used within 20 min of final dilution and glass-contact time in the drive syringes was kept to 1-2 min or less. To minimize any systematic experimental errors due to poor temperature

equilibration, we did the experiments while moving the bench temperature in different directions, such as from high to low, and then low to high within the same experiment, or by randomly jumping about to different temperatures. The lack of any discontinuities or slope changes in the subsequent Eyring plots regardless of the pattern of temperature shifts was taken as proof that the equilibration problem had been solved.

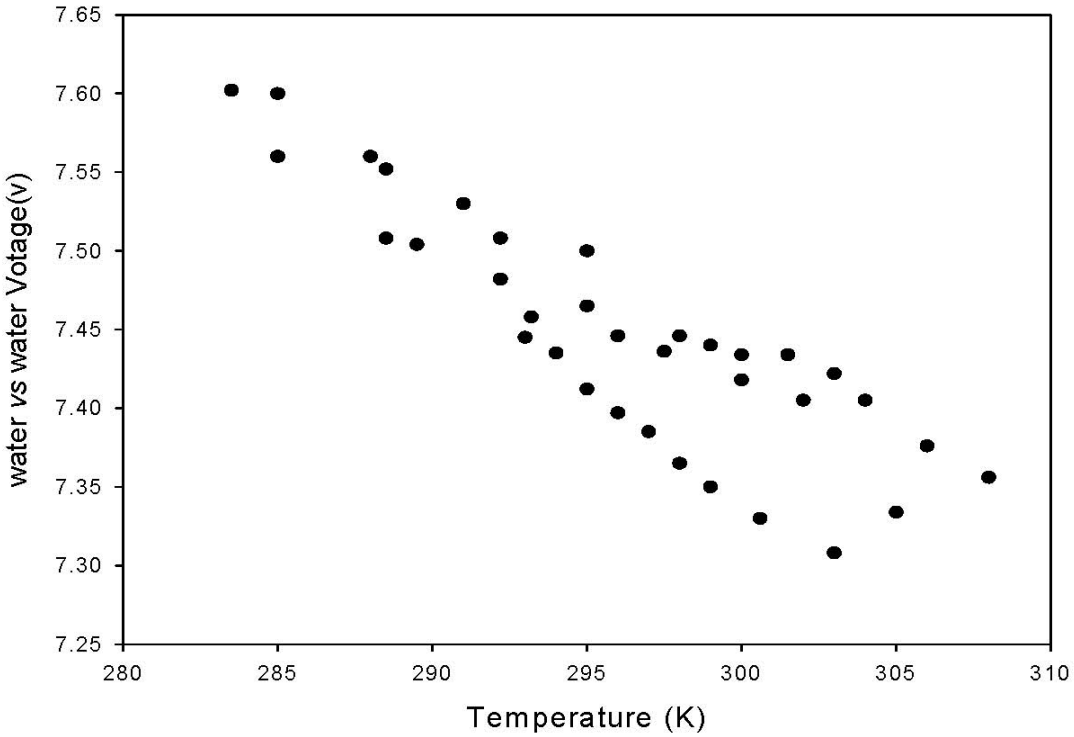

Figure 2-17. Temperature dependence of the water *vs.* water voltage from the stopped-flow photodetector obtained even when carefully keeping the light source voltage constant (by using an AC converter rather than a battery to drive the LED source).

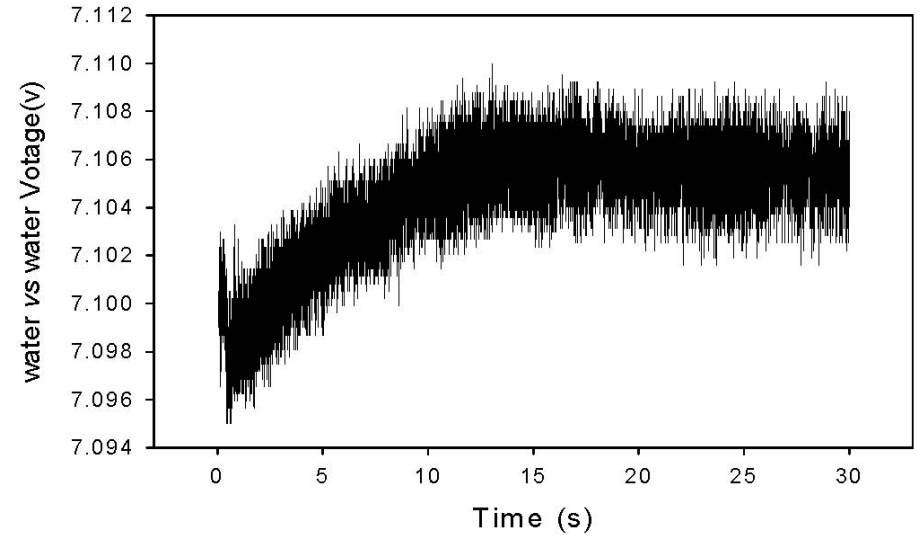

(a)

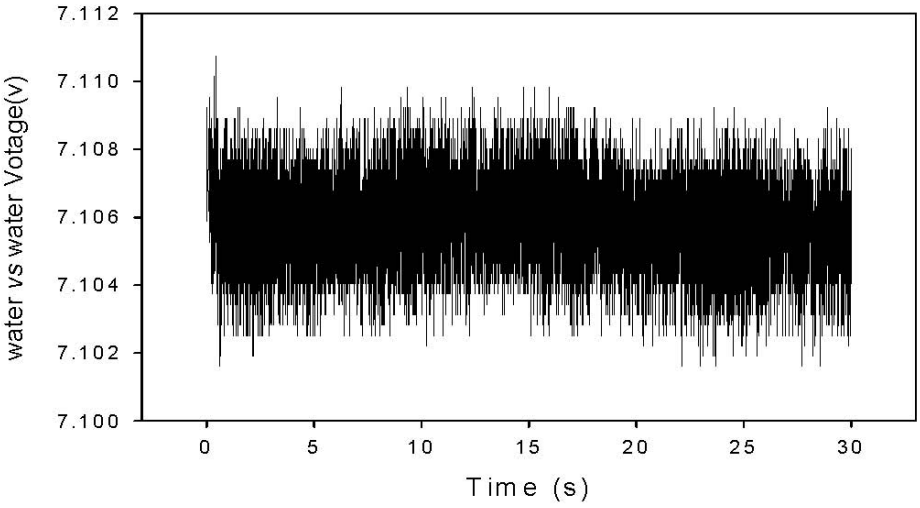

(b)

Figure 2-18. Photodetector voltage from water *vs.* water stopped-flow traces. (a) without pre-adjusting the run solution's temperature before mixing, and (b) after adjusting the water temperature by leaving the water inside the drive syringes for 5 min. (Bench temperature is 10 ^{0}C and water is at room temperature)

Ruthenium(III)pentaamminepyridine Monomer and Dimer Halide K_{ip} Measurements by UV-visible Spectroscopy

In these experiments, the ion-pair charge transfer (IPCT, *vide infra*) absorption bonds were used to determine ion pair formation constants between Ru^{III}-BPE-Ru^{III} or $(NH_3)_5Ru^{III}$3Fpy and halides. Solutions were prepared similarly to the method outlined for the studies of the electrolyte effects on IVCT bands (see Chapter III for details). Instead of adding both ruthenium (II) and (III) to the solutions, only the spectrum of the ruthenium (III) solution (either Ru^{III}-BPE-Ru^{III} or $(NH_3)_5Ru^{III}$3Fpy) was studied in the presence of added halide. The ruthenium (III) concentration was either 5.0 x 10^{-4} M or 10^{-3} M. In the case of iodide, a trace amount of H_2O_2 was added in order to minimize the reduction of the Ru (III) solution. The ion-pair charge transfer bands showed up in the UV region from 300-400 nm with added halide. The difference absorbance spectra were obtained by subtracting the pure ruthenium (III) spectrum from the ones with added halides.

K_{ip} can be obtained by fitting the ΔAbs *vs.* [halide] plots (following the method described by Waysbort. et al. for the hexaammineruthenium (III) complex) using equations 2-49 and 2-50 below,[48]

$$\Delta OD = \frac{\Delta\varepsilon K_{ip}[Ru]_0[X^-]}{1 + K_{ip}[X^-]} \qquad (2\text{-}49)^{48}$$

$$\log K_{ip} = \log K^0{}_{ip} + \frac{1.02 Z_{Ru} Z_{X-} I^{1/2}}{1 + 0.329 d I^{1/2}} + BI \qquad (2\text{-}50)^{48}$$

where ΔOD is the observed absorbance difference at λ_{max} for the IPCT, $\Delta\varepsilon$ is the difference between the molar extinction coefficients of the ion pair and its constituents, Z_{Ru} and Z_{X-} are the charges of the ruthenium complexes and halide, d is the distance of closest approach for the ruthenium complexes and halides (d = d_{ru} + d_{X-}), and B is a variable (fit) parameter taken from the Davies equation[53] and used here to obtain better fitting of the curve.

The regression transform used for in setting up the K_{ip} fitting equations from eq. 2-49 and 2-50 in the Sigma Plot 10.0 program are shown below,

Equation	Variables
I=0.5*(42*ruo+2*X) d= ruo= Kip=10^(log(Kipo)+$Z_{ru}Z_{x-}$*1.02*(I^0.5)/(1+0.329*d*(I^0.5))+B*I) y=dex*Kip*ruo*X/(1+Kip*X) Fit y to DOD	X = col(1) DOD = col (2)
Initial Parameters dex= Kipo= B=	

where dex represents $\Delta\varepsilon$, DOD represents ΔOD.

2.4 Results and Discussion

Reaction 1 (monomer pseudo-self exchange ET) and reaction 2 (dimer comproportionation ET) are both very common types of electron-transfer

reactions. The research described in this thesis was focused mostly on the kinetics of the dimer comproportionation reaction in the presence of different sources of added ionic strength. As explained in the introduction, the work of association of charged reactants and the nature of the second coordination sphere surrounding the reactants can be altered through adding different electrolytes. These added electrolytes can alter the reaction either through classical (Debye-Huckle type) or non-classical (superexchange catalytic) mechanisms.[34] All of the added electrolytes were found to increase the comproportionation reaction rate. However, their individual behaviors as shown in the kinetic plots and possibly the nature of the roles they played in catalyzing the ET reaction were different in ways which reveal various aspects of the ET process.

In order to understand the phenomena described above, we must consider the nature of the ET transition state. The lifetime of the transition state is fleeting, and it is impossible to study it directly. Temperature-dependent experiments and their application of the Eyring formulism were carried out to measure the enthalpy of activation and the entropy of activation.[27] We have also extended such studies in the presence of varying amounts of a subset of the added electrolytes.

In the final part of this section, we will describe detailed kinetic simulations of these electrolyte effects on the electron-transfer reactions. By proposing logical mechanistic pathways for the electrolyte-affected reactions, we are able to fit our experimental kinetic results in such a way as to uncover subtle details of

how the various added salts exert their influence.

2.4.1 Electrolyte Effects

Reactant Concentration Effects on ET Kinetics; Catalysis and Self-Salting

Based on typical kinetic rate laws, it is commonly accepted that the reaction rate constant for a bimolecular reaction at constant temperature and pressure conditions will, in fact, be constant and independent of reactant concentrations. However, while studying the rates of the dimer and monomer reactions in this work without any other added electrolytes present, we observed that when changing the reactants concentrations, the fitted kinetic rate constant clearly changed. In order to verify that this observation was real, we studied the reactions over a range of concentrations (from 6.0×10^{-6} M to 5.0×10^{-4} M) using reactant solutions made up in both glass and plastic volumetric labware.

We found, in agreement with observations made previously by Sista[41], that the use of glass volumetric flasks does indeed generate some unknown catalytic species which can have a great influence on the rate of electron-transfer reactions at low concentrations (< ~ 5×10^{-5} M) (see Figure 2.19). The apparent increase of the measured rate constants in the glass-exposed experiments was found to be a reproducible phenomenon. This catalytic effect becomes much smaller (but does not disappear completely) when solutions for a given kinetics experiment are prepared in plastic volumetric flasks (see Table 2.3 and note the filled circles in Figure 2.18). In Figure 2.18, the reproducible linearity of the

kinetic data at higher concentrations indicates a “safe zone” for the execution of valid further experiments. From the figure we see that this catalytic effect at low concentration solution can be negligible as long as the reactant’s concentration is lower than 5 x 10^{-5} M (GP ~ 0.38) and when the solutions are not made up in or exposed to glass labware (see the closed circles in the plot).

Some effort has been made to understand the catalytic effect of the glass by checking for catalysis due to added silicates,[41] but no conclusions have been arrived at. The possibilities remain that the catalysis observed at low reactant concentrations might due to trace amounts of some unknown glass-related (presumably silicate species) dissolved in the water, or due to some interaction between the reactants themselves and the glass giving rise to a catalytic specie.

Table 2.3 The effect of reactants concentration (and hence total GP) on the rate constant of reaction 2 (dimer) in solution made up using plastic and glass volumetric flasks.

Data from plastic volumetric flasks				
Reactant’s Concentration (M) $[Ru^{II}, Ru^{II}] = [Ru^{III}, Ru^{III}]$	μ_{tot}	GP	$logk_{ex}$	95% CI (confidence interval)[(a)]
6.0 x 10^{-6}	1.87 x 10^{-4}	.0135	3.199	0.11
1.0 x 10^{-5}	3.09 x 10^{-4}	.0173	3.054	0.06
2.0 x 10^{-5}	6.20 x 10^{-4}	.0243	3.070	0.03

3.0×10^{-5}	9.30×10^{-4}	.0296	3.083	----
4.0×10^{-5}	1.24×10^{-4}	.0340	3.058	0.11
5.0×10^{-5}	1.55×10^{-3}	.0379	3.087	0.05
6.0×10^{-5}	1.86×10^{-3}	.0413	3.131	0.06
8.0×10^{-5}	2.48×10^{-3}	.0474	3.136	0.10
1.0×10^{-4}	3.09×10^{-3}	.0527	3.220	0.08
1.2×10^{-4}	3.72×10^{-3}	.0575	3.334	0.07
1.5×10^{-4}	4.64×10^{-3}	.0638	3.340	0.08
1.6×10^{-4}	4.96×10^{-3}	.0658	3.412	0.06
2.0×10^{-4}	6.20×10^{-3}	.0730	3.450	0.07
2.5×10^{-4}	7.75×10^{-3}	.0809	3.570	0.05
3.0×10^{-4}	9.31×10^{-3}	.0880	3.663	0.07
4.0×10^{-4}	0.0124	.1002	3.820	0.04
5.0×10^{-4}	0.0155	.1107	3.933	0.03
Data from glass volumetric flasks				
Reactant's Concentration (M) $[Ru^{II}, Ru^{II}] = [Ru^{III}, Ru^{III}]$	μ_{tot}	GP		$\log k_{ex}$
4.0×10^{-6}	1.24×10^{-4}	.0110		4.257
4.0×10^{-6}	1.24×10^{-4}	.0110		4.094
4.0×10^{-6}	1.24×10^{-4}	.0110		4.060
4.0×10^{-6}	1.24×10^{-4}	.0110		4.116
4.0×10^{-6}	1.24×10^{-4}	.0110		4.257

4.0×10^{-6}	1.24×10^{-4}	.0110	4.229
4.0×10^{-6}	1.24×10^{-4}	.0110	4.072
6.0×10^{-6}	1.87×10^{-4}	.0135	3.922
6.0×10^{-6}	1.87×10^{-4}	.0135	3.904
6.0×10^{-6}	1.87×10^{-4}	.0135	3.949
6.0×10^{-6}	1.87×10^{-4}	.0135	3.870
6.0×10^{-6}	1.87×10^{-4}	.0135	3.860
6.0×10^{-6}	1.87×10^{-4}	.0135	3.951
6.0×10^{-6}	1.87×10^{-4}	.0135	4.075
6.0×10^{-6}	1.87×10^{-4}	.0135	4.032
6.0×10^{-6}	1.87×10^{-4}	.0135	4.001
6.0×10^{-6}	1.87×10^{-4}	.0135	3.971
1.0×10^{-5}	3.09×10^{-4}	.0173	3.830
1.0×10^{-5}	3.09×10^{-4}	.0173	3.818
1.0×10^{-5}	3.09×10^{-4}	.0173	3.730
1.0×10^{-5}	3.09×10^{-4}	.0173	3.722
1.0×10^{-5}	3.09×10^{-4}	.0173	3.832
2.0×10^{-5}	6.20×10^{-4}	.0243	3.584
2.0×10^{-5}	6.20×10^{-4}	.0243	3.590
2.0×10^{-5}	6.20×10^{-4}	.0243	3.559
2.0×10^{-5}	6.20×10^{-4}	.0243	3.632
2.0×10^{-5}	6.20×10^{-4}	.0243	3.669

2.0×10^{-5}	6.20×10^{-4}	.0243	3.518
2.0×10^{-5}	6.20×10^{-4}	.0243	3.576
2.0×10^{-5}	6.20×10^{-4}	.0243	3.637
2.0×10^{-5}	6.20×10^{-4}	.0243	3.558
2.0×10^{-5}	6.20×10^{-4}	.0243	3.543
3.0×10^{-5}	9.30×10^{-4}	.0296	3.347
3.0×10^{-5}	9.30×10^{-4}	.0296	3.476
3.0×10^{-5}	9.30×10^{-4}	.0296	3.363
3.0×10^{-5}	9.30×10^{-4}	.0296	3.436
3.0×10^{-5}	9.30×10^{-4}	.0296	3.445
4.0×10^{-5}	1.24×10^{-4}	.0340	3.367
4.0×10^{-5}	1.24×10^{-4}	.0340	3.342
4.0×10^{-5}	1.24×10^{-4}	.0340	3.379
4.0×10^{-5}	1.24×10^{-4}	.0340	3.324
4.0×10^{-5}	1.24×10^{-4}	.0340	3.406
4.0×10^{-5}	1.24×10^{-4}	.0340	3.318
4.0×10^{-5}	1.24×10^{-4}	.0340	3.477
4.0×10^{-5}	1.24×10^{-4}	.0340	3.324
4.0×10^{-5}	1.24×10^{-4}	.0340	3.395
4.0×10^{-5}	1.24×10^{-4}	.0340	3.444
6.0×10^{-5}	1.86×10^{-3}	.0413	3.368
6.0×10^{-5}	1.86×10^{-3}	.0413	3.397

6.0×10^{-5}	1.86×10^{-3}	.0413	3.314
6.0×10^{-5}	1.86×10^{-3}	.0413	3.227
6.0×10^{-5}	1.86×10^{-3}	.0413	3.401
6.0×10^{-5}	1.86×10^{-3}	.0413	3.378
6.0×10^{-5}	1.86×10^{-3}	.0413	3.454
8.0×10^{-5}	2.48×10^{-3}	.0474	3.260
8.0×10^{-5}	2.48×10^{-3}	.0474	3.341
8.0×10^{-5}	2.48×10^{-3}	.0474	3.369
8.0×10^{-5}	2.48×10^{-3}	.0474	3.309
8.0×10^{-5}	2.48×10^{-3}	.0474	3.414
8.0×10^{-5}	2.48×10^{-3}	.0474	3.463
8.0×10^{-5}	2.48×10^{-3}	.0474	3.432
1.0×10^{-4}	3.09×10^{-3}	.0527	3.422
1.0×10^{-4}	3.09×10^{-3}	.0527	3.464
1.0×10^{-4}	3.09×10^{-3}	.0527	3.421
1.0×10^{-4}	3.09×10^{-3}	.0527	3.444
1.0×10^{-4}	3.09×10^{-3}	.0527	3.274
1.0×10^{-4}	3.09×10^{-3}	.0527	3.462
1.2×10^{-4}	3.72×10^{-3}	.0575	3.378
1.2×10^{-4}	3.72×10^{-3}	.0575	3.433
1.2×10^{-4}	3.72×10^{-3}	.0575	3.485
1.6×10^{-4}	4.96×10^{-3}	.0658	3.528

1.6×10^{-4}	4.96×10^{-3}	.0658	3.536
1.6×10^{-4}	4.96×10^{-3}	.0658	3.403
1.6×10^{-4}	4.96×10^{-3}	.0658	3.571
2.0×10^{-4}	6.20×10^{-3}	.0730	3.494
2.0×10^{-4}	6.20×10^{-3}	.0730	3.534
2.0×10^{-4}	6.20×10^{-3}	.0730	3.507
2.0×10^{-4}	6.20×10^{-3}	.0730	3.566
2.0×10^{-4}	6.20×10^{-3}	.0730	3.630
2.0×10^{-4}	6.20×10^{-3}	.0730	3.671
2.0×10^{-4}	6.20×10^{-3}	.0730	3.650
2.0×10^{-4}	6.20×10^{-3}	.0730	3.588
3.0×10^{-4}	9.31×10^{-3}	.0880	3.679
3.0×10^{-4}	9.31×10^{-3}	.0880	3.693
4.0×10^{-4}	0.0124	.1002	3.804
4.0×10^{-4}	0.0124	.1002	3.855
5.0×10^{-4}	0.0155	.1107	3.956

(a) based on replicate measurements

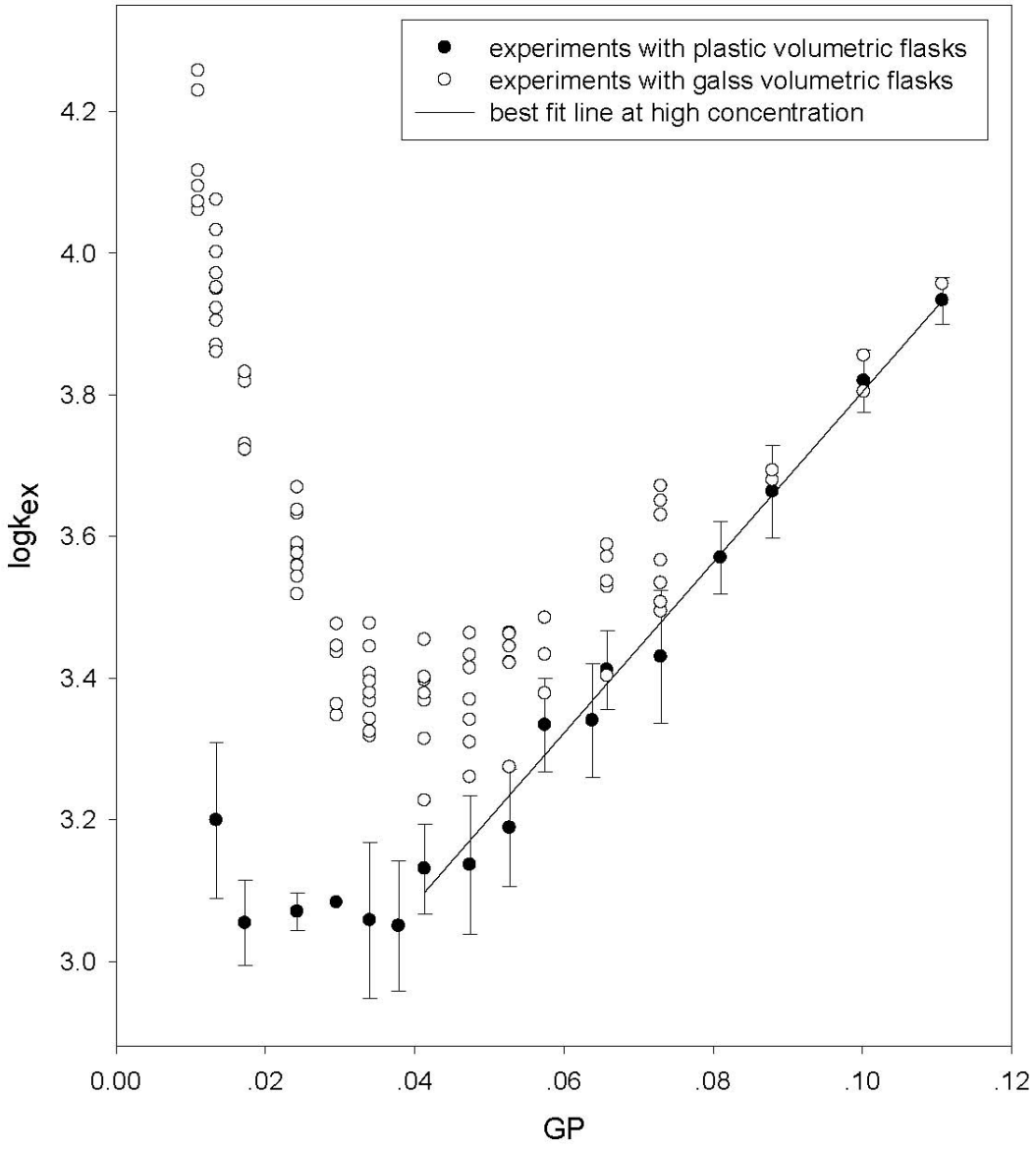

Figure 2.19 Rate constant of reaction 2 (dimer comproportionation ET) at various reactants concentrations for solutions made up in both plastic and glass volumetric labware. The Error bars are created based on 95% confident intervals calculated from replicate measurements. The slope of the best-fit-line at high concentration ($\geq 5.0\times10^{-5}$ M) is 11.5$\pm$0.3.

Figure 2.18 shows a linear relationship between the logarithm of the observed rate constant and the Guggenheim parameter at higher concentration in both plastic and glass experiments, but the linear region is clearly expanded by avoiding glass. This is an interesting and to our knowledge novel observation, and it does not conflict with what we have learned in other salt added experiments. After performing many experiments with a broad range of electrolytes, we now know that the rate of reaction between like-charged reactants increases linearly with GP as long known from early work (see equation 2-10).[12c] Thus we assign the current "self-salting" concentration effect as being due to the ionic strength being contributed by the reactants themselves. Even though there is no other "spectator" electrolyte added, the reactants themselves are in the form of chloride salts of polycationic species, and we see here that this ionic strength alone can clearly enhance the rate of electron-transfer between the ruthenium cations. More details on this will be discussed in the section on the "Olson-Simonson effect".

Classical and Non-classical Electrolyte Effects on Comproportionation ET Reaction Two

Electrolyte effects on the rate of dimer comproportionation reaction (2) were studied at three different reactant's concentrations; 5.0 $x10^{-5}$ M, 1.0 x 10^{-4} M and 2.0 x 10^{-4} M. These experiments were intended to help us to obtain a more general picture of the mechanism of the electrolyte effect on the electron-transfer process than we could by just looking at one reactants concentration. In these

experiments the reactant's concentrations were kept at constant while the increase in ionic strength was achieved solely by the addition of the various electrolytes.

Electrolyte Effects at 5.0 x10^{-5} M Reactant's Concentration

Extensive studies[12c,36,41] have shown that for the monomer pseudo-self exchange reaction (reaction 1), simple salt effects generally follow the Debye-Huckle law (with a kinetic slope in the experimental GP *vs.* logk_{ex} plots near that of the reactant's charge product, (+2)(+3) = 6. For reaction 2 however (the dimer comproportionation reaction), the reactants have higher charges (4+ and 6+) and the molecular shapes are not at all sphere-like as in the monomer case. So one of our question was to see how well the Debye-Huckle theory would be followed in this much less "ideal" case.

First, simple salts such as the chloride salts $LaCl_3$, $CaCl_2$, and KCl, and the potassium halide salts KBr and KI were used to study the kinetic behavior of the reaction (2) at a reactants concentration of 5.0 x 10^{-5} M (see table 2.4 and figure 2.20).

Table 2.4 Kinetic data (simple salts only) for reaction 2 at 5.0 x 10^{-5} M reactant's concentration

[LaCl3] (M)	Total μ	GP	logk_{ex}[a]
0.00	1.55 x 10^{-3}	0.0379	3.050 ± .092

3.33×10^{-5}	1.75×10^{-3}	0.0402	3.087
1.33×10^{-4}	2.35×10^{-3}	0.0462	3.182
3.33×10^{-4}	3.54×10^{-3}	0.0562	3.381
6.67×10^{-4}	5.54×10^{-3}	0.0693	3.610
1.00×10^{-3}	7.54×10^{-3}	0.0799	3.820
1.33×10^{-3}	9.54×10^{-3}	0.0890	3.976
1.67×10^{-3}	0.0115	0.0970	4.117
$[CaCl_2]$ (M)	Total μ	Total GP	$\log k_{ex}$
0.00	1.55×10^{-3}	0.0379	3.050 ± .092
6.67×10^{-5}	1.75×10^{-3}	0.0402	3.065
2.67×10^{-4}	2.35×10^{-3}	0.0462	3.254
6.67×10^{-4}	3.54×10^{-3}	0.0562	3.477
1.33×10^{-3}	5.54×10^{-3}	0.0693	3.770
2.00×10^{-3}	7.54×10^{-3}	0.0799	3.902
2.67×10^{-3}	9.54×10^{-3}	0.0890	4.158
3.33×10^{-3}	0.0115	0.0970	4.335
[KCl] (M)	Total μ	Total GP	$\log k_{ex}$
0.00	1.55×10^{-3}	.0379	3.050 ± .092
2.00×10^{-4}	1.75×10^{-3}	.0402	3.169 ± .122
4.00×10^{-4}	1.95×10^{-3}	.0423	3.181
8.00×10^{-4}	2.35×10^{-3}	.0462	3.335 ± .139

2.00×10^{-3}	3.54×10^{-3}	.0562	3.654 ± .084
4.00×10^{-3}	5.54×10^{-3}	.0693	4.049 ± .033
6.00×10^{-3}	7.54×10^{-3}	.0799	4.329
6.00×10^{-3}	7.54×10^{-3}	.0799	4.310
8.00×10^{-3}	9.54×10^{-3}	.0890	4.538 ± .018
0.010	0.0115	.0970	4.721
0.012	0.0136	.1043	4.855
0.015	0.0166	.1140	5.074
0.020	0.0215	.1280	5.246
0.030	0.0315	.1508	5.597
0.035	0.0366	.1605	5.654
0.045	0.0466	.1775	5.861
0.050	0.0515	.1850	5.890
0.060	0.0616	.1988	6.088
[KBr] (M)	Total μ	Total GP	$\log k_{ex}$
0.00	1.55×10^{-3}	.0379	3.050 ± .092
2.00×10^{-4}	1.75×10^{-3}	.0402	3.139
2.00×10^{-4}	1.75×10^{-3}	.0402	3.216
4.00×10^{-4}	1.95×10^{-3}	.0423	3.250
8.00×10^{-4}	2.35×10^{-3}	.0462	3.393
8.00×10^{-4}	2.34×10^{-3}	.0462	3.368

2.00×10^{-3}	3.54×10^{-3}	.0562	3.840
2.00×10^{-3}	3.54×10^{-3}	.0562	3.750
4.00×10^{-3}	5.5443e-3	.0693	4.292
4.00×10^{-3}	5.54×10^{-3}	.0693	4.131
6.00×10^{-3}	7.54×10^{-3}	.0799	4.613
8.00×10^{-3}	9.54×10^{-3}	.0890	4.822
8.00×10^{-3}	9.54×10^{-3}	.0890	4.855
0.015	0.0166	.1140	5.355
0.030	0.0315	.1508	5.882
0.045	0.0466	.1775	6.160
0.060	0.0616	.1988	6.457
[KI] (M)	Total μ	Total GP	$\log k_{ex}$
0.00	1.55×10^{-3}	.0379	3.050 ± .092
2.00×10^{-4}	1.75×10^{-3}	.0402	3.167
4.00×10^{-4}	1.95×10^{-3}	.0423	3.305
8.00×10^{-4}	2.35×10^{-3}	.0462	3.423
2.00×10^{-3}	3.54×10^{-3}	.0562	3.954
4.00×10^{-3}	5.54×10^{-3}	.0693	4.521
6.00×10^{-3}	7.54×10^{-3}	.0799	4.847
8.00×10^{-3}	9.54×10^{-3}	.0890	5.105

(a) Stated errors are based on statistical analysis of replicate measurements

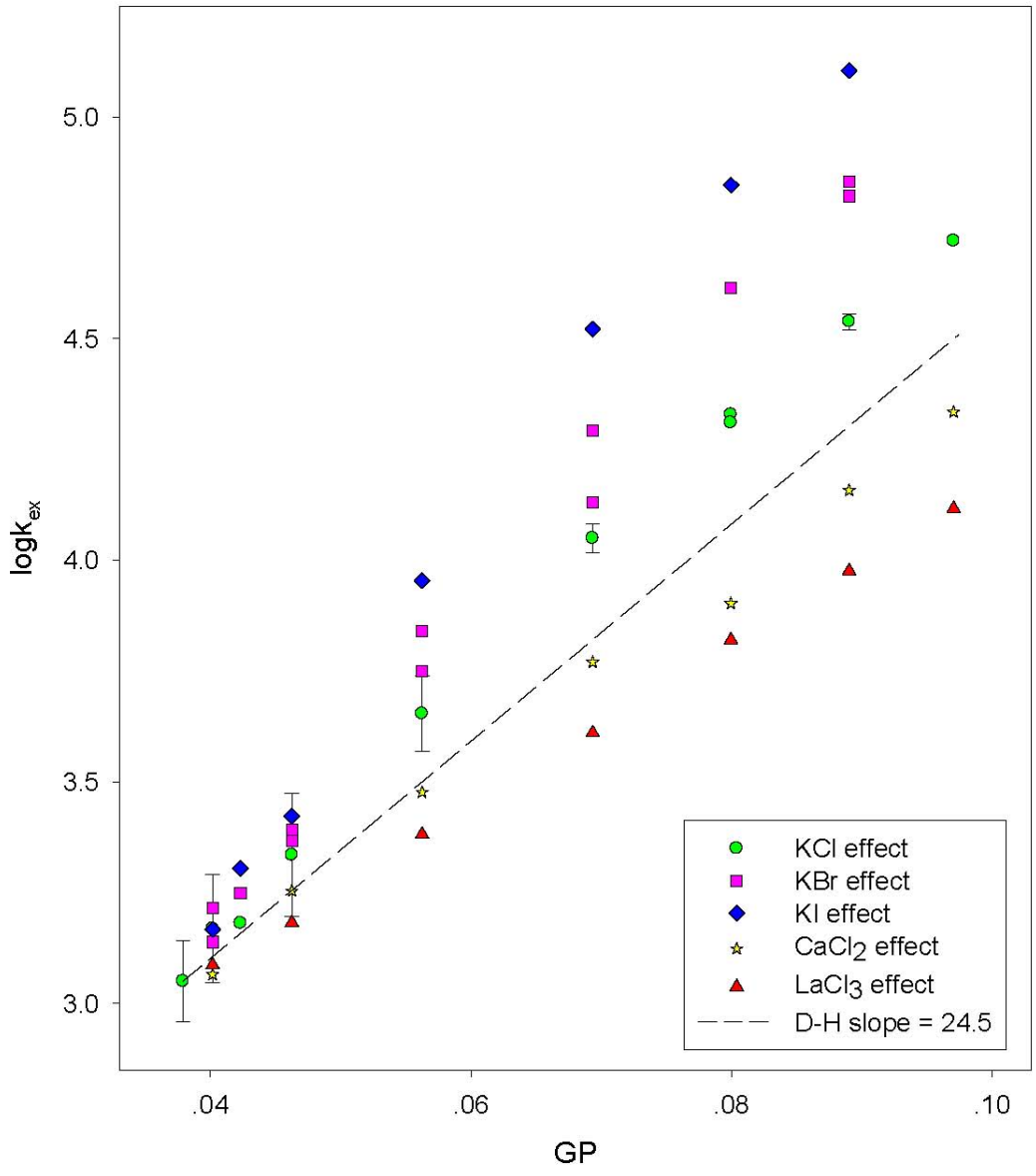

Figure 2.20 Simple salt effects on the reaction 2 (dimer comproportionation reaction) up to GP 0.1 with fixed reactants concentration at $[Ru^{II}\text{-}Ru^{II}] = [Ru^{III}\text{-}Ru^{III}] = 5.0 \times 10^{-5}$ M. The 95% confidence level error bars are included for points with replicate measurements.

From Figure 2.20, we see that for the chloride salts, the rate accelerating ability when plotted as total GP decreases in the order of KCl > $CaCl_2$ > $LaCl_2$. Both, $CaCl_2$ and $LaCl_3$ behave fairly linearly in the GP plot, whereas KCl, KBr and KI exhibit increasing curvature with steeper slopes at low GP. None of the salts follow the Debye-Huckle slope exactly (see table 2.5 for initial slopes). $CaCl_2$ with its slope of 21.7 $\pm$ 0.7 is nearly within error of the Debye-Huckle slope of 24.5, but the others are all significantly different.

Table 2.5 Initial slopes (from GP = 0.0379 to 0.0462) of the kinetic curves obtained with various halide salts at 5.0 x 10^{-5} M reactants concentration for reaction two.

Added electrolytes	Initial slope of kinetic curve in GP[a]
$LaCl_3$	18.8 ± .3
$CaCl_2$	21.7 ± .7
KCl	32.9 ± 1.6
KBr	36.0 ± 1.3
KI	48.2 ± .8

(a) Errors are based on replicate measurements

Because of the differences between the cations of these three salts, it is reasonable to assign these effects as possibly being due to specific cation effects. Following this idea, an immediate question is whether it is the size or the charge

of the cation which matters. Figure 2.21 however, shows that there is little if any difference between the KBr, NaBr, and LiBr salt effect on reaction 2. This indicates that the size of the cation does not affect the rate of electron-transfer above error level in these experiments.

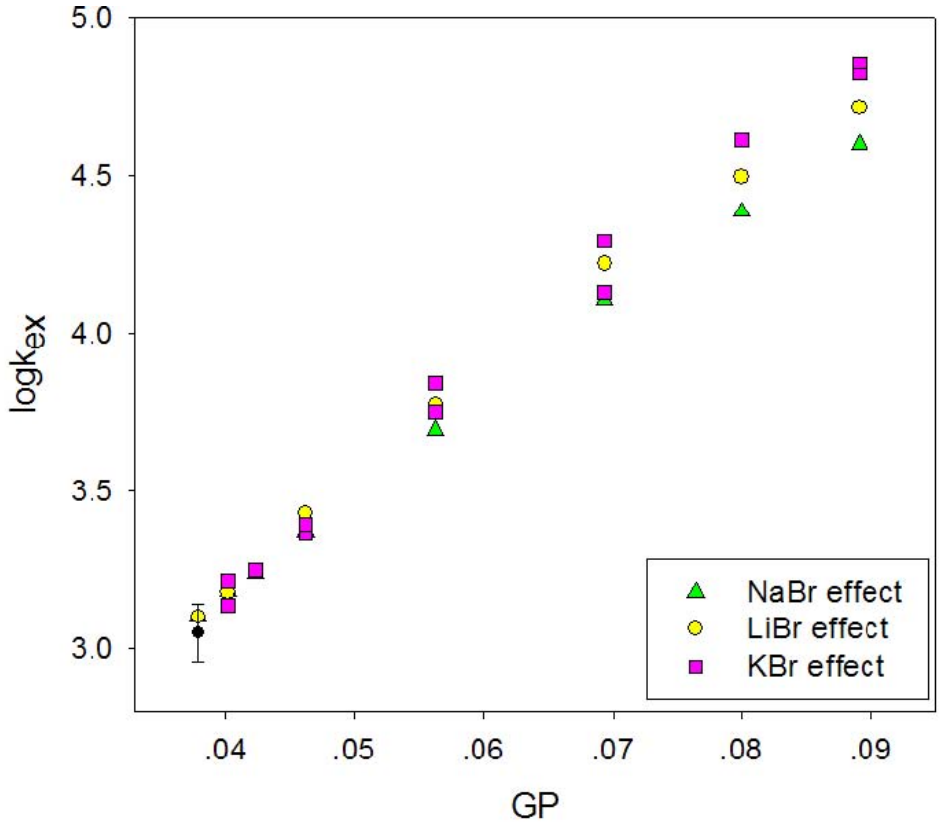

Figure 2.21 Effects of added NaBr, LiBr and KBr on reaction 2 at a reactant's concentration of 5.0 x 10^{-5} M.

Since the reactants are both positively-charged (4+ and 6+), the anions in the solution might reasonably be expected to play more important roles than the cations in the electron-transfer process. Olson and Simonson described this

kind of specific-ion effect in their study of a broad range of electrolyte effects on reactions between charged reactants.[19] By plotting the KCl, $CaCl_2$, $LaCl_3$ graphs as simple concentration of Cl^- *vs.* $\log k_{ex}$ (Figure 2.22), we observe that all the three lines from Figure 2.20 merge into one and show the same kinetic behavior regardless of the charges on the cations. Olsen and Simonson interpreted such curves as a sign that a given ion of charge opposite to the like-charge reactants was involved in some kind of specific pre-equilibrium step or in the formation of the kinetic transition state itself in addition to any ion-atmosphere/Debye-Hückel type of charge screening and activity coefficient effect.

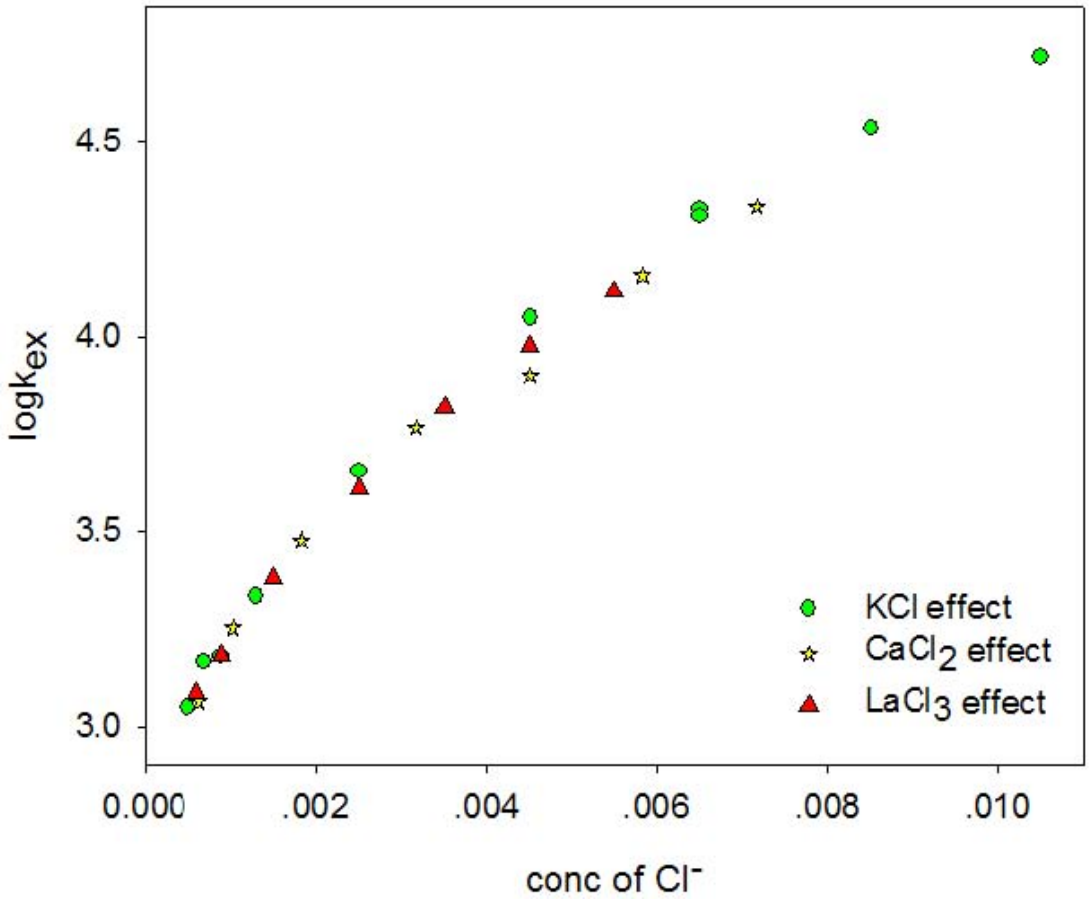

Figure 2.22 Olson-Simonson plot for KCl, $CaCl_2$ and $LaCl_3$ effects on reaction 2.

The clear differences in kinetic behavior seen between KCl, KBr, and KI effects in Figure 2.20 are necessarily due to differing anion effects. Importantly, they all exhibit much higher initial slopes than the predicted Debye-Huckel slope of 24.5 as shown in Table 2.6. I^- accelerates the rate fastest of the three halides and has an initial slope of 48.2. This progressive variation along the halide series may be related to their first ionization energies (F^-; 1681 kJ/mol, Cl^-; 1251 kJ/mol, Br^-; 1139 kJ/mol, I^-; 1008 kJ/mol)[53] and hence redox potentials in

solution, or simply to their ionic radii. A difficulty we face here is that these two properties are strongly correlated. For example, I^- has the largest ionic radius at 2.1 Å and is also the softest lewis base (most polarizable) of the halides, so it is most easily oxidized (E^0 = 0.536 V vs. in water) while Cl^- has r = 1.80 Å and E^0 = 1.358 V.[50] The greater catalytic effect with heavier halides may indicate an important role for both hole-transfer superexchange in the transition complex and radius-related solvation energy effects (*vide infra*).

The most immediate observation is that the simple salts effects do not follow the classical Debye-Huckel theory to give the predicted linear dependence between $\log k_{ex}$ and GP. This may indicate that the reactants are forming ion-pairs with the added anions in a manner consistent with the Olsen-Simonson effect. Any such specific ion-pairing would decrease the charges of the reactants, and the reduced charge products would in turn decrease the predicted $\log k_{ex}$ *vs.* GP slope at higher anion concentrations where the extent of ion pairing is higher.

Figure 2.23 shows how the slopes for KBr and KCl change when going to high GP. At the high end of the ionic strength range in the figure, the added-salt concentration is more than 1000 times larger than the reactants concentration. For KBr, we find that the initial slope is 36.0 ± 1.3 and the final slope is 12.8 ± 0.5. For KCl, the initial slope is 30 ± 0.6 and the final slope is 11.8 ± 0.5. We note that they have nearly the same final slopes within experimental error.

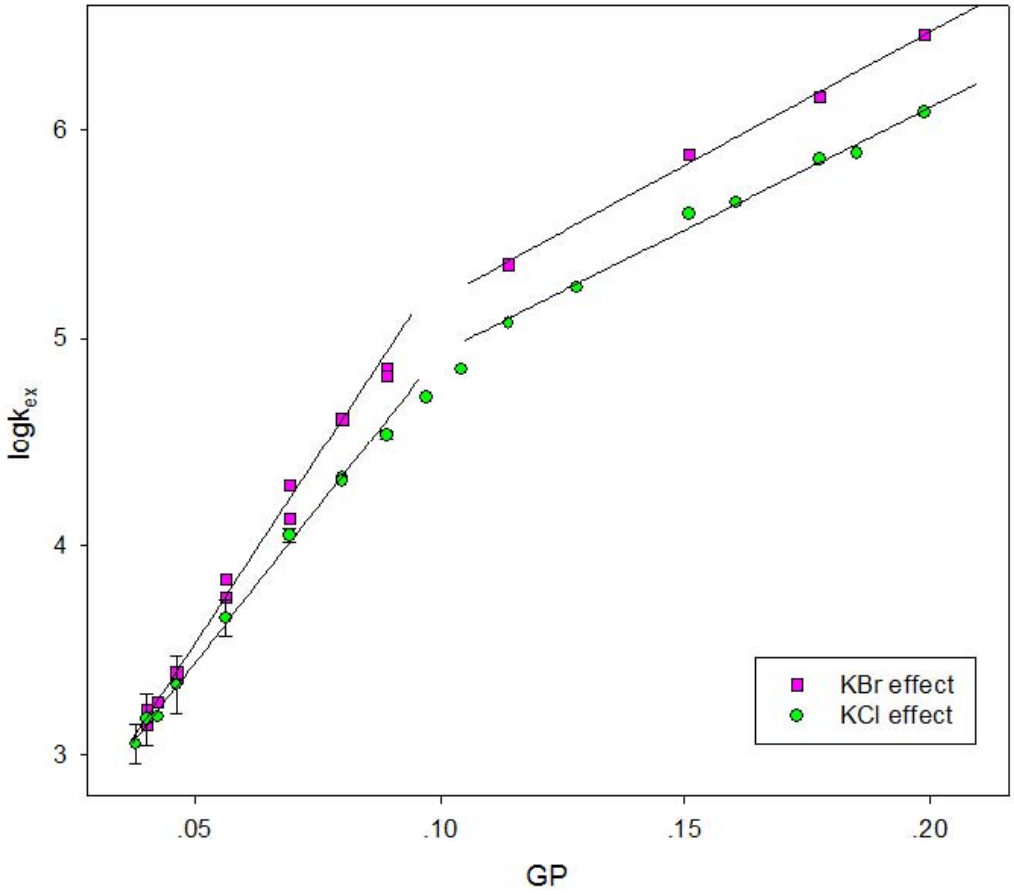

Figure 2.23 KBr and KCl salt effects on the reaction 2 at reactant's concentration of 5.0 x 10^{-5} M up to 0.2 GP.

Figure 2.24 shows the data from table 2.6 for the effects of added "catalytic" electrolytes on reaction 2 at a reactant's concentration of 5.0 x 10^{-5} M. All these added salts show much higher initial slopes than the theoretical ones, but at higher GP where more ion pairs would be formed, the final slopes all drop below the Debye-Huckel theoretical one. The situation is very obvious for the 1:2 electrolytes, such as Na_2muc, Na_2adip, Na_2(1,5NDS), Na_2terephalate, and

Na_2(chdc). These salts all show a very strong catalytic effect on the reaction in the beginning (see Table 2.7 and Figure 2.24), and end up with a much lower slope towards the end of the range (see especially the Na_2(chdc) data). A good example will be the Na_2(chdc) whose initial slope is 174 ± 24 and final slope is about 1.5.

Figure 2.25 shows an expansion plot of Figure 2.24 and clearer patterns at low GP. NaSCN has a much stronger effect on ET than KBr at the beginning, but they end up with almost the same kinetic effect at higher GP. Muc^{2-} is a much better catalyst than its saturated analogue $adip^{2-}$ even though they have almost the exact same size and identical changes. The same is true for unsaturated/saturated $terephalate^{2-}$ and $chdc^{2-}$ pair. This effect has been explained by Curtis *et al.*[12c] as being a result of the conjugated electronic structures of muc^{2-} and $terephalate^{2-}$ and their ability to provide a better electron-tunneling superexchange pathway.

Table 2.6 Catalytic salt effects on dimer comproportionation reaction at reactant's concentration 5.0 x 10^{-5} M.

[NaSCN] (M)	Total μ	Total GP	$logk_{ex}$[a]
0.00	1.55 x 10^{-3}	.0379	3.150
1.00 x 10^{-4}	1.64 x 10^{-3}	.0390	3.370
2.00 x 10^{-4}	1.75 x 10^{-3}	.0402	3.550
2.00 x 10^{-4}	1.75 x 10^{-3}	.0402	3.723

4.00×10^{-4}	1.95×10^{-3}	.0423	3.700
4.00×10^{-4}	1.95×10^{-3}	.0423	3.819
8.00×10^{-4}	2.34×10^{-3}	.0462	3.867
8.00×10^{-4}	2.34×10^{-3}	.0462	3.899
2.00×10^{-3}	3.54×10^{-3}	.0562	4.092
2.00×10^{-3}	3.54×10^{-3}	.0562	4.147
4.00×10^{-3}	5.54×10^{-3}	.0693	4.457
4.00×10^{-3}	5.54×10^{-3}	.0693	4.433
6.00×10^{-3}	7.54×10^{-3}	.0799	4.640
8.00×10^{-3}	9.54×10^{-3}	.0890	4.860
8.00×10^{-3}	9.54×10^{-3}	.0890	4.912
0.015	0.0166	.1140	5.403
0.030	0.0315	.1508	5.933
0.045	0.0466	.1775	6.291
$[Na_2(adipate)]$ (M)	Total μ	Total GP	$\log k_{ex}$
0.00	1.55×10^{-3}	.0379	3.158
6.67×10^{-5}	1.75×10^{-3}	.0402	3.478
1.33×10^{-4}	1.95×10^{-3}	.0423	3.732
2.67×10^{-4}	2.34×10^{-3}	.0462	4.13
6.67×10^{-4}	3.54×10^{-3}	.0562	4.641
1.33×10^{-3}	5.52×10^{-3}	.0692	4.965

2.67×10^{-3}	9.54×10^{-3}	.0890	5.287
4.00×10^{-3}	0.0136	.1043	5.427
6.67×10^{-3}	0.0215	.1280	5.571
1.00×10^{-2}	0.0315	.1508	5.692
$[Na_2(muconate)]$ (M)	Total μ	Total GP	$logk_{ex}$
0.00	1.55×10^{-3}	.0379	3.150
0.00	1.55×10^{-3}	.0379	3.182
1.67×10^{-5}	1.60×10^{-3}	.0385	3.459
1.67×10^{-5}	1.60×10^{-3}	.0385	3.368
3.33×10^{-5}	1.64×10^{-3}	.0390	3.673
3.33×10^{-5}	1.64×10^{-3}	.0390	3.600
6.67×10^{-5}	1.75×10^{-3}	.0402	4.115
6.67×10^{-5}	1.75×10^{-3}	.0402	3.947
1.33×10^{-4}	1.95×10^{-3}	.0423	4.691
1.33×10^{-4}	1.95×10^{-3}	.0423	4.640
2.67×10^{-4}	2.34×10^{-3}	.0462	5.134
2.67×10^{-4}	2.34×10^{-3}	.0462	5.160
5.33×10^{-4}	3.14×10^{-3}	.0531	5.523
6.67×10^{-4}	3.54×10^{-3}	.0562	5.682
1.33×10^{-3}	5.54×10^{-3}	.0693	5.959
2.00×10^{-3}	7.54×10^{-3}	.0799	6.134

2.67×10^{-3}	9.54×10^{-3}	.0890	6.193
$[Na_2(chdc)]$ (M)	Total μ	Total GP	$logk_{ex}$
0.00	1.55×10^{-3}	.0379	3.240
6.67×10^{-5}	1.75×10^{-3}	.0402	3.708
1.33×10^{-4}	1.95×10^{-3}	.0423	4.054
2.67×10^{-4}	2.34×10^{-3}	.0462	4.209
2.67×10^{-4}	2.34×10^{-3}	.0462	4.076
6.67×10^{-4}	3.54×10^{-3}	.0562	4.516
1.33×10^{-3}	5.54×10^{-3}	.0693	4.784
2.00×10^{-3}	7.54×10^{-3}	.0799	4.877
2.67×10^{-3}	9.54×10^{-3}	.0890	5.085
5.00×10^{-3}	0.0166	.1140	5.275
6.67×10^{-3}	0.0215	.1280	5.383
1.00×10^{-2}	0.0315	.1508	5.472
1.17×10^{-2}	0.0366	.1605	5.529
1.50×10^{-2}	0.0466	.1775	5.551
1.67×10^{-2}	0.0515	.1850	5.625
2.00×10^{-2}	0.0616	.1988	5.622
2.33×10^{-2}	0.0715	.2110	5.682
3.00×10^{-2}	0.0916	.2323	5.748
4.00×10^{-2}	0.1215	.2585	5.795

5.33×10^{-2}	0.1616	.2867	5.844
7.33×10^{-2}	0.2215	.3200	5.886
$[Na_2(terephthalate)]$ (M)	Total μ	Total GP	$logk_{ex}$
0.0000	1.55×10^{-3}	.0379	3.17
1.67×10^{-5}	1.60×10^{-3}	.0385	3.653
3.33×10^{-5}	1.64×10^{-3}	.0390	3.890
6.67×10^{-5}	1.75×10^{-3}	.0402	4.342
1.33×10^{-4}	1.95×10^{-3}	.0423	4.825
2.67×10^{-4}	2.34×10^{-3}	.0462	5.251
6.67×10^{-4}	3.54×10^{-3}	.0562	5.848
1.33×10^{-3}	5.54×10^{-3}	.0693	6.166
2.00×10^{-3}	7.54×10^{-3}	.0799	6.351
2.67×10^{-3}	9.54×10^{-3}	.0890	6.465
$[Na_2SO_4]$ (M)	Total μ	Total GP	$logk_{ex}$
0.0000	1.55×10^{-3}	.0379	3.15
6.67×10^{-5}	1.75×10^{-3}	.0402	4.385
1.33×10^{-4}	1.95×10^{-3}	.0423	4.801
2.67×10^{-4}	2.34×10^{-3}	.0462	5.250
6.67×10^{-4}	3.54×10^{-3}	.0562	5.790
1.33×10^{-3}	5.54×10^{-3}	.0693	6.135
2.00×10^{-3}	7.54×10^{-3}	.0799	6.270

[Na_2(1,5NDS)] (M)	Total μ	Total GP	logk_{ex}
0.0000	1.55×10^{-3}	.0379	3.150
1.67×10^{-5}	1.60×10^{-3}	.0385	3.600
1.67×10^{-5}	1.60×10^{-3}	.0385	3.411
3.33×10^{-5}	1.64×10^{-3}	.0390	3.920
3.33×10^{-5}	1.64×10^{-3}	.0390	3.771
6.67×10^{-5}	1.75×10^{-3}	.0402	4.434
6.67×10^{-5}	1.75×10^{-3}	.0402	4.607
1.33×10^{-4}	1.95×10^{-3}	.0423	5.195
1.33×10^{-4}	1.95×10^{-3}	.0423	5.049
2.67×10^{-4}	2.34×10^{-3}	.0462	5.736
2.67×10^{-4}	2.34×10^{-3}	.0462	5.760
6.67×10^{-4}	3.54×10^{-3}	.0562	6.175

(a) Stated errors are based on statistical analysis of replicate measurements

Table 2.7 Initial slopes of the kinetic curves for the strongly catalytic salts at 5.0 x 10^{-5} M reactants concentration for reaction two.

Added electrolytes	Initial slope of kinetic curve in GP[a]
NaSCN	127 ±24
Na_2 (adipate)	117 ± 6

Na_2 (muconate)	378 ± 26
Na_2 (chdc)	174 ± 24
Na_2 (terephthalate)	502 ± 71
Na_2SO_4	376 ± 100
Na_2(1,5 NDS)	579 ± 40

(a) Stated errors are based on statistical analysis of replicate measurements

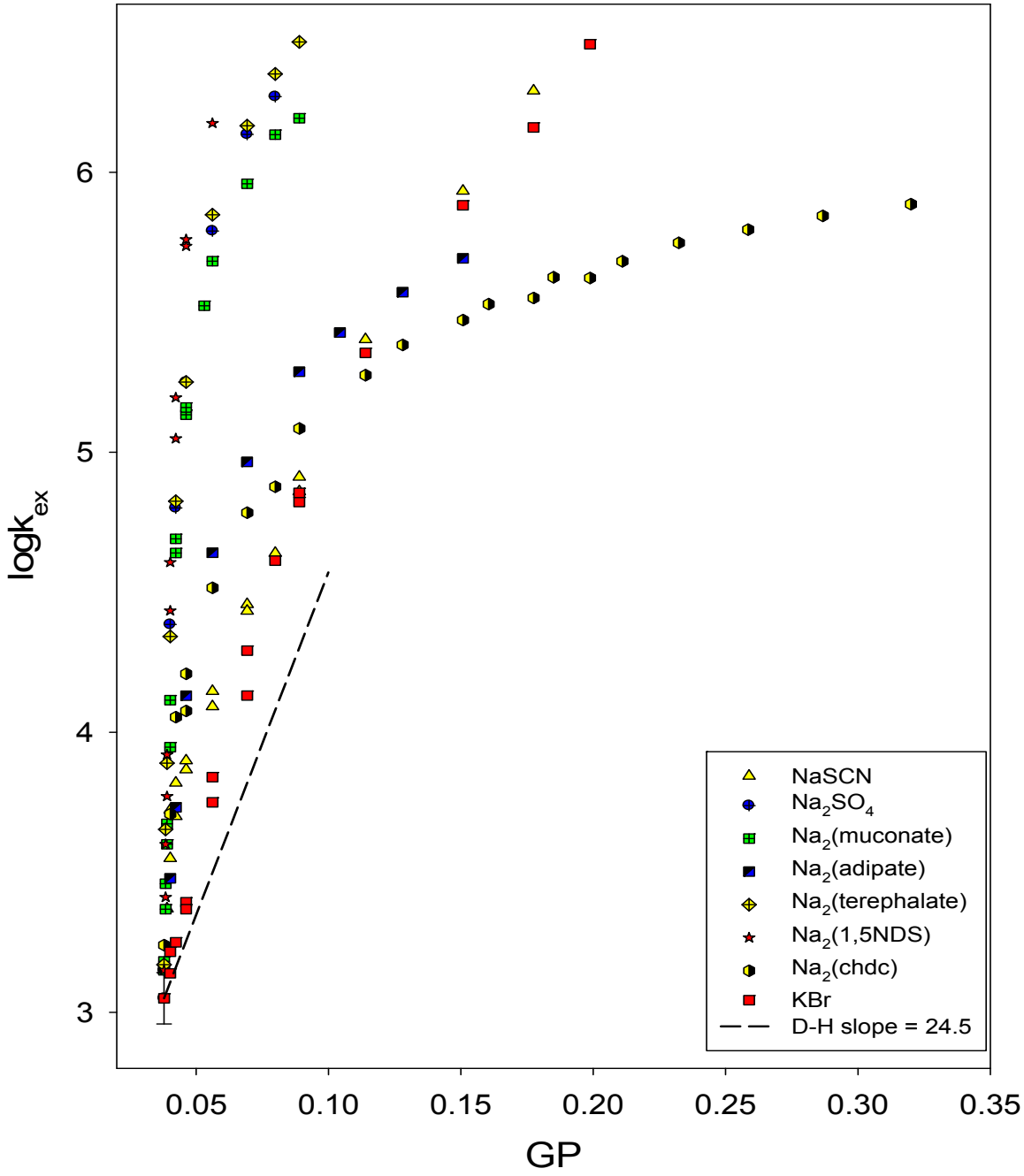

Figure 2.24 Catalytic salt effects on reaction 2 with reactants concentration at 5.0×10^{-5} M

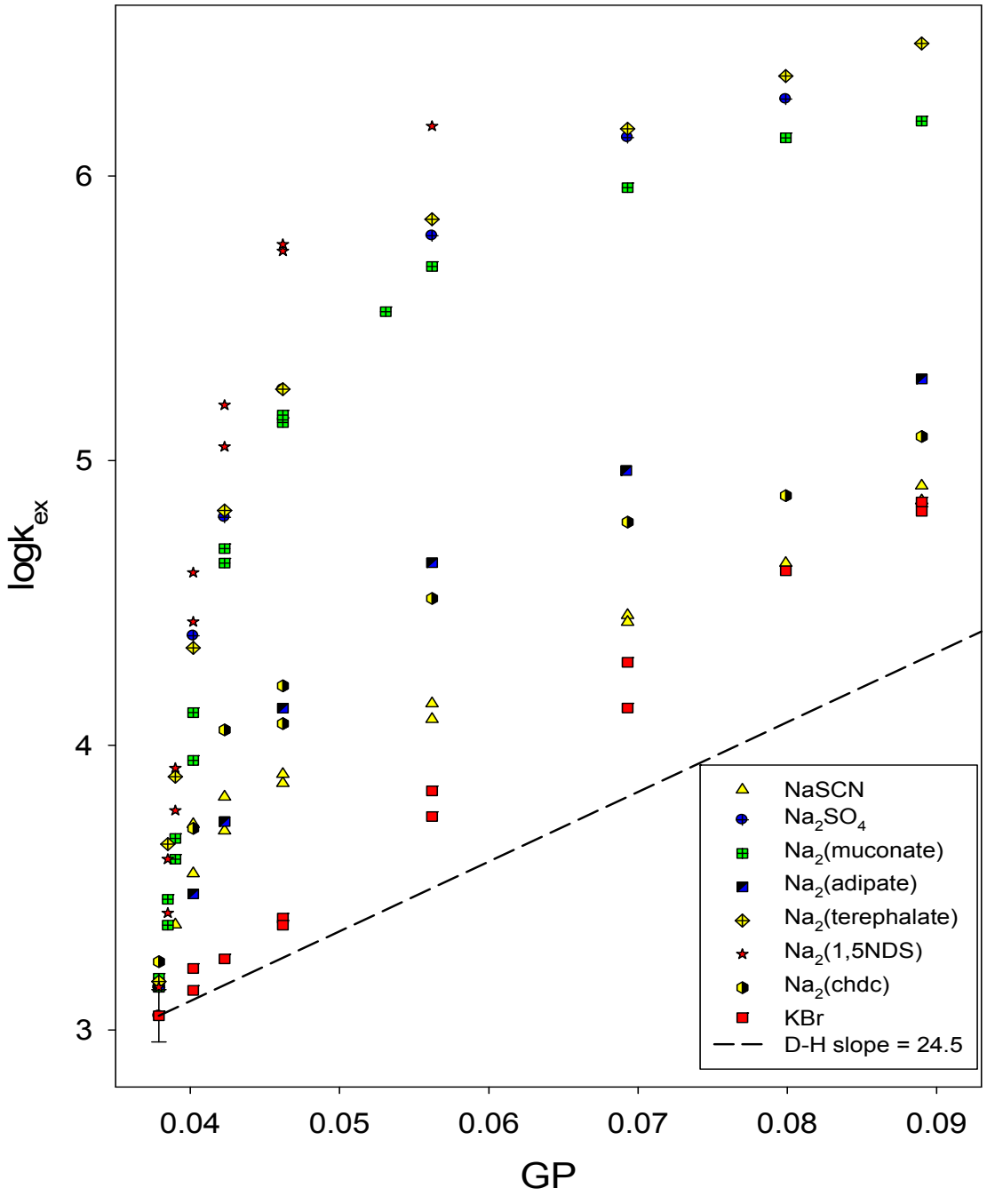

Figure 2.25 Catalytic salt effects on reaction 2 with reactants concentration at 5.0×10^{-5} M ; expansion plot at low GP (GP < 0.09, μ < 0.0096).

Electrolyte Effects at 1.0 x10^{-4} M Reactant's Concentration

Since the reactant's concentration of 5.0 x 10^{-5} M is at the low end of the range which is not contaminated by glass-related catalysis, we decided to also conduct salt studies at higher reactant's concentrations in order to check for the consistency of the behavior. Table 2.8 lists the kinetic data obtained by stopped-flow for both the simple and the "catalytic" salts already discussed as well as some additional salts (the fluorides).

Table 2.8 Kinetic data for reaction 2 at 1.0 x 10^{-4} M Reactant's Concentration

$[LaCl_3]$ (M)	Total μ	Total GP	$logk_{ex}$[a]
0	3.09 x 10^{-3}	0.0527	3.218
1.33 x 10^{-4}	3.90 x 10^{-3}	0.0588	3.317
3.33 x 10^{-4}	5.10 x 10^{-3}	0.0667	3.459
6.67 x 10^{-4}	7.09 x 10^{-3}	0.0777	3.704
1.33 x 10^{-3}	9.10 x 10^{-3}	0.0871	3.889
2.00 x 10^{-3}	0.0111	0.0953	4.021
$[LaNO_3]$ (M)	Total μ	Total GP	$logk_{ex}$
0	3.09 x 10^{-3}	0.0527	3.218
1.33 x 10^{-4}	3.90 x 10^{-3}	0.0588	3.343
3.33 x 10^{-4}	5.10 x 10^{-3}	0.0667	3.446
6.67 x 10^{-4}	7.09 x 10^{-3}	0.0777	3.673
1.33 x 10^{-3}	9.10 x 10^{-3}	0.0871	3.851

2.00×10^{-3}	0.0111	0.0953	3.945
$[CaCl_2]$ (M)	Total μ	Total GP	$logk_{ex}$
0.00	3.09×10^{-3}	0.0527	3.194
2.67×10^{-4}	3.90×10^{-3}	0.0588	3.361
6.67×10^{-4}	5.10×10^{-3}	0.0667	3.523
1.33×10^{-3}	7.09×10^{-3}	0.0777	3.796
2.00×10^{-3}	9.10×10^{-3}	0.0871	4.067
2.67×10^{-4}	0.0111	0.0953	4.218
4.00×10^{-3}	0.0151	0.1094	4.494
[KCl] (M)	Total μ	Total GP	$logk_{ex}$
0.00	3.09×10^{-3}	0.0527	3.188 +/- 0.064
8.00×10^{-4}	3.90×10^{-3}	0.0588	3.477 +/- 0.080
2.00×10^{-3}	5.10×10^{-3}	0.0667	3.803 +/- 0.059
3.00×10^{-3}	6.09×10^{-3}	0.0724	4.029 +/- 0.062
4.00×10^{-3}	7.09×10^{-3}	0.0777	4.160 +/- 0.031
6.00×10^{-3}	9.10×10^{-3}	0.0871	4.418 +/- 0.018
8.00×10^{-3}	0.0111	0.0953	4.595 +/- 0.026
0.010	0.0131	0.1027	4.753 +/- 0.050
0.012	0.0151	0.1094	4.885 +/- 0.031
[KBr] (M)	Total μ	Total GP	$logk_{ex}$
0.00	3.09×10^{-3}	0.0527	3.188 +/- 0.064

8.00×10^{-4}	3.90×10^{-3}	0.0588	3.582 +/- 0.080
2.00×10^{-3}	5.10×10^{-3}	0.0667	3.941 +/- 0.080
3.00×10^{-3}	6.09×10^{-3}	0.0724	4.231 +/- 0.060
4.00×10^{-3}	7.09×10^{-3}	0.0777	4.366 +/- 0.088
6.00×10^{-3}	9.10×10^{-3}	0.0871	4.665 +/- 0.057
8.00×10^{-3}	0.0111	0.0953	4.882 +/- 0.048
0.010	0.0131	0.1027	5.083 +/- 0.055
0.012	0.0151	0.1094	5.217 +/- 0.039
[KI] (M)	Total μ	Total GP	$\log k_{ex}$
0.00	3.09×10^{-3}	0.0527	3.188 +/- 0.064
8.00×10^{-4}	3.90×10^{-3}	0.0588	3.659 +/- 0.100
2.00×10^{-3}	5.10×10^{-3}	0.0667	4.091 +/- 0.097
3.00×10^{-3}	6.09×10^{-3}	0.0724	4.412 +/- 0.049
4.00×10^{-3}	7.09×10^{-3}	0.0777	4.571 +/- 0.103
6.00×10^{-3}	9.10×10^{-3}	0.0871	4.889 +/- 0.081
8.00×10^{-3}	0.0111	0.0953	5.138 +/- 0.050
0.010	0.0131	0.1027	5.324 +/- 0.055
0.012	0.0151	0.1094	5.493 +/- 0.034
[KF] (M)	Total μ	Total GP	$\log k_{ex}$
0.00	3.09×10^{-3}	0.0527	3.188 +/- 0.064
8.00×10^{-4}	3.90×10^{-3}	0.0588	3.300 +/- 0.060

2.00×10^{-3}	5.10×10^{-3}	0.0667	3.425 +/- 0.055
3.00×10^{-3}	6.09×10^{-3}	0.0724	3.500 +/- 0.056
4.00×10^{-3}	7.09×10^{-3}	0.0777	3.595 +/- 0.050
6.00×10^{-3}	9.10×10^{-3}	0.0871	3.708 +/- 0.042
8.00×10^{-3}	0.0111	0.0953	3.810 +/- 0.050
0.010	0.0131	0.1027	3.914 +/- 0.031
0.012	0.0151	0.1094	3.991 +/- 0.056
[LiF] (M)	Total μ	Total GP	$\log k_{ex}$
0.00	3.09×10^{-3}	0.0527	3.1183
8.00×10^{-4}	3.90×10^{-3}	0.0588	3.2350
2.00×10^{-3}	5.10×10^{-3}	0.0667	3.3612
4.00×10^{-3}	7.09×10^{-3}	0.0777	3.5416
6.00×10^{-3}	9.10×10^{-3}	0.0871	3.6646
8.00×10^{-3}	0.0111	0.0953	3.7455
$[Na_2(adipate)]$ (M)	Total μ	Total GP	$\log k_{ex}$
0.00	3.09×10^{-3}	0.0527	3.2140
6.67×10^{-5}	3.29×10^{-3}	0.0543	3.4660
1.33×10^{-4}	3.50×10^{-3}	0.0559	3.7530
2.67×10^{-4}	3.90×10^{-3}	0.0588	4.0610
6.67×10^{-4}	5.10×10^{-3}	0.0667	4.5510
1.33×10^{-3}	7.09×10^{-3}	0.0777	4.9540

2.67×10^{-3}	0.0111	0.0953	5.2980
4.00×10^{-3}	0.0151	0.1094	5.4300
6.67×10^{-3}	0.0231	0.1319	5.5190
1.00×10^{-2}	0.0331	0.1539	5.6690
$[Na_2(muconate)]$ (M)	Total μ	Total GP	$logk_{ex}$
0.00	3.09×10^{-3}	0.0527	3.2020
1.67×10^{-5}	3.14×10^{-3}	0.0531	3.5010
3.33×10^{-5}	3.19×10^{-3}	0.0535	3.6670
6.67×10^{-5}	3.29×10^{-3}	0.0543	3.8920
1.33×10^{-4}	3.50×10^{-3}	0.0559	4.4020
2.67×10^{-4}	3.90×10^{-3}	0.0588	4.9320
6.67×10^{-4}	5.10×10^{-3}	0.0667	5.5660
1.33×10^{-3}	7.09×10^{-3}	0.0777	5.9100
2.00×10^{-3}	9.10×10^{-3}	0.0871	6.0100
2.67×10^{-3}	0.0111	0.0953	6.0900

(a) Errors are based on replicate measurements

In Figure 2.26, we see that LiF and KF yield the same kinetic pattern within error and have lower slopes than the Debye-Huckel slope (24.48). The same heavier halide anion effect (Cl^-, Br^-, I^-) patterns are observed for this higher reaction concentration as were seen at 5×10^{-5} M reactant's concentrations. However, there is a larger difference upon going from the 1:1 F^- salts to KCl than

upon going from Cl^- and from Br^- or Br^- to I^-. This effect may be related to a few aspects of these ions in solution. First, the F^- ion is considered to be strongly-solvated in the water and is known to be a "structure maker" ion,[45,46] while the other halides are all relatively poorly-solvated and are classified as "structure breaker" ions.[45,46] This could mean that the larger halides would be able to approach to (or perhaps even ion pair with) the cationic reactants more easily with their less tightly-held surrounding water molecules. It is possible that this might also allow the larger halides to form ternary association complexes with the ET reactants more easily, and that this could lead in favorable cases both to a lower energy pathway to the precursor/encounter complex ("pcx", *vide infra*) and to a larger degree of electronic coupling *via* super-exchange mediated ET catalysis (in cases where reaction adiabaticity affects the magnitude of k_{et}, k_{etx}, *vide infra*).[12c,41] Supporting the second idea, we note that F^- has a very large ionization potential as compared with the others, and it is a relatively poor Lewis base for H-bond acceptance. On this basis we would expect that it might be less able to facilitate electron tunneling in any relevant encounter complexes.

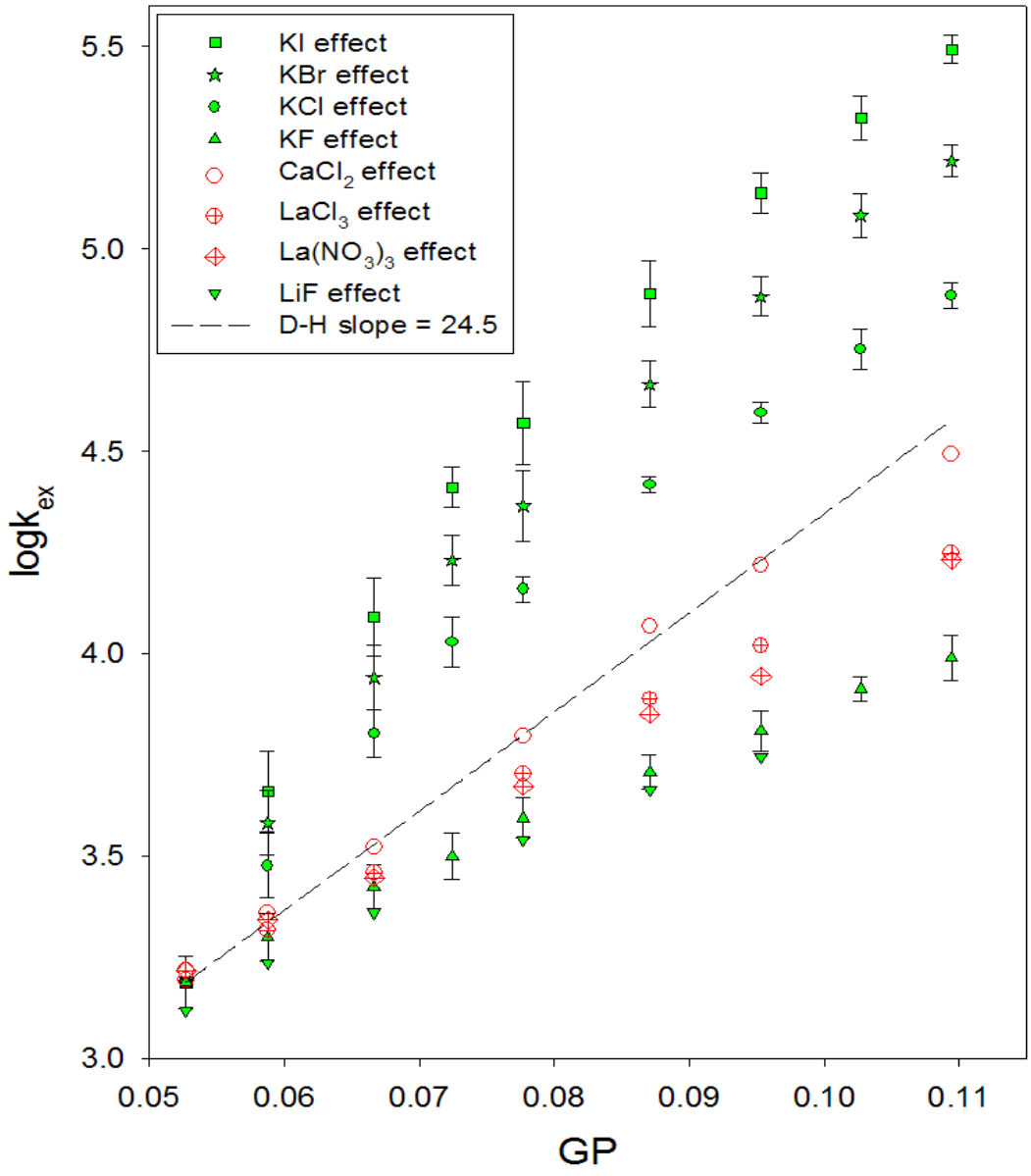

Figure 2.26 Simple salt effects on the reaction 2 (dimer comproportionation reaction) up to GP 0.11 with fixed reactant's concentration at $[Ru^{II}\text{-}Ru^{II}] = [Ru^{III}\text{-}Ru^{III}] = 1.0 \times 10^{-4}$ M.

In previous work on the monomer pseudo-self exchange reaction (1),[41] it has been noticed that 1:1 fluoride salts result in the most "classical" salt behaviors, as judged by nearly exact quantitative agreement with the Debye-Hückel $\log k_{ex}$ *vs*. GP predicted slopes, of all salts studied. Therefore their downward deviation in this dimer comproportionation case is both surprising and interesting.

The approximately "ideal" behavior of F^- as electrolyte in the monomer ET reaction was initially thought to be because of its small size and "hard" base properties since these would make F^- come closer than the other halides to satisfying the point-charge assumption required in the derivation of Debye-Hückel-Bronstead equation (if specific solvation effects, such as hydration sphere size, are neglected; see eq. 2-9).[9]

In Figure 2.26, F^- exhibits an initial slope 16-17 (see also Table 2.9) in $\log k_{ex}$ *vs.* GP and then falls even lower at GP > 0.07. If rather than using the Guggenheim approximation of "βd~1" (see eq. 2-6) we instead use βd = (0.509)(σ) = 3.548, where σ = 1.50 + 5.47 (the ionic radius of F^- and the calculated BPE dimer radius respectively) in computing the x-axis, we find that the initial slope for F^- changes to 21 which is then in much better agreement with the theoretical slope of 24 (see Figure 2.27). This better correlation of kinetic behavior with the Debye-Hückel theory implemented without using the Guggenheim approximation was also observed by Cai *et al*.[46] in the quenching of the dimeric chromophore $*[Pt_2(pop)_4]^{4-}$ by $[Co(CN)_5I]^{3-}$ with added KCl. This

may indicate that the quantitative utility of the Guggenheim approximation diminishes fairly rapidly as the ionic reactants deviate from spherical charge distributions.

Table 2.9 Initial slopes of the kinetic curves for simple and catalytic salts at 1.0 x 10^{-4} M reactant's concentration.

Added electrolytes	Initial slope of kinetic curve in GP[a]	Added electrolytes	Initial slope of kinetic curve in GP[a]
$LaCl_3$	20.0 ± .5	KCl	42.5 ± 1.2
$La(NO_3)_3$	18.5 ± .6	KBr	51.9 ± 2.8
$CaCl_2$	24.9 ± .7	KI	64.4 ± 6.5
LiF	16.8 ± 0.4	Na_2(adipate)	145 ± 15
KF	16.0 ± .5	Na_2(muconate)	436 ± 65

(a) Errors are based on replicate measurements

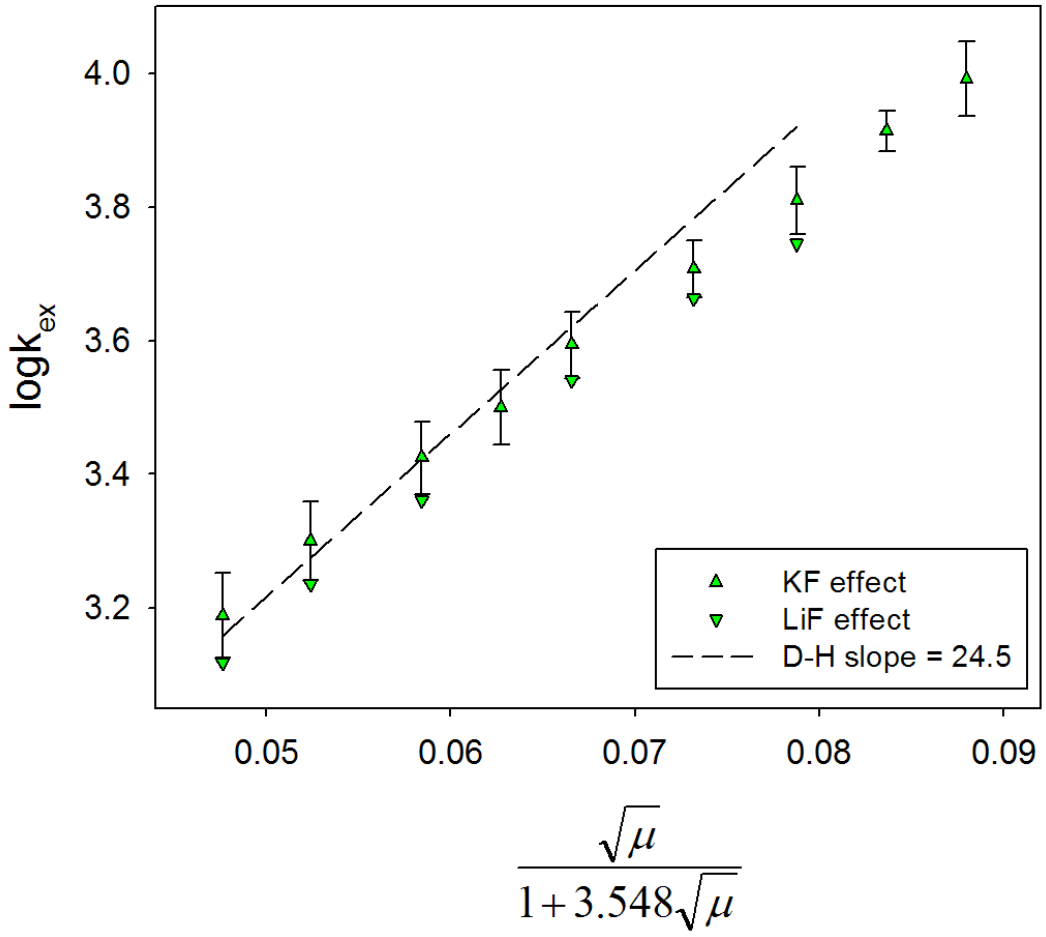

Figure 2.27 LiF and KF effect on reaction 2 plotted using "βd" = 3.548 in computing the x-axis rather than βd = 1 and "GP".

The "catalytic" salt Na_2muc and its saturated analogue Na_2adip were studied at this 1.0 x 10^{-4} M, and the results are shown in Figure 2.28. At the high end of the GP range we find that muc^{2-} increases k_{ex} by almost 250 times compared to F^- effect at the same total GP. The strong catalytic effect of muc^{2-} ion on the electron-transfer rate constant has been explained previously as

arising from its conjugated electronic structure, its dianionic charge, and its ability to participate in H- bonding at both ends.[36,37,41] The conjugated structure is thought to allow more resonance interaction between the redox partners by enhancing both hole- and electron-transfer superexchange coupling (as has been described in detail in ref. 12c). It is also possible that the 2- charge on it allows for better general charge shielding between the reactants and this helps bring them into closer contact. The acceleration effect also shows up with the saturated adipate ($adip^{2-}$) anion – and more in this dimer comproportionation ET case than was seen previously in the monomer ET case.[12c,41] This may be due to the very different charge distributions of the reactant ions in the dimer case and the possibility of a side-to-side associative pathway which would not be possible in the monomer reaction (where the dianionic adipate ion might now be able to interpose itself between the reactants in a parallel rather than end-to-end manner).

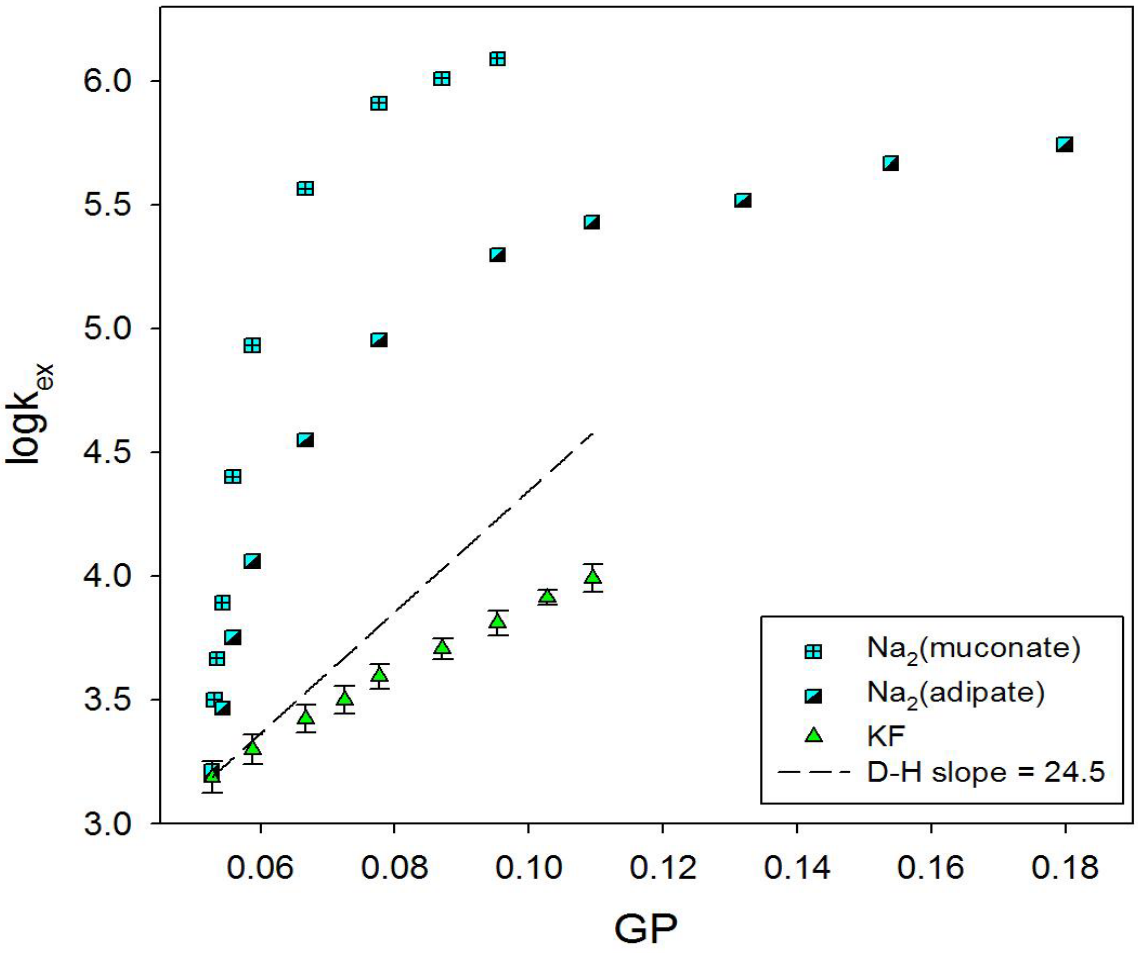

Figure 2.28 Catalytic salt effects on reaction 2 at reactants concentration 1.0 x 10^{-4} M

Evidence of the Olson-Simonson effect is observed once again with the 1:1, 1:2, 1:3 simple electrolytes at 1.0 x 10^{-4} M reactant's concentration (Figure 2.29). All the Cl^- salts (KCl, $CaCl_2$, $LaCl_3$) again correlate with each other better in the simple $logk_{ex}$ *vs.* concentration plot than in the $logk_{ex}$ *vs.* GP graph (compare to Figure 2.26). $LaNO_3$ shows the exact same pattern acceleration as its Cl^- salt.

The simplest interpretation here is that this indicates that electrostatic effects are dominating the kinetic salt effect on ET for these simple anions which are acting as hard sphere and forming ion pairs which then facilitate formation of the ternary encounter complex PCX (*vide infra*) *via* simple columbic screening.

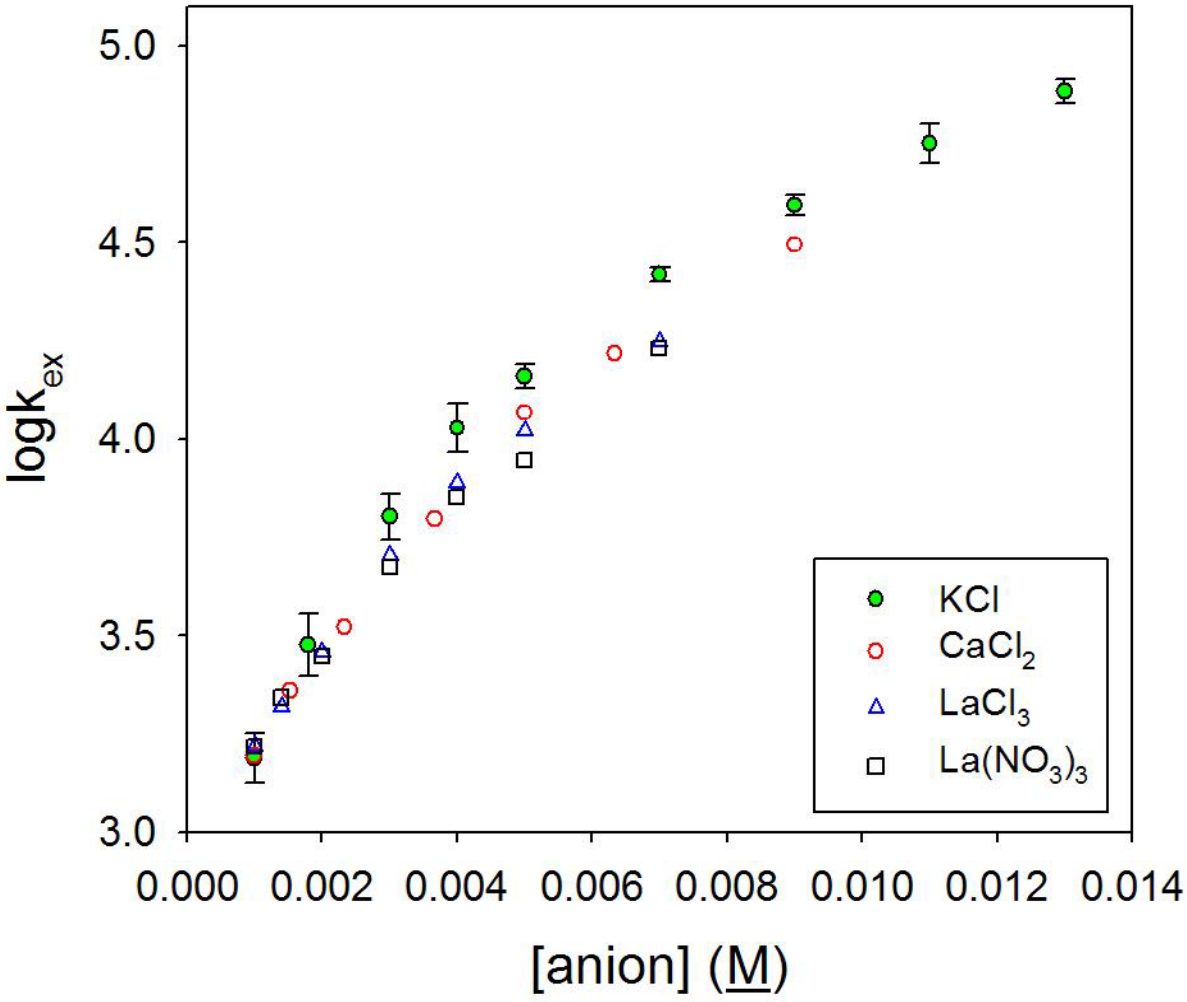

Figure 2.29 Olson-Simonson plots for KCl, $CaCl_2$, $LaCl_3$, and $La(NO_3)_3$ effect on reaction 2 in reactants concentration 1.0 x 10^{-4} M.

Electrolyte Effects at 2.0 x10^{-4} M Reactant's Concentration

The measured salt effects at this even higher reactant's concentration follow the same patterns as the others shown before, but now we have included the new salt $KClO_4$ and also pushed total GP out to higher values with KCl and $CaCl_2$ (Table 2.10). The initial rate *vs.* GP slopes for all salts studied here are listed in Table 2.11. The simple salt (LiF, KF, KCl, KBr, KI, $La(NO_3)_3$, $CaCl_2$) effects are shown in Figure 2.30.

Table 2.10 Catalytic salt effects on BPE dimer comproportionation reaction at reactant's concentration 2.0 x 10^{-4} M.

$[La(NO_3)_3]$ (M)	Total μ	Total GP	$logk_{ex}$
0	6.20 x 10^{-3}	0.0730	3.367
1.33 x 10^{-4}	6.99 x 10^{-3}	0.0772	3.460
3.33 x 10^{-4}	8.19 x 10^{-3}	0.0830	3.600
8.33 x 10^{-4}	0.0110	0.0949	3.850
1.33 x 10^{-3}	0.0142	0.1065	4.107
2.00 x 10^{-3}	0.0182	0.1189	4.300
$[CaCl_2]$ (M)	Total μ	Total GP	$logk_{ex}$
0.00	6.20 x 10^{-3}	0.0730	3.360
6.67 x 10^{-5}	6.40 x 10^{-3}	0.0741	3.407
2.67 x 10^{-4}	6.99 x 10^{-3}	0.0772	3.488
6.67 x 10^{-4}	8.19 x 10^{-3}	0.0830	3.581

1.33×10^{-3}	0.0102	0.0917	3.846
2.00×10^{-3}	0.0122	0.0995	4.070
2.67×10^{-4}	0.0142	0.1065	4.226
4.00×10^{-3}	0.0182	0.1189	4.497
6.67×10^{-3}	0.0262	0.1393	4.870
1.00×10^{-2}	0.0362	0.1598	5.100
1.50×10^{-2}	0.0512	0.1845	5.413
2.00×10^{-2}	0.0662	0.2046	5.574
[KCl] (M)	Total μ	Total GP	$\log k_{ex}$
0.00	6.20×10^{-3}	0.0730	3.295
0.00	6.20×10^{-3}	0.0730	3.428
2.00×10^{-4}	6.40×10^{-3}	0.0741	3.375
8.00×10^{-4}	6.99×10^{-3}	0.0772	3.530
8.00×10^{-4}	6.99×10^{-3}	0.0772	3.591
2.00×10^{-3}	8.19×10^{-3}	0.0830	3.769
4.00×10^{-3}	0.0102	0.0917	4.043
6.00×10^{-3}	0.0122	0.0995	4.341
8.00×10^{-3}	0.0142	0.1065	4.528
0.012	0.0182	0.1189	4.862
0.015	0.0222	0.1297	5.093
0.020	0.0262	0.1393	5.249

0.030	0.0362	0.1598	5.507
0.045	0.0512	0.1845	5.817
0.060	0.0662	0.2046	5.995
[KBr] (M)	Total μ	Total GP	$\log k_{ex}$
0.00	6.20×10^{-3}	0.0730	3.343
8.00×10^{-4}	6.99×10^{-3}	0.0772	3.636
2.00×10^{-3}	8.19×10^{-3}	0.0830	3.945
4.00×10^{-3}	0.0102	0.0917	4.364
6.00×10^{-3}	0.0122	0.0995	4.626
8.00×10^{-3}	0.0142	0.1065	4.871
0.012	0.0182	0.1189	5.197
[KI] (M)	Total μ	Total GP	$\log k_{ex}$
0.00	6.20×10^{-3}	0.0730	3.350
8.00×10^{-4}	6.99×10^{-3}	0.0772	3.693
2.00×10^{-3}	8.19×10^{-3}	0.0830	4.077
4.00×10^{-3}	0.0102	0.0917	4.572
6.00×10^{-3}	0.0122	0.0995	4.866
8.00×10^{-3}	0.0142	0.1065	5.137
0.012	0.0182	0.1189	5.565
[KF] (M)	Total μ	Total GP	$\log k_{ex}$
0.00	6.20×10^{-3}	0.0730	3.364

8.00×10^{-4}	6.99×10^{-3}	0.0772	3.467
2.00×10^{-3}	8.19×10^{-3}	0.0830	3.555
4.00×10^{-3}	0.0102	0.0917	3.700
6.00×10^{-3}	0.0122	0.0995	3.803
8.00×10^{-3}	0.0142	0.1065	3.893
0.012	0.0182	0.1189	4.029
[LiF] (M)	Total μ	Total GP	$\log k_{ex}$
0.00	6.20×10^{-3}	0.0730	3.356
8.00×10^{-4}	6.99×10^{-3}	0.0772	3.458
2.00×10^{-3}	8.19×10^{-3}	0.0830	3.552
4.00×10^{-3}	0.0102	0.0917	3.679
6.00×10^{-3}	0.0122	0.0995	3.779
$[KClO_4]$ (M)	Total μ	Total GP	$\log k_{ex}$
0.00	6.20×10^{-3}	0.0730	3.376
8.00×10^{-4}	6.99×10^{-3}	0.0772	3.606
2.00×10^{-3}	8.19×10^{-3}	0.0830	3.888
4.00×10^{-3}	0.0102	0.0917	4.248
6.00×10^{-3}	0.0122	0.0995	4.492
8.00×10^{-3}	0.0142	0.1065	4.714
$[Na_2(adipate)]$ (M)	Total μ	Total GP	$\log k_{ex}$
0.00	6.20×10^{-3}	0.0730	3.450

6.67×10^{-5}	6.40×10^{-3}	0.0741	3.650
1.33×10^{-4}	6.59×10^{-3}	0.0751	3.912
2.67×10^{-4}	6.99×10^{-3}	0.0772	4.150
6.67×10^{-4}	8.19×10^{-3}	0.0830	4.610
1.33×10^{-3}	0.0102	0.0917	4.998
2.67×10^{-3}	0.0122	0.0995	5.191
4.00×10^{-3}	0.0142	0.1065	5.280
6.67×10^{-3}	0.0182	0.1189	5.420
$[Na_2(muconate)]$ (M)	Total μ	Total GP	$logk_{ex}$
0.00	6.20×10^{-3}	0.0730	3.4200
1.67×10^{-5}	6.25×10^{-3}	0.0733	3.6070
3.33×10^{-5}	6.29×10^{-3}	0.0735	3.6920
6.67×10^{-5}	6.40×10^{-3}	0.0741	3.9250
1.33×10^{-4}	6.59×10^{-3}	0.0751	4.2410
2.67×10^{-4}	6.99×10^{-3}	0.0772	4.7060
6.67×10^{-4}	8.19×10^{-3}	0.0830	5.3986
1.33×10^{-3}	0.0102	0.0917	5.7820
2.00×10^{-3}	0.0122	0.0995	5.9190
2.67×10^{-3}	0.0142	0.1065	5.9650
[NaSCN] (M)	Total μ	Total GP	$logk_{ex}$
0.00	6.20×10^{-3}	0.0730	3.3079

5.00×10^{-5}	6.25×10^{-3}	0.0733	3.3913
1.00×10^{-4}	6.29×10^{-3}	0.0735	3.4190
2.00×10^{-4}	6.40×10^{-3}	0.0741	3.4833
4.00×10^{-4}	6.59×10^{-3}	0.0751	3.5957
8.00×10^{-4}	6.99×10^{-3}	0.0772	3.7110
2.00×10^{-3}	8.19×10^{-3}	0.0830	3.9762
4.00×10^{-3}	0.0102	0.0917	4.3432
6.00×10^{-3}	0.0122	0.0995	4.6591
8.00×10^{-3}	0.0142	0.1065	4.7779
0.012	0.0182	0.1189	5.1749
0.020	0.0262	0.1393	5.5936
0.025	0.0312	0.1501	5.6958
0.030	0.0362	0.1598	6.0170
0.040	0.0462	0.1769	6.1287

Table 2.11 Initial slopes of the kinetic curves shown in Figure 2.30 for simple and catalytic salts at 2.0×10^{-4} M reactant's concentration.

Added electrolytes	Initial slope of kinetic curve in GP	Added electrolytes	Initial slope of kinetic curve in GP
$La(NO_3)_3$	22.0 ± .2	KBr	59.6 ± 4.6
$CaCl_2$	25.9 ± .7	KI	72.0 ± 4.4

LiF	16.8 ± 1.3	$KClO_4$	50.8 ± 1.7
KF	17.5 ± 1.1	NaSCN	110 ± 1.6
LiCl	29.8 ± 1.1	Na_2(adipate)	215 ± 18
KCl	37.4 ± 2.1	Na_2(muconate)	450 ± 42

(a) Errors are based on regreesion line fit as calculated by Sigma Plot.

In prior work, ClO_4^- has been claimed to be especially catalytic towards momomeric ET reactions of ruthenium ammine complexes similar to ours.[6] We note here that $KClO_4$ does show a stronger kinetic effect than the KCl and falls between Cl^- and Br^- on the plot, but the difference is just slightly larger than error. The NaSCN, Na_2muc and Na_2adip salt effects are shown in Figure 2.31 and the pattern is similar as before. The Olson-Simonson plots for the 1:1, 1:2, 1:3 electrolyte effects are shown in Figure 2.32. They fall on one curve again even when taken to the higher total GP value of 0.20 as shown in Figure 2.33.

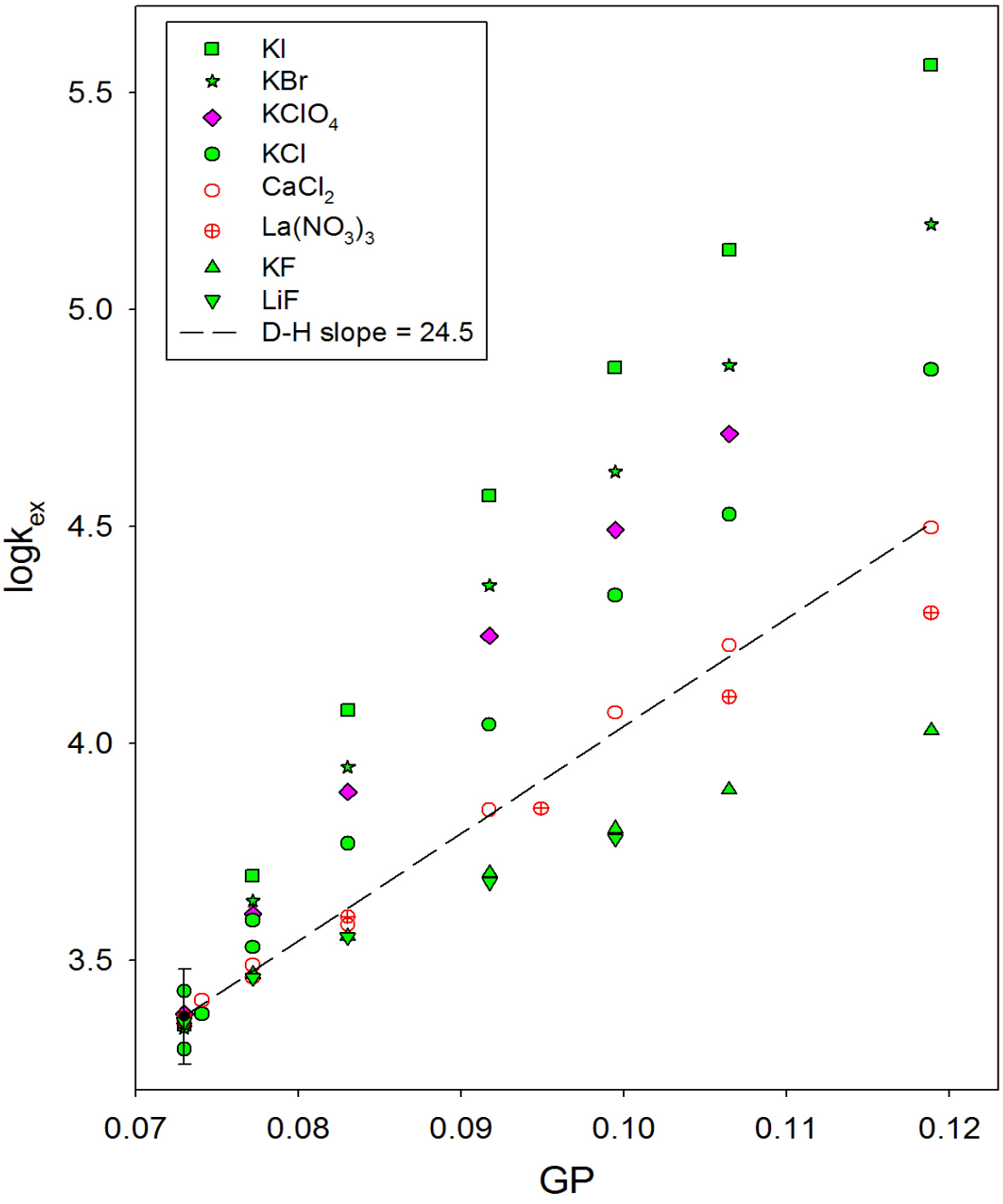

Figure 2.30 Simple salt effects on the reaction 2 (BPE dimer comproportionation reaction) up to GP 0.12 with fixed reactant's concentration at $[Ru^{II}\text{-}Ru^{II}] = [Ru^{III}\text{-}Ru^{III}] = 2.0 \times 10^{-4}$ M

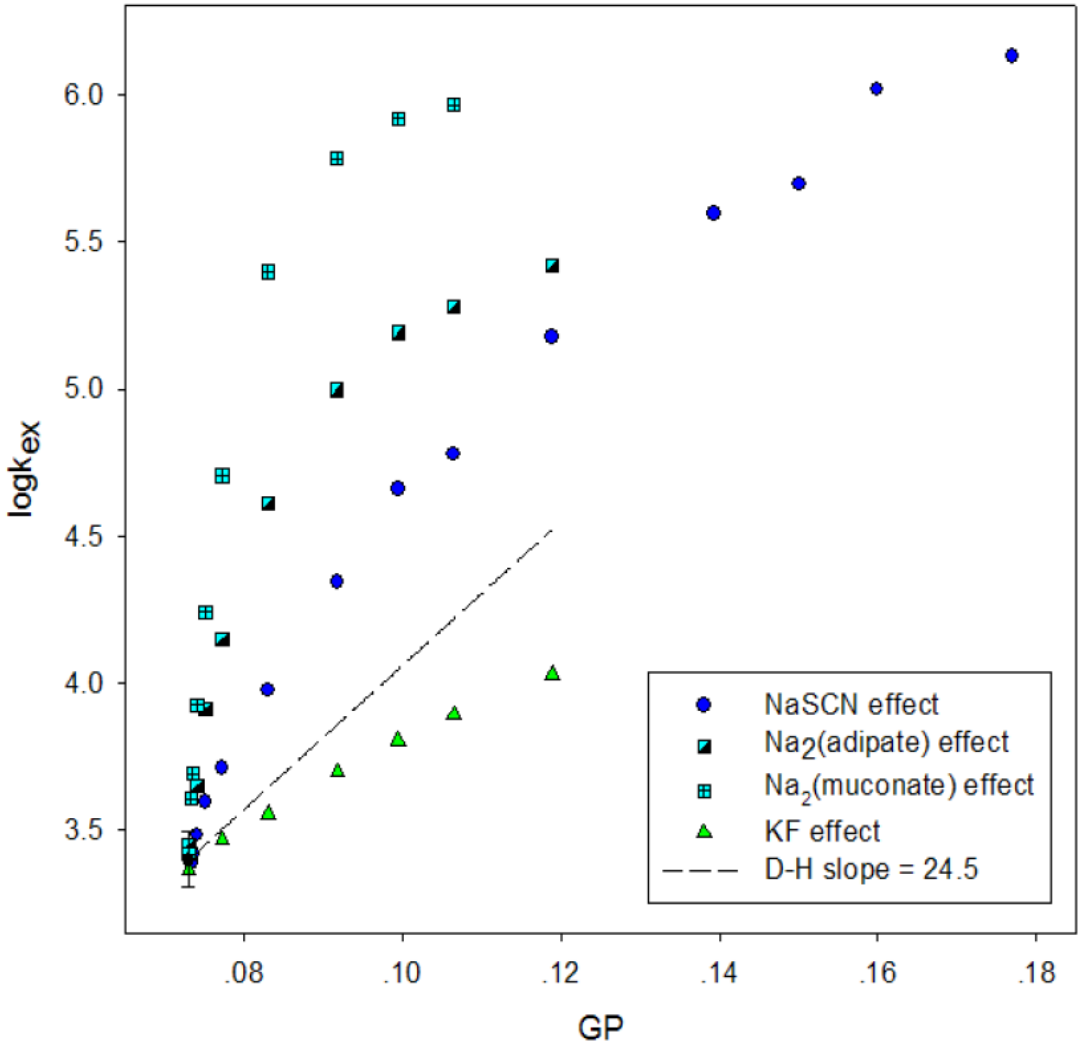

Figure 2.31 Catalytic salt effects on reaction 2 at reactant's concentration 2.0 x 10^{-4} M

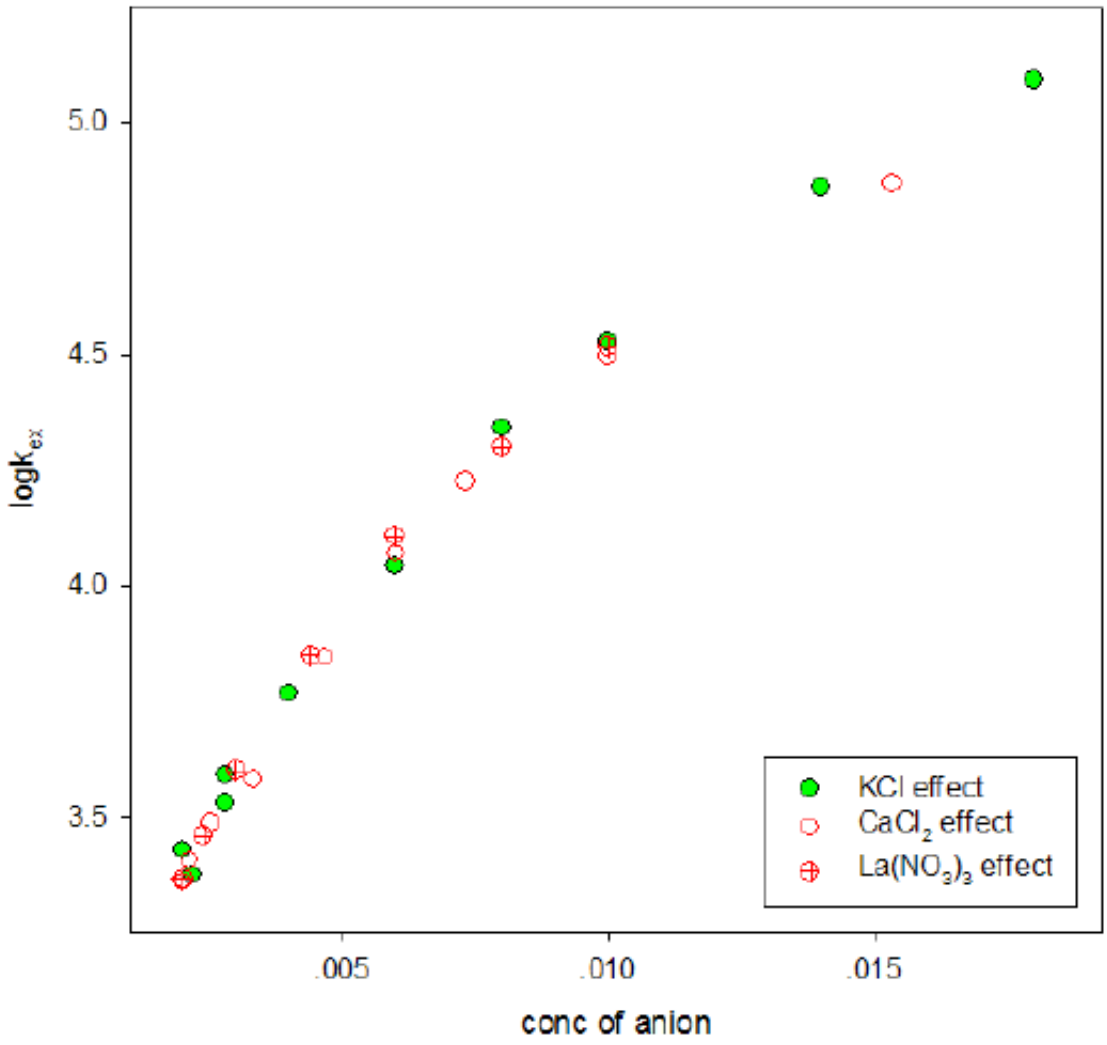

Figure 2.32 Olson-Simonson plots for reaction 2 with reactant's concentration 2.0×10^{-4} M

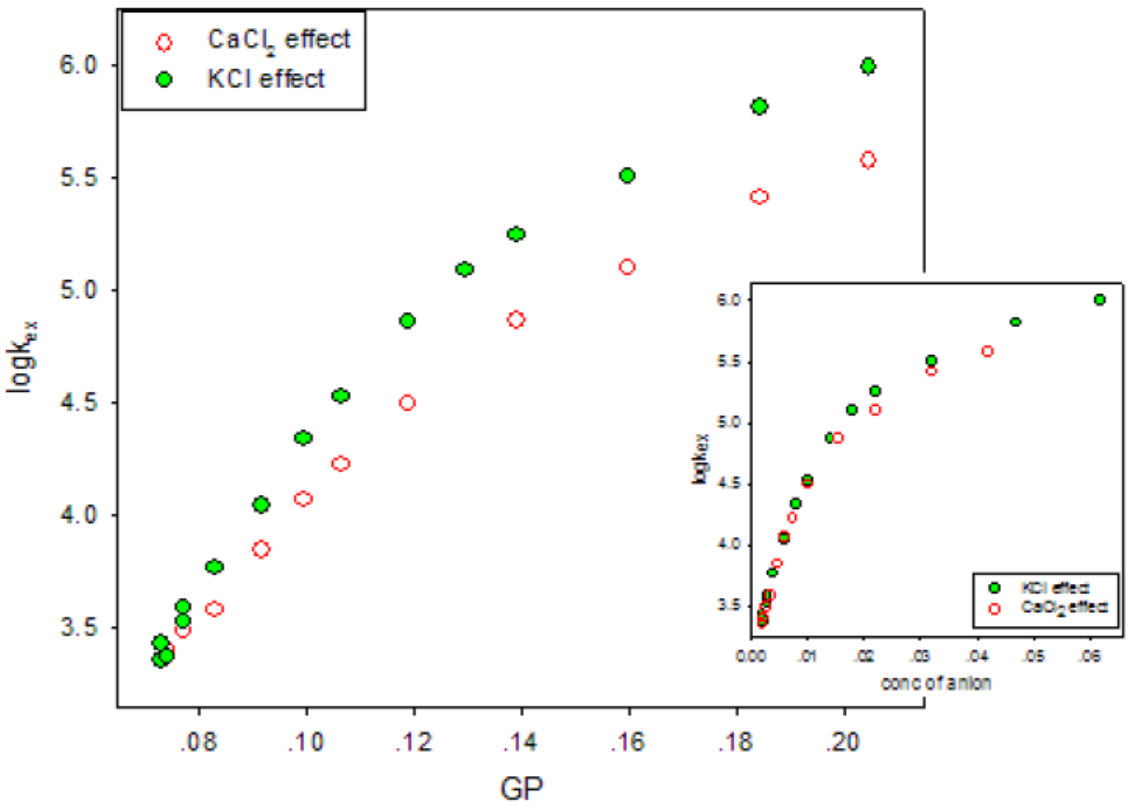

Figure 2.33 Olson-Simonson Plots for KCl and $CaCl_2$ up to 0.2 GP at reactant's concentration 2.0 x 10^{-4} M

The Olson-Simonson Effect; Plots and Data Reorganized

Even though the Olson-Simonson effect has been seen extensively in prior research,[19] it is rare to find detailed explanations of how the evident counter ion effect works. The demonstration of the effect comes when researchers plot the observed rate constant *versus* the simple molar concentration of added salt rather the ionic strength or GP. The interpretation is confirmed when it is shown that it is the added salt's ion of charge opposite to the like-charged reactants which is establishing/controlling the observed behavior (this would equate to

added anion-specific rather than cation–specific effects in our case, as observed). This effect has now been observed consistently in our study of the dimer comproportionation reaction as we have discussed in the previous sections. We will now show some more evidence and seek to explain how the Olson-Simonson effect might be working in our particular case.

In Figures 2.34, 2.35, 2.36, we compare the three catalytic salt's effects obtained at different reactant's concentrations in separate graphs by plotting the kinetic data *vs.* both GP and the added salt concentration (note: the Cl^- counter ion concentrations introduced from the reactants themselves are not considered here for easier comparison, and from the scales of Figures 2.29 and 2.33 we know that these small amounts of initial chloride will have negligible rate effects). Here we see once again that the different kinetic patterns arising from a given electrolyte when plotted as $\log k_{ex}$ *vs.* GP come together and agree precisely in the Olson-Simenson $\log k_{ex}$ *vs.* conc. plots for SCN^- and adipate, but in the case of muconate there appears to be a slight downward trend in catalytic efficacy as the reactants concentration is increased. In the concentration plots, we can see that the initial $\log k_{ex}$ difference of the lines is very small compared with the overall kinetic acceleration due to added salt, at least for these reaction concentrations. This shows that ion-pairing interactions with and the specific catalytic properties of these anions dominate their effects on the ET kinetics of reaction (2).

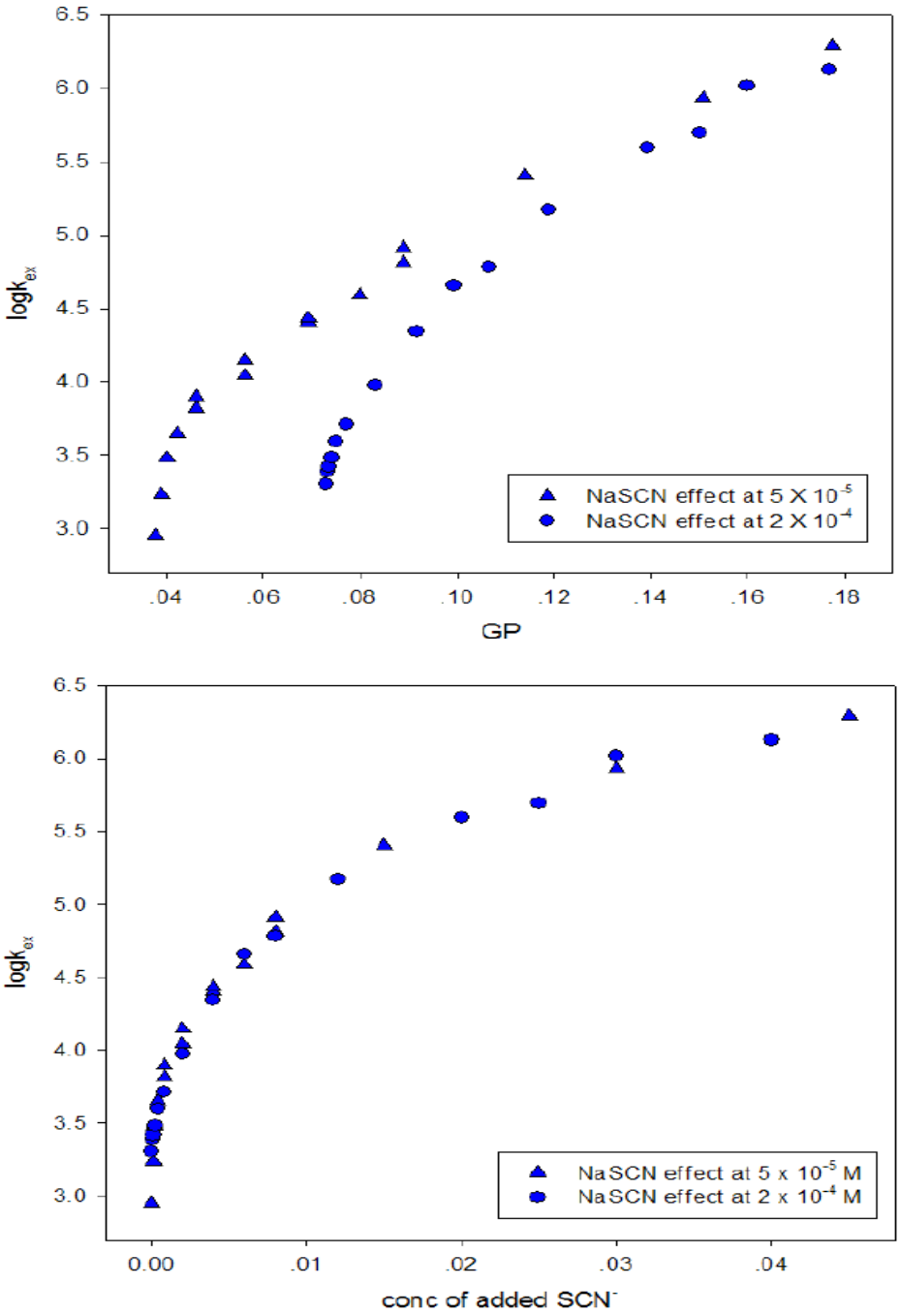

Figure 2.34 NaSCN effects on reaction (2) *vs.* total GP (upper) and *vs.* concentration (lower) at both [Ru^{II}, Ru^{II}] = [Ru^{III}, Ru^{III}] = 5.0 x 10^{-5} M and 2.0 x 10^{-4} M.

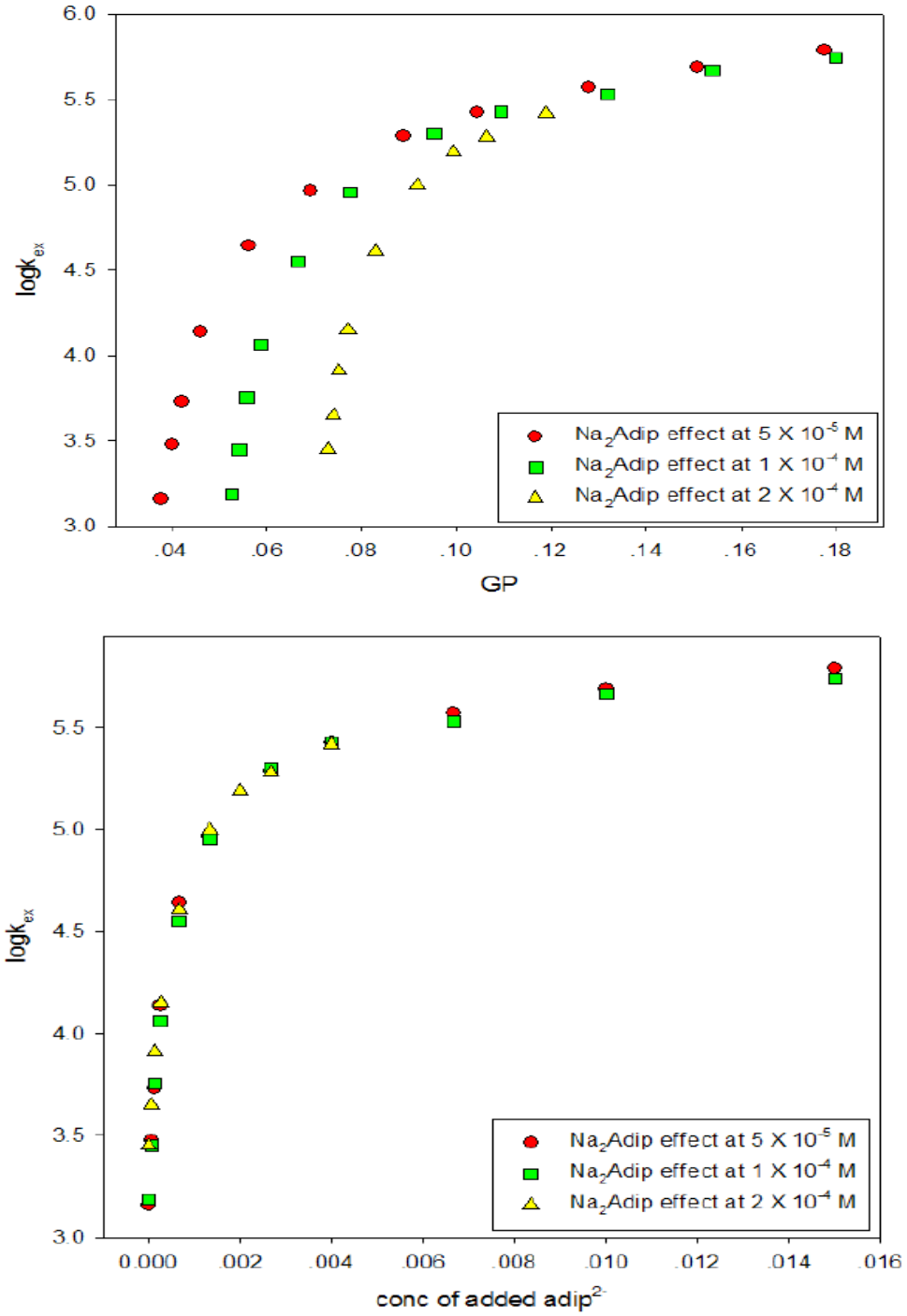

Figure 2.35 Na_2adip effects on reaction (2) *vs.* total GP (upper) and *vs.* concentraction (lower) at $[Ru^{II}, Ru^{II}] = [Ru^{III}, Ru^{III}] = 5.0 \times 10^{-5}$ M, 1.0×10^{-4} M and 2.0×10^{-4} M.

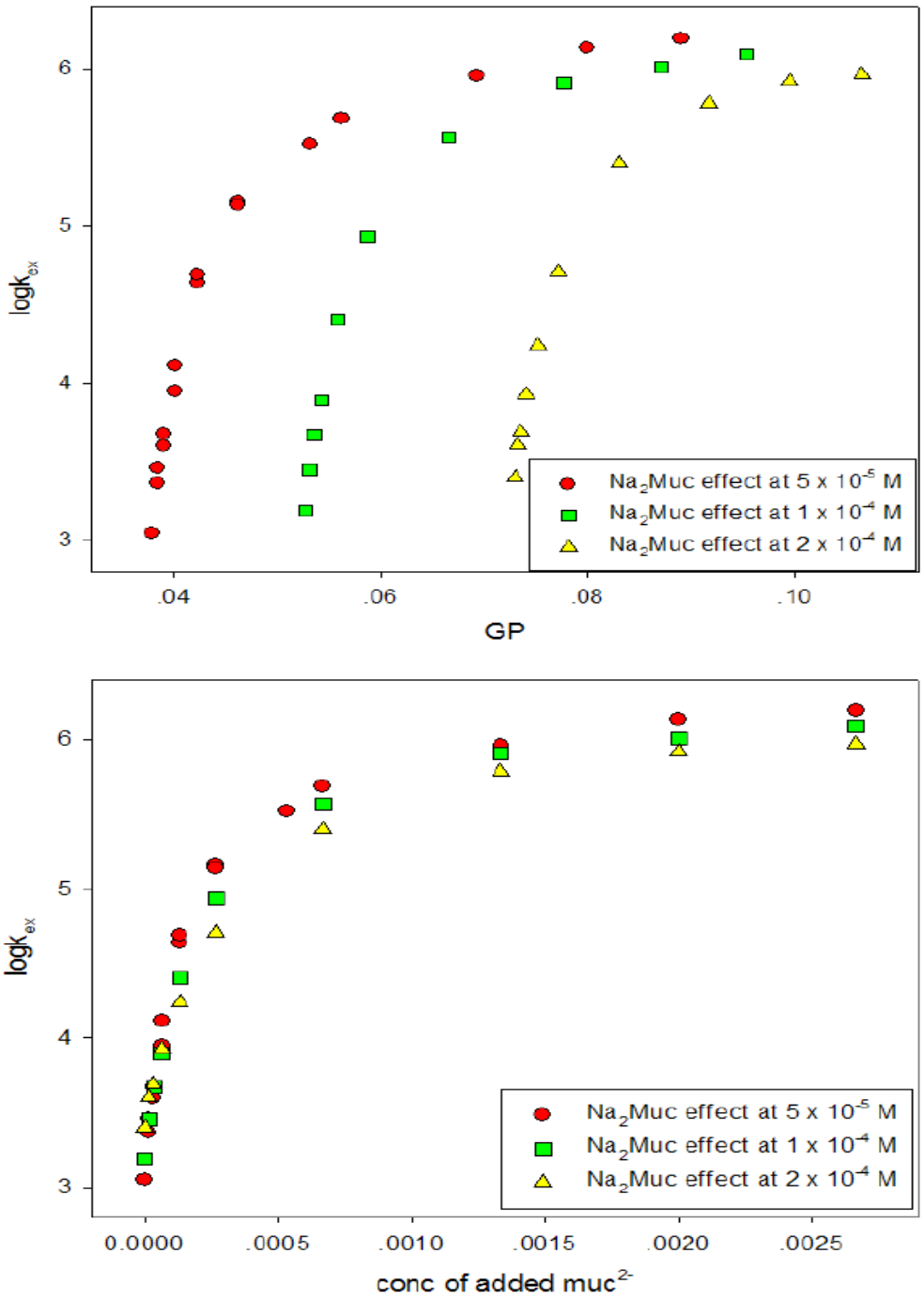

Figure 2.36 Na_2muc effects on reaction (2) *vs.* total GP (upper) and *vs.* concentraction (lower) at [Ru^{II}, Ru^{II}] = [Ru^{III}, Ru^{III}] = 5.0 x 10^{-5} M, 1.0 x 10^{-4} M and 2.0 x 10^{-4} M.

In Figure 2.37, all of the chloride and nitrate salts used in our study are combined and plotted as $\log k_{ex}$ *vs.* concentration. They generally follow the Olson-Simonson effect even though some of them don't have the same initial ruthenium concentration. The points from the linear part of the reactants-only concentration effect (see figure 2.19) we described in the previous section also falls on the line if we plot $\log k_{ex}$ *vs.* anion concentration (for the self-salting effect where Cl^- is the counter ion from the ruthenium complex). This Cl^- anion effect may thus explain part of the self-salting effect we see (though we note that the self-salting slope of 11.2 for $\log k_{ex}$ *vs.* GP_{tot} is much lower than the value of ~43 listed in Table 2.9).

Unfortunately, there is no general way to predict or interpret the exact shape of the Olson-Simonson curve, but rather the smoothness of it and variations in it can be used to infer the importance of specific ion-ion interactions in some kinetic process. Later in this chapter we will show how detailed kinetic modeling using calculated ion association/dissociation rates and best-fit first order ET rate constants within presumed ternary (or higher) encounter complexes can be used to explain the more complex $\log k_{ex}$ *vs.* GP_{tot} behavior shown in the upper panels of Figures 2.34-2.36.

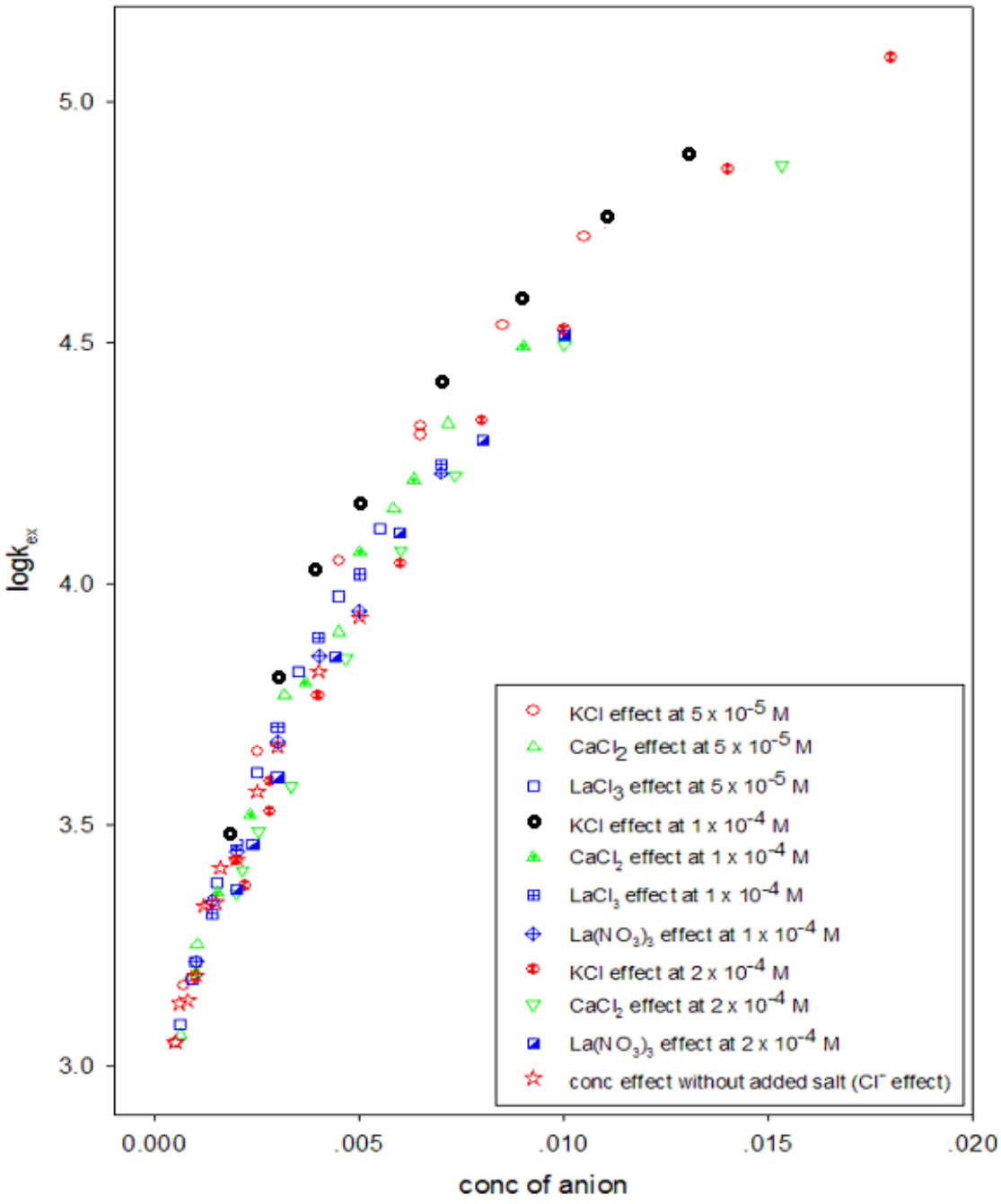

Figure 2.37 Combined concentration effects and salt effects on the rate of dimer comproportionation reaction (reaction 2) of all Cl^- and NO_3^- salts at different initial reactants concentrations.

Temperature-Dependent Kinetic Studies

To gain further mechanistic insight into the observed salt effects and self-salting effects on reaction (2), we performed temperature-dependent kinetic studies at various reactant's concentrations and with various salts so as measure how the activation enthalpy and entropy quantities behaved. Table 2.12 shows the kinetic data from experiments done with the reactant's concentrations at 1.0 X 10^{-4} M and 3.0 X 10^{-4} M and in the presence of added catalytic or non-catalytic electrolytes with reactant's concentration at 1.0 X 10^{-4} M. The resulting Eyring plots are shown in Figure 2.38 as plots of $\ln(k_{ex}/T)$ *vs.* 1/T (the best-fit line to each set of kinetic data is extended to 0 on the X-axis for easy comparison of the y-intercepts).

Table 2.12 Stopped-flow kinetic measurements of reaction (2) as a function of temperature with reactant's concentrations at 1.0 X 10^{-4} M and 3.0 X 10^{-4} M and in the presence of a variety of electrolytes at the reactant's concentration of 1.0 X 10^{-4} M.

$[Ru^{II}\text{-}Ru^{II}] = [Ru^{III}\text{-}Ru^{III}] = 3.0 \text{ X } 10^{-4}$ M with no added salt ($GP_{tot} = 0.0880$)			
T (K)	1/T (K^{-1})	k_{ex}	$\ln(k_{ex}/T)$
283.0	0.00353	2323	2.105
294.8	0.00339	2774	2.242
288.7	0.00346	2681	2.229
300.6	0.00333	3033	2.312

294.9	0.00339	2705	2.216
306.0	0.00327	3101	2.316
300.8	0.00332	3003	2.301
289.0	0.00346	2716	2.240
283.7	0.00352	2665	2.240
297.7	0.00336	3189	2.371
304.5	0.00328	3370	2.404
291.7	0.00343	2961	2.317
285.5	0.00350	2514	2.175
295.3	0.00339	3027	2.327
301.1	0.00332	3220	2.370
289.2	0.00346	2810	2.274
$[Ru^{II}\text{-}Ru^{II}] = [Ru^{III}\text{-}Ru^{III}] = 1.0 \times 10^{-4}$ M with no added salt ($GP_{tot} = 0.0527$)			
T (K)	1/T (K^{-1})	k_{ex}	$\ln(k_{ex}/T)$
294.8	0.00339	1294	1.479
288.7	0.00346	1170	1.399
300.6	0.00333	1388	1.530
294.9	0.00339	1222	1.422
306.0	0.00327	1454	1.558
300.8	0.00332	1350	1.501
289.0	0.00346	1182	1.409

283.7	0.00352	1256	1.488
297.7	0.00336	1430	1.569
304.5	0.00328	1542	1.622
291.7	0.00343	1352	1.534
285.5	0.00350	1148	1.391
295.3	0.00339	1388	1.547
301.1	0.00332	1497	1.604
289.2	0.00346	1260	1.471
$[Ru^{II}\text{-}Ru^{II}] = [Ru^{III}\text{-}Ru^{III}] = 1.0 \times 10^{-4}$ M with added KF ([KF] = 6.2 mM, GP_{tot} = 0.088)			
T (K)	1/T (K^{-1})	k_{ex}	$\ln(k_{ex}/T)$
285.5	0.00350	4695	2.800
295.7	0.00338	5661	2.952
301.1	0.00332	6474	3.068
291.1	0.00344	5222	2.887
284.0	0.00352	4487	2.760
298.8	0.00335	5976	2.996
305.0	0.00328	6932	3.124
289.1	0.00346	4897	2.830
$[Ru^{II}\text{-}Ru^{II}] = [Ru^{III}\text{-}Ru^{III}] = 1.0 \times 10^{-4}$ M with added KCl ([KCl] = 6.2 mM, GP_{tot} = 0.088)			

T (K)	1/T (K^{-1})	k_{ex}	$\ln(k_{ex}/T)$
285.5	0.00350	19710	4.235
295.7	0.00338	21900	4.305
301.1	0.00332	24020	4.379
291.1	0.00344	20900	4.274
283.6	0.00353	19102	4.210
297.8	0.00336	23096	4.351
304.7	0.00328	25574	4.430
287.3	0.00348	20140	4.250
300.6	0.00333	22829	4.330
289.8	0.00345	20727	4.270
$[Ru^{II}\text{-}Ru^{II}] = [Ru^{III}\text{-}Ru^{III}] = 1.0 \times 10^{-4}$ M with added ([KBr] = 6.2 mM, GP_{tot} = 0.088)			
T (K)	1/T (K^{-1})	k_{ex}	$\ln(k_{ex}/T)$
284.0	0.00352	38920	4.920
298.8	0.00335	41690	4.938
305.0	0.00328	44540	4.984
289.1	0.00346	40320	4.938
285.7	0.00350	39035	4.917
295.1	0.00339	41740	4.952
301.7	0.00331	43236	4.965

290.6	0.00344	41822	4.969
$[Ru^{II}\text{-}Ru^{II}] = [Ru^{III}\text{-}Ru^{III}] = 1.0 \times 10^{-4}$ M with added KI ([KI] = 6.2 mM, GP_{tot} = 0.088)			
T (K)	1/T (K^{-1})	k_{ex}	$\ln(k_{ex}/T)$
285.0	0.00351	75910	5.585
295.7	0.00338	73930	5.522
300.9	0.00332	73780	5.502
290.4	0.00344	72220	5.516
283.6	0.00353	79544	5.637
297.8	0.00336	74215	5.518
304.7	0.00328	72839	5.477
294.3	0.00340	75717	5.550
300.6	0.00333	71582	5.473
289.8	0.00345	73464	5.535
$[Ru^{II}\text{-}Ru^{II}] = [Ru^{III}\text{-}Ru^{III}] = 1.0 \times 10^{-4}$ M with added KI ([KCl] = 1.8 mM, GP_{tot} = 0.0654)			
T (K)	1/T (K^{-1})	k_{ex}	$\ln(k_{ex}/T)$
285.7	0.00350	9316	3.485
295.1	0.00339	9997	3.523
301.7	0.00331	10530	3.553
290.6	0.00344	9722	3.510

$[Ru^{II}\text{-}Ru^{II}] = [Ru^{III}\text{-}Ru^{III}] = 1.0 \times 10^{-4}$ M with added Na_2Adip ($[Na_2Adip] = 3.0$ mM, $GP_{tot} = 0.0871$)			
T (K)	1/T (K^{-1})	k_{ex}	$\ln(k_{ex}/T)$
284.9	0.00351	106400	5.923
295.9	0.00338	129500	6.081
301.6	0.00332	154400	6.238
288.6	0.00347	115100	5.989
291.9	0.00343	123789	6.050
297.8	0.00336	136820	6.130
304.7	0.00328	162645	6.280
300.2	0.00333	143570	6.170
$[Ru^{II}\text{-}Ru^{II}] = [Ru^{III}\text{-}Ru^{III}] = 1.0 \times 10^{-4}$ M with added Na_2Muc ($[Na_2Muc] = 3.0$ mM, $GP_{tot} = 0.0871$)			
T (K)	1/T (K^{-1})	k_{ex}	$\ln(k_{ex}/T)$
295.7	0.00338	1251295	8.350
300.9	0.00332	1440674	8.474
290.4	0.00344	1109436	8.248
284.9	0.00351	1047000	8.209
295.9	0.00338	1197000	8.305
301.6	0.00332	1392000	8.437
288.6	0.00347	1186000	8.321

301.6	0.00332	1527000	8.530
$[Ru^{II}\text{-}Ru^{II}] = [Ru^{III}\text{-}Ru^{III}] = 1.0 \times 10^{-4}$ M with added Na_2Muc ($[Na_2Muc] = 1.0$ mM, $GP_{tot} = 0.0667$)			
T (K)	1/T (K^{-1})	k_{ex}	$\ln(k_{ex}/T)$
284.8	0.00351	342000	7.091
295.5	0.00338	384000	7.170
301.6	0.00332	388200	7.160
288.6	0.00347	371700	7.161
284.8	0.00351	334100	7.067
295.5	0.00338	353300	7.086
301.6	0.00332	380000	7.139
288.6	0.00347	341200	7.075

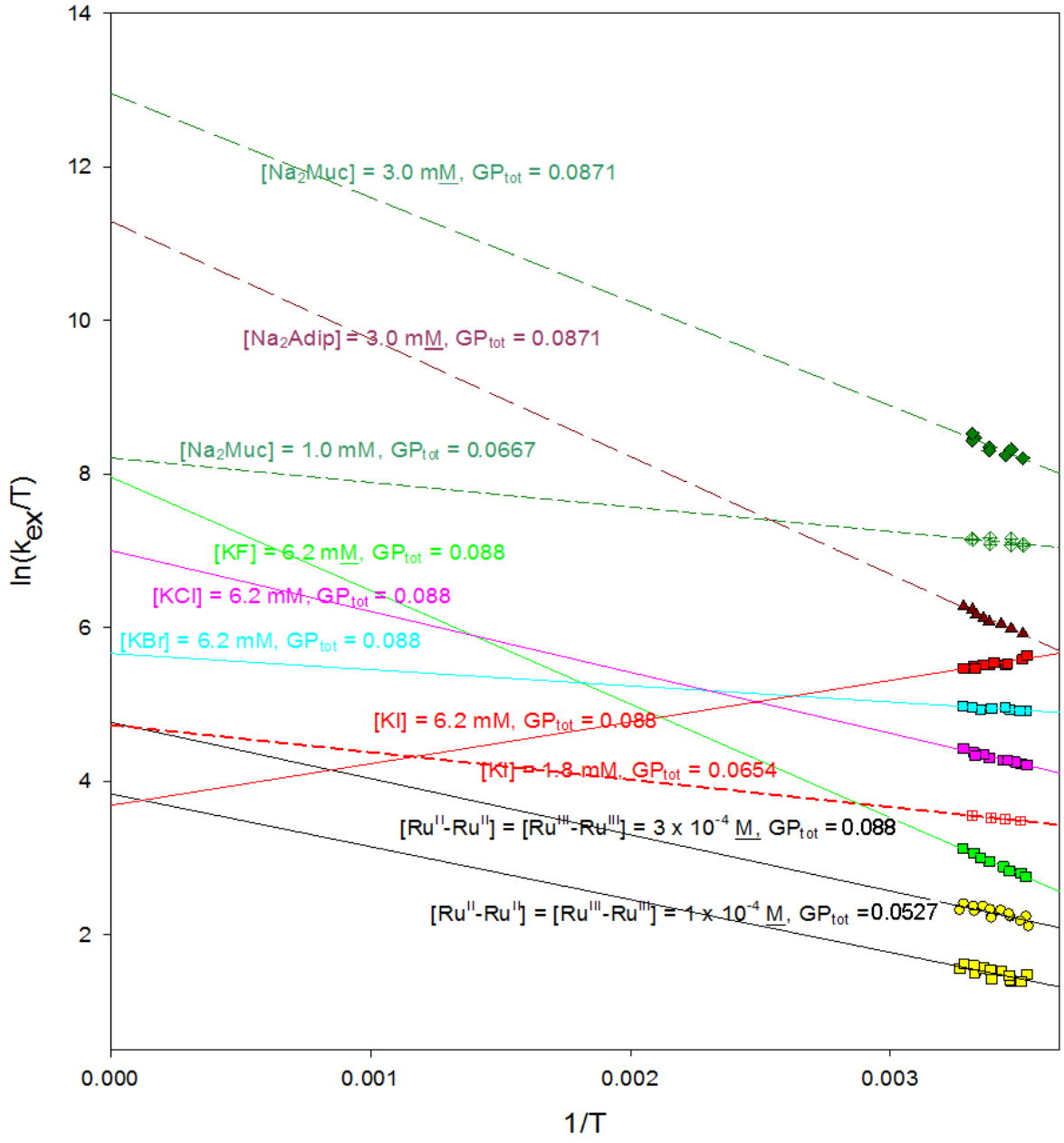

Figure 2.38 Eyring plots for reaction (2) for both reactant-only cases at 1.0 x 10^{-4} M and 3.0 x 10^{-4} M in the presence of added salts with $[Ru^{II}\text{-}Ru^{II}]$ - $[Ru^{III}\text{-}Ru^{III}]$ = 1.0 x 10^{-4} M

Table 2.13 lists the measured $\Delta H^{\neq}$ and $\Delta S^{\neq}$ values calculated for these reactions using the Eyring equation (eq. 2-22). From the T dependent experiment on the "self-salting" effect where we increase the reactant's concentrations from 1.0 x 10^{-4} M to 3.0 x 10^{-4} M, we can see the rate enhancement at higher reactant's concentration is mainly due to an entropy effect ($\Delta S^{\neq}$ goes from -166 to -158 J K^{-1} M^{-1}) and $\Delta H^{\neq}$ for both concentrations are the same within error at ~ 6 KJ/mole

When the reactant's concentration was kept constant and different potassium halides were added to the reaction (at either 18 or 62 times the Ru concentration), the $\Delta H^{\neq}$ values obtained from the T-dependence experiments decreased gradually upon gong from added F^- to I^-. An interesting and unusual negative enthalpy effect ($\Delta H^{\neq}$ = -4.5 kJ/mol) was observed for the added I^- case at 6.2 x 10^{-3} M. By plotting the magnitude of the first half life $t_{1/2}$ *vs.* T (where $t_{1/2}$ is taken from the absorbance *vs.* time kinetic curve from each of the temperature-dependent stopped-flow experiments), we can see that the first half-lives of the reactions decrease as expected when increasing T in the case of added F^- and Cl^-, but the trend goes almost flat (no change with T) for the added Br^- and I^- case (see Figure 2.39). The activation entropies for the reaction in the presence of the added halides decrease progressively (meaning that the entropic barrier, $-T\Delta S^{\neq}$, becomes larger) upon going from added F^- to I^-. This trend of an increasingly negative contribution to the enthalpic barrier from the heavier added halides, especially iodide has been reported previously by Sista in his work on

reaction (1).[41] Our overall activation free energies decrease only slightly from added F^- to I^-, and an experimentally significant enthalpy-entropy compensation effect is observed upon plotting $\Delta S^{\neq}$ *vs.* $\Delta H^{\neq}$ (see Figure 2.40).[54]

As discussed previously by Sista, we know that the hydration enthalpies of the halides drop (become less negative) as $F^- > Cl^- > Br^- > I^-$,[41] and that the entropies of hydration increase (also become less negative) over the same series (both trends thought to be related to the progressive increase in radius of X^- and hence decrease in hydration sphere electrostriction).[53] Our kinetic data are consistent with these trends and the idea of a presumed ternary (or possibly higher) precursor complex where X^- becomes desolvated so as to form a "bridge" between the two redox partners. For example, it "costs" most in terms of enthalpy to desolvate F^-, but releasing the tightly-held salvation layer also yields greatest entropic compensation of that cost. Conversely, I^- is easily desolvated but doing so provides little entropic benefic. The surprising results (note Table 2.13) is that other aspects of the overall mechanism seem to place entropic constraints on the transition state (negative contributions to $\Delta S^{\neq}$) such that the overall $\Delta H^{\neq}$, or $\Delta G^{\neq}+\Delta S^{\neq}$, sum, actually comes up negative – a rarely encountered results.[55-58]

Table 2.13 Activation parameters calculated from Eyring plots with Eq. 2-22 for reaction (2) with reactant's concentrations of 1.0 X 10^{-4} M and 3.0 X 10^{-4} M and in the presence of a variety of electrolytes at the reactant's concentration of 1.0 X 10^{-4} M.

Concentration of Reactants and Added Electrolyte	**Total $\mu^{1/2}/(1+\mu^{1/2})$**	**$\Delta H^{\ddagger}$ (kJ mol^{-1})**	**$\Delta S^{\ddagger}$ (J $K^{-1}mol^{-1}$)**	**$\Delta G^{\ddagger}$ (at 298K) (kJ mol^{-1})**
$[Ru^{II}\text{-}Ru^{II}] = [Ru^{III}\text{-}Ru^{III}]$ = 1.0 × 10^{-4} M (**no added electrolyte**)	0.0527	5.7 ± 1.3	-166 ± 4	54.7 ± 2.5
$[Ru^{II}\text{-}Ru^{II}] = [Ru^{III}\text{-}Ru^{III}]$ = 3.0 × 10^{-4} M (**no added electrolyte**)	0.088	6.1 ± 1.3	-158 ± 4	52.7 ± 2.5
$[Ru^{II}\text{-}Ru^{II}] = [Ru^{III}\text{-}Ru^{III}]$ = 1.0 × 10^{-4} M with **[KF] = 6.2 × 10^{-3} M**	0.088	12.3 ± .5	-131 ± 2	50.9 ± 1.1
$[Ru^{II}\text{-}Ru^{II}] = [Ru^{III}\text{-}Ru^{III}]$ = 1.0 × 10^{-4} M with **[KCl] = 6.2 × 10^{-3} M**	0.088	6.6 ± 0.6	-139 ± 2	47.6 ± 1.2
$[Ru^{II}\text{-}Ru^{II}] = [Ru^{III}\text{-}Ru^{III}]$ = 1.0 × 10^{-4} M with **[KBr] = 6.2 × 10^{-3} M**	0.088	1.8 ± 0.6	-150 ± 2	46.1 ± 1.2
$[Ru^{II}\text{-}Ru^{II}] = [Ru^{III}\text{-}Ru^{III}]$ = 1.0 × 10^{-4} M with **[KI] = 6.2 × 10^{-3} M**	0.088	-4.5 ± 0.8	-167 ± 2	44.8 ± 1.4
$[Ru^{II}\text{-}Ru^{II}] = [Ru^{III}\text{-}Ru^{III}]$ = 1.0 × 10^{-4} M with **[KI] = 1.8 × 10^{-3} M**	0.0654	3.0 ± 0.2	-159 ± 1	49.7 ± 0.1
$[Ru^{II}\text{-}Ru^{II}] = [Ru^{III}\text{-}Ru^{III}]$ = 1.0 × 10^{-4} M with **$[Adip^{2-}]$ = 2 × 10^{-3} M**	0.0871	12.7 ± 0.9	-104 ± 3	43.4 ± 1.8
$[Ru^{II}\text{-}Ru^{II}] = [Ru^{III}\text{-}Ru^{III}]$ = 1.0 × 10^{-4} M with **$[Muc^{2-}]$ = 2 × 10^{-3} M**	0.0871	11.3 ± 1.9	-89 ± 7	37.6 ± 4.0
$[Ru^{II}\text{-}Ru^{II}] = [Ru^{III}\text{-}Ru^{III}]$ = 1.0 × 10^{-4} M with **$[Muc^{2-}]$ = 6.7 × 10^{-4} M**	0.0667	5.8 ± 2.0	-118 ± 7	40.5 ± 4.0

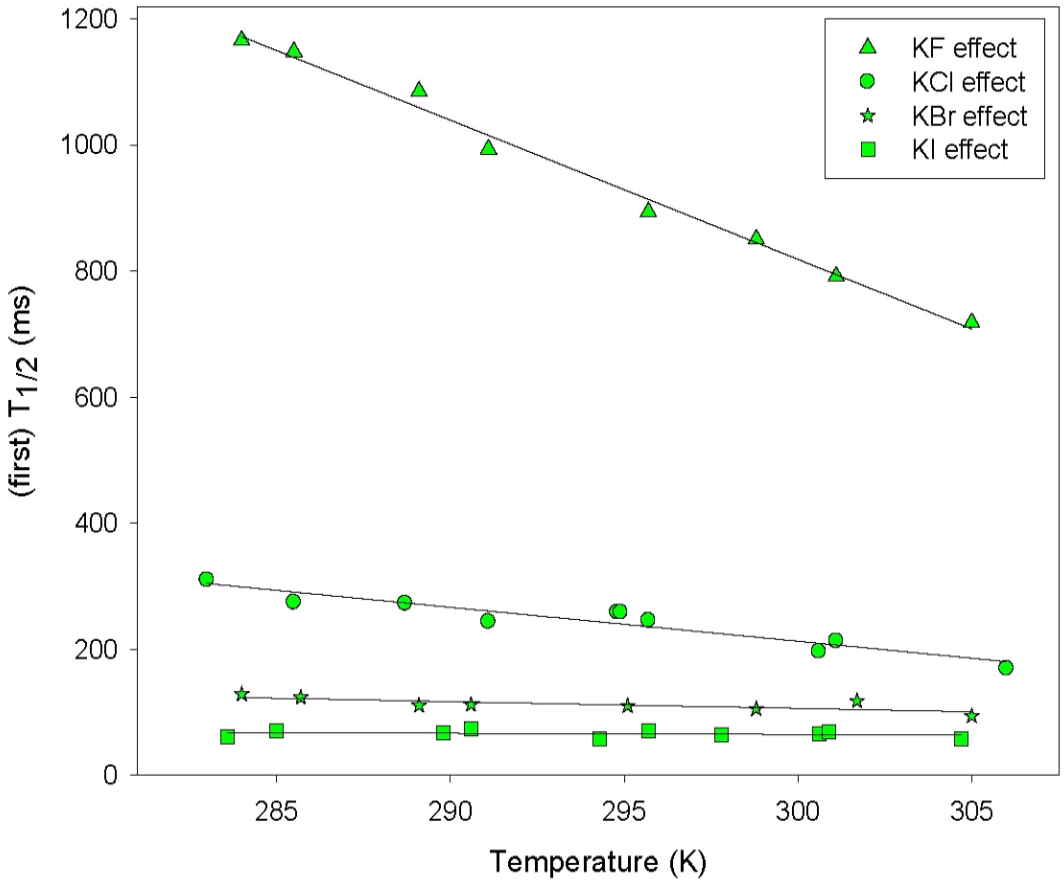

Figure 2.39 First reaction half-life $t_{1/2}$ from the absorbance *vs.* time kinetic curves from the temperature-dependent kinetics experiments for reaction (2) (all run with reactant's concentration at 1.0 x 10^{-4} M in the presence of added halides salts at 62 fold molar excess and total GP = 0.088).

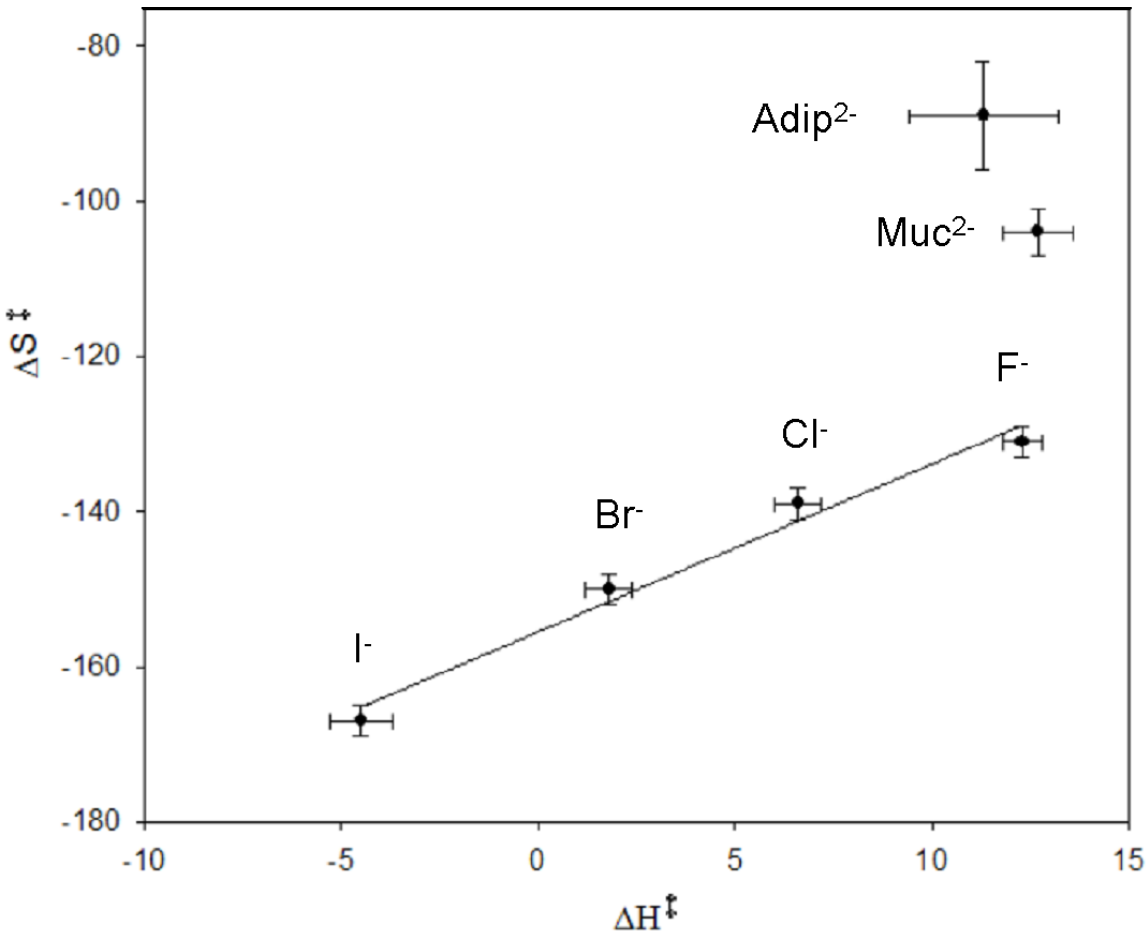

Figure 2.40 Enthalpy and entropy compensation effect for reaction (2) with reactant's concentration at 1.0 x 10^{-4} M in the presence of added halides and catalytic salts (total GP = 0.088)

We have discussed previously how the kinetic rate constants increase significantly by adding simple salts (such as F^-) and how addition of catalytic salts (such as Muc^{2-}) leads to a much greater change. From table 2.13 and Figure 2.40, we can see a clear trend in the entropy effect by comparing added F^- through I^- with added $Adip^{2-}$ or Muc^{2-} ($\Delta S^{\neq}$ is -131 J K^{-1} M^{-1} for added F-; -104 J

K^{-1} M^{-1} for added $Adip^{2-}$; -89 J K^{-1} M^{-1} for added Muc^{2-}) and interestingly, the activation of enthalpies of these cases are the same within experimental error. This trend in $\Delta S^{\neq}$ agrees with the ideas discussed previously[35,36] that the electronic structure of muconate provides strong enough electronic coupling to effect the adiabaticity of the reaction (which would be expected to show up in the intercept of an Eyring plot, see parameter κ_{el} in equation 1-12 of Ch. 1).

Ion Pair Formation Constant Measurements using UV-Vis Spectroscopy

The Ion-pair formation constant K_{ip} for association equilibria between ions in solution can be calculated by the well-known Eigen[14,15] and Fuoss[16] equations (2-12 to 2-14), or it can be obtained experimentally in favorable cases like ours where an ion-pair charge transfer band is observable[49] (from X^- to Ru^{III}) by fitting the observed absorbance difference ΔOD at the ion-pair λ_{max} to the added halide concentration through a Debye-Huckel type expression.[48] One of the drawbacks of the Eigen-Fuoss equations is that they treat the reactants as spheres, and this might be a poor approximation of the geometry of the actual molecule - especially in a case like our BPE Ru^{III}-Ru^{III} dimer which has a more rod-like shape and therefore highly non-spherical charge distribution. When forming the first ion-pair with a halide ion, for example, it is very likely that one of the Ru^{III} centers on the dimmer will interact more strongly than the other Ru^{III} center. Thus, using an overall charge of 6+ for Ru^{III}-Ru^{III} dimer in the Eigen-Fuoss equations for calculating the K_{ip} might be expected to introduce a

large error and result in overestimated K_{ip} values. Experimental measurements for more reliable K_{ip} values thus become necessary in order to evaluate the reaction mechanism.

Ion-pair charge transfer (IPCT) spectra have been characterized in early work by Navon *et al.*[48] using the $Ru^{III}(NH_3)_6^{3+}$ ion as the electron accepting center and by Sexton *et al.*[50] using the $(NH_3)_5Ru^{III}py^{3+}$ ion. In order to validate our methods here on the decaammine Ru^{III}-BPE-Ru^{III} dimer, we also performed measurements using the related $(NH_3)_5Ru^{III}(3\text{-Fpy})^{3+}$ ion since it yields more cleanly-separated and distinct IPCT spectra and λ_{max} values than the BPE dimer or $(NH_3)_5Ru^{III}py^{3+}$ does (see Figure 2.41-2.43 and Table 2.14). We note that even though the higher redox potential of the $(NH_3)_5Ru^{III}(3\text{-Fpy})^{3+}$ complex as compared to the pyridine complex studied by Sexton *et al.*[50] (0.157 V as compared to 0.095 V *vs.* SCE),[41] the IPCT λ_{max} for the chloride ion pair is at the same wavelength (312 nm) and the IPCT for Br^- is slightly blue-shifted by 1 nm compared with the reported value of 338 nm by Sexton *et al.*[50]. Applying equations 2.49 and 2.50 to the data in Table 2.14, we able to fit the ΔAbs (ΔOD in equation 2.49) as shown in Figure 2.44. The best-fit values for K_{ip} are as shown in Table 2.15. The best-fit experimental values actually show comparable association constants to the calculated Eigen-Fuoss values (in the first columnn) and also agree reasonably with the experimental values of 15.0 for Cl^- and 11.1 for Br^- arrived at by Navon *et. al.* using the hexaammine Ru(III) complex.[48]

Though the exact best-fit K_{ip} values are somewhat model-dependent (inclusion of B term from equation 2.50 or not), we see that there probably is a small difference between Cl^- and Br^- in the experimental K_{ip} which is not captured in the calculated Eigen-Fuoss value. As shown in Table 2.15, the D_{ex} (best-fit IPCT band extinction coefficient) arrived at using the Eigen-Fuoss equation without the BI term used by Navon converges on what are probably unreasonably large values of D_{ex}, especially for Cl^-.

Since these ruthenium monomer complexes are reasonably spherical, it is not surprising that the experimental best-fit and calculated K_{ip} values from the Eigen-Fuoss equations are in good agreement. To verify this, we also performed the UV-Vis measurement of the IPCT spectra with $(NH_3)_5Ru^{III}3Fpy$ by adding halides. Figure 2.41, 2.42 and 2.43 show the UV-Vis measurement of the spectra of $(NH_3)_5Ru^{III}3Fpy$ monomer at 1.0 m<u>M</u> concentration by adding KCl, KBr and KI. Since the IPCT spectra with this monomer complex obtained upon adding I^- shows a significant MLCT band which corresponds to the reduction of Ru^{III} by I^-, we did not include these results in our fitting work for K_{ip}. The measured absorbance values at λ_{max} for added Cl^- and Br^- are listed in Table 2.14, and the Δ Abs *vs.* $[X^-]$ plots are shown in Figure 2.44.

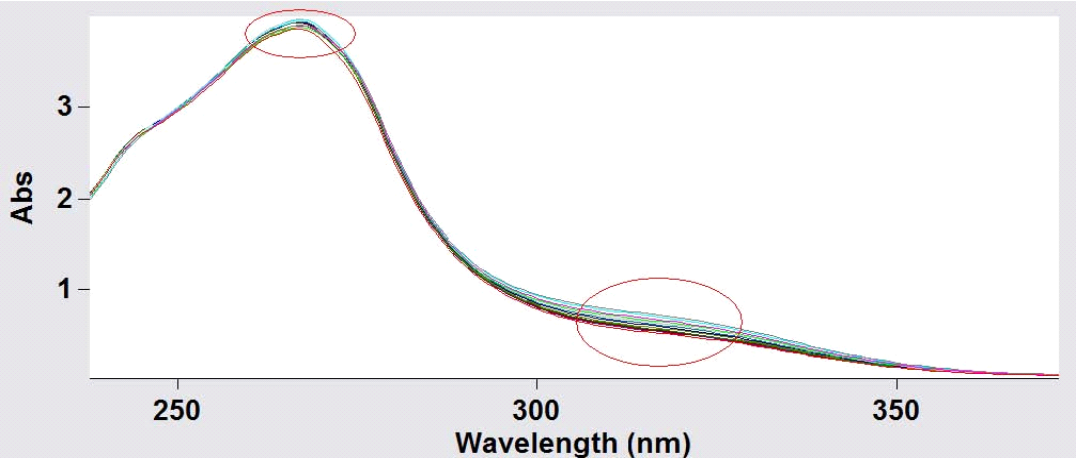

(a)

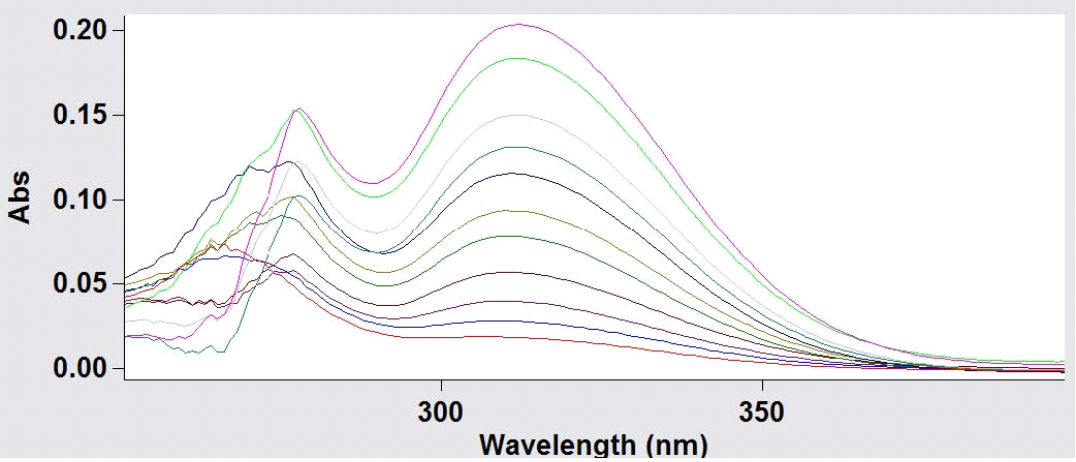

(b)

Figure 2.41 a) absolute UV-Vis (*vs.* water only) spectra generated by adding KCl (conc. of Cl^- ranges from 0.005 to 1.0 M) to the $(NH_3)_5Ru^{III}3Fpy^{3+}$ monomer with $[Ru^{III}]$ at 1.0 x 10^{-3} M; b) Spectra obtained by subtracting the spectrum of the dimer without any added KCl from the spectra with KCl; note that the absorption at λ_{max} clearly increases with added KCl. It was the longer-wavelength, fully-resolved band at 312 nm which was used in calculation of K_{ip}

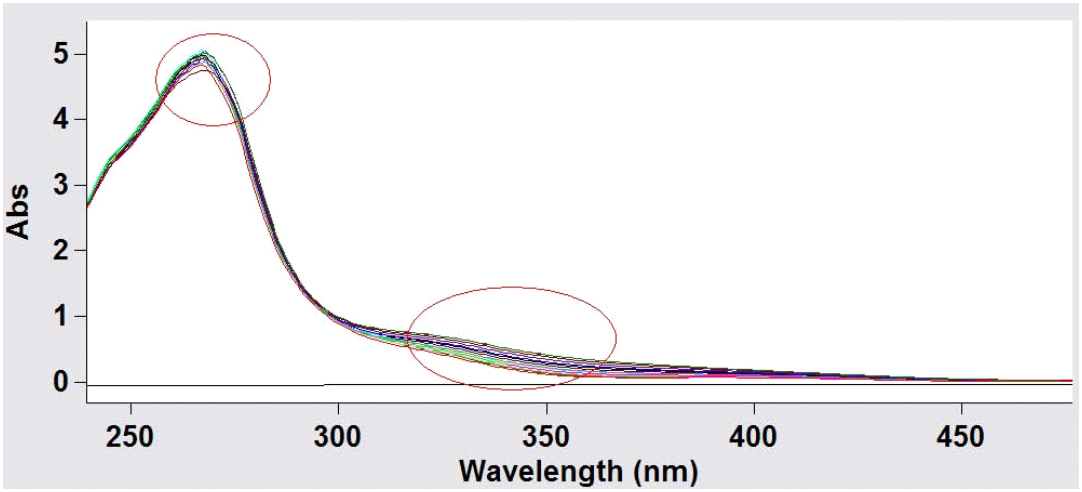

(a)

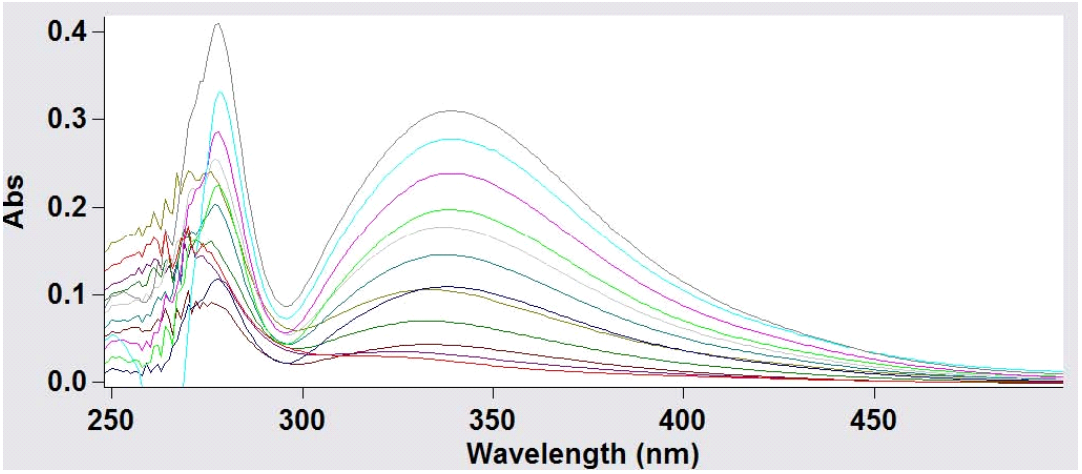

(b)

Figure 2.42 a) Absolute UV-Vis (*vs.* water only) spectra generated by adding KBr (conc. of Br^- ranges from 0.005 to 1.0 M) to the $(NH_3)_5Ru^{III}3Fpy^{3+}$ monomer with $[Ru^{III}]$ at 1.0 x 10^{-3} M; b) Spectra obtained by subtracting the spectrum of the dimer without any added KBr from the spectra with KBr; note that the IPCT absorption at λ_{max} = 339 nm clearly increases with added KBr.

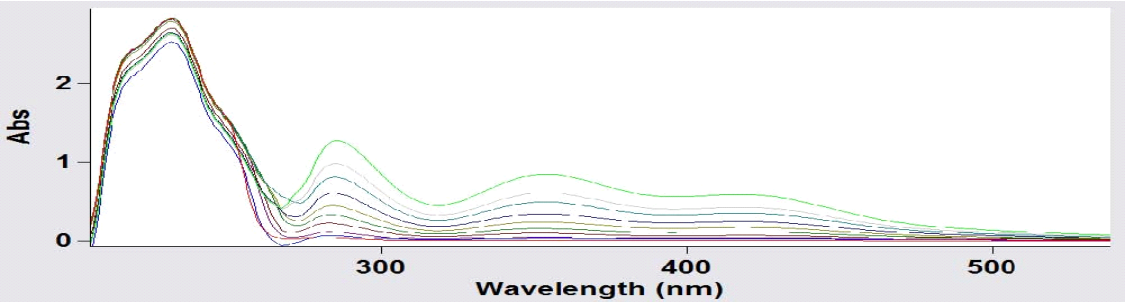

Figure 2.43 Absolute UV-Vis (*vs.* water only) spectra generated by adding KI (conc. of I^- ranges from 0.005 to 1.0 M) to the $(NH_3)_5Ru^{III}3Fpy$ monomer with $[Ru^{III}]$ at 1.0 x 10^{-3} M; note that the absorptions at λ_{max} = 290 and 355 nm may be IPCT bands (since they clearly increase with added KI) but the growing MCLT at 420 nm interferes.

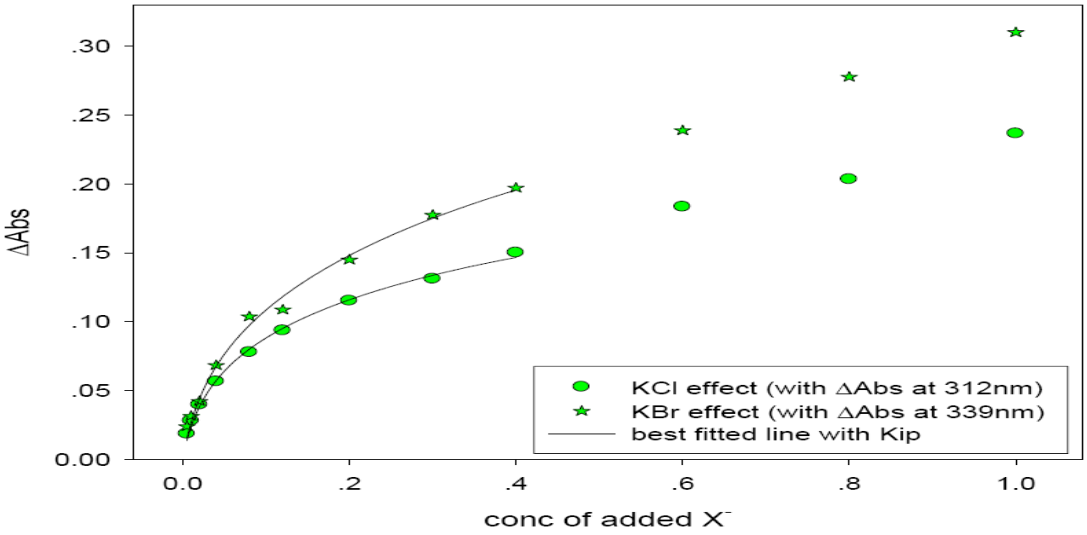

Figure 2.44 IPCT absorbance values from Table 2.15 for the $(NH_3)_5Ru^{III}3Fpy^{3+}$ complex and added Cl^- and Br^-; the presumed absorbing species is then [3+,X-] (where 3+ is the $(NH_3)_5Ru^{III}3Fpy^{3+}$ monomer). The best fitted lines with K_{ip} = 26.9 $\pm$ 2.2 for KCl and 20.4 $\pm$ 2.5 for KBr are obtained using Eq. 2.14 with B term = 0.64 and 0.62, respectively.

Table 2.14 UV-Vis absorbance data at the IPCT λ_{max} position for $(NH_3)_5Ru^{III}3Fpy^{3+}$ in the presence of added Cl^- and Br^-; the presumed absorbing species is then [3+,X-] (where 3+ is the $(NH_3)_5Ru^{III}3Fpy^{3+}$ monomer)

$[Cl^-]$ M	Abs (Cl^-) (at 312 nm)	$[Br^-]$ M	Abs (Br^-) (at 339 nm)
5.0e-3	0.0187	5.0e-3	0.0240
0.010	0.0282	0.010	0.0315
0.020	0.0398	0.020	0.0423
0.040	0.0567	0.040	0.0684
0.080	0.0779	0.080	0.1037
0.120	0.0937	0.120	0.1087
0.200	0.1153	0.200	0.1450
0.300	0.1312	0.300	0.1775
0.400	0.1502	0.400	0.1972
0.600	0.1835	0.600	0.2389
0.800	0.2035	0.800	0.2777
1.000	0.2367	1.000	0.3101
		0.010	0.0341
		0.020	0.0487
		0.080	0.0943
		0.400	0.2001
		0.533	0.2327

		0.800	0.2970

Table 2.15 Measured Kip by fitting plots in Figure 2.48 *vs.* calculated K_{ip} from Eigen-Fuoss equations (Eq. 2-14) for $(NH_3)_5Ru^{III}3Fpy^{3+}$ with X^-.

	Kip (calculated at μ≈0 with [3+, 1-])	**Kip** (from fitting with "BI" term)	**Kip** (from fitting without "BI" term)
Cl-	19.5	26.9 ± 2.2 (Dex = 199 ± 7) (B = 0.64)	17.1 ± 2.5 (Dex = 2947 ± 26)
Br-	19.4	20.4 ± 2.5 (Dex = 287 ± 16) (B = 0.62)	11.1 ± 2.5 (Dex = 493 ± 78)

a) Dex is the best-fit difference between the molar extinction coefficients for the ion pair solutions and the constituent Ru^{III} and X^- ions alone; b) the radius of the $(NH_3)_5Ru^{III}3Fpy^{3+}$ ion was taken as 4.37 Å, Cl^- as 1.90 Å and Br^- as 2.0 Å.[41]

From Figures 2.45, 2.46 and 2.47 pertaining to the BPE dimer, we see that the IPCT band λ_{max} does not shift according to the identity of the halide in the same way as it does for the monomer $Ru^{III}(NH_3)_6^{3+}$ acceptor studied by Navon, the $Ru^{III}(NH_3)_5py^{3+}$ studied by Sexton *et. al.*, or the $(NH_3)_5Ru^{III}(3\text{-}Fpy)^{3+}$ monomer complex shown in Figure 2.41-2.43. This is probably due to the actual λ_{max} of the band not being fully resolved from the $\pi - \pi^*$ band of the BPE ligand. Despite this spectral masking, we are still able to see IPCT absorbance for the

part of the band which is not masked and then apply the fitting method of Navon to the absorbance data for extraction of a best-fit K_{ip} (but the D_{ex} extinction coefficient of the IPCT band will correspond only to some random position on the low energy side of the IPCT band). Figure 2.48 shows the fit to the absorbance data and Table 2.17 summarizes the best fit K_{ip} and D_{ex} values.

For spectra with added Cl^- and Br^-, the IPCT bands with the BPE dimer are more clearly shown than the spectra with added I^-. In Figure 2.47 (b), we can see that with added I^-, a second peak shows up at ~ 540nm which corresponds in wavelength to the reduced Ru^{II}-Ru^{III} species. Even though trace of H_2O_2 was added to the Ru^{III}-Ru^{III} solution prior to adding I^-, the reduced species was still observed in UV-Vis spectrum. So, the measured K_{ip} for Ru^{III}-Ru^{III} with I^- here will be not as accurate as the other cases with added Cl^- and Br^-.

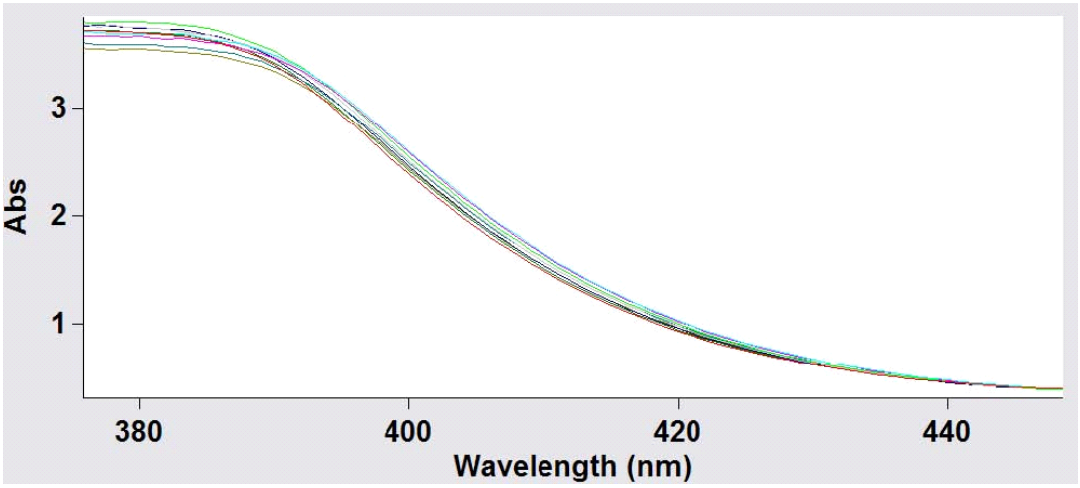

(a)

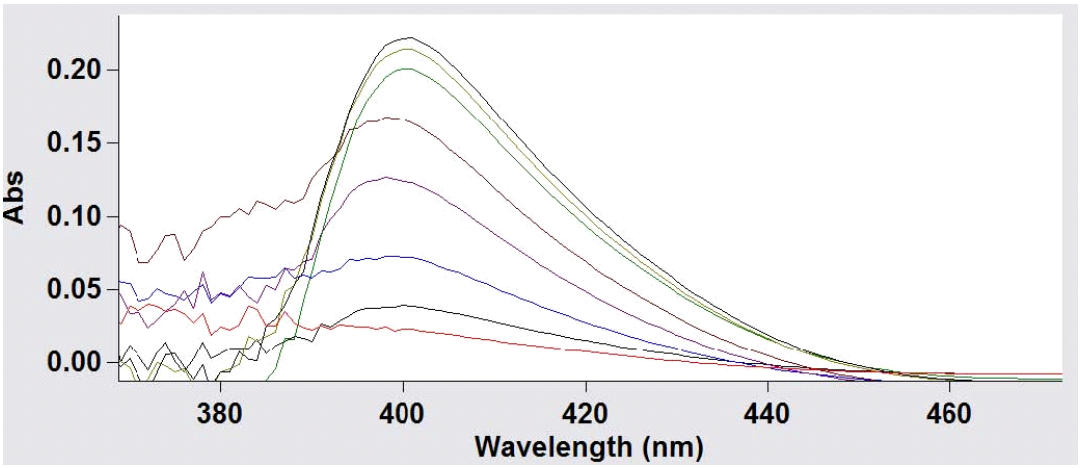

(b)

Figure 2.45 a) Absolute UV-Vis (*vs.* water only) spectra generated by adding KCl (conc. of Cl^- ranges from 0.004 to 0.5 M) to the decaammine BPE dimer with [Ru^{III}-Ru^{III}] at 5.0 x 10^{-4} M; b) Spectra obtained by subtracting the spectrum of the dimer without any added KCl from the spectra with KCl; note that the absorption at $\lambda_{max} \approx$ 390 – 440 nm clearly increases with added KCl.

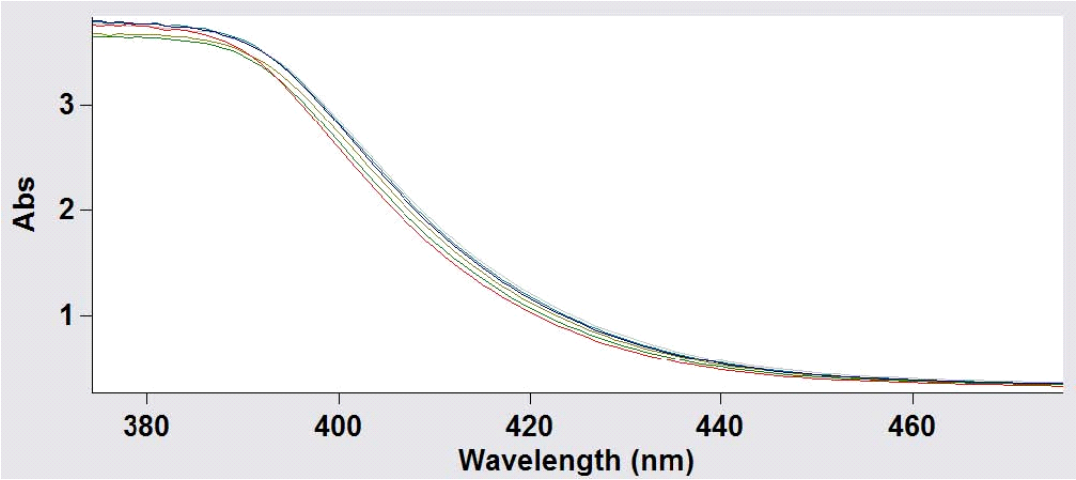

(a)

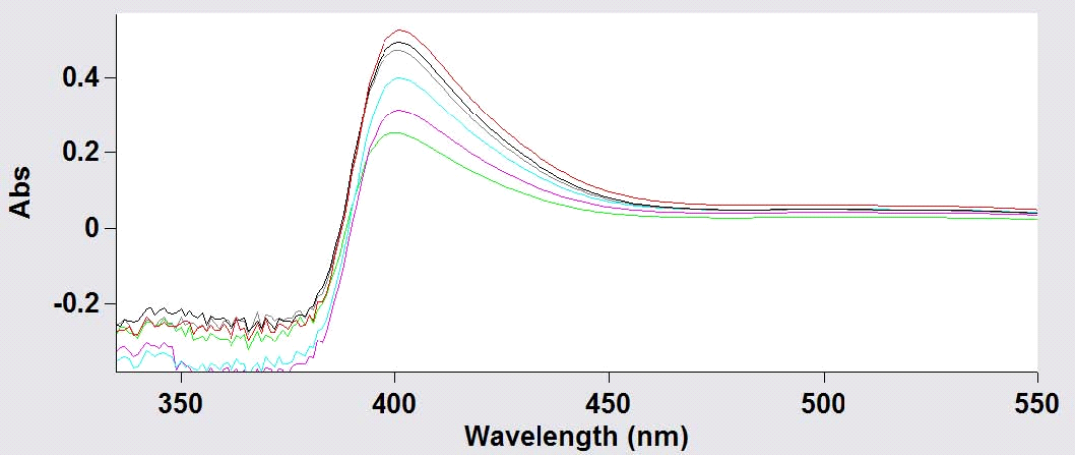

(b)

Figure 2.46 a) Absolute UV-Vis (*vs.* water only) spectra generated by adding KBr (conc. of Br^- ranges from 0.004 to 0.4 M) to the decaammine BPE dimer with $[Ru^{III}\text{-}Ru^{III}]$ at 5.0 x 10^{-4} M; b) Spectra obtained by subtracting the spectrum of the dimer without any added KBr from the spectra with KBr; note that the absorption at $\lambda_{max} \approx$ 390 – 455 nm clearly increases with added KBr.

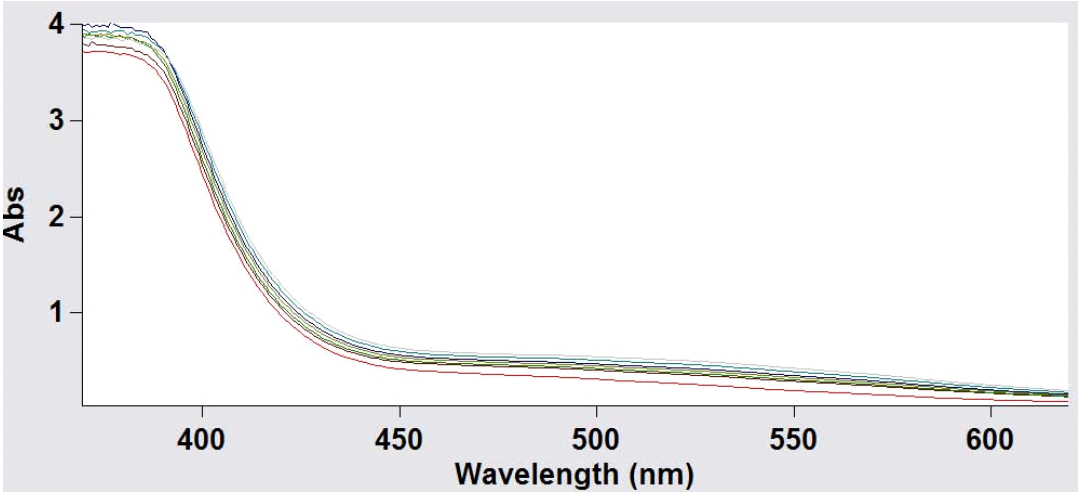

(a)

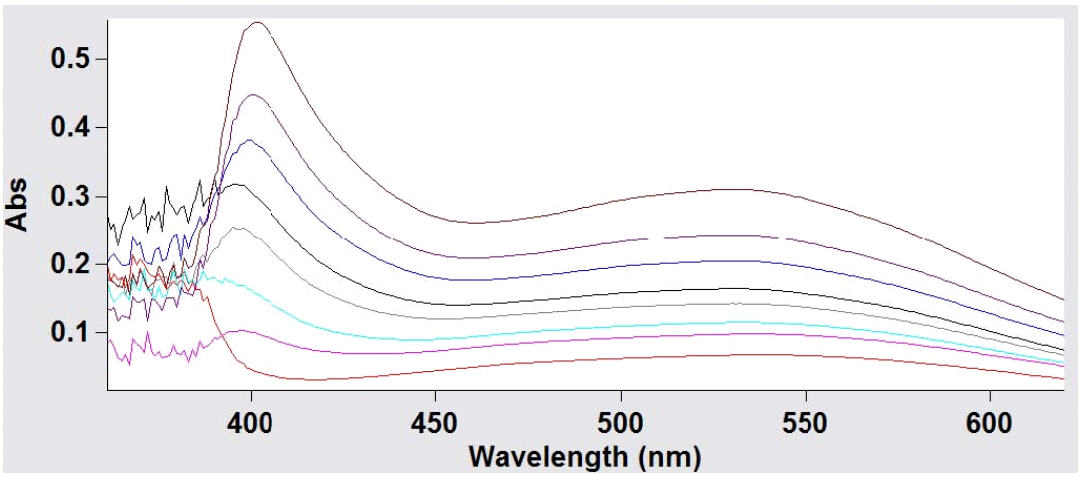

(b)

Figure 2.47 a) Absolute UV-Vis (*vs.* water only) spectra generated by adding KI (conc. of I^- ranges from 0.002 to 0.2 M) to the decaammine BPE dimer with [Ru^{III}-Ru^{III}] at 5.0 x 10^{-4} M; b) Spectra obtained by subtracting the spectrum of the dimer without any added KI from the spectra with KI; note that the IPCT absorption at $\lambda_{max} \approx$ 390 – 440 nm clearly increases with added KI, but the MLCT of the generated trace product II,III dimer partially obscured it.

Table 2.16 UV-Vis absorption values at the observed IPCT $\lambda_{max}^{(a)}$ positions from spectra obtained from the Ru^{III}-Ru^{III} BPE dimer in the presence of added halides. The presumed absorbing species is the [6+,X-] (where 6+ is the BPE dimer)

$[Cl^-]$ M	Abs (Cl^-) (at 401 nm)	$[Br^-]$ M	Abs (Br^-) (at 401 nm)	$[I^-]$ M	Abs (I^-) (at 402 nm)
4.00e-3	0.0230	1.00e-3	0.0228	2.00e-3	0.0264
5.00e-3	0.0280	2.00e-3	0.0436	4.00e-3	0.0751
8.00e-3	0.0391	3.00e-3	0.0400	8.00e-3	0.1285
0.018	0.0560	4.00e-3	0.0594	0.016	0.2054
0.032	0.0722	8.00e-3	0.0753	0.032	0.2594
0.060	0.1000	0.010	0.0900	0.064	0.3262
0.100	0.1231	0.016	0.1327	0.100	0.3885
0.150	0.1480	0.050	0.2490	0.200	0.4825
0.200	0.1638	0.080	0.3118	2.00e-3	0.0264
0.200	0.1680	0.080	0.3000	4.00e-3	0.0751
0.250	0.1800	0.120	0.3530	8.00e-3	0.1285
0.300	0.2012	0.160	0.3973	0.016	0.2054
0.400	0.2139	0.200	0.4400	0.032	0.2594
0.500	0.2224	0.240	0.4738	0.064	0.3262
		0.032	0.1892		
		0.320	0.4940		

		0.400	0.5244		

a) As noted in the text, these are not true λ_{max} values for the IPCT bands, but rather points on the sides of them not overlappings with the strong π-π* bands of the III,III dimer alone.

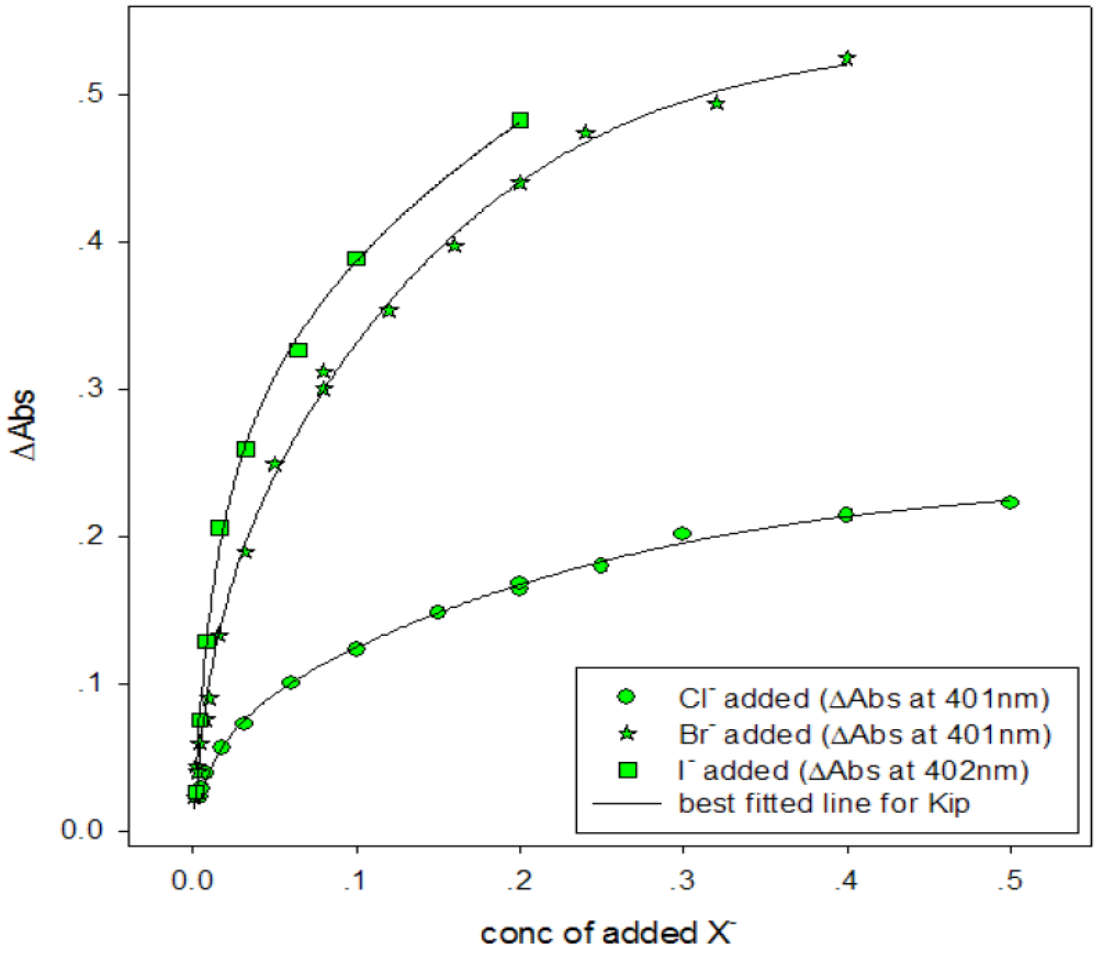

Figure 2.48 IPCT absorbance values from Table 2.16 for the Ru^{III}-Ru^{III} BPE dimer and added Cl^-, Br^- and I^-; the presumed absorbing species is then [6+,X-] (where 6+ is the Ru^{III}-Ru^{III} BPE dimer). The best fitted lines with K_{ip} = 80.0 ± 2.7 for KCl, 88.2 ± 4.5 for KBr and 106 ± 9.3 for KI are obtained using Eq. 2.14 with B term = 2.33, 3.47 and 1.35 respectively.

Table 2.17 Measured Kip by fitting plots in Figure 2.48 *vs.* calculated K_{ip} from Eigen-Fuoss equations (Eq. 2-14) for Ru^{III}-Ru^{III} BPE dimer with X^-.

	Kip (calculated at μ≈0 with [6+, 1-])	**Kip** (calculated at μ≈0 with [4.5+, 1-])	**Kip** (from fitting with "BI" term)	**Kip** (from fitting with "B=1")
Cl-	357	82	80. 0 ± 2.7 (Dex = 477 ± 5) (B = 2.33)	68 ± 6 (Dex = 637 ± 25)
Br-	344	81	88.2 ± 4.5 (Dex = 1077 ± 11) (B = 3.47)	67 ±7 (Dex = 1634 ± 81)
I-	320	78	106 ± 9.3 (Dex = 1433 ± 62) (B = 1.35)	94 ± 9 (Dex = 1583 ± 84)

a) Dex is the best-fit difference between the molar extinction coefficients for the ion pair solutions and the constituent Ru^{III}-Ru^{III} and X^- ions alone; b) the radius of the BPE Ru^{III}-Ru^{III} 6+ ion was taken as 5.47 Å (Calculated using the volume = tight option within Gaussiuan 03W[59] with the 6-31 + g(d,p)/ sdd basis set and optimizations done with the BHANDH functional,[59] *vide infra*), Cl^- as 1.90 Å, Br^- as 2.0 Å and I^- as 2.2 Å.[49]

According to Waysbort[48] the B term (see Eq. 2-50) is approximately equal to 1, thus we can fit the curves using a fixed B value (=1). However, we can get better fits by varying the B values (see Table 2.17). The calculated K_{ip} values from Eigen-Fuoss equations are also listed in the tables. We can see that by assuming the Ru^{III}-Ru^{III} dimer is a sphere with charge 6+ in the Eigen-Fuoss calculation, we arrive at very different K_{ip} values as compared with the measured K_{ip}. By putting a more reasonable charge (which can be considered as an

effective charge when interacting with halides) such as 4.5+ for Ru^{III}-Ru^{III} dimer, then the K_{ip} calculated values agree much better with the measured K_{ip}.

From Table 2.15, we can see the K_{ip} values for $(NH_3)_5Ru^{III}$3Fpy monomer with added Cl^- and Br^- are much closer to the calculated K_{ip} values obtained from Eigen-Fuoss equations than in the case for the measurement of the BPE (III,III) dimer. This confirms our hypothesis that the BPE (III,III) dimer does not behave as 6+ point charge when interacting with halides. We will try to consider this factor and make an approximation of the charges on various redox states of the dimer in the later kinetic simulation section.

Kinetic Simulation of Salt Effects on ET of Comproportionation Reaction (2) and Mechanistic Implications

Computational kinetic simulation of the observed ET reaction kinetic traces using an assumed mechanistic scheme or model can provide insight regarding which mechanisms are most plausible and allow for quantitative estimates of the rate constants for the individual elemental steps within a given or proposed ET mechanistic model. In our case, we are interested to understand the rate enhancement observed with added electrolytes in the context of schemes like the one shown in the general pre-equilibrium scheme shown in equation (2-7). Extensive kinetic modeling work along these lines using the Specfit software written by Binstead[51] has been carried out for monomer reaction (1) as described by Inagaki[12c,36] and Sista.[41] Details of the procedure and instructions for operation of the software will not be described in this section. Based on their

work, we have found that it is generally possible to obtain successful matches between simulation and experiment using three parallel ET pathways as shown in Scheme 2.1 below on dimer comproportionation reaction (2),

Scheme 2.1 Three pathway model involving association/dissociation and ET reaction steps for direct (Pathway One), singly-ion paired (Pathway Two) and doubly-ion Paired (Pathway Three) reactions.

Pathway One (Simple Encounter, see equation 2-7)

$$[Ru^{II}\text{-L-}Ru^{II}]^{4+} + [Ru^{III}\text{-L-}Ru^{III}]^{6+} \underset{k_{d1}}{\overset{k_{a1}}{\rightleftharpoons}} [Ru^{II}\text{-L-}Ru^{II}, Ru^{III}\text{-L-}Ru^{III}]^{10+} \quad (1)$$

$$[Ru^{II}\text{-L-}Ru^{II}, Ru^{III}\text{-L-}Ru^{III}]^{10+} \underset{k_{-et}}{\overset{k_{et}}{\rightleftharpoons}} [Ru^{II}\text{-L-}Ru^{III}, Ru^{II}\text{-L-}Ru^{III}]^{10+} \quad (2)$$

$$[Ru^{II}\text{-L-}Ru^{III}, Ru^{II}\text{-L-}Ru^{III}]^{10+} \underset{k_{a2}}{\overset{k_{d2}}{\rightleftharpoons}} 2\ [Ru^{II}\text{-L-}Ru^{III}]^{5+} \quad (3)$$

Pathway Two (Single Anion Catalysis)

$$[Ru^{III}\text{-L-}Ru^{III}]^{6+} + X^{-} \underset{k_{d3}}{\overset{k_{a3}}{\rightleftharpoons}} [Ru^{III}\text{-L-}Ru^{III}, X^{-}]^{5+} \quad (4)$$

$$[Ru^{III}\text{-L-}Ru^{III}, X^{-}]^{5+} + [Ru^{II}\text{-L-}Ru^{II}]^{4+} \underset{k_{d4}}{\overset{k_{a4}}{\rightleftharpoons}} [Ru^{III}\text{-L-}Ru^{III}, X^{-}, Ru^{II}\text{-L-}Ru^{II}]^{9+} \quad (5)$$

$$[Ru^{III}\text{-L-}Ru^{III}, X^-, Ru^{II}\text{-L-}Ru^{II}]^{9+} \underset{k_{-etx}}{\overset{k_{etx}}{\rightleftharpoons}} [Ru^{III}\text{-L-}Ru^{II}, X^-, Ru^{III}\text{-L-}Ru^{II}]^{9+} \quad (6)$$

$$[Ru^{III}\text{-L-}Ru^{II}, X^-, Ru^{III}\text{-L-}Ru^{II}]^{9+} \underset{k_{a5}}{\overset{k_{d5}}{\rightleftharpoons}} [Ru^{II}\text{-L-}Ru^{III}, X^-]^{4+} + [Ru^{II}\text{-L-}Ru^{III}]^{5+} \quad (7)$$

$$[Ru^{II}\text{-L-}Ru^{III}, X^-]^{4+} \underset{k_{a6}}{\overset{k_{d6}}{\rightleftharpoons}} [Ru^{II}\text{-L-}Ru^{III}]^{5+} + X^- \quad (8)$$

Pathway Three (Double Anion Catalysis)

$$[Ru^{III}\text{-L-}Ru^{III}, X^-]^{5+} + X^- \underset{k_{d7}}{\overset{k_{a7}}{\rightleftharpoons}} [X^-, Ru^{III}\text{-L-}Ru^{III}, X^-]^{4+} \quad (9)$$

$$[Ru^{II}\text{-L-}Ru^{II}]^{4+} + X^- \underset{k_{d8}}{\overset{k_{a8}}{\rightleftharpoons}} [Ru^{II}\text{-L-}Ru^{II}, X^-]^{3+} \quad (10)$$

$$[Ru^{II}\text{-L-}Ru^{II}]^{4+} + [X^-, Ru^{III}\text{-L-}Ru^{III}, X^-]^{4+} \underset{k_{d10}}{\overset{k_{10}}{\rightleftharpoons}} [Ru^{II}\text{-L-}Ru^{II},(X^-)_2, Ru^{III}\text{-L-}Ru^{III}]^{8+} \quad (11)$$

$$[Ru^{II}\text{-L-}Ru^{II}, X^-]^{3+} + [Ru^{III}\text{-L-}Ru^{III}, X^-]^{5+} \underset{k_{d11}}{\overset{k_{a11}}{\rightleftharpoons}} [Ru^{II}\text{-L-}Ru^{II},(X^-)_2, Ru^{III}\text{-L-}Ru^{III}]^{8+} \quad (12)$$

$$[Ru^{II}\text{-L-}Ru^{II},(X^-)_2, Ru^{III}\text{-L-}Ru^{III}]^{8+} \underset{k_{-etxx}}{\overset{k_{etxx}}{\rightleftharpoons}} [Ru^{II}\text{-L-}Ru^{III},(X^-)_2, Ru^{II}\text{-L-}Ru^{III}]^{8+} \quad (13)$$

$$[Ru^{II}\text{-L-}Ru^{III},(X^-)_2, Ru^{II}\text{-L-}Ru^{III}]^{8+} \underset{k_{a12}}{\overset{k_{d12}}{\rightleftharpoons}} 2\ [Ru^{II}\text{-L-}Ru^{III}, X^-]^{4+} \quad (14)$$

where $[Ru^{III}\text{-L-}Ru^{III}]^{6+}$ refers to the BPE [Ru^{III}, Ru^{III}] dimer (and so on), and X^- is the anion of the added salt under investigation.

Pathway one is relevant to the case of direct bimolecular reaction of $[Ru^{II}\text{-L-}Ru^{II}]^{4+}$ and $[Ru^{III}\text{-L-}Ru^{III}]^{6+}$ when there is only the electrostatic repulsion effect between the ruthenium reactants to give rise to any ionic strength (or GP) effect on rate. Pathway Two is relevant to the single ion-pair formation case where now the species $[Ru^{III}\text{-}Ru^{III},X]^{5+}$ also contributes to the observed ET rate. Pathway Three is relevant at high $[X^-]$ where it is possible for the specie $[Ru^{III}\text{-}Ru^{III},X_2]^{4+}$ to exist at significant (meaning kinetically relevant) concentrations along the way. It is also possible to incorporate other routes (besides the ones written above, steps 9, 11 and 12) into Pathway Three which result in formation of $[Ru^{III}\text{-}Ru^{III},X_2$, $Ru^{II}\text{-}Ru^{II}]^{8+}$ or "pcxx" (*vide infra*), but earlier work by Sista has shown that no significant changes in the best-fit values of k_{etxx} result from doing so.[41]

Importantly, all the association rate constants k_a for these pathways can be calculated (as a function of ionic strength) by the Debye-Smoluchoswski equations (Eq. 2-12) and the dissociation rate constants k_d can also be calculated as a function of ionic strength from the Debye-Eigen equations (Eq. 2-13). In calculation of these rates, we have made the simplifying assumption that the radii of the ru22, ru23 and ru33 dimers are equal at a value of 5.47 Å (sphere of equal volume radius a_0 + X as calculated).

The pathways in Scheme 2.1 are inputted into Specfit using the condensed notation shown in Figure 2.49. Of primary interest in our modeling work, we are trying to find the optimum values of k_{et}, k_{etx} and k_{etxx} which, when combined with the ionic strength-dependent k_a and k_d values, will reproduce our experimental

kinetic salt effects. Note that as we have discussed in the previous section on ion pairing, calculating the k_a, k_d rate constants with the Debye-Smoluchoswski and Debye-Eigen equations for the dimer might be risky and introduce large errors into the calculation if we were to assume that the dimer can be approximated as a spherical charge distribution containing the nominal overall charges of 6+ for the Ru^{III}-Ru^{III}, 5+ for Ru^{III}-Ru^{II} and 4+ for Ru^{II}-Ru^{II}. Our attempts to model the experimental rate data using the nominal charges at each of the k_a, k_d kinetic steps in the simulation failed. However, as with the K_{ip} measurement experiments in the previous section, we found that good fits with reasonable k_{et}, k_{etx} and k_{etxx} values could be obtained by adjusting overall charges on the 6+, 5+ and 4+ BPE dimers by the same multiplicative factor of 0.75 to 4.5+, 3.75+ and 3+ in our kinetic simulations.

Table 2.18 lists the radii of the various ions used in the kinetic simulations. The simulated overall rate constants at each GP value (arising from the reactants and any added salt) for each of the different added salts are listed in Tables 2.19 and 2.20. The best-fit rate constants for the k_{et}, k_{etx} and k_{etxx} ET steps within the presumed binary, ternary and quaternary association complexes are listed in Table 2.20. Figures 2.50 to 2.55 show the best-fit simulated kinetic data (open symbols) compared with the experimental data plotted (black circles) as $\log k_{ex}$ *vs.* GP.

Figure 2.49 Inputted format of Scheme 2.1 in Specfit software written by Dr. R. A. Binstead[52] using the condensed notation for the cases of simple encounter (Pathway 1-1), single anion catalysis (Pathway 1-2) and double anion catalysis (Pathway 1-3); where ru22 is $[Ru^{II}\text{-L-}Ru^{II}]^{4+}$, ru23 is $[Ru^{II}\text{-L-}Ru^{III}]^{5+}$ and ru33 is $[Ru^{III}\text{-L-}Ru^{III}]^{6+}$; X is corresponding halide; pc, sc, pcx, scx, pcxx, scxx are the corresponding precursor and successor complexes.

Pathway 1-1:

1	ru22 + ru33 --> pc	ka1
2	pc --> ru22 + ru33	kd1
3	pc --> sc	ket
4	sc --> pc	k-et
5	sc --> 2*ru23	kd2
6	2*ru23 --> sc	ka2

Pathway 1-2:

1	ru22 + ru33 --> pc	ka1
2	pc --> ru22 + ru33	kd1
3	pc --> sc	ket
4	sc --> pc	k-et
5	sc --> 2*ru23	kd2
6	2*ru23 --> sc	ka2
7	ru33 + x --> ru33x	ka3
8	ru33x --> ru33 + x	kd3
9	ru22 + ru33x --> pcx	ka4
10	pcx --> ru22 + ru33x	kd4
11	pcx --> scx	ketx
12	scx --> pcx	k-etx

13	scx --> ru23 + ru23x	kd5
14	ru23 + ru23x --> scx	ka5
15	ru23x --> ru23 + x	kd6
16	ru23 + x --> ru23x	ka6

Pathway 1-3:

1	ru22 + ru33 --> pc	ka1
2	pc --> ru22 + ru33	kd1
3	pc --> sc	ket
4	sc --> pc	k-et
5	sc --> 2*ru23	kd2
6	2*ru23 --> sc	ka2
7	ru33 + x --> ru33x	ka3
8	ru33x --> ru33 + x	kd3
9	ru22 + ru33x --> pcx	ka4
10	pcx --> ru22 + ru33x	kd4
11	pcx --> scx	ketx
12	scx --> pcx	k-etx
13	scx --> ru23 + ru23x	kd5
14	ru23 + ru23x --> scx	ka5
15	ru23x --> ru23 + x	kd6
16	ru23 + x --> ru23x	ka6
17	x + ru33x --> ru33xx	ka7
18	ru33xx --> x + ru33x	kd7
19	ru22 + x --> ru22x	ka8
20	ru22x --> ru22 + x	kd8
21	ru22 + ru33xx --> pcxx	ka10

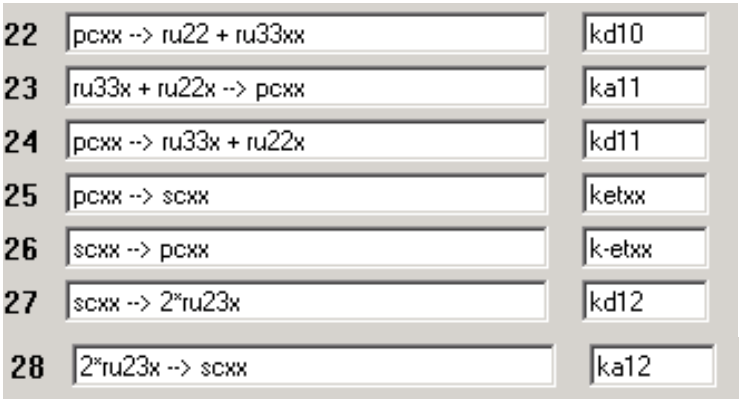

Table 2.18 Radii of the ions used in the kinetic simulation for reaction (2).

Ion	Radius (A)	Ion	Radius (A)
Ru^{III}-BPE-Ru^{III}	5.47[a]	Br^-	2.00[b]
$(NH_3)_5Ru^{III}3Fpy$	4.37[a]	I^-	2.20[b]
F^-	1.50[b]	$adipate^{2-}$	3.94[a]
Cl^-	1.90[b]	$muconate^{2-}$	3.82[a]

a) Calculated using the volume = tight option within Gaussiuan 03W[59] with the 6-31 + g(d,p)/ sdd basis set and optimizations done with the BHANDH functional; b) see ref. by Jacob Kielland.[49]

Table 2.19 Specfit simulation results for reaction (2) in the presence of added halides at reactant's concentration of 1.0 x 10^{-4} M. (see Table 2.20 for k_{et}, k_{etx} and k_{etxx} summary)

KF; k_{et} = 7.8 x 10^5 , k_{etx} = 6.5 x 10^5 , k_{etxx} = N/A			
GP	Experimental logk_{ex}	logk_{ex} (PW 1-2)	

0.0527	3.188±0.064	3.188	
0.0588	3.300±0.060	3.305	
0.0667	3.424±0.055	3.439	
0.0777	3.594±0.050	3.598	
0.0871	3.707±0.042	3.716	
0.0953	3.810±0.050	3.809	
0.1094	3.991±0.056	3.960	

KCl; k_{et} = 7.8 x 10^5 , k_{etx} = 2.1 x 10^6 , k_{etxx} = 1.3 x 10^7

GP	Experimental $logk_{ex}$	$logk_{ex}$ (PW 1-2)	$logk_{ex}$ (PW 1-3)
0.0527	3.188±0.064	3.113	3.184
0.0588	3.476±0.080	3.363	3.466
0.0667	3.802±0.059	3.621	3.799
0.0777	4.170±0.041	3.913	4.155
0.0871	4.417±0.035	4.123	4.387
0.0953	4.595±0.030	4.350	4.556
0.1094	4.885±0.031	4.542	4.742

KBr; k_{et} = 7.8 x 10^5 , k_{etx} = 2.8 x 10^6 , k_{etxx} = 2.5 x 10^7

GP	Experimental $logk_{ex}$	$logk_{ex}$ (PW 1-2)	$logk_{ex}$ (PW 1-3)
0.0527	3.188±0.064	3.188	3.188
0.0588	3.582±0.080	3.583	3.559

0.0667	3.941±0.080	3.869	3.979
0.0777	4.365±0.088	4.135	4.400
0.0871	4.665±0.057	4.304	4.666
0.0953	4.882±0.048	4.428	4.855
0.1094	5.217±0.038	4.637	5.120
KI; k_{et} = 7.8 x 10^5 , k_{etx} = 3.9 x 10^6 , k_{etxx} = 4.5 x 10^7			
GP	Experimental logk_{ex}	logk_{ex} (PW 1-2)	logk_{ex} (PW 1-3)
0.0527	3.188±0.064	3.188	3.188
0.0588	3.659±0.100	3.655	3.653
0.0667	4.090±0.097	3.963	4.160
0.0777	4.570±0.102	4.240	4.620
0.0871	4.889±0.081	4.414	4.897
0.0953	5.138±0.050	4.541	5.092
0.1094	5.493±0.034	4.724	5.360

Table 2.20 Specfit simulation results for reaction (2) in the presence of added $adip^{2-}$ and muc^{2-} at reactant's concentration of 1.0 x 10^{-4} M.

adipate^{2-}; k_{et} = 7.8 x 10^5 , k_{etx} = 6.6 x 10^6 , k_{etxx} = 1.2 x 10^6			
GP	Experimental logkex	logk_{ex} (PW 1-2)	logk_{ex} (PW 1-3)
0.0527	3.188±0.064	3.188	3.188

0.0559	3.753	3.790	3.850
0.0667	4.551	4.300	4.640
0.0777	4.954	4.500	4.930
0.0953	5.298	4.700	5.230
0.1319	5.519	4.900	5.540
0.1799	5.743	5.150	5.720

muconate^{2-}; k_{et} = 7.8 x 10^5 , k_{etx} = 2.2 x 10^6 , k_{etxx} = 1.2 x 10^7				
GP	Experimental $logk_{ex}$	$logk_{ex}$ (PW 1-2)	$logk_{ex}$ (PW 1-3)	$logk_{ex}$ (PW 1-3) (with muc- and half V)
0.0535	3.667	3.687	3.740	3.920
0.0559	4.402	4.150	4.440	4.500
0.0588	4.932	4.400	4.931	4.860
0.0667	5.566	4.700	5.510	5.350
0.0777	5.910	4.880	5.875	5.810
0.0871	6.010	5.000	6.045	6.050
0.0953	6.090	5.070	6.150	6.210

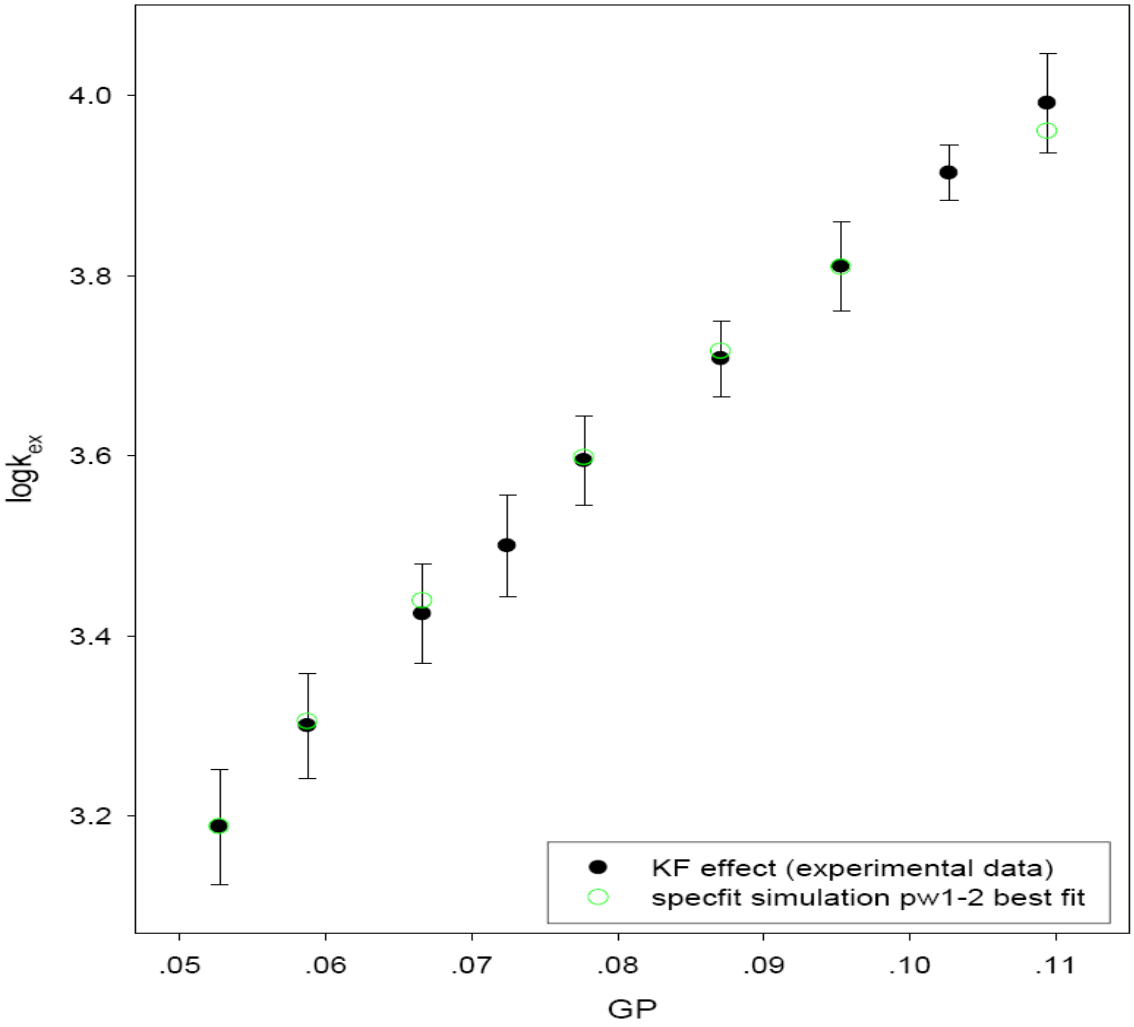

Figure 2.50 Results from modeling the kinetic data for reaction (2) at reactant's concentration of 1.0 x 10^{-4} M with added KF; experimental data = filled black circles; best fit kinetic simulation obtained using pathways One and Two = open green circles.

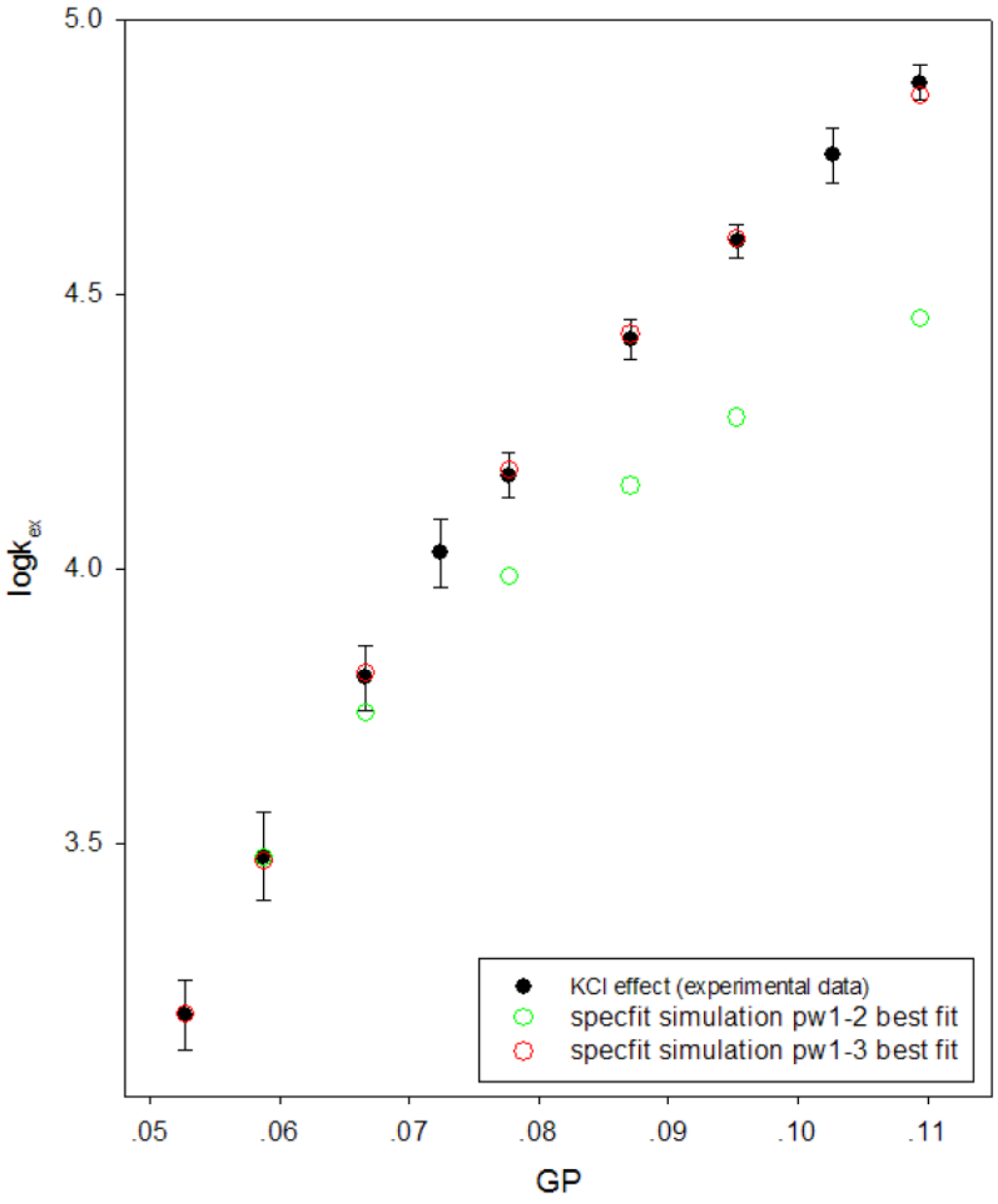

Figure 2.51 Results from modeling the kinetic data for reaction (2) at reactant's concentration of 1.0 x 10^{-4} M with added KCl; experimental data = filled black circles; best fit kinetic simulation obtained using pathways One and Two = open green circles; best fit simulation obtained using pathways One, Two and Three = open red circles.

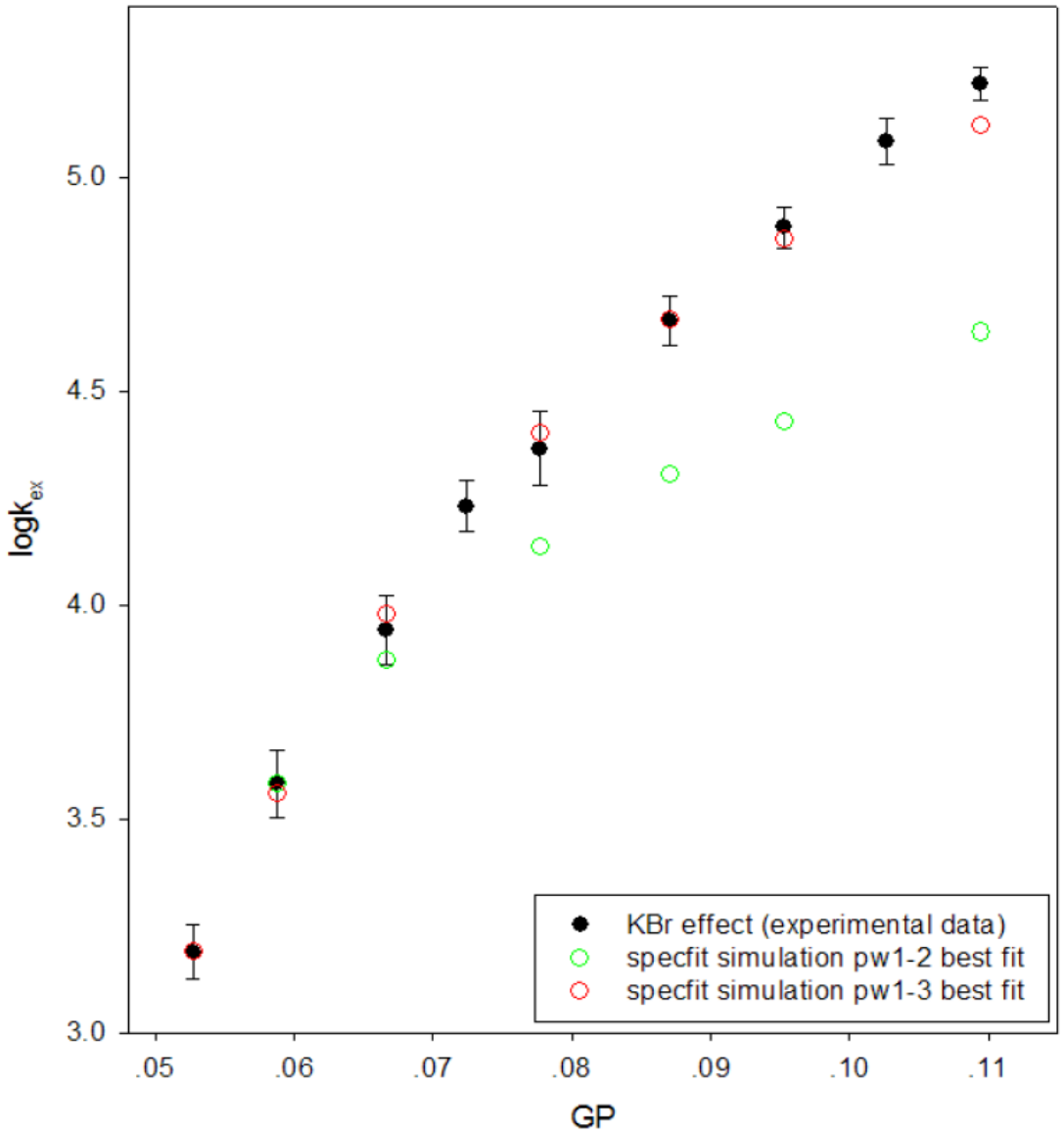

Figure 2.52 Results from modeling the kinetic data for reaction (2) at reactant's concentration of 1.0 x 10^{-4} M with added KBr; experimental data = filled black circles; best fit kinetic simulation obtained using pathways One and Two = open green circles; best fit simulation obtained using pathways One, Two and Three = open red circles.

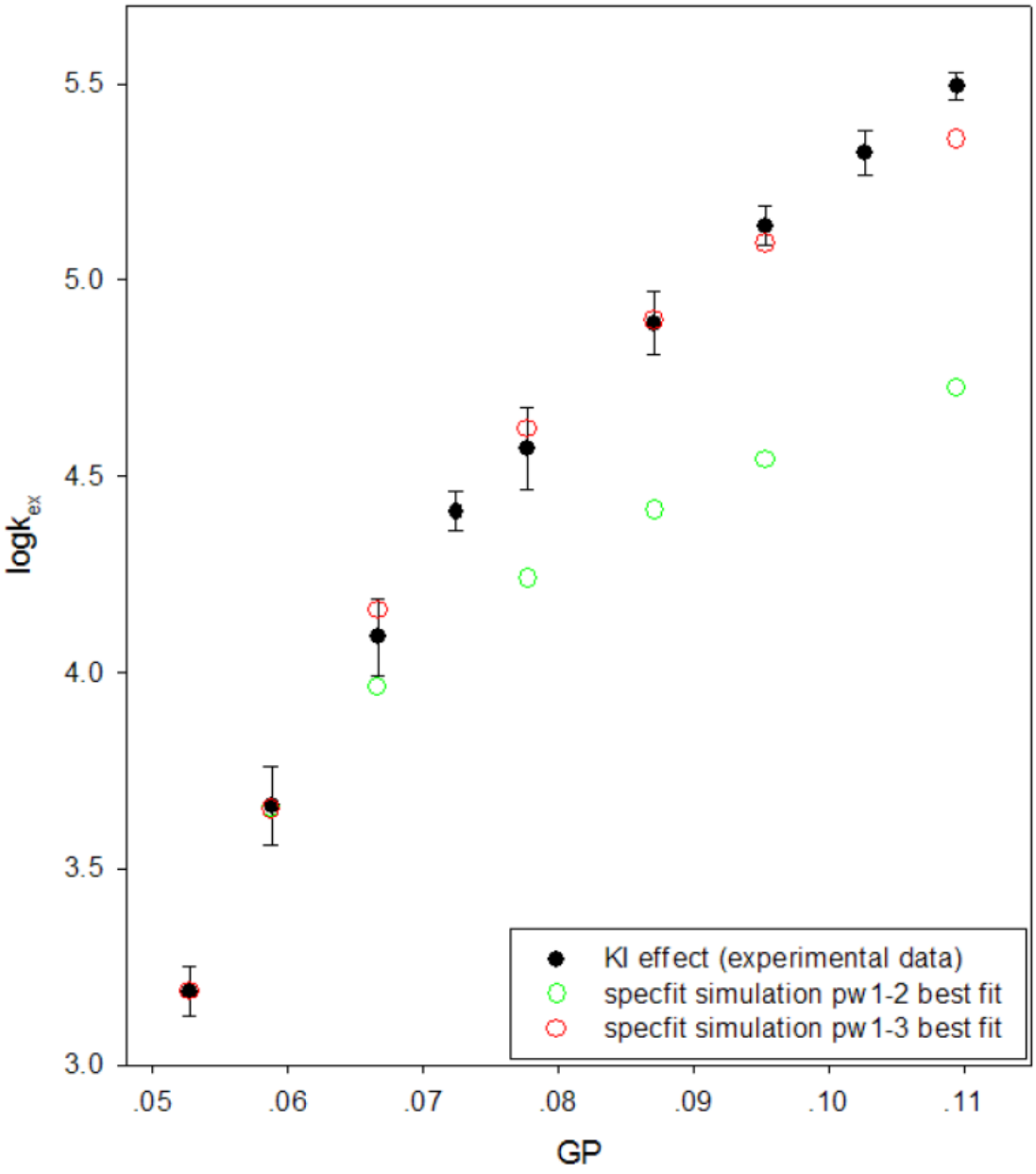

Figure 2.53 Results from modeling the kinetic data for reaction (2) at reactant's concentration of 1.0 x 10^{-4} M with added KI; experimental data = filled black circles; best fit kinetic simulation obtained using pathways One and Two = open green circles; best fit simulation obtained using pathways One, Two and Three = open red circles.

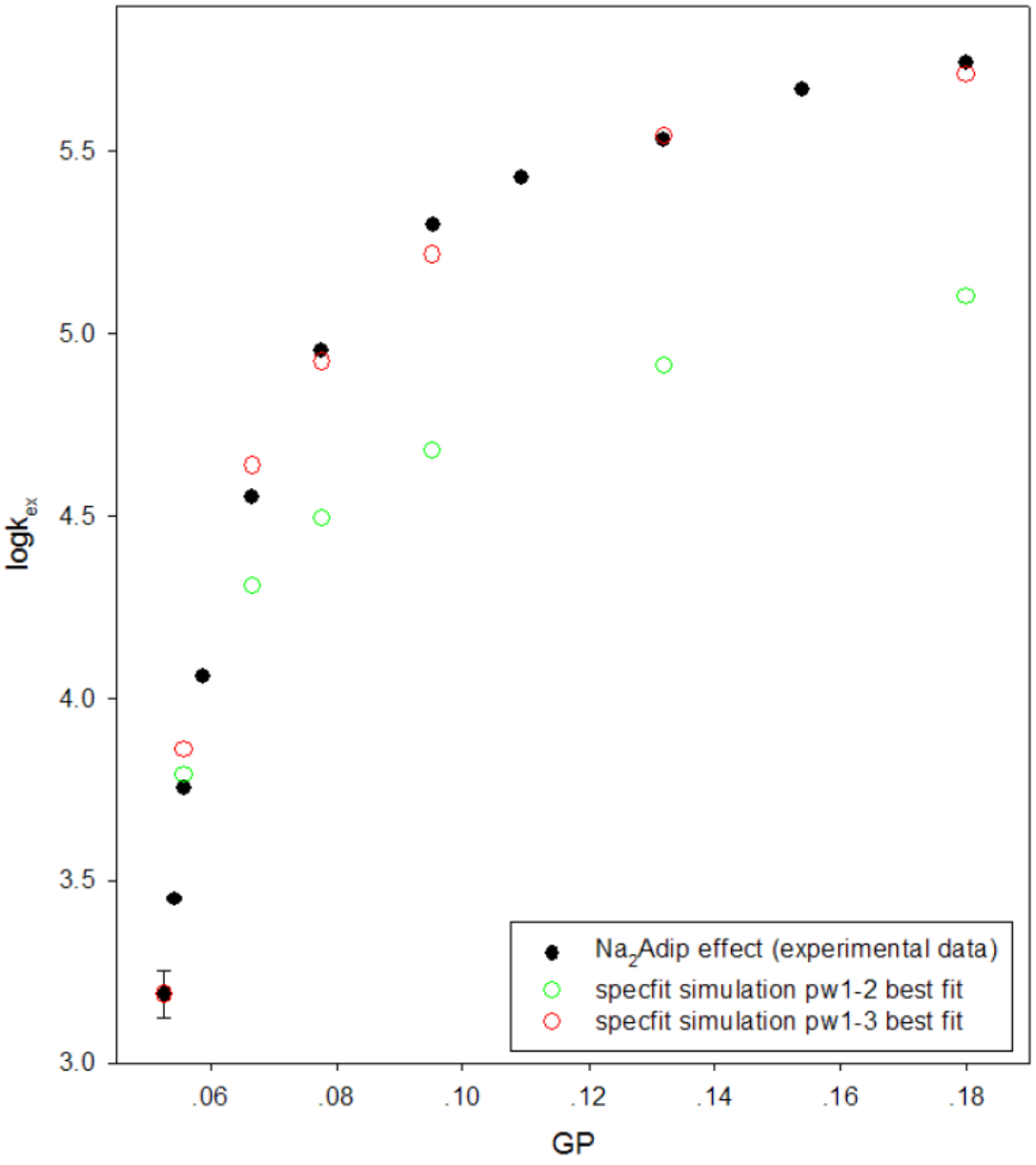

Figure 2.54 Results from modeling the kinetic data for reaction (2) at reactant's concentration of 1.0 x 10^{-4} M with added Na_2Adip; experimental data = filled black circles; best fit kinetic simulation obtained using pathways One and Two = open green circles; best fit simulation obtained using pathways One, Two and Three = open red circles.

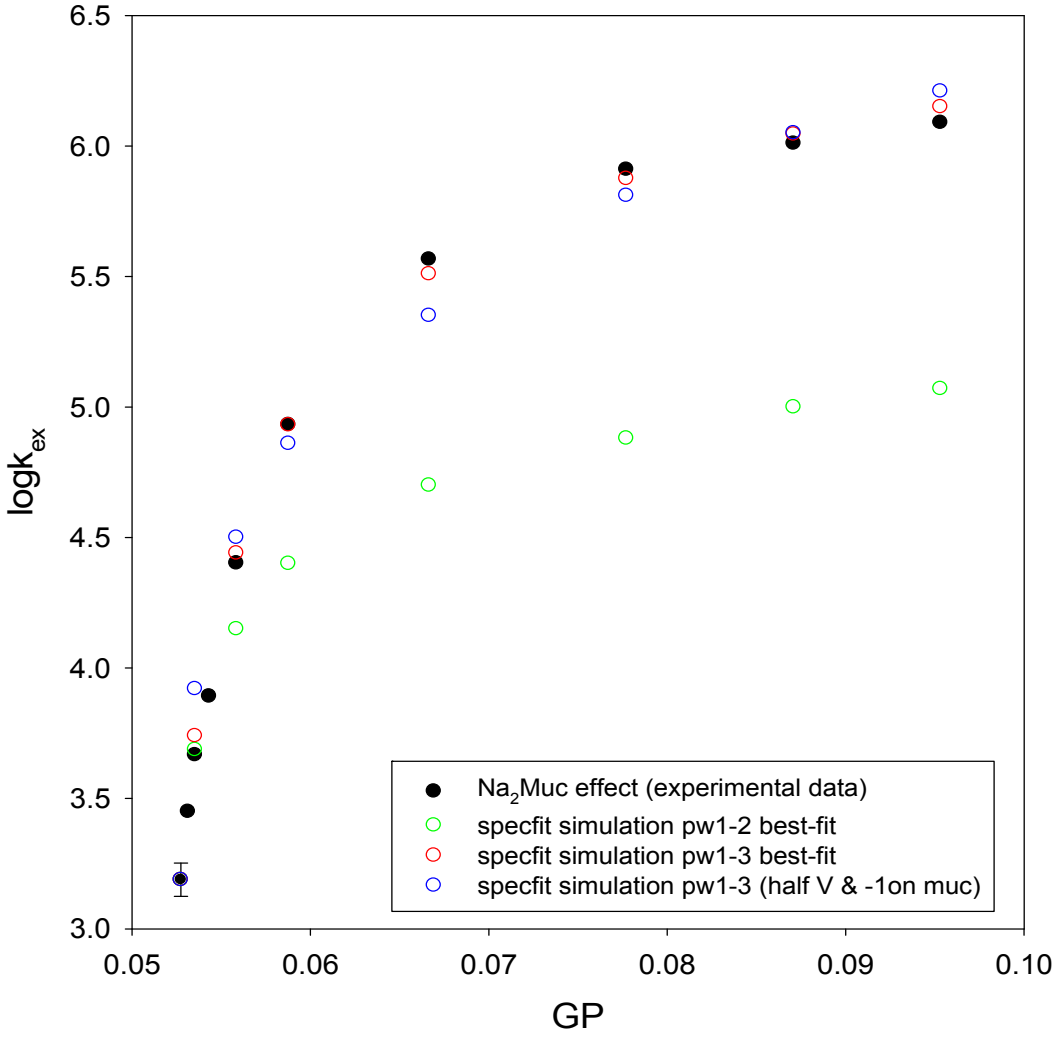

Figure 2.55 Results from modeling the kinetic data for reaction (2) at reactant's concentration of 1.0 x 10^{-4} M with added Na_2Muc; experimental data = filled black circles; best fit kinetic simulation obtained using pathways One and Two = open green circles; best fit simulation obtained using pathways One, Two and Three = open red circles; best fit simulation obtained using pathways One, Two and Three by assuming Muc as -1 charge and using half Muc volume in the rate constant calculation = open blue circles.

Table 2.21 k_{et}, k_{etx}, k_{etxx} values used when obtaining the best-fit from Specfit simulation for reaction (2) in the presence of added salts.

Added Electrolyte	k_{et}	k_{etx}	k_{etxx}
KF	7.8×10^5	6.5×10^5	N/A
KCl	7.8×10^5	2.1×10^6	1.3×10^7
KBr	7.8×10^5	2.8×10^6	2.5×10^7
KI	7.8×10^5	3.9×10^6	4.5×10^7
Na_2adip	7.8×10^5	6.6×10^5	1.2×10^6
Na_2muc	7.8×10^5	2.2×10^6	1.2×10^7
Na_2muc [a]	7.8×10^5	4.0×10^8	3.5×10^9

a) kinetic simulation with -1 charge and half volume for muconate ion

Plotting the first ionization potentials of the halides *vs.* the best-fit k_{etx} values from Spefit simulation (see Figure 2.56), we can see an almost linear relationship between them. As the ionization potential because larger upon going from I^- to F^-, meaning halides are getting more difficult to oxidize, the best-fit catalytic rate constant k_{etx} relevant to the assumed ternary association complex in our model is also seen to become smaller. This is consistent with what was observed by Sista for the monomer reaction (1).[41]

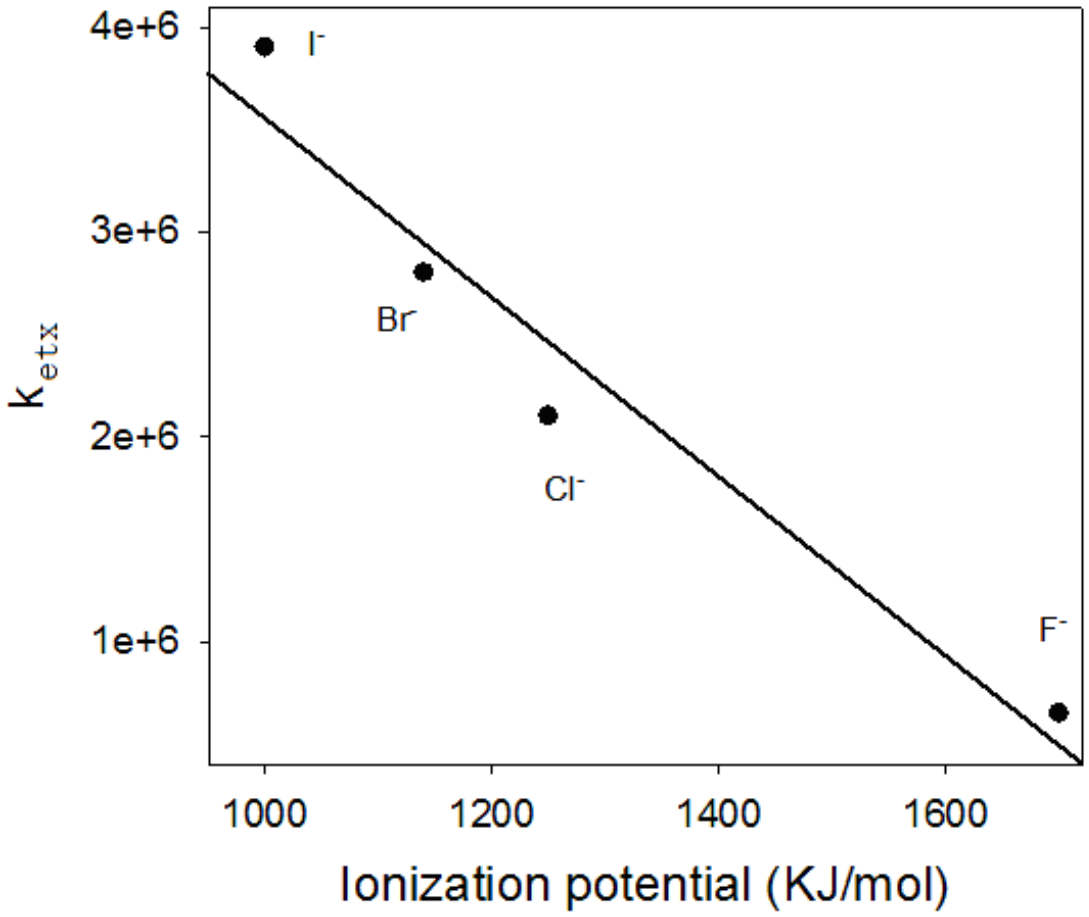

Figure 2.56 First ionization potential of the halogens plotted against k_{etx} values obtained from Specfit simulations.

For the (possibly) more ideal "point-charge" and "non-catalytic" (*vide infra*) anion F^-, we find that only pathway 1-2 (direct reaction and one ion-pair formation event between the $[Ru^{III}\text{-L-}Ru^{III}]^{6+}$ oxidant with a single F^-) is needed in order to arrive at a good fit of the experimental data for added KF (see Figure 2.50). When going to the heavier halides and the more-strongly catalytic salts ($adip^{2-}$ and muc^{2-}), pathways 1-3 (now also including double ion-pair formation between

reactants and anions so as to involve the quaternary encounter complex PCXX) are necessary in order to get a good fit to the experimental kinetic data. For the -1 charged anions, the ET rate constants within the presumed binary, ternary, and quaternary association complexes were found to increase in the order of $k_{et} < k_{etx} < k_{etxx}$ which agrees with previously reported results from this lab on monomer ET reactions.[36] However, from a close look at the k_{et}, k_{etx} and k_{etxx} values in Table 2.21, we can see that the k_{etx} value for $adip^{2-}$ is smaller than the k_{et} value. This result conflicts with the fact we have seen that added $adip^{2-}$ shows a strong catalytic effect on the experimental ET rates. Also, the k_{etx} value for muc^{2-} appears to be even smaller than those found for Br^- and I^- (very unlike the results found by Sista[41]). This led us to suspect that there might be some as-yet unaccounted for source of error within our kinetic modeling of the -2 charged catalytic anions.

Even though we have "corrected" the charges on the BPE dimers to plausible effective values for our kinetic simulations, the mechanism of how the dianions muc^{2-} and $adip^{2-}$ associate to the ruthenium dimers is still unclear. One limit is to assume that there is only one carboxylate group on each dianion forming the ion-pair with ruthenium but that the dianion can be modeled as a 2-charge in a sphere of volume a_0 as calculated by Gaussian (as was done by Sista in calculating the rate of each elemental association or dissociation step). Another plausible limit would be to assume since only *one end* of muc^{2-} is binding to the ruthenium dimer to form the ion-pair, then one might use half of the muc^{2-} dianion (-1 charge and half volume) in attempting to perform the simulation.

With this approximation we obtained larger k_{etx} and k_{etxx} values in a pattern more like the one found in SIsta's prior analysis of monomer reaction (1) without having to make this modification.[41] Even though this approach is based on a rather *ad-hoc* correction to the classical Debye-Huckel assumptions, it does appear to point towards a possible way forward in improving our kinetic modeling. It now also becomes clear that the modeling done by Sista needs to be repeated using this same half-dianion limit so that the monomer/dimer cases can be more fully compared.

Another possibility is that the dianions may ion pair with the dimers in a side-side fashion and thus present a very different case than the monomer systems (where an approximately spherical metal complex associates predominately with one end of the rigid muconate dianion but may or may not associate with both ends of the flexible adipate homolog). If this were to be the case, then the presumed ternary PCX species in our modeling scheme might be more accurately thought of as a "sandwich" structure held together by favorable electrostatic and H-bonding interaction (as contrasted to a more linear/series resistor type arrangement of monomer Ru^{II}–dianion–monomer Ru^{III} which might underlie the monomer catalytic action). In such a sandwich/parallel type of associative geometry, it might turn out that the "catalytic" effect of the dianion has more to do with their ability to ease association of the reactants than with their ability to facilitate electron (or hole) tunneling over distance. One striking difference between Sista's experimental results and our dimer cases described here is that now adipate is clearly a much better catalyst than any of the simple

salts (note Figures 2.30 and 2.31), whereas Sista's work with reaction (1) showed adipate to be only about as effective as KCl in speeding up the reaction (at a reactants concentration 1.0 x 10^{-4} M; see Sista's thesis, Figure 2.32, p. 148, and Figure 2.38, p. 162). This rather striking change (enhancement) of adipate's catalytic efficacy in the dimer case does suggest some kind of change in catalytic mechanism.

Conclusions

Our stopped-flow kinetic studies of electrolyte effects on dimer comproportionation reaction (2) have verified and extended the nature of known salt effects on electron-transfer reactions of ruthenium ammine dimeric complexes and shown a reactant's concentration or "self-salting" effect on the rate of reaction (2) similar to prior work in this lab.[41] In our case the observed $\log k_{ex}$ *vs.* GP slope for self-salting is 11.5 $\pm$ 0.3 (see Figure 2.19) which is in poor agreement with the predicted Debye-Huckel slope of 24.5 based on the nominal (+6)(+4) charge product (see equation 2.10). By altering the nominal 6+ and 4+ charge types to 4.5+ and 3+ using the measured K_{ip} values, however, the predicted slope based on the "effective" charges drops to 13.5 which is in much closes to the self-salting slope. Also in agreement with prior monomer work, we observe non-classical kinetic accelerations which deviate strongly from Debye-Huckle theory over a range of different added "inert" electrolytes. The observed catalytic effects with the heavier halides and the especially catalytic

dicarboxylates are again in agreement with a possible important role for hole-transfer superexchange in the ET reaction transition state complex.

We have quantitatively explored the hypothesis of catalytic ternary and quaternary association complexes, [Ru^{II}-L-Ru^{II}, X^-, Ru^{III}-L-Ru^{III}]$^{9+}$ and [Ru^{II}-L-Ru^{II}, $2X^-$, Ru^{III}-L-Ru^{III}]$^{8+}$, by doing kinetic modeling of the reaction. In fitting our experimental data, we find an increasing ratio of k_{etx} (the electron-transfer rate constant inside the presumed ternary association complex) to k_{et} (the rate constant inside the classical precursor complex) upon proceeding down the halide series (see Figure 2.56). Our measured activation parameters for comproportionation reaction (2) show a strong enthalpy-entropy compensation effect according to the identity of the added halide. Interestingly, the enthalpy of activation drops successively as we go to the heavier halides and in fact $\Delta H^{\ddagger}$ becomes negative in the most extreme case of added I^-. We ascribed this striking behavior to the enthalpy-entropy compensation effect in the formation of ternary association complexes.

Reference

1. Dill, K.A.; Bromberg, S. *Molecular Driving Forces*. Garland Science: NY, New York, **2003**
2. Robinson, R.A.; Stokes, R.H. *Electrolyte solutions, 2nd edit*. Dover Publications: Mineola, New York, **1959**
3. (a) Brown, G. M.; Sutin, N. *J. Am. Chem. Soc*. **1979**, *101*, 883

(b) N. Sutin, "Bioinorganic Chemistry", Vol. 2, G. L. Eichhorn, Ed., American Elsevier, New York, N.Y., **1973**, Chapter 19, p 611.

4. Chun, S. J.; Master's Thesis, University of San Francisco, **2001**

5. (a) Debye and Hűckel, *Physik. Z.*, **1923**, *24*, 185

   (b) Debye *ibid.*, **1924**, *25*,97

   (c) Debye, P. and Pauling, L. *J. Am. Chem. Soc.* **1925**, *47* (8), pp 2129–2134

6. (a) Sutin, N. *Acc. Chem. Res.* **1982**,*15*, 275

   (b) Brown, G. M.; Sutin, N. *J. Am. Chem. Soc*. **1979**, *101*, 883

7. Manov, G. G.; Bates, R. G., Hamer, W. J.; and Acree, S. F. *J. Am. Chem. Soc.* **1943**, *65*, 1765-1767.

8. Robinson, R. A. and Stokes, R. H. *Electrolyte Solutions. 2nd ed*. Butterworth & Co. Ltd., London. **1959**. 468.

9. (a) Bronsted, J. N. *Z. Phys. Chem*. **1922**, *102*,169-207.

   (b) Bronsted, J. N., *Z. Physic Chem*. **1925**, *115*, 337

10. (a) Bjerrum, N., *Z. Phys. Chem.* **1924**, *108*, 82-100.

    (b) Bjerrum, N., *Z. Phys. Chem.* **1926**, *118*, 251-254.

11. Koppenol, W. H., *BIOPHYS. J.* **1980**, *29*, 493-508

12. (a) Guggenheim, E.A.; Schindler, T. D. *J. Phys. Chem.* **1934**, *38* (4), 543–556

    (b) Guggenheim, E.A.; Turgen, J.C., *Trans Farady Soc*. **1955**, *15*, 747

    (c) Curtis, J. C.; Inagaki, M.; Chun, S. J.; Eskandari, V.; Luo, V. X.; Pan, N. Z.; Sankararaman, U.; Pengra, G. E.; Zhou, J.; Hailey, P.; Laurent, J.; Utalan, D. *Chem. Phys.* **2006**, *326*, 43

13. Smoluchowski, M. *Z. phys. Chem., Stoechiom. Verwandtschaftsl*. **1917**, *92*, 129

14. Debye, P. *Trans. Electrochem. Soc*. **1942**, *82*, 265

15. Eigen, M. *Z. Phys. Chem. (Munich)* **1954**, *1*, 176

16. Fuoss, R. M. *J. Am. Chem. Soc.* **1958**, *80*, 5059

17. (a) Chirboli, C., Indelli, M. T., Rampi Scandola, M.A., Scandola, F. *J. Phys. Chem*. **1988**, *92*, 156

    (b) Chirboli, C.,Scandola, F.; Kisch, F. *J. Phys. Chem*. **1986**, *90*, 2211

18. Sutin, N. *Prog. Inorg. Chem.* **1983**, *30*, 441

19. Olson, A. R.; Simonson, T. R. *J. Chem*. *Phys*. **1949**, *17*, 1167

20. (a) Clark, C.D. and Hoffman, M.Z. *J. Chem*. *Phys*. **1996**, *100*, 7526-7532

    (b) Clark, C.D. and Hoffman, M.Z. *Coord. Chem. Rev.* **1997**, *159*, 359

21. Rampi Scandola, M.A.; Scandola, F.; Indelli, *A. Faraday Trans. 1,* **1985**, *81*, 2967

22. Creaser, I.I.; Harrowfield, J. MacB.; Herlt, A.J.; Sargeson, A.M.; Springborg, J.; Geue, R.G.; Snow, M.R. *J. Am. Chem. Soc*. **1977**, *99*, 3181

23. Perlmutter-Hayman, B. *Progr. React. Kinet.* **1971**, *6*, 239

24. Chirboli, C., Indelli, M. T., Rampi Scandola, M.A., Scandola, F. *J. Phys. Chem*. **1988**, *92*, 156

25. Connors, K.A. *Chemical Kinetics,* VCH Pubilshers, Inc, **1990**

26. Anslyn, E. V.; Dougherty, D. A. *Modern Physical Organic Chemistry* University Science Books, **2006**, pp 365-373

27. Erying, H. *Chem. Rev.* **1935**, *17* (1), pp 65–77

28. Vogt, L. H.; Katz, J. S.; Wiberly, S. E. *Inorg. Chem.* **1965**, *4*, 1156

29. Baumann, J. A. Ph.D. Thesis, The University of North Carolina, Chapel Hill, **1978**.

30. Curtis, J.C.; Sullivan, B.P.; Meyer, T. *J. Inorg. Chem.* **1983**, *22*, 224

31. Sutton, J.; Taube. H. *Inorg. Chem.* **1981**, *20*, 3125

32. Blackbourn, R.; Hupp,, J. T. *J. Phys. Chem.* **1988**, *92*, 2817

33. Tom, G. M.; Creutz, C.; Taube, H. *J. Am. Chem. Soc.* **1974**, *96*, 7827

34. (a) Lewis, F. D.; Wu, T.; Zhang, Y.; Letsinger, R. L.; Greenfield, S.R.; Wasielewski, M. R. *Science* **1997**, 277, 673-676.

(b) Fukui, K.; Tanaka, K. *Angew. Chem., Int. Ed.* **1998**, 37, 158-161.

(c) Meggers, E.; Kusch, D.; Spichty, M.; Wille, U.; Giese, B. *Angew. Chem., Int. Ed.* **1998**, 37, 460-462.

35. Chun, S. J. Master's Thesis, University of San Francisco, **2001**

36. Inagaki, M. Master's Thesis, University of San Francisco, **2006**

37. Chen, P. Master's Thesis, University of San Francisco, in progress

38. IUPAC, *Compendium of Chemical Terminology*, 2nd ed. (the "Gold Book") (1997)

39. Van Valkenburg, M. E. *Network Analysis* (3rd edition ed.). pp. 383–384

40. Website: http://en.wikipedia.org/wiki/Gain

41. Sista. P. Master's Thesis, University of San Francisco, in progress

42. Pearson, R. G. "Kinetics and Mechanisms", 3rd ed.

43. Pladziewicz, J. R.; Lesniak, J. S.; Abrahamson, A. J. *J. Chem. Educ.* **1986,**

63, 850

44. King, E. L. *Int. J. Chem. Kinet.* **1982,** *14*, 1285

45. Marcus, Y. *Chem. Rev.* **2009**, *109*, 1346–1370

46. Abbas, Z. *et al. J. Phys. Chem. B* **2002**, *106*, 1403-1420

47. Cai, L.Z.; Kneeland, M, D.; Kirk, D. A.; *J. Phys. Chem. A* **1997**, *101*, 3871-3879

48. Waysbort, D.; Evenor, M. and Navon, G. *Inorg. Chem.* **1975**, *14*, 514

49. Kielland, J. *J. Am. Chem. Soc.* **1937**, *59*, 1675

50. Sexton, D.A.; Curtis, J.C.; Cohen, H. and Ford, P.C. *Inorg. Chem.* **1984**, 23, 49

51. Spectrum Software Associates (website). Available from <http://www.kromatek.co.uk/Specfit_Global_Analysis_129.asp>

52. Davies, C.W. *Ion Association*. London: Butterworths. **1962**, pp. 37–53

53. Atkins, P,; Overton, T.; Rourke, J.; Weller M.; Armstrong, F. *Inorganic Chemistry,* 4th ed.; Oxford, **2006**; p 27.

54. Liu, L.; Guo, Q. X. *Chem. Rev.* **2001**, 101, 673

55. Braddock, J.N.; Meyer, T.J. *J. Am. Chem. Soc.* **1973**, *95*, 3158

56. Reilly, T.J.; Burg, A.B. *Inorg. Chem.* **1974**, *13*, 1250

57. Fukuzumi, S.; Ohkubo, K.; Tokuda, Y.; Suenobu, T. *J. Am. Chem. Soc.* **2000**, *122*, 4286

58. Mader, E.A.; Larsen, A.S.; Mayer, J.M. *J. Am. Chem. Soc.* **2004**, *126*, 8067

59. Frisch, M.J. *et al.* Gaussian 03 Revision A.1, Gaussian Inc., Pittsburgh, PA, 2003.

Chapter Three

The Effects of Added Salts and Temperature Variations on the Inter-Valence Charge Transfer (IVCT) Bands of Mixed-Valence Dimeric Systems in Water

3.1 Introduction

Mixed-valence complexes containing two or more metal centers in different oxidation states have received intensive study over the past few decades.[1] Much of the focus in these studies has centered on the unique metal-to-metal charge-transfer (MMCT) or inter-valence charge-transfer (IVCT or IT) absorption band in which photon absorption essentially transfers an electron from one redox site to the other. Experimental characterization of the mixed-valence IVCT band and its relevance to the topic of ET in general was brought to prominence in the pioneering studies of the Creutz and Taube ion,[2] and later in related systems such as the 4,4' bipyridine-bridged diruthenium decaammine dimer.[1a] Trinuclear and tetranuclear transition metal complexes were also synthesized and had their IVCT band spectra studied and interpreted by Kneene and coworkers.[3] A general formulation of the IVCT "optical" ET process is shown below in equation 3-1,

$$[(NH_3)_5Ru^{III}\text{-}L_{br}\text{-}Ru^{II}(NH_3)_5]^{5+} \xrightarrow{h\nu} [(NH_3)_5Ru^{II}\text{-}L_{br}\text{-}Ru^{III}(NH_3)_5]^{5+*} \qquad (3\text{-}1)$$

where L_{br} is some "bridging ligand" such as pyrazine (Pz), 4,4′-dipyridylethylene (BPE) and 4,4′-dipyridyl (BPY) or 4-cyanopyridine (4CNP).

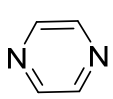

Pz

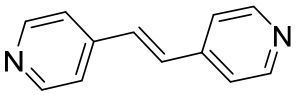

BPE

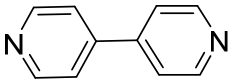

BPY

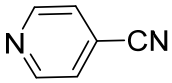

4CNP

The energy, intensity and shape of the IVCT absorption bands of binuclear complexes can be powerful tools for inferring details of the activation barrier relevant to the corresponding thermal intramolecular electron-transfer which must necessarily be taking place in these systems.[4] For a symmetrical mixed-valence system that contains the same metal center and coordinated ligands at each end, such as the $(NH_3)_5Ru^{II}$-L-$Ru^{III}(NH_3)_5$ example shown above (where L is the bridging ligand; L = BPE and BPY in our study), the thermodynamic driving force for the thermal ET reaction is necessarily zero, and there is thus no "0-0" energy gap for the optical ET process. This means that to a first-approximation, the IVCT band energy is a pure Franck-Condon energy which directly reflects the extent to which the ground-state nuclear coordinates are out of equilibrium with the excited-state electronic wave function after photon absorption (this level of approximation requires that we ignore minor corrections having to do with spin-orbit coupling effects at the Ru(III) center created in the IVCT excitation as well as small symmetry-induced splittings of the t_{2g} orbital set[5]). An IT transition of the type shown in equation 3-1 can at least be conceptualized (if not always measured) in the case of outer-sphere self-exchange ET process where the reorganization energy (λ) of the reaction would be equal to the optical ET energy

(E_{op} or E_{IT} relevant to the encounter or precursor complex discussed in chapter one, see figure 1-3). In favorable cases, E_{op} can be measured through UV-Vis-NIR spectroscopy and the actual reorganization energy of the intramolecular ET can be obtained if the IT band is well-separated from other electronic transition bands of the molecule. Extensive research has shown how λ responds to varying the inner-coordination sphere (including ligands and bridging ligand variations[6]) and the outer-coordination sphere (as with solvent,[7] temperature,[8] ionic strength[9] and counter ion variations[10]). All of these factors affect the energetics of the intramolecular ET process.

According to Hush,[4,11] the maximum absorbance ($E_{op} = h\nu_{\max} = hc/\lambda_{\max}$) of the IVCT band can be expressed in the following equation,

$$E_{op} = \lambda_{in} + \lambda_{out} + \Delta G^0 + \Delta E' \qquad (3\text{-}2)$$

where λ_{in} and λ_{out} are the inner- and outer-sphere reorganization energies (see chapter one for details), ΔG^0 is the free energy change associated with the thermal ET reaction (equal to 0 for a bimolecular self-exchange or a symmetrical intra-molecular ET process), and $\Delta E'$ reflects any additional energy contributed from spin-orbit coupling effects and ligand-field asymmetry (t_{2g} orbital non-degeneracy due to deviations from O_h symmetry at the metal center).[12]

Hupp and coworkers have found that the added SO_4^{2-} can first blue shift then red shift the IT band of some Fe and Ru dinuclear complexes in water.[13] Similar effects were also observed in mixed-solvent systems[5a] and with added

crown ethers[5g] on the IT band of the decaammine BPY dimer (as shown in eq. 3-1). They attributed these shifts to specific ion-pairing events which either destroyed or restored the end-to-end symmetry of the IT chromophore. We have recently discovered that added F^- and other halides can shift the IT bands of the L_{br} = BPY and 1,2-bis-bipyridylethylene (BPE) dimers in different directions depending on the identity of the halide (in water as solvent). We observe consistent blue shifts with added F^- salts, but consistent red shifts are obtained with the other halides. These novel salt effects on the IT band energy cannot be explained simply by considering some kind of transiently-induced ΔG^0 or 0-0 energy gap as was used by Hupp *et al.* in explaining their observations.

The work to be described in this chapter will show that our observed spectroscopic shifts are related to the fact that these different halides have demonstrably different effects on the structure of the liquid water they are dissolved in (see ref. 14 for a recent and thorough review; F^- is known to be "structure making" and the other halides are "structure breaking" with respect to how they tighten or loosen the overall H-bonded network of water). We will show how these water-structure making/breaking properties of different added ions seem to be affecting the Franck-Condon energy (as measured by spectroscopic studies of E_{op} and band width) for mixed-valence dimers as shown in eq. 3-1 with L_{br} = BPE and BPY. The effects of temperature variations were also investigated. It is well-known that molecules of this type (Ru(II) and Ru(III) ammine complexes in general) are capable of strong hydrogen-bonding type interactions with solvent,

including water.[5,12,15] Our salt-effect data will show that the IT band of these mixed-valence dimers is in fact a sensitive new probe of water structure and that the most-likely mechanism of the solvent-solute interaction is related to the previously-identified strong H-bonding interactions characteristic of these systems.[15]

MLCT (metal to ligand charge transfer) and LMCT (ligand to metal charge transfer) absorption bands are known to respond sensitively to solvent *via* H-bonding interactions at the ammine ligands as mentioned above, and both of these types of absorption bands are present in our dimers as well (at higher energies than the NIR region of the IT band). The dimers thus exhibit MLCT, d-d (d-orbital or "ligand field" transitions on Ru), and $\pi - \pi^*$ band (π to π^* orbital transitions centered on bridging the ligands) in the fully-reduced II,II redox forms, and MLCT, $\pi - \pi^*$, d-d, LMCT and IT bands in the mixed-valence II,III redox forms (and d-d, $\pi - \pi^*$ and LMCT bands in the III,III redox states). Of these, we would expect the LMCT and IT bands to show the largest solvent and/or salt-induced water structure effects since the ammine ligands bound to Ru(III) are known to interact most strongly with solvents (in cases where the solvent has sufficient Lewis-base strength to act as a hydrogen bond "acceptor"[5,12,15]).

Unfortunately, direct measurement of the LMCT energies of the bridged dimers proved to be impossible in both the 5+ and 6+ dimers because of spectral overlap with the much more intense $\pi - \pi^*$ transitions of the ligand.[5a] For this reason, the electrolyte and temperature-dependent behaviors of LMCT band were

studied using the $[(NH_3)_5Ru^{III}(dmapy)]^{3+}$ (dmapy = 4-(dimethylamino)pyridine) monomeric complex as a model and the effects on the MLCT band were studied using both the fully-reduced (II,II) BPE dimer and the $[(NH_3)_5Ru^{II}py]^{2+}$ monomer complex.

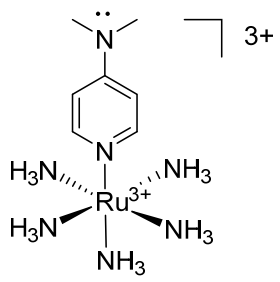

$[(NH_3)_5Ru^{III}(dmapy)]^{3+}$

3.2 Experimental

Materials and Syntheses

The BPE and BPY dimers were synthesized as described in Chapter two (see section 2.2.1 for details). $[(NH_3)_5Ru^{II}py]Cl_2$ was synthesized as described by Sista.[16] *N,N*-dimethyl aminopyridine (dmapy) was purchased from Aldrich and used without further purification.

Synthesis of $(NH_3)_5Ru^{III}(dmapy)]Cl_3$ (dmapy = 4-(Dimethylamino)pyridine)

This complex was synthesized using a modification of the method described by Curtis.[5] 0.2 g of $[Ru^{II}(NH_3)_5(OH_2)](PF_6)$ (see Chapter two for synthesis) was

dissolved in 80 mL of argon-degassed acetone giving a yellow-colored solution. Three equivalents of dmapy (as the solid) were added to the solution followed by stirring for 4 h at room temperature under an argon blanket. The final solution volume was reduced to about 20 mL by bubbling N_2. The solution was then filtered under an argon blanket into 20 mL of argon-degassed diethyl ether in order to precipitate the product. The solid $[(NH_3)_5Ru^{II}(dmapy)](PF_6)_2$ product was collected by another filtration under argon, washed with ether and dried under *vacuo*. Yields were typically 40-60%.

We found that the $[(NH_3)_5Ru^{II}(dmapy)](PF_6)_2$ decomposes rapidly under O_2 to form traces of the blue-colored Ru(III) complex, thus Ru(II) complex should be stored in an Ar or N_2-filled vial in the freezer and used within a day of initial preparation.

The chloride salt can be synthesized by dissolving a small amount (typically 10 mg) of $[(NH_3)_5Ru^{II}(dmapy)](PF_6)_2$ in Ar degassed acetone and then precipitating it as the chloride by adding a few mL of 1/8 saturated tetra-*n*-butylammonium chloride in degassed acetone. The gray solid was collected *via* filtration and dissolved in minimum amount of 0.2 M HCl. The Ru^{II} was then oxidized to Ru^{III} by adding a few drops of 30% H_2O_2, yielding a deep blue solution. The product was precipitated with addition of 10 volumes of acetone, collected *via* filtration and dried *in vacuo*. Yields were 30-40%

(The yield calculation for this step is somewhat uncentain due to the large deviation introduced by starting with a relatively small amount of

$[(NH_3)_5Ru^{II}(dmapy)](PF_6)_2$ initially and product loss during filtration and collection.)

Spectroscopic Measurements

The intervalence-charge transfer bands of the dimeric systems were measured using either a Cary 5G or a Cary 5000 UV-Vis-NIR spectrophotometer. The height of the cell holder in the instrument had to be carefully adjusted to the proper level so that all light would pass through a 1cm pathlength quartz cell containing only 2 mL solution (this relatively small volume being helpful for conservation of sample). A relatively-slow scan rate of 120nm per minute was used so as to obtain a better signal-to-noise ratio than the default setting of 600nm per minute. Each run solution was prepared by diluting/mixing ruthenium (III, III) and (II, II) dimer stock solutions of a given dimer and an electrolyte (added salt) stock solution in a 2.00 mL volumetric flask. In all run solutions, the ruthenium dimer concentrations were kept the same (typically 2.5×10^{-4} M for both (II, II) and (III, III)) and the added-electrolyte concentrations were varied from 2.5×10^{-3} M to the maximum possible before either the saturation point of that salt was reached or precipitation of the ruthenium complex occured. For example, to study the effect of added KBr on the IVCT band of the (II, III) BPE dimer, the nominal ruthenium (II, III) concentration was 5.0×10^{-4} M. The "nominal" concentration is the concentration which would apply if the comproportionantion reaction went to 100% conversion. The actual concentration of (II, III) was calculated based on the known K_{eq} of the comproportionation reaction. In a

typical experiment, 0.50 mL ruthenium (III, III) dimer, 0.50 mL of the ruthenium (II, II) stock solutions at 1.0 x 10^{-3} M and up to 1.00 ml (volume added depending on the desired salt concentration) of salt-containing solution were mixed in a 2.00 ml volumetric flask (in a final volume of 2.00 ml; distilled water was added if needed). This solution in the flask was then transferred to a cuvette for UV-vis measurement.

Even in the absence of the di-ruthenium dimer (or other) chromophore, there were some relatively narrow absorption bands in the near infrared region which appear and then become more significant as the concentration of a given added salt is increased past ~0.1 M (presumably due to salt-induced changes of the hi-order H_2O overtone bands in the IR which appear if the "blank" scan is taken as a simple water *vs.* water scan). In order to correct the IT spectra of our mixed-valence chromophores for the obscuring effect of these salt-induced bands at higher salt concentrations, a "blank" solution was prepared consisting solely of the pure electrolyte solution at the same salt concentration as a given dimer spectrum, and this was used as the "blank" solution in the reference cell which was scanned (now as salt *vs.* salt) prior to recording a given run solution of dimer + salt. Thus the salt-induced absorbance changes in the NIR water spectrum where cleanly zeroed-out of the IT spectra.

The absorbance *vs.* λ data obtained from a given scan can be exported as an Excel file using the Cary Scan software (of the Cary spectrometer) *via* the following procedure: First, double click the "WinUV" icon to open the software,

then choose “Clear report” in the main menu and click “Recalculate” to open a new window. Select “Include X-Y Pairs Table”, choose “OK” to generate spectra data in a table of Abs vs. λ on screen. From the main menu, select the “File” tab. Choose “Save Data As” and then select “Files of type” as [*. CSV] and input the file name and click “Save”. The absorbance *vs.* wavelength data will now open as two columns in an Excel spreadsheet file. These data can be converted into absorbance *vs.* energy (in eV) and processed using Sigmaplot or PeakFit software (both obtained from Systate Software Inc) deconvolute and analyze the IVCT spectrum for best-fit λ_{max}, E_{max} (eV), ε_{max} and bandwidth (also known as “fwhm” or $\Delta\nu_{1/2}$).

Note: the same method was used in the study of electrolyte effects on the MLCT and LMCT bands of the ruthenium monomer complexes. Details on operating the PeakFit program for spectral deconvolution have been described in detail by Qin.[17]

Temperature Dependent Studies of the IVCT Bands

The temperature-dependent UV-Vis spectroscopy experiments were carried out with or without added electrolyte using an experimental temperature range from 4 to 45 ^{o}C. The experimental temperatures were chosen at random (rather than sequential) so as to avoid any systematic errors due to time-dependent spectral changes. The solutions were prepared according to the same procedure

as used for the electrolyte effect experiments described previously. The run solution concentration (either ruthenium chromophore only or with added electrolyte) was held constant at the experimental temperature by suspending it in the reservoir of the circulating temperature bath (Lab-line instruments VWR1165) at each experimental temperature. Argon gas was blown into the cell compartment of the instrument in order to exclude water vapor and thus prevent condensation on the cell at low temperatures (this was typically a significant problem at temperatures lower than 10 ^{o}C). The temperature was controlled using a temperature circulation system with a 50:50 water:antifreeze mixture as coolant. The exact temperature at the cell was read on a digital Pt thermometer immersed in the cell solution at the time of measurement (after 1-2 min of equilibration time). We found it necessary to record a separate water *vs.* water baseline correction at each experimental temperature to avoid absorbance errors due to the baseline drifting with temperature. The same method was used in the study of the MLCT and LMCT band temperature dependence effects.

3.3 Results and Discussion

3.3.1 Halide Effects on Charge Transfer Bands

Our results indicated that adding simple electrolytes to solutions of both monomeric and mixed-valence dimeric ruthenium systems can bring about complex and qualitatively different spectral shifts depending on the specific

identities of the added electrolyte ions. Tables 3.1 and 3.2 list how E_{IT} or "E_{op}" for the BPE and BPY-bridged dimers vary with concentration for added potassium halide salts as well as sodium sulfate and sodium nitrate. Figures 3.1 and 3.2 show the IVCT energetic graphically. We see that E_{op} for the intramolecular [Ru^{II}, Ru^{III}] intervalence transfer transition shows a clear blue shift with added F^- but red shifts with the other halides (Cl^-, Br^- and I^-). The extent of the red-shift correlates with is related to the molecular weight of the halide, increasing in the order Cl^- < Br^- < I^-. The blue shift with added KF is more rapid with the appearance of possible saturation effect at lower concentration for the BPE dimer as compared with other added halides. Added $NaNO_3$ was observed to have an effect similar to Cl^- for the BPY dimer case. With added SO_4^{2-}, we observed an IT band shift pattern that is similar to what was discovered by Hupp in his studies of the BPY dimer in D_2O as solvent.[10]

Table 3.1 Salt effects on the position of the IT band of the $[(NH_3)_5Ru^{II}$-BPE-$Ru^{III}[(NH_3)_5]^{5+}$ dimer in aqueous solution (nominal concentration of the II, III system = 5.0 x 10^{-4} M and calculated actual conc. = 3.6 x 10^{-4} M based on K_c = 14.48).[19]

[KF] (M)	E_{op} (ev) [(a)]	[KCl] (M)	E_{op} (ev) [(a)]	[KBr] (M)	E_{op} (ev) [(a)]
0.000	1.270	0.000	1.266	0.000	1.268
0.005	1.271	0.005	1.266	0.005	1.266

0.010	1.273	0.010	1.268	0.010	1.267
0.020	1.274	0.020	1.266	0.020	1.267
0.040	1.280	0.040	1.263	0.040	1.263
0.100	1.283	0.100	1.262	0.100	1.258
0.200	1.285	0.200	1.261	0.200	1.256
0.400	1.288	0.300	1.258	0.300	1.250
0.600	1.288	0.400	1.259	0.400	1.246
0.800	1.290	0.600	1.256	0.500	1.243
1.200	1.292	0.800	1.252	0.600	1.239
1.600	1.294	1.000	1.251	0.800	1.238

[KI] (M)	**E_{op} (ev) [(a)]**	**[Na_2SO_4] (M)**	**E_{op} (ev) [(a)]**	**[Na_2SO_4] (M)**	**E_{op} (ev) [(a)]**
0.000	1.269	0.000	1.271	0.400	1.269
0.005	1.264	0.005	1.290	0.600	1.261
0.010	1.260	0.010	1.291	0.800	1.261
0.020	1.258	0.020	1.291	1.000	1.254
0.040	1.253	0.040	1.287		
0.100	1.246	0.100	1.286		
0.200	1.240	0.200	1.278		

a) All E_{op} values are obtained by refining the experimental raw spectra with Peakfit as described by Qin[17]; error limits on Eop are $\pm$ 0.002 eV.

Table 3.2 Salt effects on the position of the IT band of the $[(NH_3)_5Ru^{II}\text{-BPY-}Ru^{III}[(NH_3)_5]^{5+}$ dimer in aqueous solution (nominal concentration of the II, III system = 5.0×10^{-4} M and calculated actual conc. = 3.5×10^{-4} M

[KF] (M)	E_{op} (ev) [(a)]	[KCl] (M)	E_{op} (ev) [(a)]	[KBr] (M)	E_{op} (ev) [(a)]
0.000	1.189	0.000	1.186	0.000	1.188
0.005	1.192	0.005	1.186	0.005	1.184
0.010	1.193	0.010	1.187	0.010	1.182
0.020	1.195	0.020	1.186	0.020	1.180
0.040	1.198	0.040	1.186	0.040	1.180
0.100	1.202	0.100	1.183	0.100	1.173
0.200	1.204	0.200	1.180	0.200	1.170
0.400	1.206	0.400	1.177	0.400	1.160
0.600	1.207	0.600	1.172	0.600	1.156
0.800	1.207	0.800	1.170	0.800	1.148
1.200	1.210	1.000	1.166	1.000	1.141
1.600	1.206				
[KI] (M)	**E_{op} (ev) [(a)]**	**[Na_2SO_4] (M)**	**E_{op} (ev) [(a)]**	**[$NaNO_3$] (M)**	**E_{op} (ev) [(a)]**
0.000	1.189	0.000	1.189	0.000	1.189
0.005	1.181	0.005	1.209	0.005	1.188
0.010	1.180	0.010	1.210	0.010	1.188

0.020	1.177	0.020	1.207	0.020	1.187
0.040	1.170	0.040	1.205	0.040	1.185
0.100	1.154	0.100	1.202	0.100	1.182
0.200	1.150	0.200	1.199	0.200	1.182
		0.400	1.189	0.400	1.179
		0.600	1.184	0.600	1.177
		0.800	1.183	0.800	1.176
		1.000	1.177	1.000	1.174

a) All E_{op} values are obtained by refining the experimental raw spectra with Peakfit as described by Qin[17]; error limits on Eop are $\pm$ 0.002 eV.

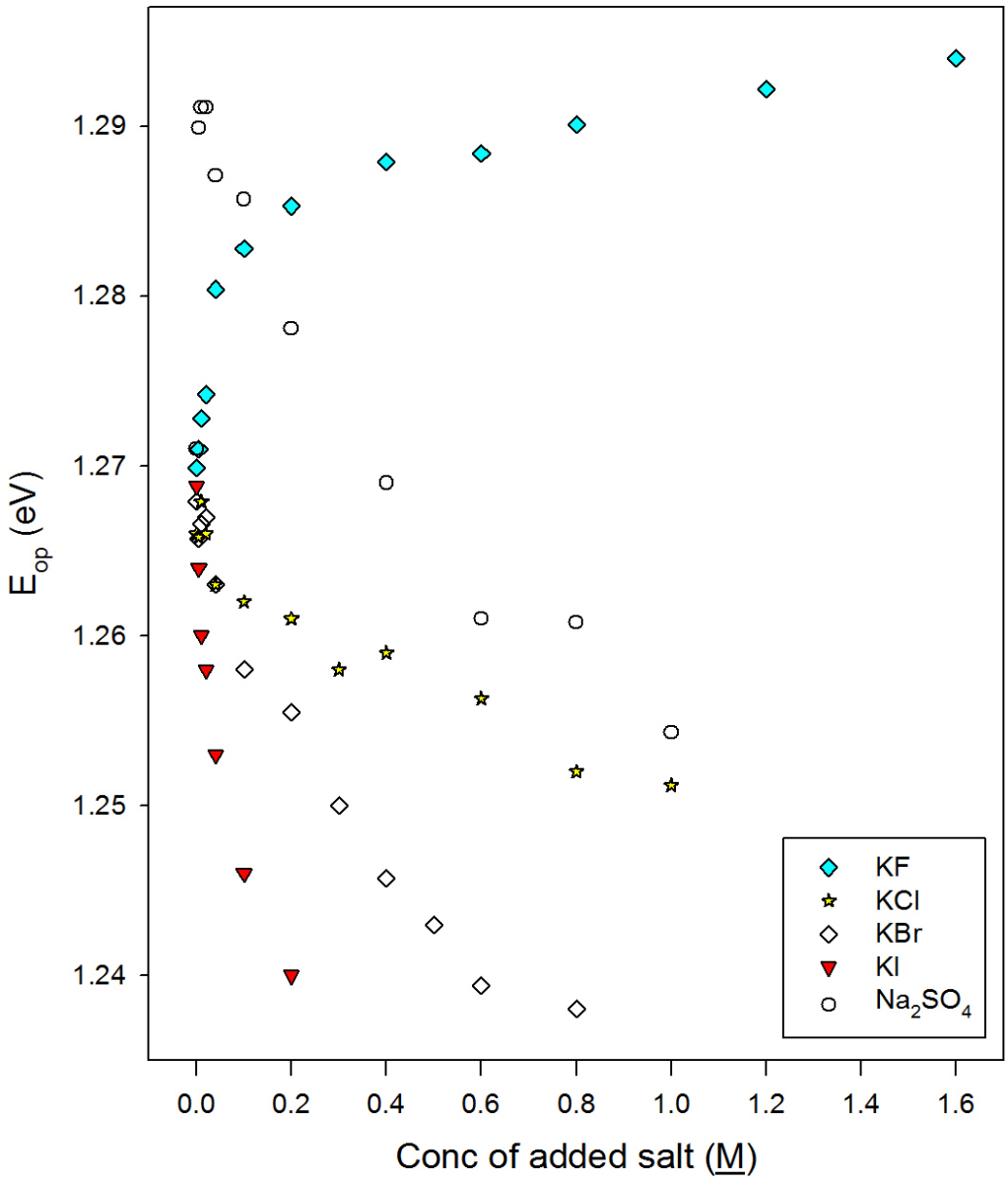

Figure 3.1 E_{op} for the $[(NH_3)_5Ru^{II}\text{-BPE-}Ru^{III}[(NH_3)_5]^{5+}$ IVCT band *vs.* concentration of various added salts in water. (Nominal concentration of the II, III system = 5.0 x 10^{-4} M and calculated actual conc. = 3.6 x 10^{-4} M based on K_c = 14.48).[19]

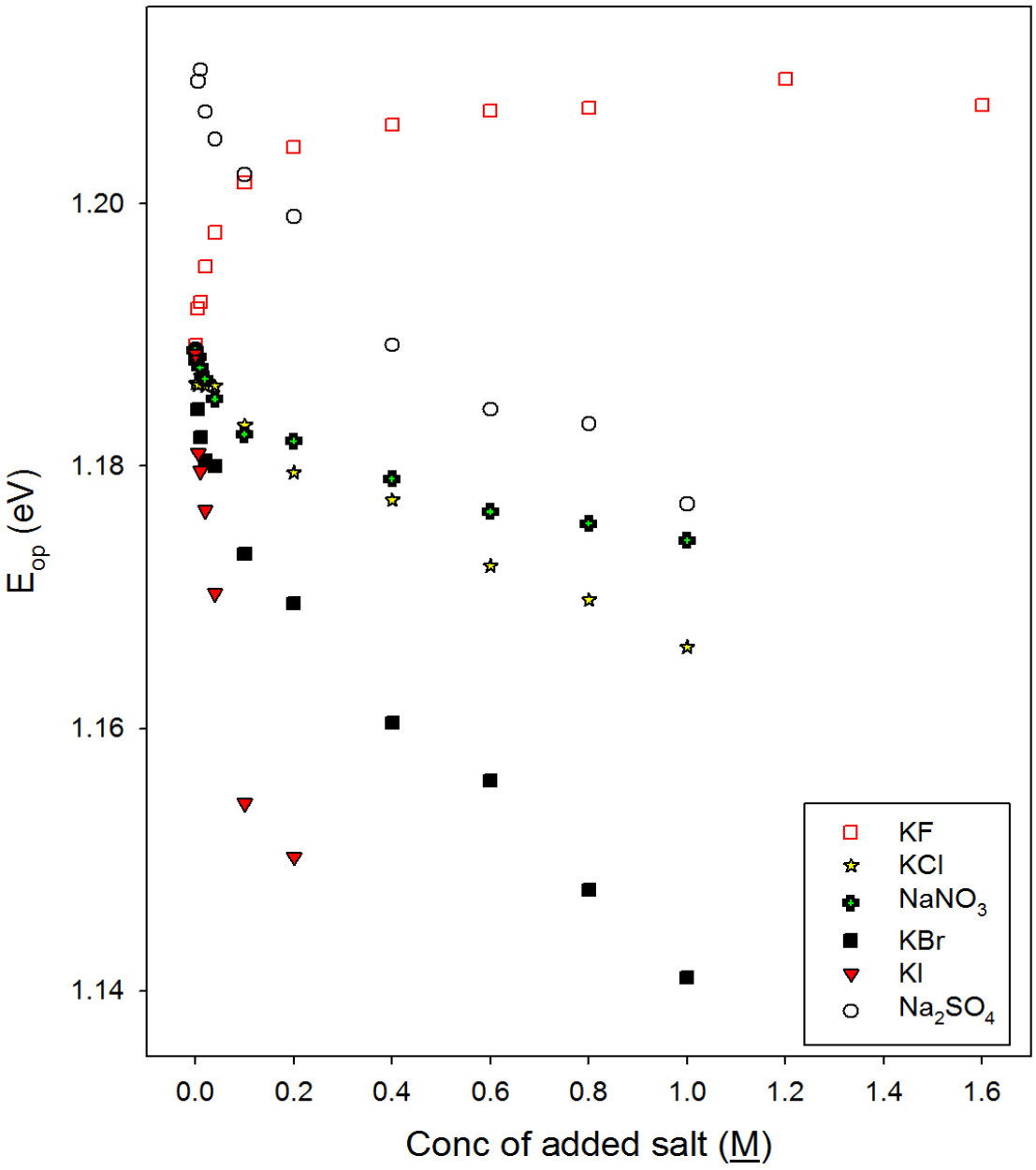

Figure 3.2 E_{op} for the $[(NH_3)_5Ru^{II}\text{-BPY-}Ru^{III}[(NH_3)_5]^{5+}$ IVCT band *vs.* concentration of various added salts in water. (Nominal concentration of the II, III system = 5.0 x 10^{-4} M and calculated actual conc. (a) = 3.5 x 10^{-4} M based on K_c = 14.48).[19]

The salt effects on the IVCT band energies of the dimers would be expected to be related to salt effects on the MLCT and LMCT band energies of the related Ru^{II} and Ru^{III} monomer species (since these charge-transfer transitions also involve redox state changes at Ru and thus lewis acidity changes at the ammine hydrgens and presumably changes in the solvent-solute H-bonding in the excited state[12,20]). There are both MLCT and LMCT bands present in the "II,III" mixed-valence dimers, but, there is considerable spectral overlap of the LMCT band on these dimers and the π to π^* transitions centered on the aromatic ligands.[5a] For this reason, we used the LMCT band of $[(NH_3)_5Ru^{III}(dmapy)]Cl_3$ as a surrogate for the half of the dimer which gets "photo-reduced" upon intervalence-transfer photon absorption. Table 3.3 shows the LMCT band energy as a function of concentration of varous added halides. Figure 3.3 shows how added KF and KBr affect the LMCT transition of $[(NH_3)_5Ru^{III}(dmapy)]Cl_3$ in aqueous solution. As seen previously with the IT bands in our dimers, the LMCT of the Ru(III) monomer was blue-shifted by F^- and red-shifted by Br^-. In the same concentration range of added F^- and Br^-, the LMCT and IVCT bands show very similar (F^-) and nearly identical "iono-chromic shift" behaviors (Br^-) (see Figures 3.4 and 3.5).

Table 3.3 Salt effects on the energy of $[(NH_3)_5Ru^{III}(dmapy)]Cl_3$ LMCT band in aqueous solution.

[KF] (M)	E_{op} (ev) [(a)]	[KBr] (M)	E_{op} (ev) [(a)]
0.000	2.118	0.000	2.118
0.005	2.118	0.005	2.115
0.010	2.118	0.010	2.114
0.020	2.120	0.020	2.112
0.040	2.121	0.040	2.110
0.100	2.124	0.100	2.105
0.200	2.126	0.200	2.100
0.400	2.129	0.400	2.094
0.800	2.134	0.600	2.088
1.200	2.138	0.800	2.084
		1.200	2.076

a) All LMCT band energies reported here are as obtained directly from the UV-vis measurements without further spectral refinement or deconvolution with Peakfit

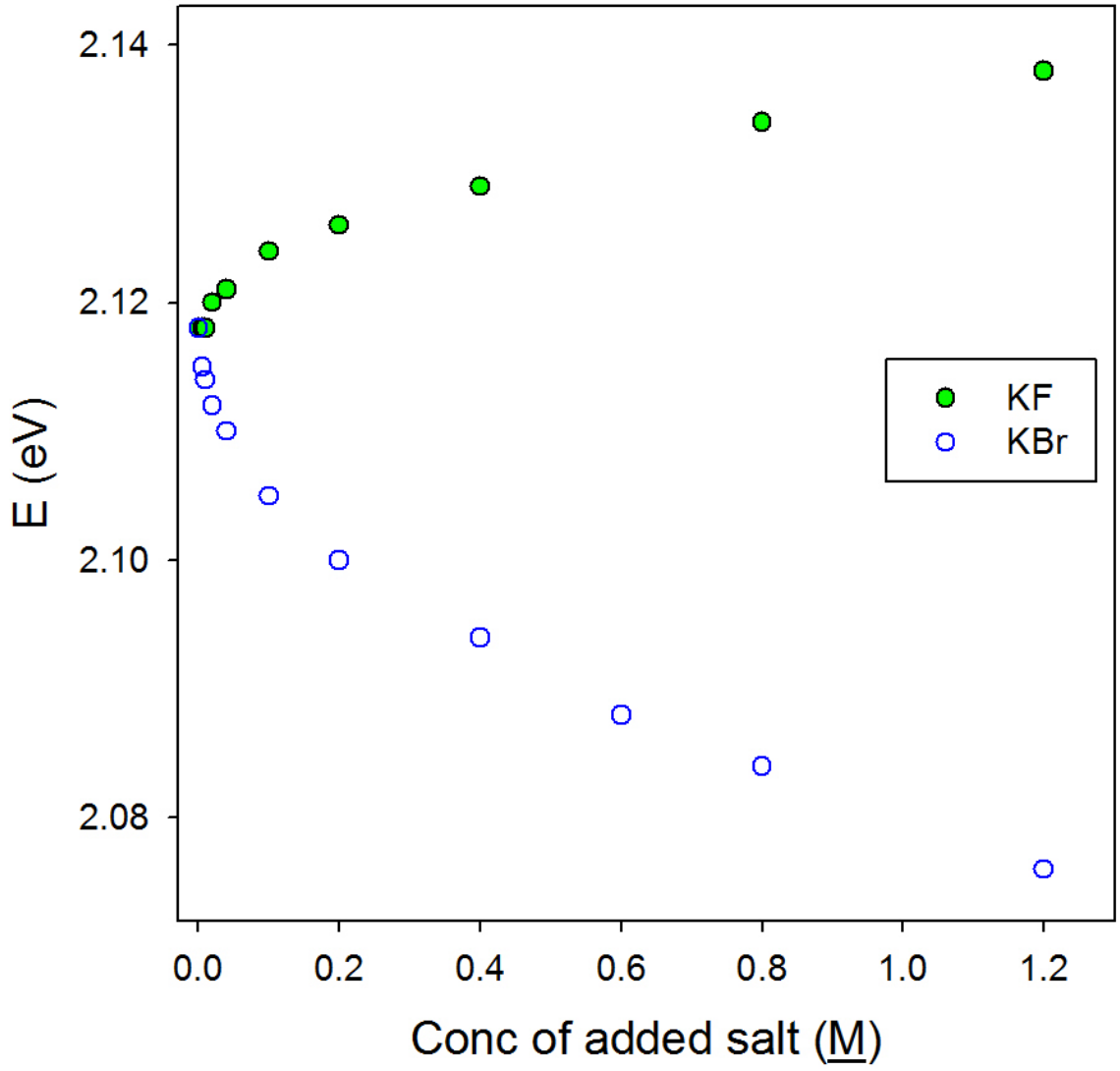

Figure 3.3 The energy of the $[(NH_3)_5Ru^{III}(dmapy)]Cl_3$ LMCT band (with $[Ru^{III}]$ = 5.0 X 10^{-4} M) at varying concentrations of added KF and KBr in water.

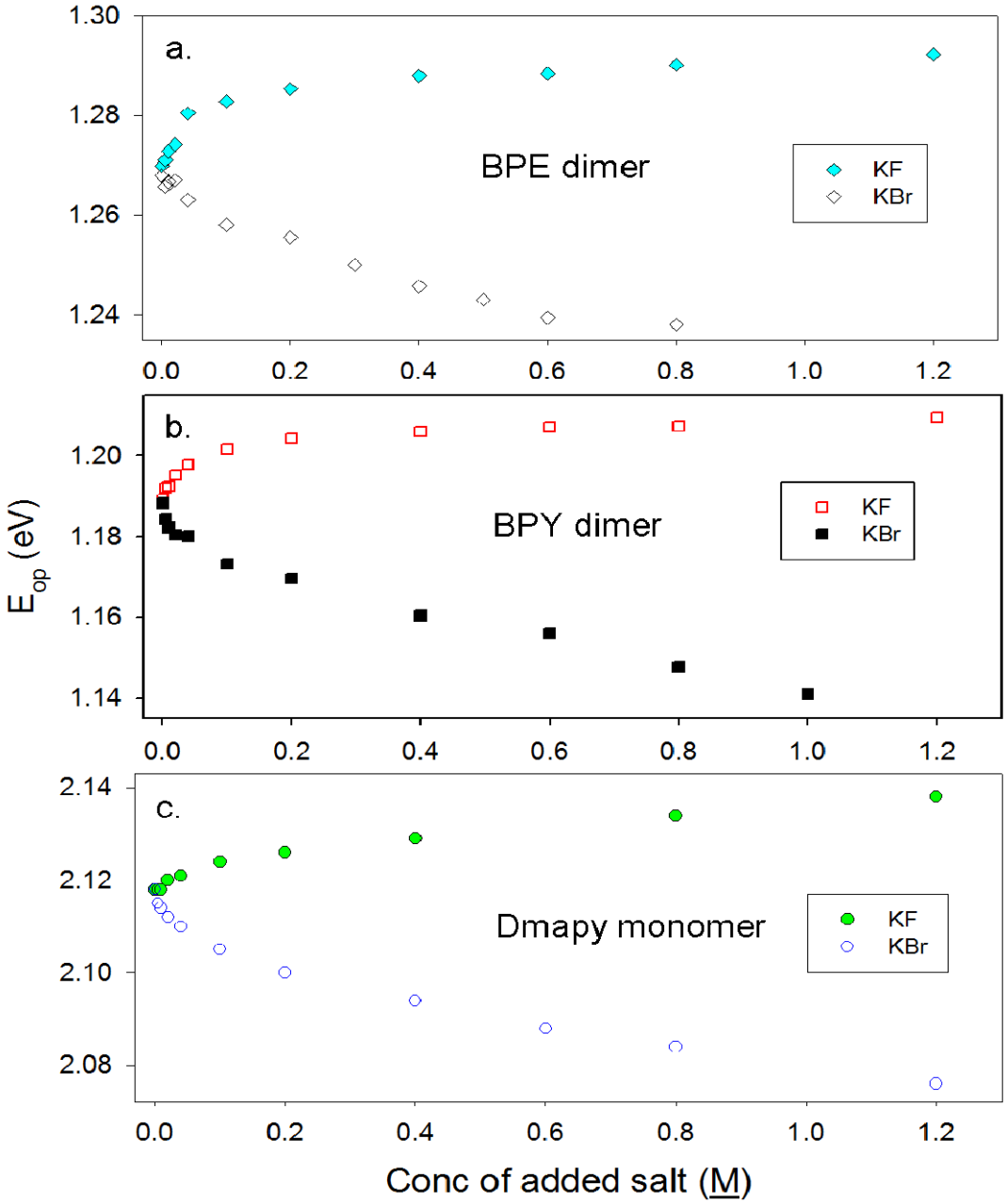

Figure 3.4 Added KF and KBr effects on the energies of a) the BPE dimer IVCT band, b) the BPY dimer IVCT band, and c) the $[(NH_3)_5Ru^{III}(dmapy)]Cl_3$ LMCT band (with [Ru] = 5.0 X 10^{-4} M) in water.

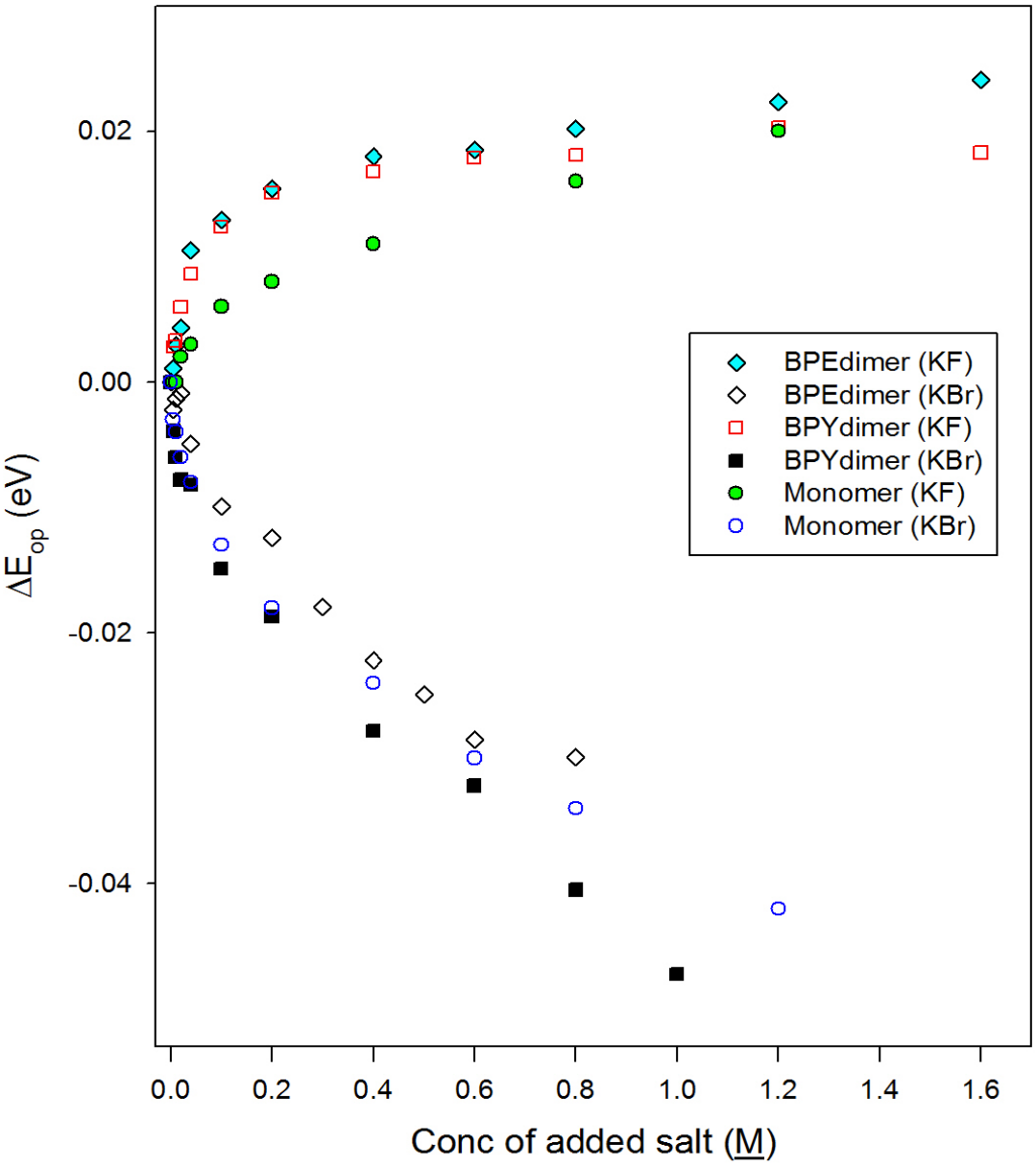

Figure 3.5 The energy shifts, ΔE_{op} for the BPE and BPY dimer IT bands and the $[(NH_3)_5Ru^{III}(dmapy)]Cl_3$ LMCT band with added KF and KBr

In contrast to the IVCT and LMCT data, the measured λ_{max} and E_{op} values

(Table 3.4) of the MLCT transition of the $[(NH_3)_5Ru^{II}py]Cl_2$ monomer complex show only small dependences on the added halides (see Figures 3.6 and 3.7). Figure 3.8 shows that there is a slight red shift in E_{op} for the $[(NH_3)_5Ru^{II}py]Cl_2$ MLCT band with both added KF and KBr; this is obviously a significant qualitative difference than what we see in those cases where the charge-transfer transition brings about photoreduction at an Ru(III) center. From Figure 3.6 and 3.7 we see that the MLCT absorption band at 408 nm drops and a new absorption in the region around 260 nm grows in with both added F^- and Br^-. Spectra at low added salt concentration (< 0.1 M) have nice isosbestic points (see Figures 3.6c and 3.7c) indicating that the added salt is affecting some equilibrium relation between two species in solution. The spectra seem to deviate slightly away from the isosbestic points at higher added salt concentrations. It is possible that the isosbestic point might be due to an ion-pair formation of the $[(NH_3)_5Ru^{II}py]^{2+}$ chromophore with the added halides; and this would be not surprising since the ion-pair formation constant between $[(NH_3)_5Ru^{II}py]^{2+}$ and F^- would be expected to be on the order of ~ 15 M^{-1} (see Ch.2, Table 2.12 for Ru^{III} data) and so ion-pairing would be ~ 90% halfway through the range of concentrations, used here going through the isosbstic point at ~ 340 nm.

Table 3.4 KF and KBr effects on the energy of $[(NH_3)_5Ru^{II}py]Cl_2$ MLCT band in

aqueous solution.

Added salt concentration (M)	E_{MLCT} (KF)	E_{MLCT} (KBr)
0	3.043	3.043
0.005	3.043	3.043
0.010	3.043	3.043
0.020	3.043	3.043
0.040	3.043	3.043
0.100	3.042	3.042
0.200	3.040	3.042
0.400	3.039	3.042
0.800	3.038	3.039
1.200	3.034	N/A

a) All MLCT band energies are obtained directly from UV-vis measurements without further spectral deconvolution or refinement with Peakfit

Figure 3.6 (below) Effect of added KF on the $[(NH_3)_5Ru^{II}py]Cl_2$ MLCT band (with $[Ru^{II}] = 3.0 \times 10^{-4}$ M, arrow indicates increasing KF concentration). (a) UV-Vis spectra changes with added KF (up to 1.2 M concentration); (b) zoom in of (a) at ~ 408nm; (c) Difference absorption spectra with added KF; [spectrum of $[(NH_3)_5Ru^{II}py]Cl_2$ with added KF] minus [spectrum without added KF].

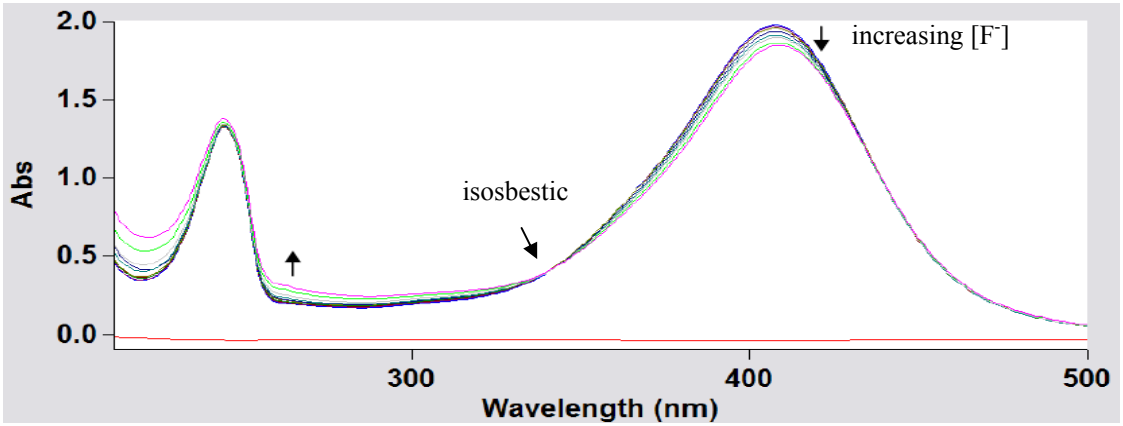
2.0
1.5
1.0
0.5
0.0
Abs
300
400
500
Wavelength (nm)
isosbestic
increasing [F-]

(a)

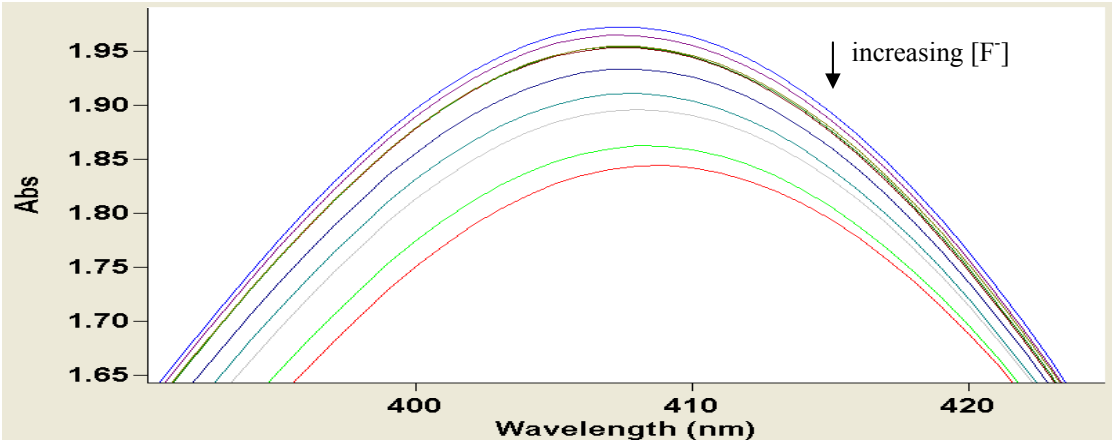
1.95
1.90
1.85
1.80
1.75
1.70
1.65
Abs
400
410
420
Wavelength (nm)
increasing [F-]

(b)

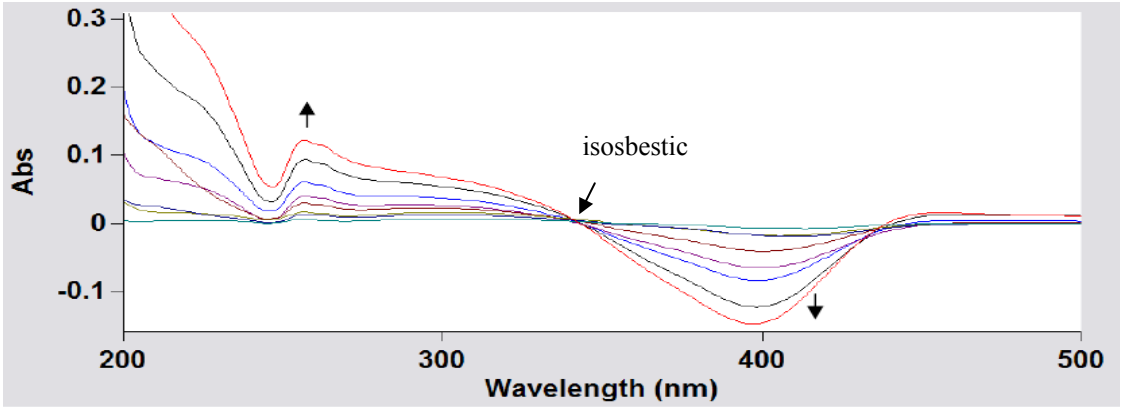
0.3
0.2
0.1
0
-0.1
Abs
200
300
400
500
Wavelength (nm)
isosbestic

(c)

Figure 3.7 (below) Effect of added KBr on the $[(NH_3)_5Ru^{II}py]Cl_2$ MLCT band (with $[Ru^{II}]$ = 3.0 x 10^{-4} M, arrow indicates increasing KBr concentration). (a) UV-Vis spectra changes with added KBr (up to 0.8 M concentration); (b) zoom in of (a) at ~ 408nm; (c) Difference absorption spectra with added KBr; [spectrum of $[(NH_3)_5Ru^{II}py]Cl_2$ with added KBr] minus [spectrum without added KBr].

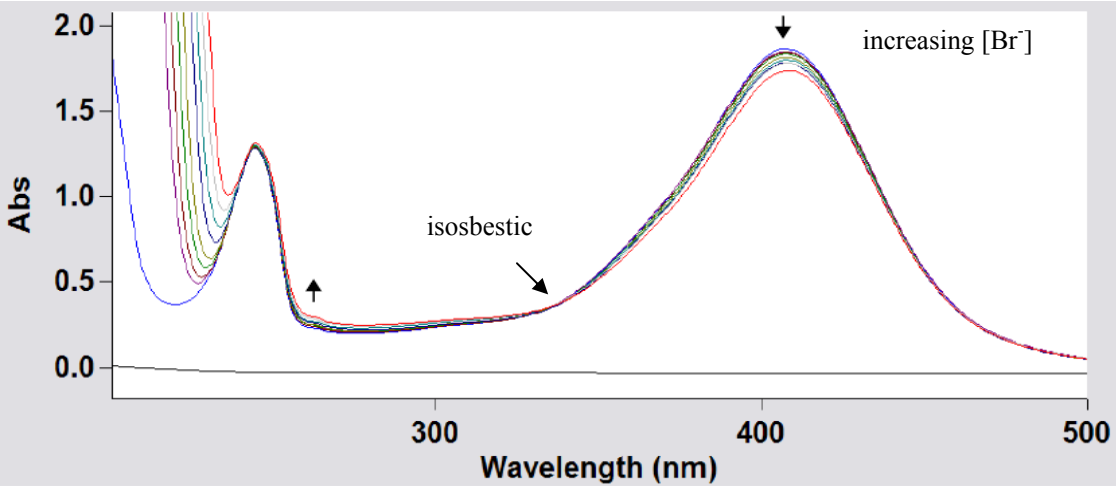

(a)

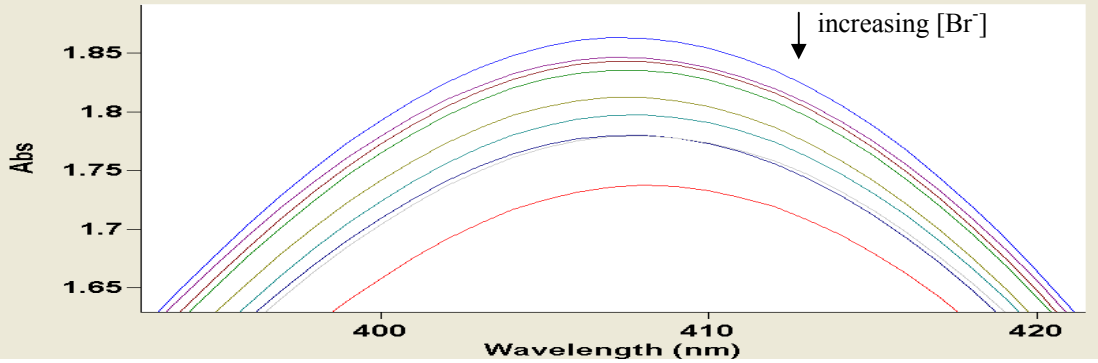

(b)

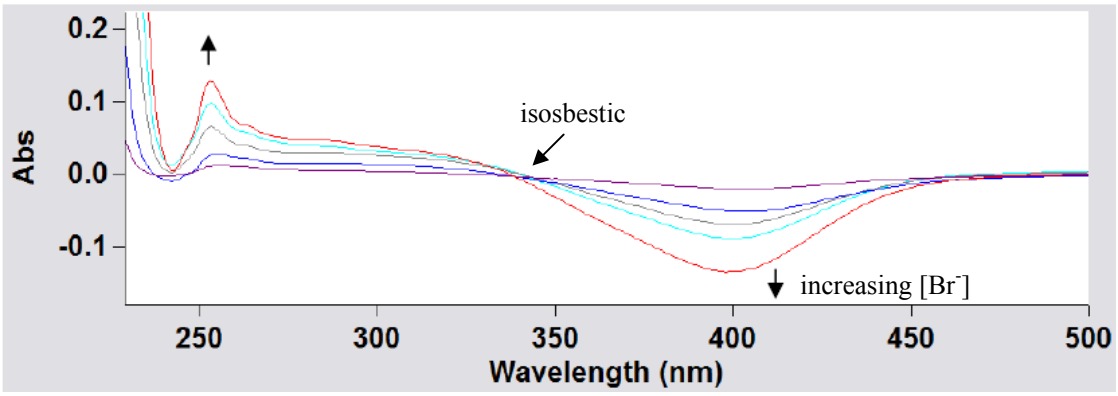

(c)

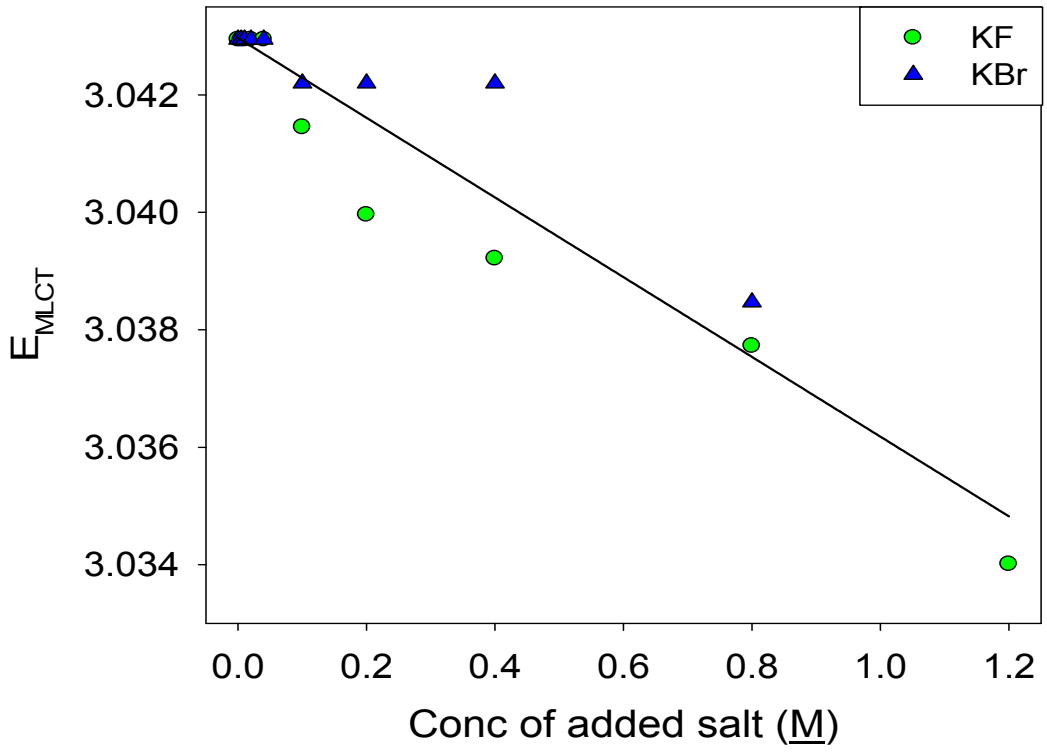

Figure 3.8 The energy of the $[(NH_3)_5Ru^{II}py]Cl_2$ MLCT band (with $[Ru^{II}]$ = 3.0 X 10^{-4} M) as a function of added KF and KBr in water.

The striking result here is that now *both* F^- and Br^- lead to an approximately-linear red shift, and the magnitude of the shift is much less than what we see in the IVCT and LMCT cases. This qualitative difference in behavior suggests that the mechanism of the salt-induced spectral shift changes upon going from the IVCT and LMCT transitions (where photon absorption leads to "reduction" at Ru(III) in the excited state) to MLCT transitions where absorption causes "oxidation" at Ru(II) (by creating an excited state which can be approximately described as $[(NH_3)_5Ru(III)\dot{p}\dot{y}]^{2+*}$.

Since it is well-known that Ru(III) ammine complexes (in their ground states) are very strongly solvated by specific H-bonding interactions with solvents,[5,15] we hypothesize that the IVCT and LMCT salt effects documented here probably reflect the salt-induced changes to this specific solvation structure somehow, while the qualitatively-different MLCT salt effects must reflect some kind of weaker, more general "ionic strength" or "ion-atmosphere" type effect. A plausible mechanism here might simply be that the added salt is able to favorably polarize and form a denser and more stabilizing ion atmosphere around the more polar LMCT excited state (where $\psi^{el}_{ground} \sim (NH_3)_5Ru^{II}py^{2+}$ and $\psi^{el}_{ground} \sim [(NH_3)_5Ru(III)\dot{p}\dot{y}]^{2+*}$). The qualitatively similar F^- and Br^- shifts in Figure 3.8 are different to explain without considering such a "o-o" energy gap effect.

As discussed in the recent extensive review by Marcus, [11] it is well-known

that the F^- ion in water has a positive Jones-Doyle viscosity B coefficient[18] ($B_\eta = 0.107$), and this is deemed to be a manifestation of an overall "structure making" effect of F^- in water (meaning that water becomes more viscous or "stiffer" upon F^- addition). The other halides all have negative B_η values (-0.005 for Cl^-, -0.033 for Br^-, -0.073 for I^-) which means that they are overall "structure breaking" ions and are thought to loosen the structure of water based on their viscosity effects. If we plot the total IVCT spectral shift obtained at 0.2 M added salt for the BPE dimer (see Figure 3.1) *vs.* the Jones-Doyle B coefficient for each halide, we obtain Figure 3.9 below,

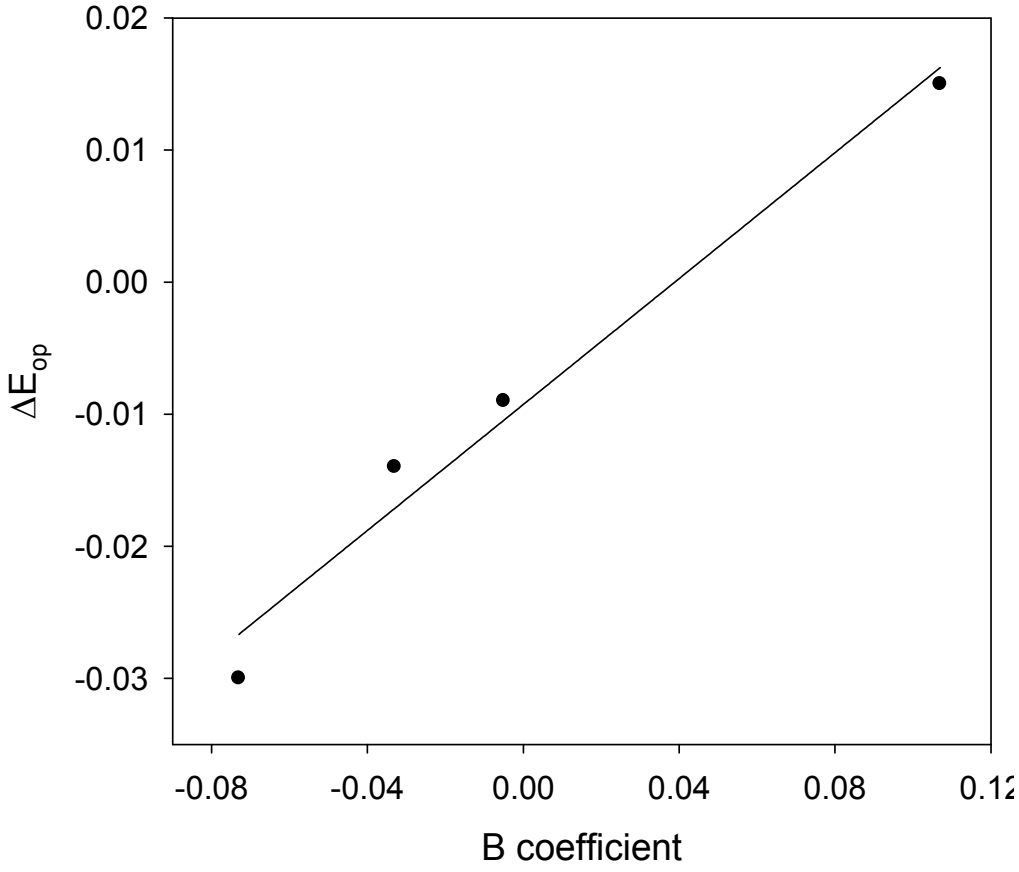

Figure 3.9 (above) The relation of energetic differences of IVCT shifts (obtained at 0.2 M added potassium halides) and Jones-Doyle B coefficients for the BPE dimer.

Doing the same thing for the BPY dimer data (see Figure 3.2), we obtain Figure 3.10 below,

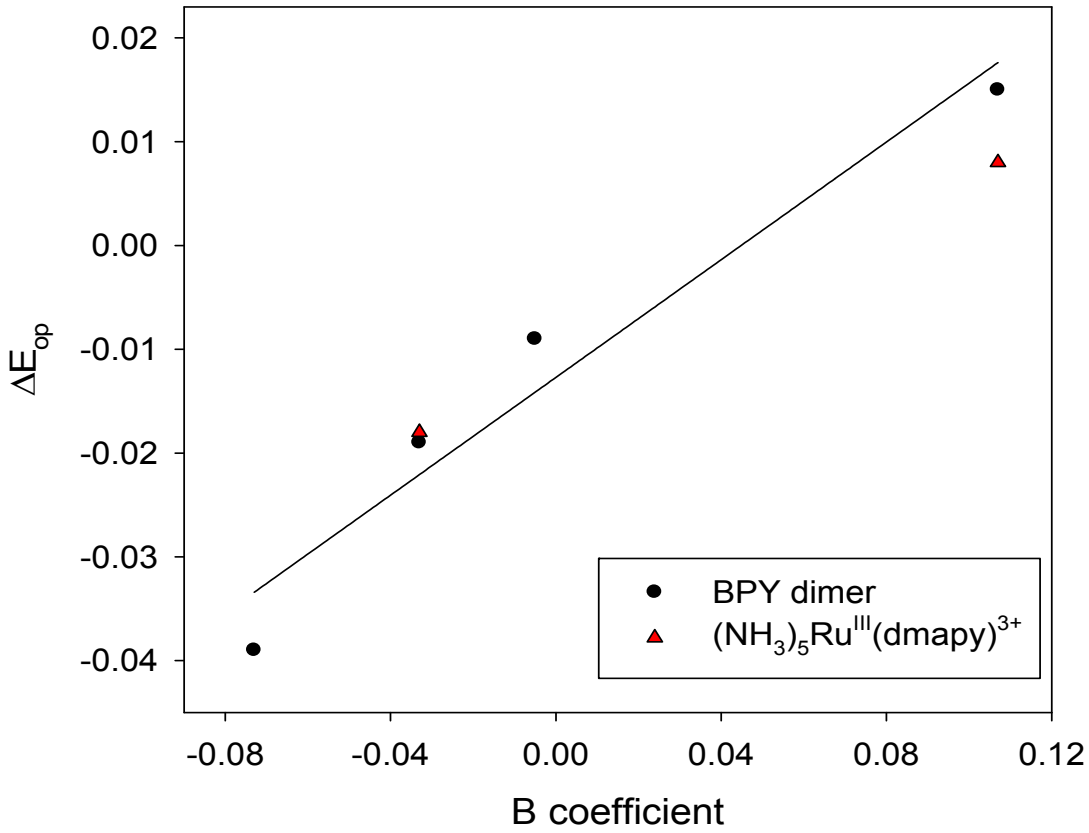

Figure 3.10 The relation of energetic differences of IVCT shifts (obtained at 0.2 M added potassium halides) and Jones-Doyle B coefficients for the BPY dimer and $(NH_3)_5Ru^{III}(dmapy)^{3+}$ monomer.

Also included in Figure 3.10 are the KF and KBr data points that we have for the LMCT band of $(NH_3)_5Ru^{III}(dmapy)^{3+}$.

In the simplest sense, current thinking is that the F^- anion, acting as "structure maker" is somehow able to enhance the solvent-solvent interaction (presumably because of the overall increase in hydrogen bonding in the water). Conversely, the heavier halides disrupt the hydrogen bond network in water.[14] The spectroscopic effects we observe in TVCT and LMCT absorption bands correlates well with the water-structure related viscometric "B" coefficient, including the sign change between F^- and Cl^-.

Comparison of the combined ΔE_{op} *vs.* [salt] data for the two dimeric chromophores and the single monomeric chromophore studied imply (though don't yet prove) that more than half of the measured "salt effect" in the dimers arises from changes occurring at the Ru(III) end of the dimers. As mentioned before, the Ru(III) ends of ruthenium ammine dimers such as these is where the strongest solvent-solute interaction (H-bonding) is known to be taking place,[5,15] and this means there would be more "structure" to disrupt or enhance by added salt at that end. In the bridged dimeric complexes, it may also be true that the electronic structure at the Ru(III) site would be affected more than at the Ru(II) site upon salt addition since changing the solvent structure will change the amount of electron density which ultimately flows from the surrounding water (acting as Lewis base) to the ruthenium center *via* H-bonding between water and ammine hydrogens.15 Thus there are two mechanisms, both effects on water structure

and on electronic structure, by which added salts might change the degree of asymmetry between the two ends of the dimer.

Figure 3.11 illustrates how the magnitude of the total shift in $\Delta^{tot}_{F-Br}E_{op}$ *vs.* [salt] concentration behaves for the BPE and BPY dimer IVCT bands and the $[(NH_3)_5Ru^{III}(dmapy)]Cl_3$ monomer LMCT band. Here we see that the $\Delta^{tot}_{F-Br}E_{op}$ values (simply E_{op} obtained with added KF minus E_{op} obtained with added KBr at a given concentration) at 0.8 M are 0.050, 0.058 and 0.050 eV for the BPE, BPY dimers and $[(NH_3)_5Ru^{III}(dmapy)]Cl_3$ monomer, respectively. $\Delta^{tot}_{F-Br}E_{op}$ for the monomer at 0.8 M is thus 93% of the average value for the two dimmers, which is probably identical within experimental error. This quantitatively suggests that most of the salt effect "happens" at the Ru(III) ends of the dimers since this is where there would probably be more "water structure" to enhance or disrupt in the first place. We note that this is also where added anions would form the most-dense "ion atmosphere" and therefore be expected to exert maximum effect on the water structure.

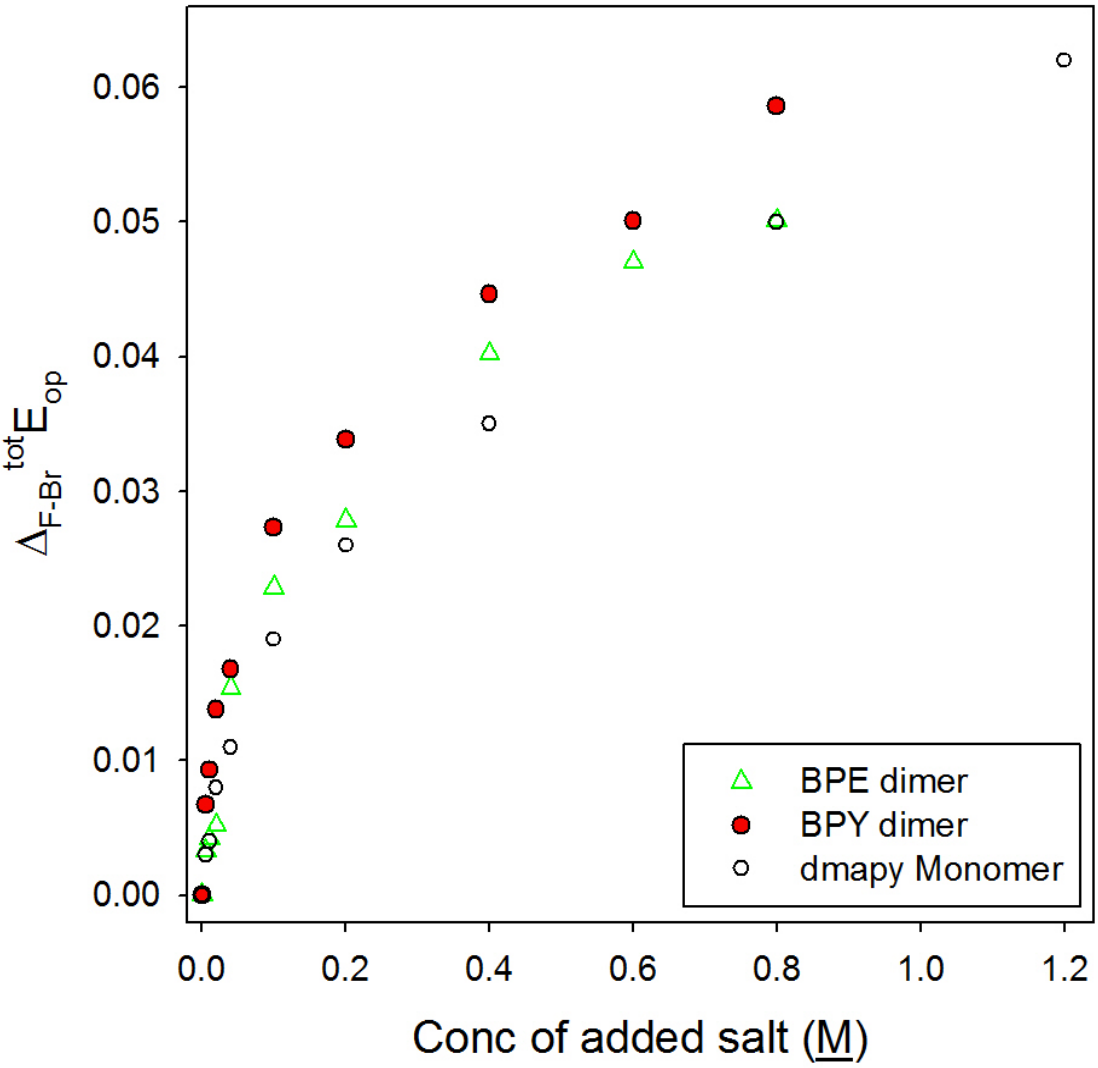

Figure 3.11 The energy differences of the BPE and BPY dimer IT bands and the $[(NH_3)_5Ru^{III}(dmapy)]Cl_3$ monomer LMCT band with added KF and KBr (E_{op} of spectra with added KF minus E_{op} of spectra with added KBr)

This result present something of a puzzle in the context of Marcus-Hush theory and how IVCT bands are generally interpreted, since the dimer will undergo

both “oxidation” at one end and “reduction” at the other upon photon absorption into the IVCT band, one would expect both tightening and loosening, respectively, of the associated hydration spheres (and these reorganizational changes would contribute to the total Franck-Condon energy which defines the energy of the band). One would thus expect only about one half as much effect with the $A_5Ru^{III}dmapy^{3+}$ monomer (upon modulation of water structure by salt addition) since there is only one hydration sphere to be reorganized upon photon absorption. Our measurements strongly contradict this simple idea and suggest that there much be another effect at work in the $A_5Ru^{III}dmapy^{3+}$ case, such as salt-induced variations in the electronic ground *vs*. excited-state energy gap for the Ru^{III} monomer which are clearly irrelevant in the dimeric systems. Work in progress now by Fabrizio and Doran in the Curtis lab seeks to explore this possibility.[21]

3.3.2 Temperature-Dependence of the Charge-Transfer Bands

Altering the solution temperature is another way to change the second-coordination (hydration) sphere surrounding ruthenium ammine solute ions such as ours, and these changes in the solvent-solute interaction would also be expected to show up in the energy of an optical ET process. Only a few examples[8] in the literature have focused on the temperature dependence of E_{IT}. According to Hupp, temperature dependence of the IVCT bands in mixed-valence systems are essentially large in asymmetrical complexes, [8a] and also presumably

exist in valence-localized systems.[8c] Here we will show an unusual example of a temperature dependence of E_{IT} for a symmetrical mixed-valence ruthenium dimeric system, the BPE-bridged dimmer.

The temperature dependences of the BPE and BPY dimer IT bands were measured from 5 to 45 °C and the E_{op} values are listed in Tables 3.5 and 3.6. Figures 3.12 and 3.13 show that E_{IT} for the BPE dimer exhibits a positive temperature coefficient (dE_{op}/dT = 2.75 $\pm$ 0.2 x 10^{-4} eV/°C in D_2O and 3.29 $\pm$ 0.29 x 10^{-4} eV/°C in H_2O), and, puzzlingly, the BPY dimer exhibits almost no temperature coefficient above noise level (dE_{op}/dT = 2.99 $\pm$ 1.1 x 10^{-5} eV/°C). The temperature range used in our study was constrained to 40 °C by the freezing point of the aqueous solution and the instability of the ruthenium dimers at higher temperature. Even though the temperature effect on the BPE dimer was small, multiple runs gave consistent results with variations well-above experimental error (as taken from the standard deviation in slope of the best-fit line; see Figure 3.12). To our knowledge, there is no reported symmetric system in water which exhibits a positive temperature coefficient for E_{IT}.

Table 3.5 Temperature effects on the IT band energy of the BPE dimer in both H_2O and D_2O

T (K) in H_2O	E_{op} (eV) [(a)]	T (K) in D_2O	E_{op} (eV) [(a)]
278.4	1.263	280.8	1.267
279.8	1.260	280.8	1.266
279.8	1.258	285.4	1.268
280.1	1.263	292.8	1.270
281.5	1.262	293.2	1.271
284.8	1.260	301.6	1.274
286.7	1.265	304.5	1.273
286.7	1.266	307.4	1.275
287.7	1.262	313.2	1.275
290.1	1.262	316.8	1.277
291.5	1.265		
295.4	1.266		
296.5	1.268		
298.6	1.2666		
301.3	1.267		
301.4	1.267		
301.4	1.266		

304.5	1.271
304.9	1.269
308.6	1.267
312.2	1.270
312.2	1.275
314.0	1.274
315.1	1.272
315.1	1.272

a) All E_{op} values are obtained by refining the experimental raw spectra with Peakfit as described by Qin[17]; error limits on E_{op} are $\pm$ 0.002 eV.

Table 3.6 Temperature effects on the IT band energy of the BPY dimer in H_2O

T (K)	**E_{op} (eV) [(a)]**	**T (K)**	**E_{op} (eV) [(a)]**
278.4	1.190	294.5	1.191
279.7	1.190	298.0	1.191
281.5	1.190	301.2	1.190
285.5	1.191	305.7	1.190
285.8	1.192	307.2	1.191
287.0	1.190	311.0	1.191
290.0	1.191	313.5	1.192
293.5	1.191	316.7	1.192

a) All E_{op} values are obtained by refining the experimental raw spectra with Peakfit as described by Qin[17]; error limits on E_{op} are $\pm$ 0.002 eV.

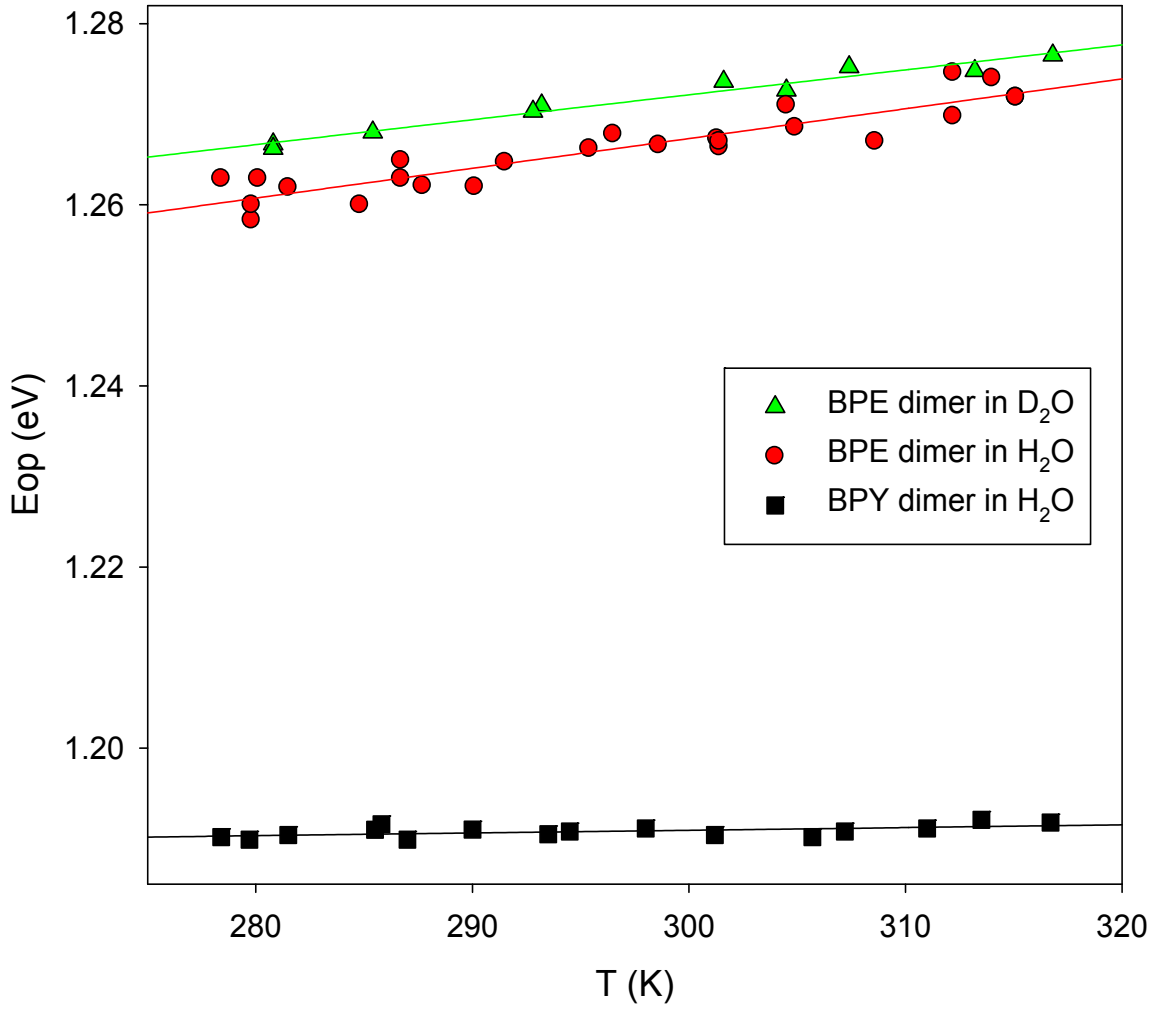

Figure 3.12 Temperature dependences of the IT bands for BPE and BPY dimers in H_2O and D_2O , [Ru^{II}, Ru^{III}] = 5 X 10^{-4} M. Best-fit regression equations are

$y = (2.75 \pm 0.2 \times 10^{-4})x + (1.190 \pm 0.006)$ for BPE dimer in D_2O,

$y = (3.29 \pm 0.29 \times 10^{-4})x + (1.169 \pm 0.008)$ for BPE dimer in H_2O and

$y = (3.0 \pm 0.12 \times 10^{-5})x + (1.182 \pm 0.003)$ for BPY dimer in H_2O.

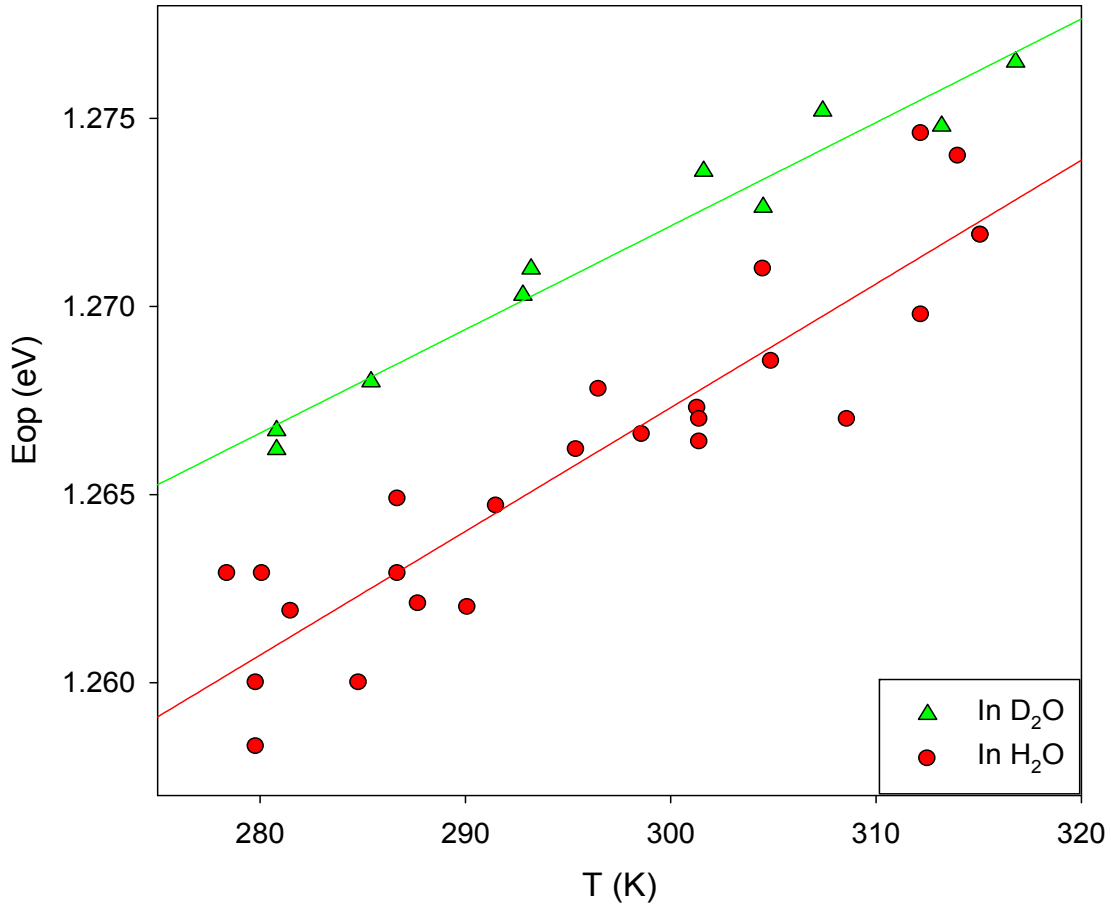

Figure 3.13 Temperature dependences of the IT band for the mixed-valence BPE dimer in H_2O and D_2O, [Ru^{II}, Ru^{III}] = 5 X 10^{-4} M.

Temperature effects on the MLCT bands of the $[(NH_3)_5Ru^{II}py]Cl_2$ and BPE (2,3) dimer as well as the LMCT band of the $[(NH_3)_5Ru^{III}(dmapy)]Cl_3$ were also studied, and these data are listed in Tables 3.7, 3.8 and 3.9. Figures 3.14 and 3.15 show the blue-shifts observed upon heating for the MLCT bands, and Figure 3.16 shows the red-shift obtained for the LMCT band.

Table 3.7 The effect of temperature on the MLCT band energy of $[(NH_3)_5Ru^{II}py]Cl_2$

Experiment order	T (K)	E_{op} (eV)
1	295.0	3.0435
2	278.0	3.0402
3	286.0	3.0425
4	317.0	3.0505
5	303.0	3.0468

a) Temperature order was chosen so as to minimize any systematic error due to sample decomposition

Table 3.8 The effect of temperature on the MLCT band energy of (2,3) BPE dimer

Experiment order	T (K)	E_{op} (eV)
1	281.5	2.2707
2	303.8	2.2794
3	291.8	2.2745
4	313.1	2.2838

a) Temperature order was chosen so as to minimize any systematic error due to sample decomposition

Table 3.9 The effect of temperature on the LMCT band energy of $(NH_3)_5Ru^{III}dmapyCl_3$

Experiment order	T (K)	E_{op} (eV)	Experiment order	T (K)	E_{op} (eV)
1	278.0	2.134	6	320.1	2.107
2	285.0	2.128	7	305.0	2.117
3	293.0	2.123	8	295.0	2.124
4	302.0	2.119	9	282.0	2.134
5	310.5	2.114	10	314.5	2.112

a) Temperature order was chosen so as to minimize any systematic error due to sample decomposition

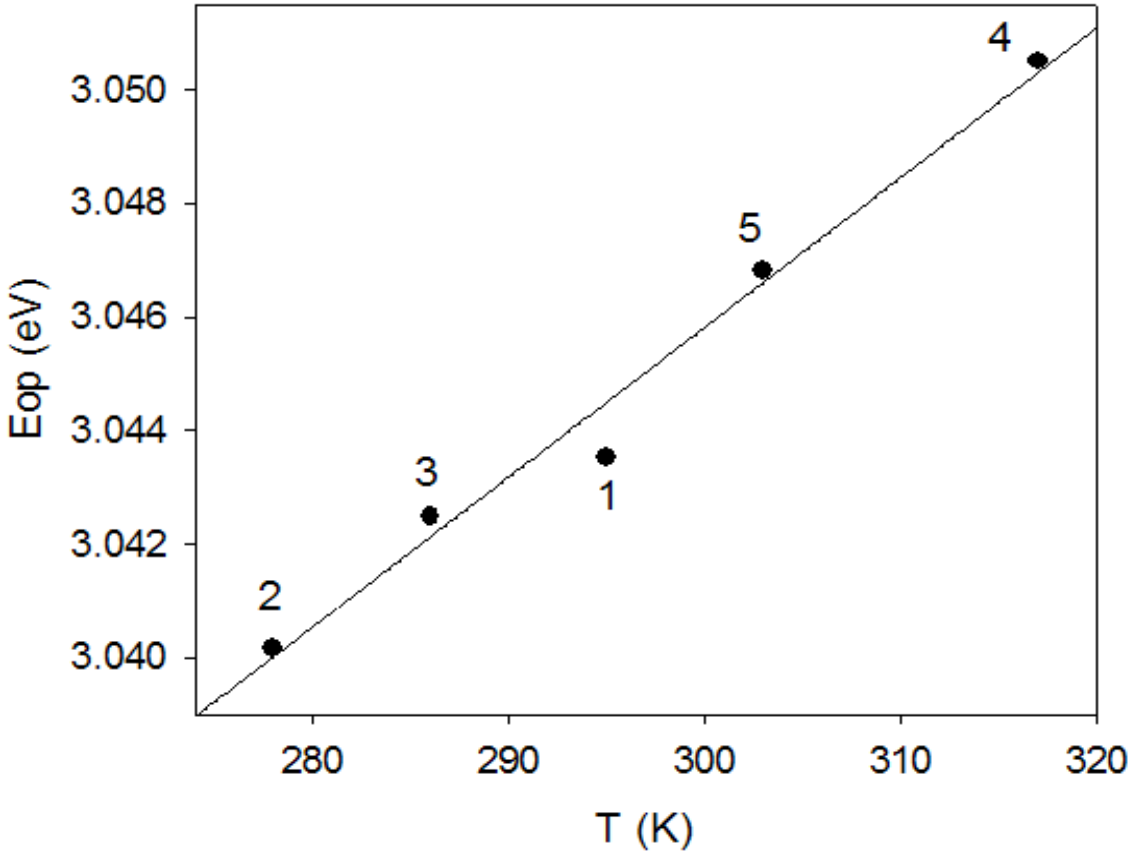

Figure 3.14 Temperature dependence of E_{MLCT} for the $[(NH_3)_5Ru^{II}py]Cl_2$ in H_2O (taken from table 3.7, $[Ru^{II}]$ = 1.0 X 10^{-4} M). The order in which the data points were taken is labeled with numbers in the graph (chosen so as to minimize any systematic error due to sample decomposition); the best-fit regression equation for the data is $y = (2.64 \pm 0.21 \times 10^{-4})x + (2.967 \pm 0.006)$.

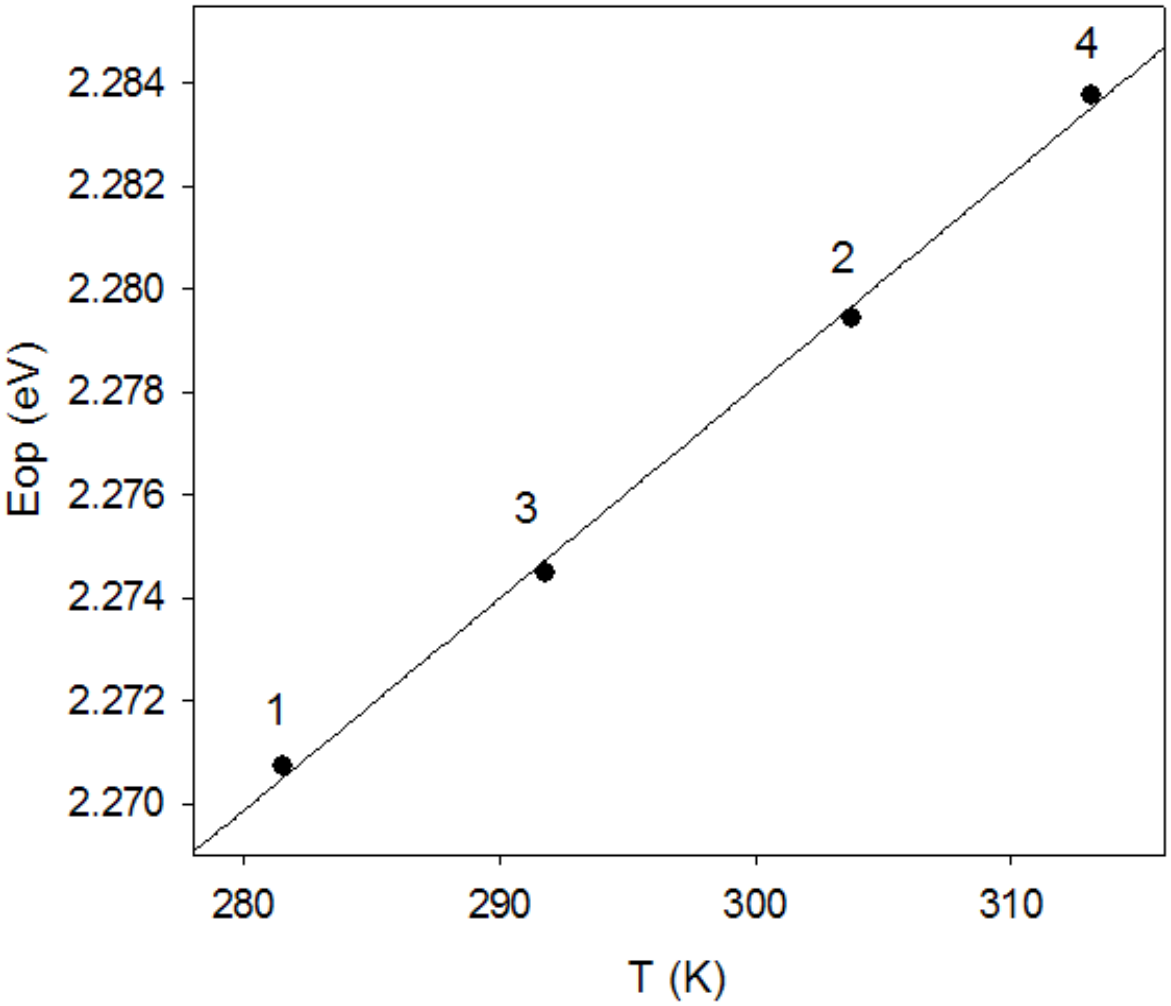

Figure 3.15 Temperature dependence of E_{MLCT} for the 2,3 BPE dimer in H_2O (taken from table 3.8 [Ru^{II}, Ru^{III}] = 1.0 X 10^{-4} M). The order in which the data points were taken is labeled with number in the graph (chosen so as to minimize any systematic error due to sample decomposition); the best-fit regression equation for the data is $y = (4.12 \pm 0.15 \times 10^{-4})x + (2.154 \pm 0.005)$.

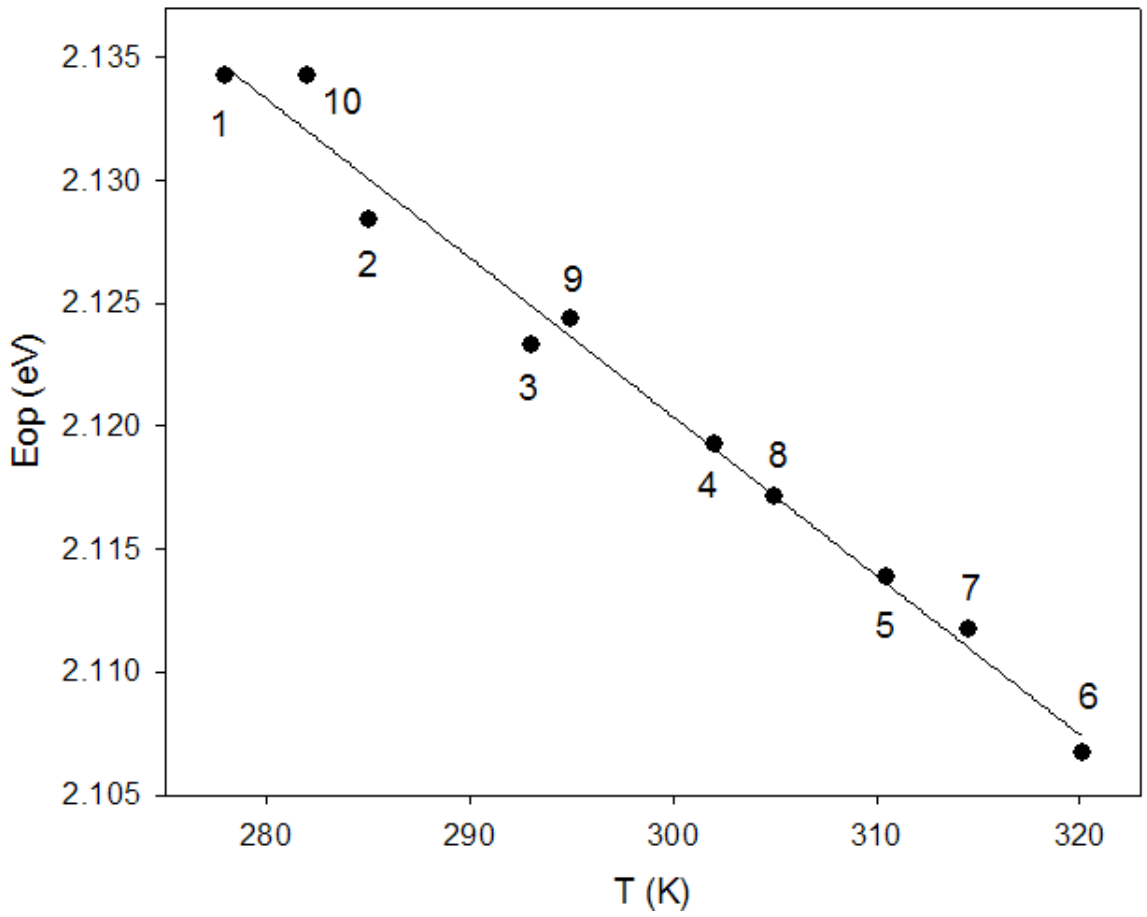

Figure 3.16 Temperature dependence of E_{LMCT} for the $[(NH_3)_5Ru^{III}(dmapy)]Cl_3$ in H_2O (taken from table 3.9 $[Ru^{III}]$ = 5.0 X 10^{-4} M). The order in which the data points were taken corresponds to the numbers in the graph (chosen so as to minimize any systematic errors due to sample decomposition); the best-fit regression equation for the data is $y = (-6.47 \pm 0.29 \times 10^{-4})x + (2.314 \pm 0.009)$.

If we consider how the temperature effects on the LMCT and MLCT bands might combine in the context of a mixed-valence dimer, we might make a simple

prediction for the expected temperature effect on the IVCT bands of the dimers. As shown in Figures 3.15 and 3.16, these two distinct effects shift the spectra in opposite directions (the MLCT slope for the (2,3) BPE dimer is 4.12 $\pm$ 0.15 x 10^{-4} eV/K, and the slope for the LMCT band of the $[(NH_3)_5Ru^{III}(dmapy)]Cl_3$ monomer is -6.46 $\pm$0.29 x 10^{-4} eV/K). The larger red shift of the LMCT and the smaller relative blue shift of the MLCT band might therefore lead to an overall red shift in the IT band energy if the temperature effects were simply additive. This prediction is inconsistent, however, with the observed IVCT shifts of the dimmers shown in Figure 3.12 and 3.13. The dimer systems thus seem to be more complicated and cannot be explained by simply combining these two LMCT and MLCT energies since it appears that (especially for the (2,3) BPE dimer IVCT band shift) the relatively weaker MLCT band blue shift seen with the monomer somehow dominates the expected strong negative contribution from the LMCT red shift seen with the monomer. The IVCT band shift of the 2,3 BPY dimer falls closer to an average value between the MLCT and LMCT shifts, but it too comes out closer the positive MLCT value. We note also that from the Marcus-Hush expression for λ_0 shown in equation 1-10, we would expect λ_0 (and thus E_{IT}) to drop with increasing temperature for a symmetrical dimer since it is well-known that “Ds” always drop with increased temperature. Thus the explanation of the temperature dependence of the optical ET process stands as an open question at this point and is clearly not related in a simple way to the behaviors of the MLCT

and LMCT processes. Further more, we not that this behavior contradicts expectations based on extrapolation of the salt-induced changes to the water structure as well. Fluoride, a “structure maker” with a positive Jones-Dole “B” coefficient, gives us a blue shift in what is presumably “stiffer” water with increased structure, yet heating a solution of dimer with no added salt also gives rise to a blue shift even though the overall H-bonding network necessarily becomes weakened at higher temperature.

3.4 Conclusions

In this chapter, we have shown that the IT bands of ruthenium mixed-valence dimeric complexes exhibit distinctly-different halide ion effects depending on the identity of the added halide. F^- gives rise to a consistent blue shift while the heavier halides red shift the IT bands of both dimers. As shown in Figures 3.9 and 3.10, the shifts correlate with the known water structure “making” or “breaking” effects of the added halide anions.

Comparing the effects of added halides on the MLCT band of the monomeric complex $[(NH_3)_5Ru^{II}py]Cl_2$ and the LMCT of $[(NH_3)_5Ru^{III}(dmapy)]Cl_3$ indicate that the halide effects on the IT bands of the dimers are most closely related to the LMCT transition. Thus the water structure “making” behavior of F^- and “breaking” behaviors of the other added halides seem to exert their strongest influence at the Ru(III) site (presumably due to their effects on its hydration sphere).

Temperature dependent experiments in water alone show a more

complicated pattern. There is a positive temperature coefficient for the energy dependence of the BPE dimer IT band, but almost no temperature dependence in the BPY dimer case. The MLCT bands of the 2,3-BPE dimer and the $[(NH_3)_5Ru^{II}py]Cl_2$ monomer both show positive temperature coefficients, while the LMCT band of the $[(NH_3)_5Ru^{III}(dmapy)]Cl_3$ monomer shows a stronger negative temperature dependent effect. So, in this case, the dimer IT band energies are shifting more like the MLCT bands do (or somewhere in between as with the BPY dimer). This latter observation stands as an unresolved puzzle and the results will need to be repeated and extended before an interpretation can be advanced.

References

1. (a) Creutz, C. *Prog. Inorg. Chem.* **1983**, *30*, 1

   (b) Taube, H. *Ann.* N.Y. *Acad. Sci.* **1978**, *313*, 481

2. (a) Creutz, C.; Taube, H. *J. Am. Chem. Soc.* **1969,** *91*, 3988

   (b) Creutz, C.; Taube, H. *J. Am. Chem. Soc.* **1973,** *95*, 1086

3. (a) D'Alessandro, D. M.; Davies, M. S.; Keene R. F. *Inorg. Chem.* **2006***, 45,* 1656

   (b) D'Alessandro, D. M.; Keene R. F. *Chem. Rev.* **2006**, *106*, 2270-2298

4. Hush, N. S. *Prog. Inorg. Chem.* **1967**, *8*, 391-444.

5. Curtis, J. C.; Sullivan, B. P.; Meyer, T. J. *Inorg. Chem.* **1980**, *19*, 3833-3839

6. (a) D'Alessandro, D. M.; Dinolfo, P. H.; Davies, M. S.; Hupp, J. T.; and Keene R. F. *Inorg. Chem.* **2006***, 45,* 3261

   (b) Yokogawa, D.; Sato, H.; Nakao,Y. and Sakaki, S. *Inorg. Chem.* **2007**, *46*, 966

(c) Isied, S. S; Vassilian, A. and Wishart, J. F. *J. Am. Chem.* Soc. **1988**, *110,* 635

(d) Fischer, H.; Tom, G. M. and Taube, H. *J. Am. Chem. Soc.* **1976**, *98,* 5512

(e) Reimers, J. R. and Hush, N. S. *J. Phys. Chem. A* **1999**, *103,* 3066-3072

(f) Stein, A. C.; Lewis, N. A. and Seitz, G. *J. Am. Chem. Soc.* **1982**, *104,* 2596

(g) Brown, G. M.; Sutin, N. *J. Am. Chem. Soc*. **1979**, *101*, 883

7. (a) Hupp, J. T.; Weydert, J. *Inorg. Chem.* **1987**, *26*, 2657-2660

(b) Blockbourn, R. L.; Hupp, J. T. *J. Phys. Chem.* **1988**, *92,* 2817-2820

(d) Hupp, J. T.; *J. Am. Chem. Soc.* **1990**, *112,* 1563-1565

(e) Hupp, J. T.; Dong, Y.; Blackbourn, R. L.; Lu, H. *J. Phys. Chem.* **1993**, *97,* 3278-3282

(f) Matyushov, D. V. and Schmid, R. *J. Phys. Chem.* **1994***, 98,* 5152-5159

(g) Todd, M. D.; Yuhua Dong, Y. and Hupp, J. T. *Inorg. Chem.* **1991**, 30, 4685

8. (a) Dong, Y.; Hupp, J. T. *Inorg. Chem.* **1992**, *31,* 3322-3324

(b) Hupp, J. T.; Neyhart, G. A.; Meyer, T. J.; Kober, E. M. *J. Phys. Chem.* **1992**, *96,* 10820-10830

(c) Hupp, J. T.; Dong, Y. *J. Am. Chem. Soc.* **1993**,*115*, 6428-6429

(d) D'Alessandro, D. M.; Kelso, S. L.; Keene R. F. *Inorg. Chem.* **2001**, *40,* 6841

(e) Vath, P. and Zimmt, M. B. *J. Phys. Chem. B* **1999**, *103,* 9130

9. (a) Lewis, N. A. and Obeng, Y. S. *J. Am. Chem. Soc.* **1988**, *110,* 2307

10. (a) Fellows E. A. and Keene R. F. *J. Phys. Chem. B* **2007**, *111,* 6667-6675

(b) Piotrowiak, P. and Miller, J. R. *J. Phys. Chem.* **1993***, 97,* 13052-13060

11. Hush, N. S. *Electrochim. Acta* **1968**, *13,* 1005-1023.

12. Curtis, J. C.; Sullivan, B. P.; Meyer, T. J. *Inorg. Chem.* **1983**, *22*, 224

13. Blackbourn, R. L.; Dong, Y.; Lyon, L. A.; Hupp, J. T. *Inorg. Chem.* **1994**, *33*, 4446-4452

14. Marcus, Y. *Chem. Rev.* **2009**, *109*, 1346-1370

15. Lau, K. W.; Aron M-H. H.; Yen, M. H-J.; Fung, E.Y.; Grzybicki, S.; Matamoros, R.; Curtis, J.C. *Inorg. Chim. Acta* **1994**, *226*, 137

16. Sista. P. Master's Thesis, University of San Francisco

17. Qin, Y. Master's Thesis, University of San Francisco

18. Jones, G.; Dole, M. *J. Am. Chem. Soc.* **1929**, *51*, 2950

19. Sutton, J.; Taube. H. *Inorg. Chem.* **1981**, 20, 3125

20. Chang, J.P.; Fung, E.Y.; Curtis, J.C. *Inorg. Chem.* **1986**, *25*, 4233

21. Fabrizio, A.S.; Doran, S; Curtis, J.C. work in progress.